THE UNIVERSITY OF CHICAGO

URANIUM ISOTOPE VARIATIONS TRACING OCEANIC ANOXIA AND ZIRCONIUM AND HAFNIUM ISOTOPE VARIATIONS TRACING PLANETARY DIFFERENTIATION PROCESSES

A DISSERTATION SUBMITTED TO

THE FACULTY OF THE DIVISION OF THE PHYSICAL SCIENCES

IN CANDIDACY FOR THE DEGREE OF

DOCTOR OF PHILOSOPHY

DEPARTMENT OF THE GEOPHYSICAL SCIENCES

BY

XI CHEN

CHICAGO, ILLINOIS

MARCH 2022

Table of Contents

LIST OF FIGURES.....IV

LIST OF TABLES……...XIV

ACKNOWLEDGEMENT XV

ABSTRACT XVII

1 INTRODUCTION 1

1.1 U ISOTOPES AS A PALEO-REDOX PROXY 1
1.2 EMERGING ZIRCONIUM AND HAFNIUM STABLE ISOTOPES 6
1.3 REFERENCES 12

2 URANIUM ISOTOPE VARIATIONS TRACING OCEANIC ANOXIA. 28

2.1 INTRODUCTION 29
2.2 MATERIALS AND METHODS 30
2.2.1 Sample Selections 30
2.2.2 Sample preparation 38
2.2.3 Uranium extraction chromatography 39
2.2.4 Uranium mass spectrometry 39
2.3 RESULTS 41
2.4 DISCUSSION 51
2.4.1 Excess $\delta^{234}U$ in ancient carbonates 51
2.4.2 U concentration and isotopic records through time 54
2.4.3 Residence time for U in Archean and Proterozoic oceans 58
2.4.4 Mixing time in Archean and Proterozoic oceans 81
2.4.5 Non-uniformitarian U isotopic fractionation during deposition of Precambrian black shales 85
2.5 CONCLUSIONS 91
2.6 APPENDIX 93
2.6.1 Geological Settings of Samples 93
2.7 REFERENCES 114

3 ZIRCONIUM AND HAFNIUM ISOTOPE VARIATIONS TRACING PLANETARY DIFFERENTIATION PROCESS 143

3.1 INTRODUCTION 144
3.2 METHODS 145

3.2.1 Equilibrium mass-dependent isotopic fractionation 145
3.2.2 First-principle calculations 147
3.2.3 Mineral structures 150
3.3 RESULTS 162
3.4 DISCUSSION 173
3.4.1 Equilibrium Zr isotopic fractionation during zircon crystallization from silicate melts 174
3.4.2 Equilibrium Zr isotopic fractionation before the onset of zircon crystallization in melts 181
3.4.3 Diffusion-driven kinetic isotopic fractionations during crystal growth from silicate melt 190
3.4.4 Combined Zr and Hf fractionations 214
3.4.5 Potential usage in metamorphic zircons 215
3.5 CONCLUSION 215
3.6 APPENDIX 216
3.6.1 Derivation of diffusion-driven kinetic isotopic effects produced by the accumulation of an incompatible element in a diffusive boundary layer 216
3.7 REFERENCES 221

4 LU-HF MEASUREMENTS OF SINGLE ZIRCON GRAINS 234

4.1 INTRODUCTION 235
4.2 METHODS 236
4.2.1 Zirconium and Hafnium separation 236
4.2.2 Mass spectrometry for Hf isotopic analyses 239
4.3 RESULTS AND DISCUSSIONS 240
4.3.1 Correction of interferences and internal normalization for Hf isotopes 240
4.3.2 Achievable precision tests 241
4.3.3 Terrestrial zircon standards 244
4.3.4 Lunar zircons 245
4.4 CONCLUSIONS 254
4.5 REFERENCES 255

5 CONCLUSIONS 257

SUPPLEMENTARY MATERIALS (AVAILABLE ONLINE)

LIST OF FIGURES

Figure 2.1 (A). [U] in carbonates through time. [U] data measured in this study (orange diamonds = limestones; blue diamonds = dolostones) are for the leached carbonates fractions (U per unit mass of carbonate dissolved; see detail in Section 2.2.2). Grey diamonds are [U] literature data (see compilation in Supplementary Table 1). The red bars are the median uranium concentrations of carbonates in the six intervals of 3.25-2.43 Ga (preGOE), 2.43-2.06 Ga (GOE), 2.06-0.8 Ga (postGOE-preNOE), 0.8-0.68 Ga (ruNOE, ramp up to NOE), 0.68-0.54 Ga (NOE), and 0.54 Ga- 42

Figure 2.2 $\delta^{238}U$ in carbonates through time. $\delta^{238}U$ data measured in this study on leached carbonates fraction are displayed as orange diamonds for limestones and blue diamonds for dolostones. For both [U] and $\delta^{238}U$, the data shows no systematic difference between dolostones and limestones in the Precambrian. Grey diamonds are literature data (see Supplementary Table 1). $\delta^{238}U$ of the continental crust (-0.29 ± 0.03‰) and modern seawater (-0.392 ± 0.005‰, (Tissot and Dauphas, 2015)) are shown for comparison. The red lines are the median uranium isotopic composition of carbonates in the same six intervals as shown in Fig. 2.1. The purple dashed line shows the first-order expected $\delta^{238}U$ value (-0.9 ‰) of carbonates and seawater in a steady-state ocean if the uranium oceanic sink is predominantly anoxic (the U fraction going into anoxic sediment is close to 100%). Contrary to expectations, carbonates show $\delta^{238}U$ values similar to 43

Figure 2.3 Histograms of [U] (left) and $\delta^{238}U$ (right) values in shallow-marine and deep-marine carbonates in our sample set. Most of the samples are shallow-marine carbonates, which were deposited above the storm- and fair-weather-wave base. Two sample sets were inferred to deposited in a deeper environment and are designated in the histogram as "deep-marine". Although the number of deep-marine carbonates is limited, the current dataset shows that there is no difference in [U] and $\delta^{238}U$ values between the two groups. 46

Figure 2.4 (A). $\delta^{238}U$ *vs*. [U] in carbonates. Data are from this study and literature (see Supplementary Table 1). The distribution of the U data clearly shows that there are differences in the U oceanic cycle and reservoir size before and after NOE (~ 0.54 Ga), while differences among other time intervals are not clear based on the current dataset. (B). $\delta^{238}U$ *vs*. U fraction in carbonates (fU). Neither $\delta^{238}U$ *vs*. [U], nor $\delta^{238}U$ *vs*. fU show any correlation that point to contamination by a detrital component. 47

Figure 2.5 $\delta(^{234}U/^{238}U)$ in Precambrian carbonates. Symbol colors as in Fig. 2.1. The purple horizontal line shows the secular equilibrium value (0 ‰), and the blue line shows the modern seawater value of ~145‰ (*e.g.* (Ku et al., 1977; Chen et al., 1986; Andersen et al., 2010)). Many of the $\delta(^{234}U/^{238}U)$ values of the carbonates measured in this study are much larger than the seawater value, suggesting that these excesses cannot be simply explained by post-depositional alteration by seawater alone. They most likely reflect recoil of ^{234}U into the carbonate fraction from the detrital fraction (see Fig. 2.7 and main text for details). 49

Figure 2.6 (A). [U] *vs*. $\delta(^{234}U/^{238}U)$ and (B) $\delta^{238}U$ *vs.* $\delta(^{234}U/^{238}U)$ in the Precambrian carbonates measured in this study. The lack of correlation between these data suggests that the factor responsible for the $\delta(^{234}U/^{238}U)$ excesses in the sample had no impact on their [U] and $\delta^{238}U$ values. 50

Figure 2.7 $\delta(^{234}U/^{238}U)$ value in the carbonates measured in this study as a function of the ratio of U mass fractions in detritus and carbonate. The different lines correspond to predicted excesses due to alpha-recoil for different effective detritus grain sizes (r) (see Section 2.4.1 for details). The $\delta(^{234}U/^{238}U)$ value of our Precambrian carbonates show a broad correlation with the calculated index ($Udetritus \times fdetritusUcarbonate \times fcarbonate$) of each sample, and the dispersion in the data can be explained by different detrital grain sizes, suggesting that the ^{234}U excesses observed in the carbonates were most likely caused by the alpha-recoil effect from the detrital fraction of the sediments. 53

Figure 2.8 (A). $\delta^{238}U$ in carbonates, shales, and iron-rich sedimentary rocks through time. $\delta^{238}U$ in carbonates are from this study and the literature (as in Figs. 2.1 and 2.2). $\delta^{238}U$ values for shales and iron-rich sedimentary rocks are from the literature (see compilation in Supplementary Table 1). If no $\delta^{238}U_{auth}$ were reported, the data were all corrected for detrital contribution using the method described in (Asael et al., 2013). Samples with Al/U ratio larger than the detrital ratio were excluded from this figure. (B). The two broad bands illustrate the expected $\delta^{238}U$ trends in carbonates and shales under the assumption of constant offset between anoxic sinks and seawater (which is based on our current understanding of the modern seawater U cycle). The differences between the observed trends and the expected ones show that the assumption of a constant offset between anoxic sediments and seawater might not be valid for the Precambrian, and great care should be exercised when applying knowledge of the modern U isotopic cycle to periods in Earth's history when the extent of anoxia was much greater than at the present. 57

Figure 2.9 Seawater depth *vs*. seafloor area above that depth (ζm function in the main text). The blue curve is the modern Global Topography V19.1 database ((Smith and Sandwell, 1997)). The orange line is an approximate best fit line (Eq. 2.21). 62

Figure 2.10 Modeled U residence time with increasing seafloor anoxia based on the assumption of constant modern-like U riverine flux after the GOE ((Reinhard et al., 2013) with different θa exponents. The blue box shows the probable ocean mixing timescale range in the Precambrian (0.1-10 kyr, see discussion in Section 2.4.4). The thick solid lines are those that yield realistic U concentrations in carbonates and shales (see Fig. 2.12). 65

Figure 2.11 U concentration in seawater modeled in method 1 using Eq. 2.25. The blue dashed line is the modern seawater concentration. 66

Figure 2.12 U concentrations predicted in carbonates (A) and black shales (B) using modeled $[U]sw,t$ in method 1 and Eqs. 2.28, 2.32. The thick solid lines in Fig. 2.10 are parameters that yield (*i*) $38\ ppb \leq [U]carb \leq 1075\ ppb$ for the postGOE-preNOE (see also Fig. 2.1A, note that

the lower bound of 38 ppb are the 5th percentile $[U]_{carb}$ (ppb) of the measured values, while upper bound of 1075 ppb are the 95th percentile $[U]_{carb}$ (ppb) of the measured values), and (*ii*) yield .. 66

Figure 2.13 Modeled U residence time with increasing seafloor anoxia using authigenic U enrichment in shales with different assumptions for the sedimentation rates (top panels S=5, middle panels S=33, and bottom panels S=100 m/Myr) in the Archean (left) and mid-Proterozoic 70

Figure 2.14 U concentrations predicted in carbonates using modeled Usw,t in method 2 and Eq. 2.32. Each panel corresponds to the panel in Fig. 2.13. The thick solid lines in Fig. 2.13 correspond to parameters that yield $25\ ppb \leq Ucarb \leq 475\ ppb$ in the Archean and $38\ ppb \leq Ucarb \leq$. 72

Figure 2.15 U concentration in seawater calculated using black shale data and Eq. 2.29. Each panel corresponds to the panels in Fig. 2.13. The blue dashed line is the modern seawater concentration. 74

Figure 2.16 U input flux calculated using black shale data and Eq. 2.30. Each panel corresponds to the panel in Fig. 2.13. The blue dashed line is the U modern input flux. The thick solid lines in Fig. 2.13 correspond to parameters that yield U input flux in the Archean and mid-Proterozoic less than the modern value. 75

Figure 2.17 (A) Secular evolution of Mg/Ca in seawater (Halevy and Bachan 2017; Hardie 1996, 2003) and U concentrations in carbonates (average values binned in ~100 Ma), the grey dashed line at $(Mg/Ca)_{sw} = 2$, is the divide between aragonite and calcite seas. (B) [U] in carbonates *vs*. Mg/Ca in seawater. Uranium concentration is generally low in Precambrian carbonates and there is no clear correlation between $[U]_{carb}$ and $(Mg/Ca)_{sw}$, suggesting that the influence of primary carbonate mineralogy on U enrichment in old samples is small. 78

Figure 2.18 Modeled U residence time with increasing seafloor anoxia using U in carbonates in the Archean (left) and mid-Proterozoic (right) (see text for details). Different lines correspond to different θa exponents. The residence times calculated here relax the assumption of a constant influx of U to the oceans made in plotting Fig. 2.10. The blue box shows the probable ocean mixing timescale range in the Precambrian (0.1-10 kyr, see discussion in Section 2.4.4). The thick solid lines correspond to parameters that yield realistic U concentrations in black shales (Fig. 2.19) and U input flux (Fig. 2.20). As shown, the residence time decreases with a greater extent of anoxia 79

Figure 2.19 U concentrations predicted in shales using modeled $[U]sw,t$ in method 3 and Eq. 2.28. Each panel corresponds to the panels in Fig. 2.18. The thick solid lines in Fig. 2.18 correspond to parameters that yield $0.04\ ppm \leq Ubs \leq 3.06\ ppm$ for Archean, and $0.1\ ppm \leq Ubs \leq 11.7\ ppm$ for mid-Proterozoic (see also Fig. 2.1B, note that the lower bound of 0.04, 0.1 ppm are the 5th percentile $[U]_{bs}$ (ppm) of the measured values, while upper bound of 3.06, 11.7 ppm are the 95th percentile $[U]_{bs}$ (ppm) of the measured values from Partin et al. 2013a). 80

Figure 2.20 U input flux calculated using carbonate data and Eq. 2.33. Each panel corresponds to the panels in Fig. 2.18. The blue dashed line is the U modern input flux. The thick solid lines in Fig. 2.18 correspond to parameters that yield U input flux in the Archean and mid-Proterozoic less than the modern value. 80

Figure 2.21 Cartoon showing the possible scenario for the observed U isotopic composition in Precambrian carbonates and shales. Due to the similar magnitudes of the U residence time in ancient seawater and ocean mixing timescale, $\delta^{238}U$ values in carbonates and shales may not necessarily reflect the global redox state of the ocean, but instead only provide information about the provenance of U where the carbonates or shales were deposited. 85

Figure 2.22 U-speciation-induced secular variations of U isotopic fractionation factors. Panel (A) shows the U speciation through geologic time calculated using the PHREEQC program. Panel (B) shows the predicted influence of speciation on carbonate-seawater (Chen et al. 2016, 2017), shale-seawater (Brown et al. 2018), and carbonate-shale $\delta^{238}U$ values using the calculated proportions of U species. 89

Figure 3.1 Comparison of the calculated vibrational frequencies with experimental data (Raman spectra) with the same vibrational modes. Experimental data sources: zircon (Syme et al., 1977; Gucsik et al., 2004); baddeleyite (Quintard et al., 2004). 161

Figure 3.2 (A) Zr mean force constant (N/m) as a function of Zr coordination number in minerals calculated in this study. Lower coordination number generally corresponds to higher force constant 163

Figure 3.3 Polynomial expansion coefficient (left) A_2 vs $F2$ and (right) A_3 vs $F3$ for $1000\ln\beta(^{94}Zr/^{90}Zr)$. The regressions give the estimated values of B_2 and B_3 in the one-parameter approximate formula (see eq. 3.9 and 3.10)..... 165

Figure 3.4 Relative error in the high temperature approximation $1000ln\beta = B1F/T2$ (Eqs. 3.6, 3.7) calculated using the 1-parameter 3-term expansion $1000\ln\beta = B1F/T2 + B2F2/T4 + B3F3/T6$ (Eqs. 3.10, 3.12). The curves were calculated following Dauphas et al. (2012) for different values of T and F. (A) Relative departure from Eq. (3.10) when truncating the polynomial to the first order for Zr. The force constants of Zr bonds in all calculated minerals are between 280 and 566 N/m (red dashed lines). When the temperature is higher than ~300-500 ℃, truncating the expansion to the first order (Eq. 3.6) will give a $1000\ln\beta$ value that is within 1% of the value given by the whole expansion (Eq. 3.4). (B) Relative departure from Eq. (3.12) when truncating the polynomial to the first order for Hf. When the temperature is higher than ~300-500 ℃, truncating the expansion to the first order (Eq. 3.7) will give a $1000\ln\beta$ value that is within 1% of the value given by the whole expansion (Eq. 3.4). The high temperature approximation can be applied to calculate equilibrium Zr and Hf isotopic fractionation in igneous and metamorphic geochemistry/petrology without compromising accuracy. 166

Figure 3.5 Differences of Zr $1000\ln\beta$ between (A) the 1-parameter 3-term expansion (eq. 3.9) and the full polynomial expansion equation (eq. 3.4), and (B) the 1-parameter 1-term high-temperature approximation (eq. 3.9 truncated to the first term) and the full polynomial expansion equation (eq. 3.4). 167

Figure 3.6 (A) Temperature-dependent $1000\ln\beta$ for Zr isotopes in minerals investigated in this study. (B) Temperature-dependent $1000\ln\alpha_{\mathrm{mineral-melt}}$ for Zr isotopes in the same set of minerals. The fractionation factors between minerals and melt are calculated by taking the difference between each mineral and Ca-catapleiite (which we use as silicate melt proxy). The calculation results for minerals with different Zr substitution mechanisms as well as different Zr concentrations are also shown in the figure. See main text and Table 3.2 for details. 169

Figure 3.7 (A) Temperature-dependent $1000\ln\beta$ for Hf isotopes in zircon, ilmenite and Ca-catapleiite investigated in this study. (B) Temperature-dependent $1000\ln\alpha_{\mathrm{mineral-melt}}$ for Hf isotopes in zircon and ilmenite. As with Zr isotopes, the fractionation factors between minerals and melt are calculated by taking the difference between each mineral and Ca-catapleiite (which we use as silicate melt proxy). Solid and dash lines are calculation results for minerals with different Hf concentrations (see Table 3.2 for details). Our results show that Hf stable isotope fractionation during equilibrium process is very limited. 170

Figure 3.8 Zr and Hf mean force constants in several minerals (zircon, ilmenite with two concentrations, Ca-catapleiite). The current calculation results indicate that in minerals, Zr and Hf form bonds with nearly identical bond strengths. The black dashed line is the 1:1 line and the green dotted line is a regression through the data. 171

Figure 3.9 Polynomial expansion coefficient (left) A_2 vs $F2$ and (right) A_3 vs $F3$ for $1000\ln\beta(^{179}\mathrm{Hf}/^{177}\mathrm{Hf})$. The regressions give the estimated values of B_2 and B_3 in the one-parameter approximate formula (see eq. 3.9 and 3.12). 172

Figure 3.10 Same as Figure 3.5 but for Hf rather than Zr. 173

Figure 3.11 Zr isotope equilibrium fractionation factor between zircon and melt as a function of temperature. The two vertical dash lines bracket the temperatures relevant to igneous zircon crystallization of around 700-1000 °C. 177

Figure 3.12 $\delta'^{94}\mathrm{Zr}$ in the instantaneous zircon and melt during Rayleigh distillation process at two temperatures of 700 and 1000 °C. fZr is the fraction of Zr remaining in the melt (see Eq. 3.18). $1-\mathrm{fZr}$ is the fraction of Zr in zircon. 180

Figure 3.13 Calculated trends of ZrHf and $\delta'^{94}\mathrm{Zr}$ variations in instantaneous zircon assuming melt-zircon equilibrium at each step of a distillation. The free parameters are the fraction of Zr remaining in melt (fZr from 0.99 to 0.01) and the crystallization temperature. The calculations are 180

Figure 3.14 Evolution of Zr concentration remaining in the melt (blue and orange curves) and zircon saturation during fractional crystallization of a (A) calc-alkaline and (B) tholeiitic magmas. Calculations are done with different bulk partition coefficients (K) using the modeled mineral assemblage results of the Rhyolite-MELTS program (i.e., Fig. 3.15). The zircon saturation curves (green and gray lines) were calculated using Watson and Harrison (1983) and Boehnke et al. (2013) and taking the melt major-element compositions and temperature from the Rhyolite-MELTS program as input. The initial compositions used in Rhyolite-MELTS modeling are (A) calc-alkaline (Millet et al., 2016) (in wt%) SiO_2: 49.7; TiO_2: 0.99; Al_2O_3: 18.39; Fe_2O_3: 2.13; Cr_2O_3: 0; FeO: 9.00; MnO: 0.19; MgO: 5.46; CaO: 8.94; Na_2O: 2.49; K_2O: 0.69; P_2O_5: 0.19; H_2O: 1.78; P: 1 kbar; (B) tholeiitic (Helz et al., 1994) (in wt%) SiO_2: 47.78; TiO_2: 1.98; Al_2O_3: 17.31; Fe_2O_3: 1.22; Cr_2O_3: 0.04; FeO: 7.66; MnO: 0; MgO: 8.92; CaO: 12.2; Na_2O: 2.58; K_2O: 0.02; P_2O_5: 0.07; H_2O: 0.2; P: 0.6 kbar. 183

Figure 3.15 Mass fractions of Zr in crystallized minerals and melt as a function of the mass fraction of Zr remaining in melt for (A) calc-alkaline and (B) tholeiitic magmas. Before zircon crystallization, only a small fraction of Zr is removed from the melt (mostly in clinopyroxene and feldspar), and here we use the geometric mean of the partition coefficients for each mineral. These calculations were run before zircon saturation (see Fig. 3.14). 184

Figure 3.16 (A) Zr and (B) Hf concentration and (C) Zr/Hf (weight ratio) evolutions during magmatic differentiation along calc-alkaline and tholeiitic series. Modeling was done using Rhyolite-MELTS and the results are compared with Andes (calc-alkaline) and Iceland (tholeiitic) rocks (compiled from the GEOROC database). The darker color trends were calculated using the geometric mean of the partition coefficients compiled in GERM database, while the bracketing lighter color trends correspond to minimum and maximum partition coefficients. 186

Figure 3.17 Fractions of Zr (left) and Hf (right) remaining in the melt as a function of the mass fraction of the residual melt for calc-alkaline magma during fractional crystallization before zircon starts to crystallize. These curves were calculated with the Rhyolite-MELTS program (see Section 3.4.2. for details). 187

Figure 3.18 Same as Fig. 3.17 but for a tholeiitic magma. 187

Figure 3.19 Modelled evolution of the Zr isotopic composition of residual melt before zircon crystallization for (A) calc-alkaline and (B) tholeiitic magmas. The Zr isotopic fractionation factors between minerals and melt from our *ab initio* calculations were used in the modeling, using results from Rhyolite-MELTS as input (Fig. 3.15). The different trends are mainly caused by two factors: (i) the various bulk Zr partition coefficients used in our calculations and (ii) the different isotopic fractionation factors calculated using different substitution mechanisms for Zr in several silicate minerals. The blue lines labelled Si-Zr are calculated using $1000\ln\beta$ values for olivine, cpx and opx using the $^{IV}Si^{4+} \leftrightarrow Zr^{4+}$ substitution with minimum, mean, and maximum mineral/melt K values. The yellow lines are calculated using $1000\ln\beta$ values in olivine, cpx and opx using the $^{VI}Mg^{2+} + {}^{VI}Mg^{2+} \leftrightarrow Zr^{4+} + \square$ substitution with minimum, mean, and maximum mineral/melt K

values. In all cases, the Zr isotopic compositions of the melts evolve towards lighter values before zircon starts to crystallize but the magnitude of this fractionation is relatively small given the current analytical precision on δ' 94Zr measurements (~±0.01 to ±0.04 ‰, Ibañez-Mejia and Tissot 2019). 189

Figure 3.20 Schematic models of diffusive Zr isotopic fractionation during crystallization. Left panel: In the diffusion-limited crystallization model (DLC), the growth of zircon is limited by the diffusive supply of Zr to the surface from a far-field medium that is supersaturated. Because the light isotopes diffuse faster than the heavier ones, the liquid at the interface with the zircon will have low δ' 94Zr, while further away from the interface the liquid will have high δ' 94Zr. This model would predict zircons to have low δ' 94Zr but reservoir effects in the liquid would also lead to the crystallization of zircons with high δ' 94Zr. Right panel: In the diffusion-triggered crystallization model (DTC), the growth of a Zr-poor mineral would push Zr away from the interface and lead to high δ' 94Zr at the interface in the liquid and low δ' 94Zr further away. The whole diffusive boundary layer would have elevated Zr concentration. This could trigger the saturation and crystallization of zircon, which would inherit some of the fractionated Zr isotopic composition from the diffusive boundary from which they grew. 192

Figure 3.21 β exponents as a function of the ratio of cation diffusivities normalized by those of Si in silicate melt (modified from Watkins et al. (2017)). The β exponents for Zr and Hf isotopes were estimated by linearly regressing this trend to $\ln[D\mathrm{Zr}D\mathrm{Si}]$ and $\ln[D\mathrm{Hf}D\mathrm{Si}]$ ~0 because the diffusivities of both Zr and Hf are close to Si (Zhang et al., 2010). The two grey lines are the 95% prediction intervals. This empirical correlation correlates the degree of diffusion-driven isotopic fractionation (β) with a measure of solute-solvent interaction $\ln[D\mathrm{i}D\mathrm{Si}]$ (Watkins et al., 2017). In aluminosilicate melt, the solvent molecule is SiO44-, which is the reason why the quantity $\ln[D\mathrm{i}D\mathrm{Si}]$ is used to describe solute-solvent interaction. 193

Figure 3.22 Zr concentration (A) and isotopic composition (B) profiles in the liquid away from the interface of a growing zircon in a diffusion-limited regime (DLC model) at the time when the zircon has reached 10 μm in size (the blue line is the liquid-solid interface). The red dot is the liquid concentration and isotopic composition at the interface. Both concentration and isotopic composition are relative to the liquid at infinity. As zircon grows from a supersaturated medium, the liquid and crystal near the liquid-crystal interface get enriched in the light isotopes of Zr due to their faster diffusion, while the liquid further away in the diffusive boundary layer gets enriched in the heavy isotopes due to their slower diffusion. The calculations were done using Eqs. 55, 49, 50 for diffusion-limited growth in a spherical geometry (Dauphas and Rouxel, 2006) with a Zr diffusivity of $\mathrm{D} = 10 - 4\ \mu\mathrm{m}2/\mathrm{s}$ (Zhang and Xu, 2016), Zr saturation concentrations $\mathrm{Csat} = 1806$ ppm (Boehnke et al., 2013), Zr concentration in zircon of 500,000 ppm, and a supersaturation $S = C \infty Csat = 7.8$, a diffusive Zr isotopic fractionation factor $\Delta D = -4.9$ ‰ ($\beta Zr = 0.113$ in Eq. 3.24). (A and B correspond to Movie 1 and 2). 198

Figure 3.23 Expected δ' 94Zr variations in zircon as a function of the degree of supersaturation during diffusion-limited zircon growth from silicate melt with different diffusive β exponents for

Zr isotopes (Eq. 3.26). δ'^{94}Zrzircon is the isotopic composition in the crystal relative to that in the far-field growth medium. 199

Figure 3.24 Expected δ'^{94}Zr fractionations in zircon as a function of growth rate at different temperatures and different supersaturations (Eqs. 3.26 and 3.30). (A)-(B) use a diffusive Zr isotopic fractionation factor $\Delta D = -2.3$ ‰ ($\beta Zr = 0.054$ in Eq. 3.24); (C)-(D) use a diffusive Zr isotopic fractionation factor $\Delta D = -4.9$ ‰ ($\beta Zr = 0.113$ in Eq. 3.24). δ'^{94}Zrzircon is the isotopic composition in the crystal relative to that in the far-field growth medium. This figure shows that measuring δ'^{94}Zrzircon can help estimate the degree of supersaturation and zircon growth rate if the temperature can be independently constrained. 200

Figure 3.25 Evolution of the Zr concentration (A) and isotopic composition (B, C) in a growing Zr-poor crystal (blue line) and in the surrounding melt growth medium (black line) in three snapshots taken at 0.6, 1.9, and 3.2 kyr (DTC model; see Sect. 2.4.3.2. for details). The concentration and isotopic composition are normalized to the far-field growth medium. The diffusive boundary layer has elevated Zr concentration, which could trigger zircon saturation and crystallization, thus inheriting the isotopic composition in the diffusive boundary layer. The curves were calculated using Eqs. 3.31-34, and A21, A23. We used the partition coefficient of clinopyroxene $K = 0.08$ (the geometric mean of the values compiled in GERM database), diffusivity for Zr in melt $D = 10 - 4\ \mu m2/s$ at 950 ℃ (Zhang and Xu, 2016), a growth rate of $R = 10 - 7 \mu m/s$ (so that $RD = 10\ cm - 1$ which is in the realm of possibilities (Watkins et al. 2017)), and a diffusive isotopic fractionation factor $\Delta D = -2.3$ and -4.9 ‰ ($\beta Zr = 0.054$ and 0.113 in Eq. 3.24, respectively). (A, B and C correspond to Movie 3, 4 and 5). 207

Figure 3.26 Same as Fig. 3.25 but for a longer duration allowing the system to achieve steady-state (note that this calculation is not aimed at reproducing natural conditions as crystals would stop growing before reaching steady-state). Zr concentration (A) and isotopic composition (B, C) in the growing Zr-poor crystal (blue line) and in the melt growth medium (black line) in three snapshots taken at 6, 19, and 32 kyr. Note the difference in x-axis scale with Fig. 3.25. (A, B and C correspond to Movie 6, 7 and 8). 209

Figure 3.27 Same as Fig. 3.25 except that we use the partition coefficient of plagioclase $K = 0.004$ (the geometric mean of the values compiled in GERM database)..... 211

Figure 3.28 Same as Fig. 3.26 except that we use the partition coefficient of plagioclase $K = 0.004$ (the geometric mean of the values compiled in GERM database), and the three snapshots are taken at 126, 380, and 634 kyr..... 212

Figure 3.29 Expected probability density distribution functions (PDFs) of the Zr isotopic compositions of Zr atoms in the diffusive boundary layer around a low-Zr growing crystal at 4 and 7 kyr. The dashed red vertical line is the average isotopic composition of the boundary layer where the melt is Zr-supersaturated by at least of factor of 3. We only consider here locations where $CC0 > 3$ possibly conducive to zircon saturation. (A)-(B) use a diffusive Zr isotopic fractionation

factor $\Delta D = -2.3$ ‰ ($\beta Zr = 0.054$ in Eq. 3.24); (C)-(D) use a diffusive Zr isotopic fractionation factor $\Delta D = -4.9$ ‰ ($\beta Zr = 0.113$ in Eq. 3.24). As the Zr-poor mineral grows (time increases from (A) to (B), or from (C) to (D)), the δ' 94Zr distributions of the diffusion-triggered crystallized (DTC) zircons shift to more negative δ' 94Zr values. (A, B and C, D correspond to Movie 9 and 10). 213

Figure 4.1 The elution curve of a multi-element standard solution on a 0.35 mL Teflon column loaded with Ln-Spec resin. Matrix elements were removed with 12 mL of 6 N HCL + 1 % H_2O_2. Zirconium was first eluted in 22 mL of 6 N HCL + 0.06N HF. Hafnium was finally eluted in 7 mL of 6 N HCL + 0.2 N HF. 238

Figure 4.2 The elution curve of terrestrial zircon standard AS3 retrieved after U-Pb chemistry on a 0.35 mL Teflon column loaded with Ln-Spec resin. Matrix elements were removed with 12 mL of 6 N HCL + 1 % H_2O_2. Zirconium was first eluted in 18 mL of 6 N HCL + 0.06N HF. Hafnium was finally eluted in 7 mL of 6 N HCL + 0.2 N HF. 239

Figure 4.3 The measurement uncertainties (2σ) of ε^{176}Hf as a function of (A) ^{177}Hf signal intensity; (B) corresponding Hf concentration in the measured solutions (at the sensitivity of 0.22V for ^{177}Hf (18.60%) at 1ng/g (ppb) for Hf with a sample uptake rate of ~100 μL/min). The solid blue line is the theoretically achievable precision on ε^{176}Hf by calculating the isotope ratio uncertainties resulting from counting statistics and Johnson noise (Dauphas et al., 2014). The pink dashed line is where the 2σ equals 0.5ε. The internal and external errors from actual measurements agree well with the theoretically achievable precisions, which demonstrates that the current instrumental setup is already at the best conditions for Hf isotopes measurements using MC-ICP-MS. 243

Figure 4.4 The relative difference to the literature values (expressed in ε^{176}Hf, Woodhead and Hergt 2005) of the four zircon references (AS3, 91500, MUD TANK and MUNZirc 32a) as a function of ^{177}Hf signal intensity. As the signal (correspondly Hf concentration) of the measured solutions increases, the differences between measurements of zircon standards and literature reported values (Woodhead and Hergt, 2005) become smaller along with smaller uncertainties. 245

Figure 4.5 The single zircon corrected $\varepsilon^{176}Hf_{CHUR}$ values as a function of the $\varepsilon^{176}Hf_{CHUR}$ values before neutron capture corrections. Each zircon $\varepsilon^{176}Hf_{CHUR}$ value in this study was corrected for neutron capture effects using the lunar zircon ε^{178}Hf, ε^{180}Hf and combing ε^{178}Hf and ε^{180}Hf values with the correlations derived from data reported by Sprung et al. (2013). The results show that the corrected $\varepsilon^{176}Hf_{CHUR}$ values using different NC-correction methods agree well with each other. 247

Figure 4.6 The single zircon $\varepsilon^{176}Hf_{CHUR}$ value as a function of $^{207}Pb/^{206}Pb$ zircon crystallization age (A) each zircon $\varepsilon^{176}Hf_{CHUR}$ value in this study was corrected for neutron capture effects using the lunar zircon ε^{178}Hf value with the correlation derived from data reported by Sprung et al. (2013); (B) similar as (A) except for using lunar zircon ε^{180}Hf value; (C) similar as (A,B) except

for combing lunar zircon $\varepsilon^{178}Hf$ and $\varepsilon^{180}Hf$ values for the correction of neutron capture effects. All the errors are 2σ. 251

LIST OF TABLES

Table 2.1 Sample age and locality, Mn/Sr, Mg/Ca ratios, stable isotopic compositions and U concentrations and isotopic composition for the carbonates measured in this study. 33

Table 2.2 Parameters used in U residence time modelling 63

Table 3.1 The k-point mesh used to calculate Brillouin zone summations over electronic states. 148

Table 3.2 Average Zr-O and Hf-O bond lengths, coordination numbers (CN), force constant of Zr and Hf in relaxed mineral structures, and polynomial expansion coefficients of the reduced partition function ratios ($10^3 \ln\beta$) of $^{94}Zr/^{90}Zr$ and $^{179}Hf/^{177}Hf$ of the studied minerals. 156

Table 3.3 Calculated cell parameters and volumes of zircon, baddeleyite, and Ca catapleiite under static conditions. 161

Table 4.1 Chromatographic extraction protocol of Zr and Hf 237

Table 4.2 Hf isotopic compositions of 9 lunar zircons 253

Table 4.3 Error contributions (%) of each term to the final error of ε176HfCHUR in zircon data 253

ACKNOWLEDGEMENT

I am greatly indebted to my advisor, Nicolas Dauphas, without whose help I could not have gone this far. I am very grateful for all the things that I have learned from him, for his passion and devotion to science that set a great example for every one of us, for his always availability for discussion and guidance, for his infinite novel ideas and extensive knowledge of this field which support me to explore deep into several interesting research work, for his strict and thorough efforts on high-quality publications and his dedication of time to help me work through a lot of problems.

I would also like to express my gratitude toward the members of my committee: Andrew Campbell, Andrew Davis, Frank Richter and Jacob Waldbauer, for their very helpful discussions and insightful comments to guide me in further improvements in each project.

I am really grateful to some other professors and scientists at UChicago: Fred Ciesla, Philipp Heck, Reika Yokochi, Dorian Abbot, Noboru Nakamura, David Archer, Douglas MacAyeal, Malte Jansen, Clara Blättler, for their kind help and wonderful collaborations.

I would also like to acknowledge the countless help and support from my former and current colleagues at the Origins Lab and beyond: Nicole Nie, Justin Hu, Francois Tissot, Nicolas Greber, Sarah Aarons, Timo Hopp, Aleisha Johnson, James Zhang, Andrew Heard, Hao Zeng, Matous Ptacek, Camilla Liu, Andrew Regula, Jennika Greer, Levke Koop, Krysten Villalon,

Xiufeng Ma, for their kind help in experiments and instruments, and their patient encouragement during my time of doubts.

I would like to extend my sincere thanks to former and current administrative staff: David Taylor, Katie Casey, Thomas Indelli, James Eason, Susan Hubbard, Jolene Hanchar, Victor Gavin, Sarah Lippert, Fahad Sajid, Ryan McNerney, for their timely help in administrative affairs and making us easier to focus on research.

And finally, my deepest gratitude to my parents and my families in Christ, for their selfless love, unconditional care and supportive accompany through a lot of up and downs during these years, for their filling up my memories of all the lasting sweetness that make this journey meaningful.

ABSTRACT

This dissertation is part of the efforts in developing novel non-traditional isotopic systems and applying them to enhance our understanding of the histories of our Earth and other planetary bodies. Specifically in this thesis I study the uranium isotopic variations in marine sediments to trace the oceanic anoxia in the ancient times, and I also study the zirconium and hafnium isotopic variations in igneous rocks and explore their potentials to trace magmatic differentiation processes.

U concentrations and isotopic compositions of a large sample set of old-age carbonates are measured and compared with compiled U datasets of shales and young-age carbonates. Several new modeling results are also presented to reconcile the measurement results of ancient samples with the common understanding of modern U oceanic cycle. This study points out the invalidity of applying some assumptions of modern models into the past time and also calls for more interesting modeling and experimental work (Chapter 2).

This dissertation also provides the first *ab initio* calculation results of the Zr, Hf equilibrium isotopic fractionation factors and they are readily to be used and applied in many interesting questions. Several equilibrium and kinetic modeling results are further presented to explain the documented Zr isotopic variations in igneous rocks and minerals. Our study shows that Zr equilibrium isotopic fractionation is negligible during zircon crystallization and magmatic differentiation, while the diffusion-driven kinetic isotopic fractionation can readily explain the actual observed data (Chapter 3).

Finally, this dissertation also presents an ongoing effort to develop high-precision and high-accuracy Hf isotopic measurements in individual zircon grains with low amount of Hf available.

The whole analytical procedure is improved and this novel method will be further applied on lunar zircons to provide better constraints on the differentiation age of the Moon (Chapter 4).

1 INTRODUCTION

As the advancement of powerful instrumentation (*i.e.* MC-ICP-MS) with improved analytical capabilities, the various non-traditional stable isotope systems have been widely explored and developed into powerful and unique tracers of different important physical processes. Distinct isotope systems have their own characteristics which can tell us specific information about their host samples, and more often it is multiple systematics that can powerfully provide a more complementary view of the questions under investigations. This dissertation is part of the effort using multiple non-traditional stable isotope systems to probe several fundamental questions on the origins as well as the natural processes that shaped our physical world. Specifically this dissertation focuses on applying the uranium isotope variation as a paleo-redox tracer, and developing the zirconium and hafnium stable isotopes to gain new insights on the cooling history of magma.

1.1 U isotopes as a paleo-redox proxy

Compared to the relatively well-understood oxygenation history of Earth's atmosphere, the timing and magnitude of oceanic oxygenation is still a matter of debate (*e.g.*, (Lyons et al., 2014)). Indeed, our understanding of the temporal dynamics and cause-and-effect relationships during critical redox transitions remains limited. Diverse proxies have been developed to address these questions, including the presence or absence of redox-sensitive detrital minerals such as pyrite,

uraninite, and siderite in terrestrial and coastal sandstones and conglomerates ((Ramdohr, 1958; Rasmussen and Buick, 1999)), variations in the elemental abundance of redox-sensitive elements in organic-rich shales (*e.g.*, Co, Cr, I, Mo, Re, U, V, and Zn; (Anbar et al., 2007; Scott et al., 2008; Sahoo et al., 2012; Partin et al., 2013a; Reinhard et al., 2013; Hardisty et al., 2014; Scott et al., 2014; Swanner et al., 2014; Hardisty et al., 2017)), variations in the isotopic composition of traditional stable isotopes in sedimentary rocks (*e.g.*, S, C, and N; (Holland, 2006; Farquhar et al., 2011, 2014)), and more recently, variations in the non-traditional stable isotopic compositions (*e.g.*, Fe, Mo, Cr, Se, and U; see the review chapters in (Teng et al., 2017)) of marine sediments (*e.g.*, shales, iron formations, sedimentary pyrites, and carbonates).

The ratio of the two long-lived isotopes of U ($^{238}U/^{235}U$; expressed as $\delta^{238}U$, which is the per mil $^{238}U/^{235}U$ deviation of a sample relative to the CRM-112a standard) has been extensively used to track the global extent of oceanic anoxia through time ((Stirling et al., 2007a; Weyer et al., 2008a; Montoya-Pino et al., 2010a; Brennecka et al., 2011; Asael et al., 2013; Kendall et al., 2013; Andersen et al., 2014; Dahl et al., 2014; Azmy et al., 2015; Kendall et al., 2015; Tissot and Dauphas, 2015; Andersen et al., 2016; Hood et al., 2016; Lau et al., 2016; Wang et al., 2016; Dahl et al., 2017; Elrick et al., 2017; Jost et al., 2017; Lau et al., 2017; Lu et al., 2017; Song et al., 2017; Yang et al., 2017; Andersen et al., 2018; Bartlett et al., 2018; Bura-Nakić et al., 2018; Chen et al., 2018a, b; Clarkson et al., 2018; Herrmann et al., 2018; Phan et al., 2018; Wang et al., 2018; Wei et al., 2018; White et al., 2018; Zhang et al., 2018a, b, c; Dahl et al., 2019; Gilleaudeau et al., 2019; Tostevin et al., 2019; F. Zhang et al., 2019b, a; Abshire et al., 2020; Brüske et al., 2020b, a; Bura-Nakić et al., 2020; Cao et al., 2020; Cheng et al., 2020; Cole et al., 2020; Kendall et al., 2020; Li et al., 2020; Mänd et al., 2020; del Rey et al., 2020; Stockey et al., 2020; X. Wang et al., 2020;

Wei et al., 2020; Zhang et al., 2020c, a, b; Zhao et al., 2020)). Indeed, uranium is a redox-sensitive element, and its isotopic composition in modern seawater ($\delta^{238}U_{sw}$) reflects the mass balance between riverine input of U (assumed to be the major source) and removal into several sinks (Tissot and Dauphas, 2015; Andersen et al., 2016). In the modern ocean, U occurs in two main oxidation states: highly soluble U(VI), which exists as uranyl carbonate complexes (Langmuir, 1978; Dong and Brooks, 2006; Endrizzi and Rao, 2014; Maloubier et al., 2015), and insoluble U(IV).

The sinks of U in the modern ocean are Fe-Mn nodules, suboxic sediments, oceanic crust alteration, carbonates, deep-sea and anoxic sediments (Dunk et al., 2002). In anoxic settings, U(VI) is reduced to U(IV), which has low solubility and precipitates, presumably through adsorption onto organic matter or as uraninite in sediment pore-waters (Anderson et al., 1989; Klinkhammer and Palmer, 1991; Cochran, 1992; Barnes and Cochran, 1993; Morford and Emerson, 1999; Bone et al., 2017). Regardless of the mechanism involved, studies of anoxic basins have shown that precipitation of U under anoxic to euxinic conditions preferentially enriches the sediments in ^{238}U (relative to ^{235}U), which lowers $^{238}U/^{235}U$ ratios in residual aqueous U(VI) (see review of (Andersen et al., 2017)). The positive fractionation imparted by U reduction contrasts with most traditional and non-traditional stable isotope systems where the oxidized species tend to be enriched in heavier isotopes. This peculiar behavior in U isotopes arises from the dominance in the total equilibrium isotopic fractionation of nuclear volume effect rather than vibrational (mass-dependent) control (Bigeleisen, 1996; Schauble, 2007; Abe et al., 2008).

The large isotopic fractionation during reduction of U(VI) to U(IV) causes the U isotopic composition of anoxic sediments to be highly fractionated relative to seawater. Along with the U burial rate in anoxic settings, the $\delta^{238}U$ value of seawater is largely controlled by the size of the

anoxic sinks. An increase in the extent of oceanic anoxia will shift the seawater composition towards lower [U] and $\delta^{238}U$ values. Accordingly, the U isotopic composition of modern seawater can help constrain the extent of modern anoxia (Stirling et al., 2007b; Weyer et al., 2008b)Tissot and Dauphas 2015; (Andersen et al., 2017)). A virtue of the uranium isotope system is that the residence time of U in the well-oxygenated modern ocean ($\tau \approx 400$ kyr) is much longer than the global ocean mixing time (~1-2 kyr), meaning that U concentration and isotopic composition in the open ocean are relatively uniform vertically and laterally. To first order, the U isotopic composition of carbonate and anoxic sediments that interacted with overlying seawater are expected to record global oceanic redox conditions, providing a means of assessing quantitatively the extent of ocean anoxia through time.

Shales were the first sediments used to estimate the U isotopic composition of ancient seawater (Montoya-Pino et al., 2010a). A notable difficulty with these sediments is that a fraction of their U has a detrital origin, which requires a correction. Chemical tracers of detrital input, such as Al/U ratios, are commonly used to infer the U isotopic composition of the authigenic component (Asael et al., 2013). This correction can be significant and contributes to the uncertainty in paleoredox reconstructions. A second difficulty with the shale record is that the apparent isotopic fractionation in anoxic/euxinic settings is large and variable and it can be influenced by the efficiency of U transport to the sediments and deep-water renewal (Andersen et al., 2014, 2018; Noordmann et al., 2015).

Marine carbonates provide an alternative and possibly more faithful and straightforward archive of seawater $\delta^{238}U$ values through time. Indeed, modern primary carbonate precipitates are found to have a $\delta^{238}U$ composition that is close to that of seawater (Stirling et al., 2007a; Weyer et

al., 2008a; Romaniello et al., 2013; Chen et al., 2018b, a; Tissot et al., 2018), and the small detrital contribution can be minimized by partial dissolution of the carbonates in dilute acid. Based on the assumption that there is little fractionation between carbonates and seawater, several studies have used carbonates to track redox transitions during critical intervals such as at the Cambrian-Ordovician boundary, the end of the Sturtian Snowball Earth, and the Permian-Triassic boundary (Brennecka et al., 2011; Dahl et al., 2014; Azmy et al., 2015; Hood et al., 2016; Lau et al., 2016; Dahl et al., 2017; Elrick et al., 2017; Jost et al., 2017; Lau et al., 2017; Song et al., 2017; Bartlett et al., 2018; Chen et al., 2018a, b; Clarkson et al., 2018; Herrmann et al., 2018; Phan et al., 2018; White et al., 2018; Zhang et al., 2018a, b, c; Dahl et al., 2019; Gilleaudeau et al., 2019; Tostevin et al., 2019; F. Zhang et al., 2019b, a; Brüske et al., 2020a; Bura-Nakić et al., 2020; Cao et al., 2020; Cheng et al., 2020; Li et al., 2020; del Rey et al., 2020; Zhang et al., 2020c, a, b; Zhao et al., 2020). Most of these studies focused on variations in the U isotopic composition of carbonates during short time intervals to trace the expansion or contraction of anoxia in the oceans. A complication to the carbonate $\delta^{238}U$ paleoredox is that it is affected by diagenesis (see review in (Zhang et al., 2020b)), which can shift the $\delta^{238}U$ values of carbonates by ~+0.2 ‰ to +0.4 ‰ relative to seawater (Romaniello et al., 2013; Chen et al., 2018a; Tissot et al., 2018). Precipitation of abiotic (Chen et al., 2016, 2017) and biogenic (Chen et al., 2018b) carbonates can also induce a small shift in the U isotopic composition of carbonates relative to seawater (<+0.1 ‰). When available, calcitic brachiopod shells may be a better proxy for ambient seawater composition as they are more resistant to isotopic exchange with porewater during diagenesis (del Ray et al. 2020; (Livermore et al., 2020)). Regardless of these complications, carbonates have proven to be a useful sedimentary archive for reconstructing the extent of oceanic anoxia through time.

In Chapter 2, we show the measurement results of U concentrations and isotopic compositions of 95 ancient carbonates spanning ages from 3.25 to 0.63 Ga, and compiled large datasets from the literature for carbonates and shales aiming for a more comprehensive view with the combined proxies. We provide two plausible explanations as to the discrepancy with the expectations derived from the mass-balance model of the modern U oceanic cycle using in-depth modeling, and for the first time we raise the interesting questions concerning trace element residence time comparing with ancient ocean mixing time which is currently under further detailed exploration. Our study also highlights the challenges inherent to applying knowledge of the modern marine U isotopic cycle to periods of Earth's history when ocean-floor anoxia was much more extended, anoxic basins were ferruginous, and atmospheric oxygen content was significantly lower than present. We bring to attention among the community that some of the assumptions used in the modern oceanic model may be invalid for the past, and we provide new insights for alternative mechanisms which call for more interesting field and experimental work (Chapter 2).

1.2 Emerging zirconium and hafnium stable isotopes

High Field Strength Elements [HFSEs; Ti(IV), Zr(IV), Hf(IV), Nb(V), Ta(V)] have high ionic charge (Z) over radius (r) ratio. They behave incompatibly during magmatic processes, resulting in their enrichment in the continental crust relative to the bulk silicate Earth (by factors of ~3 to 24 (McDonough and Sun, 1995; Rudnick and Gao, 2003)). They are insoluble in aqueous fluids under most circumstances, and are characterized by low concentrations and short residence times in seawater (Zr: 5600 yr, Hf: 1300 yr (Sohrin et al., 1998), Ti: 150 yr (Orians et al., 1990)). They are highly refractory, with 50% condensation temperatures under solar nebula conditions of

1546 and 1741 K for Zr and Hf, respectively (Lodders, 2003; Wood et al., 2019). Because of all these characteristics (incompatibility, insolubility in aqueous fluids, and refractoriness), they have proven to be extremely useful in geochemistry for normalizing concentrations of water-soluble (Brimhall and Dietrich, 1987; Sheldon and Tabor, 2009) and moderately volatile (O'Neill and Palme, 2008) elements.

HFSEs are also useful in their own right: (1) In cosmochemistry, their relative abundances in refractory inclusions are found to be fractionated by high-temperature evaporation/condensation processes (Martin and Mason, 1974; Grossman and Ganapathy, 1976a, b; MacPherson, 1994; Simon et al., 1996; El Goresy et al., 2002). (2) The ^{176}Lu-^{176}Hf decay system ($t_{1/2}$= 37.8 Gyr) has been widely used as both a chronometer and a tracer of planetary differentiation processes (Vervoort et al., 1996; Blichert-Toft and Albarède, 1997a; Vervoort and Blichert-Toft, 1999; Harrison et al., 2005). (3) Titanium enrichment during fractional crystallization is a feature that distinguishes tholeiitic from calc-alkaline series (Miyashiro and Shido, 1975) (other trace HFSEs can also be used to distinguish these two series (Ross and Bédard, 2009)). (4) The sub-chondritic Nb/Ta ratios in all the major terrestrial reservoirs (the missing Nb-paradox) points to the existence of high-temperature processes that can fractionate these twin elements at large scales (Rudnick et al., 2000; Wade and Wood, 2001; Münker et al., 2003; Pfänder et al., 2007, 2012; Nebel et al., 2010). (5) The elevated Ti, Ta, and Nb (TITAN) concentrations in ocean island basalts with high ^{3}He/^{4}He indicates the presence of a non-primitive recycled component in the deep mantle (Jackson et al., 2008). (6) The abundances and isotopes of these elements in terrigenous sediments can help constrain the nature (felsic or mafic) of the provenance region of the detritus (Taylor and McLennan, 1985a; Greber and Dauphas, 2019; Ptáček et al., 2020).

Isotopic variations that depart from the laws of mass-dependent fractionation (Dauphas and Schauble, 2016) have been documented for Ti, Zr, and Hf. These variations arise from (1) incomplete mixing of nucleosynthetic anomalies for Ti (Niederer et al., 1981; Niemeyer and Lugmair, 1981; Ireland et al., 1985; Zinner et al., 1986; Fahey et al., 1987; Leya et al., 2008; Trinquier et al., 2009; Zhang et al., 2011a), Zr (Schönbächler et al., 2003; Akram et al., 2013, 2015) and Hf (Akram et al., 2013; Peters et al., 2017; Elfers et al., 2018, 2020), (2) cosmogenic neutron capture effects from irradiation of solar system materials by cosmic rays for Ti (Zhang et al., 2012) and Hf (Sprung et al., 2010a, 2013a), and (3) radioactive decay of short-lived ^{92}Nb ($t_{1/2}$= 34.7 Myr) for ^{92}Zr (Harper Jr, 1996; Schönbächler et al., 2002; Iizuka et al., 2016), and long-lived ^{176}Lu for ^{176}Hf (Patchett and Tatsumoto, 1980; Patchett et al., 1982a; Vervoort et al., 1996; Blichert-Toft and Albarède, 1997a). Over the past several years, considerable progress has been made in documenting the mass-dependent component of isotopic variations for Ti (Millet et al., 2016; Greber et al., 2017b, a; Simon et al., 2017; Davis et al., 2018; Deng et al., 2018, 2019; Johnson et al., 2019) and Zr (Inglis et al., 2018, 2019; Ibañez-Mejia and Tissot, 2019; W. Zhang et al., 2019; Feng et al., 2020; Tian et al., 2020; Tompkins et al., 2020). Mass-dependent Ti isotopic variations in calcium-aluminum-rich inclusions (CAIs) reflect evaporation/condensation processes (Simon et al., 2017; Davis et al., 2018). Titanium isotopic variations have also been found in igneous rocks resulting from mantle depletion (Greber et al., 2017b; Deng et al., 2018) and magmatic differentiation (Millet et al., 2016; Greber et al., 2017a; Deng et al., 2019; Johnson et al., 2019). These variations are driven by differences in coordination between Ti in melt and minerals (Millet et al., 2016; Johnson et al., 2019; W. Wang et al., 2020). Zirconium isotopic variations have more recently been documented in igneous rocks and minerals (Inglis et al., 2018,

2019; Ibañez-Mejia and Tissot, 2019; W. Zhang et al., 2019; Feng et al., 2020; Tian et al., 2020; Tompkins et al., 2020) but the mechanism responsible for those variations is uncertain.

Much focus in recent Zr isotope studies has focused on zircon ($ZrSiO_4$). Zircon is an accessory mineral commonly found in igneous, metamorphic and detrital sedimentary rocks. It can be readily dated using the U-Pb system and hosts important geochemical tracers (Hf, U, Th and REE). These features, combined with the high resistance of zircon to secondary processes, have made it the focus of a wide variety of geochemical, petrological, and geological studies interrogating major questions of Earth sciences, such as the timing of mass extinctions, onset of subduction, and growth and maturation of the continental crust (Patchett et al., 1982a; Bowring et al., 1998; Amelin et al., 1999; Mojzsis et al., 2001; Wilde et al., 2001; Harrison et al., 2005; Valley et al., 2005; Watson and Harrison, 2005; Hopkins et al., 2008; Hawkesworth et al., 2010; Schoene et al., 2019).

Zirconium has five naturally occurring stable isotopes, ^{90}Zr (51.45%), ^{91}Zr (11.22%), ^{92}Zr (17.15%), ^{94}Zr (17.38%) and ^{96}Zr (2.80%). Zirconium isotopic compositions are typically reported in $\delta^{94}Zr$ or $\delta'^{94}Zr$ notations, which are departures in permil (‰) of the $^{94}Zr/^{90}Zr$ ratio relative to a reference material. Zirconium stable isotope systematics is a relatively new field and there is no widespread agreement on which reference material to use. In the following, we report $\delta^{94}Zr$ values relative to NIST 3169 (Feng et al., 2020). Zirconium isotopic analyses have also been reported relative to a NIST standard under development (Ibañez-Mejia and Tissot, 2019) and the IPGP-Zr standard (Inglis et al., 2018, 2019; Ibañez-Mejia and Tissot, 2019; W. Zhang et al., 2019; Feng et al., 2020; Tian et al., 2020; Tompkins et al., 2020). Converting Zr isotopic compositions from

NIST 3169 to IPGP-Zr would involve shifting all $\delta^{94}Zr$ values by ~ -0.04 ‰ (Feng et al., 2020; Tian et al., 2020).

The role that zircon plays in controlling Zr isotopic fractionation in igneous rocks is debated. Inglis et al. (2019) measured the Zr isotopic compositions of bulk magmatic rocks from Hekla volcano and found that $\delta^{94}Zr$ increases with SiO_2 content, which is a tracer of magmatic differentiation. Combining these data with the zirconium concentrations of these rocks, they concluded that zircon crystallization within the Hekla differentiation suite was the main driver of the observed variations in the bulk samples. They argued based on coordination considerations that equilibrium isotopic fractionation could explain qualitatively why zircon would preferentially incorporate light Zr isotopes, leaving the residual melt enriched in heavy Zr isotopes (elevated $\delta^{94}Zr$ values). Feng et al. (2020) and Tian et al. (2020) found that among igneous rock standards, felsic rocks tend to have heavier Zr isotopic compositions than mafic rocks, which agree with the trend documented by Inglis et al. (2018, 2019). Ibanez-Mejia and Tissot (2019) measured single zircon and baddeleyite crystals from an anorthositic gabbro (FC-1) and found widespread $\delta^{94}Zr$ values ranging from -4.3 to +0.9 ‰. Unlike Inglis et al. (2019), they argued that their data could be explained using a distillation model if zircon and baddeleyite were isotopically heavy relative to the melt from which they crystallized, driving the residual liquid to extremely low $\delta^{94}Zr$ values. The rocks measured in these studies were different and the discrepancy illustrates the fact that the driver behind Zr isotopic fractionation in igneous rocks remains highly uncertain, which limits the usefulness of this system to draw petrogenetic inferences on zircon formation based on Zr isotopic analyses. Zhang et al. (2019) analyzed the Zr isotopic compositions in several zircons using laser

ablation multiple collector inductively coupled plasma mass spectrometry (LA-MC-ICPMS) and found relatively constant values.

Available Zr isotopic data (Inglis et al., 2018, 2019; Ibañez-Mejia and Tissot, 2019; W. Zhang et al., 2019; Feng et al., 2020; Tian et al., 2020; Tompkins et al., 2020) in igneous rocks hint at the possibility that they could provide new insights into the conditions of zircon formation but there are outstanding questions that need to be addressed before Zr isotopes can be developed into a useful petrogenetic tracer. Are the measured variations the result of equilibrium fractionation between minerals and melts? If yes, is it the crystallization of zircon or other Zr-bearing phases that drives Zr isotopic fractionation measured in bulk rocks? Alternatively, are the observed variations due to kinetic processes such as diffusion? If yes, what does it tell us about magma cooling and zircon crystallization history?

Hafnium has very similar chemical behavior to zirconium. It possesses six stable or long-lived (the half live of ^{174}Hf is ~2×10^{15} yr) isotopes ^{174}Hf (0.16%), ^{176}Hf (5.26%), ^{177}Hf (18.60%), ^{178}Hf (27.28%), ^{179}Hf (13.62%) and ^{180}Hf (35.08%). To our knowledge, no high precision measurements of Hf stable isotopic fractionation have been reported. As discussed in Chapter 3, such data would shed light on the processes responsible for Zr isotopic fractionation in igneous rocks.

To understand what controls Zr isotopic variations in igneous rocks, we have performed *ab initio* calculations of the equilibrium isotopic fractionation factors of Zr and Hf in a variety of minerals using the technique of density functional theory (DFT). Following Farges et al. (1991), Ca-catapleiite ($CaZrSi_3O_9 \cdot 2H_2O$) was used as a model structure for Zr in silicate melts. The Zr-rich minerals investigated here are zircon ($ZrSiO_4$) and baddeleyite (ZrO_2). We also investigated

equilibrium isotopic fractionation for Zr in a variety of minerals where Zr substitutes other elements: ilmenite ($FeTiO_3$), geikielite ($MgTiO_3$), apatite ($Ca_5(PO_4)_3F$), magnetite ($MgFe_2O_4$), forsterite (Mg_2SiO_4), diopside ($MgCaSi_2O_6$), enstatite ($MgSiO_3$), K-feldspar ($KAlSi_3O_8$), quartz (SiO_2), tremolite ($Ca_2Mg_5Si_8O_{22}(OH)_2$) and pyrope ($Mg_3Al_2(SiO_4)_3$). Besides these calculations, we have also explored how diffusion-driven kinetic isotopic fractionation during crystallization of zircon and other Zr-poor minerals could fractionate Zr isotopes in igneous rocks. We find that both (1) diffusion-limited zircon crystallization from a supersaturated liquid and (2) Zr diffusion in the liquid boundary-layer around a Zr-poor growing crystal, can explain the Zr isotopic variations that have been documented in igneous rocks. Our favored scenario is that the Zr isotopic variations documented in some zircons reflect their crystallizations in a supersaturated diffusion boundary layer, in a process of diffusion-triggered crystallization (Chapter 3).

1.3 References

Abe M., Suzuki T., Fujii Y., Hada M. and Hirao K. (2008) An ab initio molecular orbital study of the nuclear volume effects in uranium isotope fractionations. *J. Chem. Phys.* **129**, 164309.

Abshire M. L., Romaniello S. J., Kuzminov A. M., Cofrancesco J., Severmann S. and Riedinger N. (2020) Uranium isotopes as a proxy for primary depositional redox conditions in organic-rich marine systems. *Earth Planet. Sci. Lett.* **529**, 115878.

Akram W., Schönbächler M., Bisterzo S. and Gallino R. (2015) Zirconium isotope evidence for the heterogeneous distribution of s-process materials in the solar system. *Geochimica et Cosmochimica Acta* **165**, 484–500.

Akram W., Schönbächler M., Sprung P. and Vogel N. (2013) Zirconium—hafnium isotope evidence from meteorites for the decoupled synthesis of light and heavy neutron-rich nuclei. *The Astrophysical Journal* **777**, 169.

Amelin Y., Lee D.-C., Halliday A. N. and Pidgeon R. T. (1999) Nature of the Earth's earliest crust from hafnium isotopes in single detrital zircons. *Nature* **399**, 252–255.

Anbar A. D., Duan Y., Lyons T. W., Arnold G. L., Kendall B., Creaser R. A., Kaufman A. J., Gordon G. W., Scott C. and Garvin J. (2007) A whiff of oxygen before the great oxidation event? *Science.* **317**, 1903–1906.

Andersen M. B., Matthews A., Vance D., Bar-Matthews M., Archer C. and de Souza G. F. (2018) A 10-fold decline in the deep Eastern Mediterranean thermohaline overturning circulation during the last interglacial period. *Earth Planet. Sci. Lett.* **503**, 58–67.

Andersen M. B., Romaniello S., Vance D., Little S. H., Herdman R. and Lyons T. W. (2014) A modern framework for the interpretation of $^{238}U/^{235}U$ in studies of ancient ocean redox. *Earth Planet. Sci. Lett.* **400**, 184–194.

Andersen M. B., Stirling C. H. and Weyer S. (2017) Uranium isotope fractionation. *Rev. Mineral. Geochemistry* **82**, 799–850.

Andersen M. B., Vance D., Morford J. L., Bura-Nakić E., Breitenbach S. F. M. and Och L. (2016) Closing in on the marine 238U/235U budget. *Chem. Geol.* **420**, 11–22.

Anderson R. F., Fleisher M. Q. and LeHuray A. P. (1989) Concentration, oxidation state, and particulate flux of uranium in the Black Sea. *Geochim. Cosmochim. Acta* **53**, 2215–2224.

Asael D., Tissot F. L. H., Reinhard C. T., Rouxel O., Dauphas N., Lyons T. W., Ponzevera E., Liorzou C. and Chéron S. (2013) Coupled molybdenum, iron and uranium stable isotopes as oceanic paleoredox proxies during the Paleoproterozoic Shunga Event. *Chem. Geol.* **362**, 193–210.

Azmy K., Kendall B., Brand U., Stouge S. and Gordon G. W. (2015) Redox conditions across the Cambrian–Ordovician boundary: Elemental and isotopic signatures retained in the GSSP carbonates. *Palaeogeogr. Palaeoclimatol. Palaeoecol.* **440**, 440–454.

Barnes C. E. and Cochran J. K. (1993) Uranium geochemistry in estuarine sediments: controls on removal and release processes. *Geochim. Cosmochim. Acta* **57**, 555–569.

Bartlett R., Elrick M., Wheeley J. R., Polyak V., Desrochers A. and Asmerom Y. (2018) Abrupt global-ocean anoxia during the Late Ordovician–early Silurian detected using uranium isotopes of marine carbonates. *Proc. Natl. Acad. Sci.* **115**, 5896–5901.

Bekker A., Holland H. D., Wang P.-L., Rumble D., Stein H. J., Hannah J. L., Coetzee L. L. and Beukes N. J. (2004) Dating the rise of atmospheric oxygen. *Nature* **427**, 117–120.

Bigeleisen J. (1996) Nuclear size and shape effects in chemical reactions. Isotope chemistry of the heavy elements. *J. Am. Chem. Soc.* **118**, 3676–3680.

Blichert-Toft J. and Albarède F. (1997) The Lu-Hf isotope geochemistry of chondrites and the evolution of the mantle-crust system. *Earth and Planetary Science Letters* **148**, 243–258.

Bone S. E., Dynes J. J., Cliff J. and Bargar J. R. (2017) Uranium (IV) adsorption by natural organic matter in anoxic sediments. *Proc. Natl. Acad. Sci.* **114**, 711–716.

Bowring S. A., Erwin D., Jin Y., Martin M., Davidek K. and Wang W. (1998) U/Pb zircon geochronology and tempo of the end-Permian mass extinction. *Science* **280**, 1039–1045.

Brimhall G. H. and Dietrich W. E. (1987) Constitutive mass balance relations between chemical composition, volume, density, porosity, and strain in metasomatic hydrochemical systems: results on weathering and pedogenesis. *Geochimica et Cosmochimica Acta* **51**, 567–587.

Brennecka G. A., Herrmann A. D., Algeo T. J. and Anbar A. D. (2011) Rapid expansion of oceanic anoxia immediately before the end-Permian mass extinction. *Proc. Natl. Acad. Sci.* **108**, 17631–17634.

Brüske A., Martin A. N., Rammensee P., Eroglu S., Lazarov M., Albut G., Schuth S., Aulbach S., Schoenberg R. and Beukes N. (2020a) The onset of oxidative weathering traced by uranium isotopes. *Precambrian Res.* **338**, 105583.

Brüske A., Weyer S., Zhao M.-Y., Planavsky N. J., Wegwerth A., Neubert N., Dellwig O., Lau K. V and Lyons T. W. (2020b) Correlated molybdenum and uranium isotope signatures in modern anoxic sediments: Implications for their use as paleo-redox proxy. *Geochim. Cosmochim. Acta* **270**, 449–474.

Bura-Nakić E., Andersen M. B., Archer C., de Souza G. F., Marguš M. and Vance D. (2018) Coupled Mo-U abundances and isotopes in a small marine euxinic basin: constraints on processes in euxinic basins. *Geochim. Cosmochim. Acta* **222**, 212–229.

Bura-Nakić E., Sondi I., Mikac N. and Andersen M. B. (2020) Investigating the molybdenum and uranium redox proxies in a modern shallow anoxic carbonate rich marine sediment setting of the Malo Jezero (Mljet Lakes, Adriatic Sea). *Chem. Geol.* **533**, 119441.

Cao M., Daines S. J., Lenton T. M., Cui H., Algeo T. J., Dahl T. W., Shi W., Chen Z.-Q., Anbar A. and Zhou Y.-Q. (2020) Comparison of Ediacaran platform and slope δ238U records in South China: Implications for global-ocean oxygenation and the origin of the Shuram Excursion. *Geochim. Cosmochim. Acta*.

Chen X., Romaniello S. J. and Anbar A. D. (2017) Uranium isotope fractionation induced by aqueous speciation: Implications for U isotopes in marine CaCO3 as a paleoredox proxy. *Geochim. Cosmochim. Acta* **215**, 162–172.

Chen X., Romaniello S. J., Herrmann A. D., Hardisty D., Gill B. C. and Anbar A. D. (2018a) Diagenetic effects on uranium isotope fractionation in carbonate sediments from the Bahamas. *Geochim. Cosmochim. Acta* **237**, 294–311.

Chen X., Romaniello S. J., Herrmann A. D., Samankassou E. and Anbar A. D. (2018b) Biological effects on uranium isotope fractionation (238U/235U) in primary biogenic carbonates. *Geochim. Cosmochim. Acta* **240**, 1–10.

Chen X., Romaniello S. J., Herrmann A. D., Wasylenki L. E. and Anbar A. D. (2016) Uranium isotope fractionation during coprecipitation with aragonite and calcite. *Geochim. Cosmochim. Acta* **188**, 189–207.

Cheng K., Elrick M. and Romaniello S. J. (2020) Early Mississippian ocean anoxia triggered organic carbon burial and late Paleozoic cooling: Evidence from uranium isotopes recorded in marine limestone. *Geology* **48**, 363–367.

Clarkson M. O., Stirling C. H., Jenkyns H. C., Dickson A. J., Porcelli D., Moy C. M., von Strandmann P. A. E. P., Cooke I. R. and Lenton T. M. (2018) Uranium isotope evidence for two episodes of deoxygenation during Oceanic Anoxic Event 2. *Proc. Natl. Acad. Sci.* **115**, 2918–2923.

Cochran J. K. (1992) The oceanic chemistry of the uranium-and thorium-series nuclides. In *Uranium-series disequilibrium: applications to earth, marine, and environmental sciences. 2. ed*

Cole D. B., Planavsky N. J., Longley M., Böning P., Wilkes D., Wang X., Swanner E. D., Wittkop C., Loydell D. and Busigny V. (2020) Uranium isotope fractionation in non-sulfidic anoxic settings and the global uranium isotope mass balance. *Global Biogeochem. Cycles*, e2020GB006649.

Dahl T. W., Boyle R. A., Canfield D. E., Connelly J. N., Gill B. C., Lenton T. M. and Bizzarro M. (2014) Uranium isotopes distinguish two geochemically distinct stages during the later Cambrian SPICE event. *Earth Planet. Sci. Lett.* **401**, 313–326.

Dahl T. W., Connelly J. N., Kouchinsky A., Gill B. C., Månsson S. F. and Bizzarro M. (2017) Reorganisation of Earth's biogeochemical cycles briefly oxygenated the oceans 520 Myr ago.

Dahl T. W., Connelly J. N., Li D., Kouchinsky A., Gill B. C., Porter S., Maloof A. C. and Bizzarro M. (2019) Atmosphere–ocean oxygen and productivity dynamics during early animal radiations. *Proc. Natl. Acad. Sci.* **116**, 19352–19361.

Dauphas N. and Schauble E. A. (2016) Mass fractionation laws, mass-independent effects, and isotopic anomalies. *Annual Review of Earth and Planetary Sciences* **44**, 709–783.

Davis A. M., Zhang J., Greber N. D., Hu J., Tissot F. L. and Dauphas N. (2018) Titanium isotopes and rare earth patterns in CAIs: evidence for thermal processing and gas-dust decoupling in the protoplanetary disk. *Geochimica et cosmochimica acta* **221**, 275–295.

Deng Z., Chaussidon M., Savage P., Robert F., Pik R. and Moynier F. (2019) Titanium isotopes as a tracer for the plume or island arc affinity of felsic rocks. *Proceedings of the National Academy of Sciences* **116**, 1132–1135.

Deng Z., Moynier F., Sossi P. and Chaussidon M. (2018) Bridging the depleted MORB mantle and the continental crust using titanium isotopes.

Dong W. and Brooks S. C. (2006) Determination of the formation constants of ternary complexes of uranyl and carbonate with alkaline earth metals (Mg2+, Ca2+, Sr2+, and Ba2+) using anion exchange method. *Environ. Sci. Technol.* **40**, 4689–4695.

Dunk R. M., Mills R. A. and Jenkins W. J. (2002) A reevaluation of the oceanic uranium budget for the Holocene. *Chem. Geol.* **190**, 45–67.

El Goresy A., Zinner E., Matsunami S., Palme H., Spettel B., Lin Y. and Nazarov M. (2002) Efremovka 101.1: A CAI with ultrarefractory REE patterns and enormous enrichments of Sc, Zr, and Y in fassaite and perovskite. *Geochimica et Cosmochimica Acta* **66**, 1459–1491.

Elfers B.-M., Sprung P., Messling N. and Münker C. (2020) The combined Zr and Hf isotope inventory of bulk rock and sequentially leached chondrite samples. *Geochimica et Cosmochimica Acta* **270**, 475–491.

Elfers B.-M., Sprung P., Pfeifer M., Wombacher F., Peters S. T. and Münker C. (2018) Variable distribution of s-process Hf and W isotope carriers in chondritic meteorites–Evidence from 174Hf and 180W. *Geochimica et Cosmochimica Acta* **239**, 346–362.

Elrick M., Polyak V., Algeo T. J., Romaniello S., Asmerom Y., Herrmann A. D., Anbar A. D., Zhao L. and Chen Z.-Q. (2017) Global-ocean redox variation during the middle-late Permian through Early Triassic based on uranium isotope and Th/U trends of marine carbonates. *Geology* **45**, 163–166.

Endrizzi F. and Rao L. (2014) Chemical Speciation of U (VI) in Marine Environments: Complexation of Ca2+ and Mg2+ with (UO2)(CO3) 3 4-and the Effect on the Extraction of Uranium from Seawater.

Fahey A., Goswami J., McKeegan K. and Zinner E. (1987) 26Al, 244Pu, 50Ti, REE, and trace element abundances in hibonite grains from CM and CV meteorites. *Geochimica et Cosmochimica Acta* **51**, 329–350.

Farquhar J., Zerkle A. L. and Bekker A. (2014) Geologic and geochemical constraints on Earth's early atmosphere.

Farquhar J., Zerkle A. L. and Bekker A. (2011) Geological constraints on the origin of oxygenic photosynthesis. *Photosynth. Res.* **107**, 11–36.

Feng L., Hu W., Jiao Y., Zhou L., Zhang W., Hu Z. and Liu Y. (2020) High-precision stable zirconium isotope ratio measurements by double spike thermal ionization mass spectrometry. *Journal of Analytical Atomic Spectrometry* **35**, 736–745.

Gilleaudeau G. J., Romaniello S. J., Luo G., Kaufman A. J., Zhang F., Klaebe R. M., Kah L. C., Azmy K., Bartley J. K. and Zheng W. (2019) Uranium isotope evidence for limited euxinia in mid-Proterozoic oceans. *Earth Planet. Sci. Lett.* **521**, 150–157.

Greber N. D. and Dauphas N. (2019) The chemistry of fine-grained terrigenous sediments reveals a chemically evolved Paleoarchean emerged crust. *Geochimica et cosmochimica acta* **255**, 247–264.

Greber N. D., Dauphas N., Bekker A., Ptáček M. P., Bindeman I. N. and Hofmann A. (2017a) Titanium isotopic evidence for felsic crust and plate tectonics 3.5 billion years ago. *Science* **357**, 1271–1274.

Greber N. D., Dauphas N., Puchtel I. S., Hofmann B. A. and Arndt N. T. (2017b) Titanium stable isotopic variations in chondrites, achondrites and lunar rocks. *Geochimica et cosmochimica acta* **213**, 534–552.

Grossman L. and Ganapathy R. (1976a) Trace elements in the Allende meteorite—I. Coarse-grained, Ca-rich inclusions. *Geochimica et Cosmochimica Acta* **40**, 331–344.

Grossman L. and Ganapathy R. (1976b) Trace elements in the Allende meteorite—II. Fine-grained. Ca-rich inclusions. *Geochimica et Cosmochimica Acta* **40**, 967–977.

Gumsley A. P., Chamberlain K. R., Bleeker W., Söderlund U., de Kock M. O., Larsson E. R. and Bekker A. (2017) Timing and tempo of the Great Oxidation Event. *Proc. Natl. Acad. Sci.* **114**, 1811–1816.

Hardisty D. S., Lu Z., Bekker A., Diamond C. W., Gill B. C., Jiang G., Kah L. C., Knoll A. H., Loyd S. J. and Osburn M. R. (2017) Perspectives on Proterozoic surface ocean redox from iodine contents in ancient and recent carbonate. *Earth Planet. Sci. Lett.* **463**, 159–170.

Hardisty D. S., Lu Z., Planavsky N. J., Bekker A., Philippot P., Zhou X. and Lyons T. W. (2014) An iodine record of Paleoproterozoic surface ocean oxygenation. *Geology* **42**, 619–622.

Harper Jr C. L. (1996) Evidence for 92gNb in the early solar system and evaluation of a new p-process cosmochronometer from 92gNb/92Mo. *The Astrophysical Journal* **466**, 437.

Harrison T., Blichert-Toft J., Müller W., Albarede F., Holden P. and Mojzsis S. J. (2005) Heterogeneous Hadean hafnium: evidence of continental crust at 4.4 to 4.5 Ga. *Science* **310**, 1947–1950.

Hawkesworth C. J., Dhuime B., Pietranik A., Cawood P., Kemp A. I. and Storey C. (2010) The generation and evolution of the continental crust. *Journal of the Geological Society* **167**, 229–248.

Herrmann A. D., Gordon G. W. and Anbar A. D. (2018) Uranium isotope variations in a dolomitized Jurassic carbonate platform (Tithonian; Franconian Alb, Southern Germany). *Chem. Geol.* **497**, 41–53.

Holland H. D. (2006) The oxygenation of the atmosphere and oceans. *Philos. Trans. R. Soc. B Biol. Sci.* **361**, 903–915.

Hood A. vS, Planavsky N. J., Wallace M. W., Wang X., Bellefroid E. J., Gueguen B. and Cole D. B. (2016) Integrated geochemical-petrographic insights from component-selective δ238U of Cryogenian marine carbonates. *Geology* **44**, 935–938.

Hopkins M., Harrison T. M. and Manning C. E. (2008) Low heat flow inferred from> 4 Gyr zircons suggests Hadean plate boundary interactions. *Nature* **456**, 493–496.

Ibañez-Mejia M. and Tissot F. L. (2019) Extreme Zr stable isotope fractionation during magmatic fractional crystallization. *Science Advances* **5**, eaax8648.

Iizuka T., Lai Y.-J., Akram W., Amelin Y. and Schönbächler M. (2016) The initial abundance and distribution of 92Nb in the Solar System. *Earth and Planetary Science Letters* **439**, 172–181.

Inglis E. C., Creech J. B., Deng Z. and Moynier F. (2018) High-precision zirconium stable isotope measurements of geological reference materials as measured by double-spike MC-ICPMS. *Chemical Geology* **493**, 544–552.

Inglis E. C., Moynier F., Creech J., Deng Z., Day J. M., Teng F.-Z., Bizzarro M., Jackson M. and Savage P. (2019) Isotopic fractionation of zirconium during magmatic differentiation and the stable isotope composition of the silicate Earth. *Geochimica et Cosmochimica Acta* **250**, 311–323.

Ireland T., Compston W. and Heydegger H. (1985) Titanium isotopic anomalies in hibonites from the Murchison carbonaceous chondrite. *Geochimica et Cosmochimica Acta* **49**, 1989–1993.

Jackson M. G., Hart S. R., Saal A. E., Shimizu N., Kurz M. D., Blusztajn J. S. and Skovgaard A. C. (2008) Globally elevated titanium, tantalum, and niobium (TITAN) in ocean island basalts with high 3He/4He. *Geochemistry, Geophysics, Geosystems* **9**.

Johnson A. C., Aarons S. M., Dauphas N., Nie N. X., Zeng H., Helz R. T., Romaniello S. J. and Anbar A. D. (2019) Titanium isotopic fractionation in Kilauea Iki lava lake driven by oxide crystallization. *Geochimica et Cosmochimica Acta* **264**, 180–190.

Johnston D. T., Poulton S. W., Goldberg T., Sergeev V. N., Podkovyrov V., Vorob'Eva N. G., Bekker A. and Knoll A. H. (2012) Late Ediacaran redox stability and metazoan evolution. *Earth Planet. Sci. Lett.* **335**, 25–35.

Jost A. B., Bachan A., van de Schootbrugge B., Lau K. V, Weaver K. L., Maher K. and Payne J. L. (2017) Uranium isotope evidence for an expansion of marine anoxia during the end-Triassic extinction. *Geochemistry, Geophys. Geosystems* **18**, 3093–3108.

Kendall B., Brennecka G. A., Weyer S. and Anbar A. D. (2013) Uranium isotope fractionation suggests oxidative uranium mobilization at 2.50 Ga. *Chem. Geol.* **362**, 105–114.

Kendall B., Komiya T., Lyons T. W., Bates S. M., Gordon G. W., Romaniello S. J., Jiang G., Creaser R. A., Xiao S. and McFadden K. (2015) Uranium and molybdenum isotope evidence for an episode of widespread ocean oxygenation during the late Ediacaran Period. *Geochim. Cosmochim. Acta* **156**, 173–193.

Kendall B., Wang J., Zheng W., Romaniello S. J., Over D. J., Bennett Y., Xing L., Kunert A., Boyes C. and Liu J. (2020) Inverse correlation between the molybdenum and uranium isotope compositions of Upper Devonian black shales caused by changes in local depositional conditions rather than global ocean redox variations. *Geochim. Cosmochim. Acta*.

Klinkhammer G. P. and Palmer M. R. (1991) Uranium in the oceans: where it goes and why. *Geochim. Cosmochim. Acta* **55**, 1799–1806.

Langmuir D. (1978) Uranium solution-mineral equilibria at low temperatures with applications to sedimentary ore deposits. *Geochim. Cosmochim. Acta* **42**, 547–569.

Lau K. V, Macdonald F. A., Maher K. and Payne J. L. (2017) Uranium isotope evidence for temporary ocean oxygenation in the aftermath of the Sturtian Snowball Earth. *Earth Planet. Sci. Lett.* **458**, 282–292.

Lau K. V, Maher K., Altiner D., Kelley B. M., Kump L. R., Lehrmann D. J., Silva-Tamayo J. C., Weaver K. L., Yu M. and Payne J. L. (2016) Marine anoxia and delayed Earth system recovery after the end-Permian extinction. *Proc. Natl. Acad. Sci.* **113**, 2360–2365.

Leya I., Schönbächler M., Wiechert U., Krähenbühl U. and Halliday A. N. (2008) Titanium isotopes and the radial heterogeneity of the solar system. *Earth and Planetary Science Letters* **266**, 233–244.

Li Z., Cao M., Loyd S. J., Algeo T. J., Zhao H., Wang X., Zhao L. and Chen Z.-Q. (2020) Transient and stepwise ocean oxygenation during the late Ediacaran Shuram Excursion: Insights from carbonate δ238U of northwestern Mexico. *Precambrian Res.*, 105741.

Livermore B. D., Dahl T. W., Bizzarro M. and Connelly J. N. (2020) Uranium isotope compositions of biogenic carbonates–Implications for U uptake in shells and the

application of the paleo-ocean oxygenation proxy. *Geochim. Cosmochim. Acta* **287**, 50–64.

Lodders K. (2003) Solar system abundances and condensation temperatures of the elements. *The Astrophysical Journal* **591**, 1220.

Lu X., Kendall B., Stein H. J., Li C., Hannah J. L., Gordon G. W. and Ebbestad J. O. R. (2017) Marine redox conditions during deposition of Late Ordovician and Early Silurian organic-rich mudrocks in the Siljan ring district, central Sweden. *Chem. Geol.* **457**, 75–94.

Lyons T. W., Reinhard C. T. and Planavsky N. J. (2014) The rise of oxygen in Earth's early ocean and atmosphere. *Nature* **506**, 307–315.

MacPherson G. J. (1994) Refractory inclusions in the prototypical CM chondrite, Mighei. *Geochimica et Cosmochimica Acta* **58**, 5599–5625.

Maloubier M., Solari P. L., Moisy P., Monfort M., Den Auwer C. and Moulin C. (2015) XAS and TRLIF spectroscopy of uranium and neptunium in seawater. *Dalt. Trans.* **44**, 5417–5427.

Mänd K., Lalonde S. V, Robbins L. J., Thoby M., Paiste K., Kreitsmann T., Paiste P., Reinhard C. T., Romashkin A. E. and Planavsky N. J. (2020) Palaeoproterozoic oxygenated oceans following the Lomagundi–Jatuli Event. *Nat. Geosci.* **13**, 302–306.

Martin P. M. and Mason B. (1974) Major and trace elements in the Allende meteorite. *Nature* **249**, 333–334.

McDonough W. F. and Sun S.-S. (1995) The composition of the Earth. *Chemical geology* **120**, 223–253.

Millet M.-A., Dauphas N., Greber N. D., Burton K. W., Dale C. W., Debret B., Macpherson C. G., Nowell G. M. and Williams H. M. (2016) Titanium stable isotope investigation of magmatic processes on the Earth and Moon. *Earth and planetary science letters* **449**, 197–205.

Miyashiro A. and Shido F. (1975) Tholeiitic and calc-alkalic series in relation to the behaviors of titanium, vanadium, chromium, and nickel. *American Journal of Science* **275**, 265–277.

Mojzsis S. J., Harrison T. M. and Pidgeon R. T. (2001) Oxygen-isotope evidence from ancient zircons for liquid water at the Earth's surface 4,300 Myr ago. *Nature* **409**, 178–181.

Montoya-Pino C., Weyer S., Anbar A. D., Pross J., Oschmann W., van de Schootbrugge B. and Arz H. W. (2010) Global enhancement of ocean anoxia during Oceanic Anoxic Event 2: A quantitative approach using U isotopes. *Geology* **38**, 315–318.

Morford J. L. and Emerson S. (1999) The geochemistry of redox sensitive trace metals in sediments. *Geochim. Cosmochim. Acta* **63**, 1735–1750.

Münker C., Pfänder J. A., Weyer S., Büchl A., Kleine T. and Mezger K. (2003) Evolution of planetary cores and the Earth-Moon system from Nb/Ta systematics. *Science* **301**, 84–87.

Nebel O., van Westrenen W., Vroon P. Z., Wille M. and Raith M. M. (2010) Deep mantle storage of the Earth's missing niobium in late-stage residual melts from a magma ocean. *Geochimica et Cosmochimica Acta* **74**, 4392–4404.

Niederer F., Papanastassiou D. and Wasserburg G. (1981) The isotopic composition of titanium in the Allende and Leoville meteorites. *Geochimica et Cosmochimica Acta* **45**, 1017–1031.

Niemeyer S. and Lugmair G. (1981) Ubiquitous isotopic anomalies in Ti from normal Allende inclusions. *Earth and Planetary Science Letters* **53**, 211–225.

Noordmann J., Weyer S., Montoya-Pino C., Dellwig O., Neubert N., Eckert S., Paetzel M. and Böttcher M. E. (2015) Uranium and molybdenum isotope systematics in modern euxinic basins: Case studies from the central Baltic Sea and the Kyllaren fjord (Norway). *Chem. Geol.* **396**, 182–195.

O'Neill H. S. C. and Palme H. (2008) Collisional erosion and the non-chondritic composition of the terrestrial planets. *Philosophical Transactions of the Royal Society A: Mathematical, Physical and Engineering Sciences* **366**, 4205–4238.

Orians K. J., Boyle E. A. and Bruland K. W. (1990) Dissolved titanium in the open ocean. *Nature* **348**, 322–325.

Partin C. A., Bekker A., Planavsky N. J., Scott C. T., Gill B. C., Li C., Podkovyrov V., Maslov A., Konhauser K. O. and Lalonde S. V (2013a) Large-scale fluctuations in Precambrian atmospheric and oceanic oxygen levels from the record of U in shales. *Earth Planet. Sci. Lett.* **369**, 284–293.

Patchett P. J., Kouvo O., Hedge C. E. and Tatsumoto M. (1982) Evolution of continental crust and mantle heterogeneity: evidence from Hf isotopes. *Contributions to Mineralogy and Petrology* **78**, 279–297.

Patchett P. and Tatsumoto M. (1980) Hafnium isotope variations in oceanic basalts. *Geophysical Research Letters* **7**, 1077–1080.

Peters S. T., Münker C., Pfeifer M., Elfers B.-M. and Sprung P. (2017) Distribution of p-process 174Hf in early solar system materials and the origin of nucleosynthetic Hf and W isotope anomalies in Ca–Al rich inclusions. *Earth and Planetary Science Letters* **459**, 70–79.

Pfänder J. A., Jung S., Münker C., Stracke A. and Mezger K. (2012) A possible high Nb/Ta reservoir in the continental lithospheric mantle and consequences on the global Nb budget–Evidence from continental basalts from Central Germany. *Geochimica et Cosmochimica Acta* **77**, 232–251.

Pfänder J. A., Münker C., Stracke A. and Mezger K. (2007) Nb/Ta and Zr/Hf in ocean island basalts—implications for crust–mantle differentiation and the fate of Niobium. *Earth and Planetary Science Letters* **254**, 158–172.

Phan T. T., Gardiner J. B., Capo R. C. and Stewart B. W. (2018) Geochemical and multi-isotopic (87Sr/86Sr, 143Nd/144Nd, 238U/235U) perspectives of sediment sources, depositional conditions, and diagenesis of the Marcellus Shale, Appalachian Basin, USA. *Geochim. Cosmochim. Acta* **222**, 187–211.

Ptáček M. P., Dauphas N. and Greber N. D. (2020) Chemical evolution of the continental crust from a data-driven inversion of terrigenous sediment compositions. *Earth and planetary science letters* **539**, 116090.

Ramdohr P. (1958) New observations of the ores of the Witwatersrand in South Africa and their genetic significance. *Geol. Soc. South Africa Trans.* **61**, 1–50.

Rasmussen B. and Buick R. (1999) Redox state of the Archean atmosphere: evidence from detrital heavy minerals in ca. 3250–2750 Ma sandstones from the Pilbara Craton, Australia. *Geology* **27**, 115–118.

Reinhard C. T., Planavsky N. J., Robbins L. J., Partin C. A., Gill B. C., Lalonde S. V, Bekker A., Konhauser K. O. and Lyons T. W. (2013) Proterozoic ocean redox and biogeochemical stasis. *Proc. Natl. Acad. Sci.* **110**, 5357–5362.

del Rey Á., Havsteen J. C., Bizzarro M. and Dahl T. W. (2020) Untangling the diagenetic history of uranium isotopes in marine carbonates: a case study tracing the δ238U composition of late Silurian oceans using calcitic brachiopod shells. *Geochim. Cosmochim. Acta*.

Romaniello S. J., Herrmann A. D. and Anbar A. D. (2013) Uranium concentrations and 238U/235U isotope ratios in modern carbonates from the Bahamas: Assessing a novel paleoredox proxy. *Chem. Geol.* **362**, 305–316.

Ross P.-S. and Bédard J. H. (2009) Magmatic affinity of modern and ancient subalkaline volcanic rocks determined from trace-element discriminant diagrams. *Canadian Journal of Earth Sciences* **46**, 823–839.

Rudnick R. and Gao S. (2003) Composition of the continental crust. *The crust* **3**, 1–64.

Rudnick R. L., Barth M., Horn I. and McDonough W. F. (2000) Rutile-bearing refractory eclogites: missing link between continents and depleted mantle. *Science* **287**, 278–281.

Sahoo S. K., Planavsky N. J., Kendall B., Wang X., Shi X., Scott C., Anbar A. D., Lyons T. W. and Jiang G. (2012) Ocean oxygenation in the wake of the Marinoan glaciation. *Nature* **489**, 546–549.

Schauble E. A. (2007) Role of nuclear volume in driving equilibrium stable isotope fractionation of mercury, thallium, and other very heavy elements. *Geochim. Cosmochim. Acta* **71**, 2170–2189.

Schoene B., Eddy M. P., Samperton K. M., Keller C. B., Keller G., Adatte T. and Khadri S. F. (2019) U-Pb constraints on pulsed eruption of the Deccan Traps across the end-Cretaceous mass extinction. *Science* **363**, 862–866.

Schönbächler M., Lee D.-C., Rehkämper M., Halliday A. N., Fehr M. A., Hattendorf B. and Günther D. (2003) Zirconium isotope evidence for incomplete admixing of r-process components in the solar nebula. *Earth and Planetary Science Letters* **216**, 467–481.

Schönbächler M., Rehkämper M., Halliday A. N., Lee D.-C., Bourot-Denise M., Zanda B., Hattendorf B. and Günther D. (2002) Niobium-zirconium chronometry and early solar system development. *Science* **295**, 1705–1708.

Scott C., Lyons T. W., Bekker A., Shen Y., Poulton S. W., Chu X. and Anbar A. D. (2008) Tracing the stepwise oxygenation of the Proterozoic ocean. *Nature* **452**, 456–459.

Scott C., Wing B. A., Bekker A., Planavsky N. J., Medvedev P., Bates S. M., Yun M. and Lyons T. W. (2014) Pyrite multiple-sulfur isotope evidence for rapid expansion and contraction of the early Paleoproterozoic seawater sulfate reservoir. *Earth Planet. Sci. Lett.* **389**, 95–104.

Sheldon N. D. and Tabor N. J. (2009) Quantitative paleoenvironmental and paleoclimatic reconstruction using paleosols. *Earth-Science Reviews* **95**, 1–52.

Simon J., Jordan M., Tappa M., Schauble E., Kohl I. and Young E. (2017) Calcium and titanium isotope fractionation in refractory inclusions: tracers of condensation and inheritance in the early solar protoplanetary disk. *Earth and Planetary Science Letters* **472**, 277–288.

Simon S. B., Davis A. M. and Grossman L. (1996) A unique ultrarefractory inclusion from the Murchison meteorite. *Meteoritics & Planetary Science* **31**, 106–115.

Sohrin Y., Fujishima Y., Ueda K., Akiyama S., Mori K., Hasegawa H. and Matsui M. (1998) Dissolved niobium and tantalum in the North Pacific. *Geophysical research letters* **25**, 999–1002.

Song Huyue, Song Haijun, Algeo T. J., Tong J., Romaniello S. J., Zhu Y., Chu D., Gong Y. and Anbar A. D. (2017) Uranium and carbon isotopes document global-ocean redox-productivity relationships linked to cooling during the Frasnian-Famennian mass extinction. *Geology* **45**, 887–890.

Sprung P., Kleine T. and Scherer E. E. (2013) Isotopic evidence for chondritic Lu/Hf and Sm/Nd of the Moon. *Earth and Planetary Science Letters* **380**, 77–87.

Sprung P., Scherer E. E., Upadhyay D., Leya I. and Mezger K. (2010) Non-nucleosynthetic heterogeneity in non-radiogenic stable Hf isotopes: Implications for early solar system chronology. *Earth and Planetary Science Letters* **295**, 1–11.

Stirling C. H., Andersen M. B., Potter E.-K. and Halliday A. N. (2007) Low-temperature isotopic fractionation of uranium. *Earth Planet. Sci. Lett.* **264**, 208–225.

Stockey R. G., Cole D. B., Planavsky N. J., Loydell D. K., Frýda J. and Sperling E. A. (2020) Persistent global marine euxinia in the early Silurian. *Nat. Commun.* **11**, 1–10.

Swanner E. D., Planavsky N. J., Lalonde S. V, Robbins L. J., Bekker A., Rouxel O. J., Saito M. A., Kappler A., Mojzsis S. J. and Konhauser K. O. (2014) Cobalt and marine redox evolution. *Earth Planet. Sci. Lett.* **390**, 253–263.

Taylor S. R. and McLennan S. M. (1985) The continental crust: its composition and evolution.

Teng F.-Z., Dauphas N. and Watkins J. M. (2017) Non-traditional stable isotopes: retrospective and prospective. *Rev. Mineral. geochemistry* **82**, 1–26.

Thomson D., Rainbird R. H., Planavsky N., Lyons T. W. and Bekker A. (2015) Chemostratigraphy of the Shaler Supergroup, Victoria Island, NW Canada: A record of ocean composition prior to the Cryogenian glaciations. *Precambrian Res.* **263**, 232–245.

Tian S., Inglis E., Creech J., Zhang W., Wang Z., Hu Z., Liu Y. and Moynier F. (2020) The zirconium stable isotope compositions of 22 geological reference materials, 4 zircons and 3 standard solutions. *Chemical Geology*, 119791.

Tissot F. L. H., Chen C., Go B. M., Naziemiec M., Healy G., Bekker A., Swart P. K. and Dauphas N. (2018) Controls of eustasy and diagenesis on the 238U/235U of carbonates and evolution of the seawater (234U/238U) during the last 1.4 Myr. *Geochim. Cosmochim. Acta* **242**, 233–265.

Tissot F. L. H. and Dauphas N. (2015) Uranium isotopic compositions of the crust and ocean: Age corrections, U budget and global extent of modern anoxia. *Geochim. Cosmochim. Acta* **167**, 113–143.

Tompkins H. G., Zieman L. J., Ibañez-Mejia M. and Tissot F. L. (2020) Zirconium stable isotope analysis of zircon by MC-ICP-MS: Methods and application to evaluating intra-crystalline zonation in a zircon megacryst. *Journal of Analytical Atomic Spectrometry*.

Tostevin R., Clarkson M. O., Gangl S., Shields G. A., Wood R. A., Bowyer F., Penny A. M. and Stirling C. H. (2019) Uranium isotope evidence for an expansion of anoxia in terminal Ediacaran oceans. *Earth Planet. Sci. Lett.* **506**, 104–112.

Trinquier A., Elliott T., Ulfbeck D., Coath C., Krot A. N. and Bizzarro M. (2009) Origin of nucleosynthetic isotope heterogeneity in the solar protoplanetary disk. *Science* **324**, 374–376.

Turner E. C. and Bekker A. (2016) Thick sulfate evaporite accumulations marking a mid-Neoproterozoic oxygenation event (Ten Stone Formation, Northwest Territories, Canada). *GSA Bull.* **128**, 203–222.

Valley J., Lackey J., Cavosie A., Clechenko C., Spicuzza M., Basei M., Bindeman I., Ferreira V., Sial A. and King E. (2005) 4.4 billion years of crustal maturation: oxygen isotope ratios of magmatic zircon. *Contributions to Mineralogy and Petrology* **150**, 561–580.

Vervoort J. D. and Blichert-Toft J. (1999) Evolution of the depleted mantle: Hf isotope evidence from juvenile rocks through time. *Geochimica et cosmochimica acta* **63**, 533–556.

Vervoort J., Patchett P., Gehrels G. E. and Nutman A. (1996) Constraints on early Earth differentiation from hafnium and neodymium isotopes. *Nature* **379**, 624–627.

Wade J. and Wood B. (2001) The Earth's 'missing'niobium may be in the core. *Nature* **409**, 75–78.

Wang W., Huang S., Huang F., Zhao X. and Wu Z. (2020) Equilibrium inter-mineral titanium isotope fractionation: Implication for high-temperature titanium isotope geochemistry. *Geochimica et Cosmochimica Acta* **269**, 540–553.

Wang X., Ossa F. O., Hofmann A., Agangi A., Paprika D. and Planavsky N. J. (2020) Uranium isotope evidence for Mesoarchean biological oxygen production in shallow marine and continental settings. *Earth Planet. Sci. Lett.* **551**, 116583.

Wang X., Planavsky N. J., Hofmann A., Saupe E. E., De Corte B. P., Philippot P., LaLonde S. V, Jemison N. E., Zou H. and Ossa F. O. (2018) A Mesoarchean shift in uranium isotope systematics. *Geochim. Cosmochim. Acta* **238**, 438–452.

Wang X., Planavsky N. J., Reinhard C. T., Hein J. R. and Johnson T. M. (2016) A Cenozoic seawater redox record derived from 238U/235U in ferromanganese crusts. *Am. J. Sci.* **316**, 64–83.

Watson E. B. and Harrison T. (2005) Zircon thermometer reveals minimum melting conditions on earliest Earth. *Science* **308**, 841–844.

Wei G.-Y., Planavsky N. J., Tarhan L. G., Chen X., Wei W., Li D. and Ling H.-F. (2018) Marine redox fluctuation as a potential trigger for the Cambrian explosion. *Geology* **46**, 587–590.

Wei G.-Y., Planavsky N. J., Tarhan L. G., He T., Wang D., Shields G. A., Wei W. and Ling H.-F. (2020) Highly dynamic marine redox state through the Cambrian explosion highlighted by authigenic δ238U records. *Earth Planet. Sci. Lett.* **544**, 116361.

Weyer S., Anbar A. D., Gerdes A., Gordon G. W., Algeo T. J. and Boyle E. A. (2008) Natural fractionation of 238U/235U. *Geochim. Cosmochim. Acta* **72**, 345–359.

White D. A., Elrick M., Romaniello S. and Zhang F. (2018) Global seawater redox trends during the Late Devonian mass extinction detected using U isotopes of marine limestones. *Earth Planet. Sci. Lett.* **503**, 68–77.

Wilde S. A., Valley J. W., Peck W. H. and Graham C. M. (2001) Evidence from detrital zircons for the existence of continental crust and oceans on the Earth 4.4 Gyr ago. *Nature* **409**, 175–178.

Wood B. J., Smythe D. J. and Harrison T. (2019) The condensation temperatures of the elements: A reappraisal. *American Mineralogist: Journal of Earth and Planetary Materials* **104**, 844–856.

Yang S., Kendall B., Lu X., Zhang F. and Zheng W. (2017) Uranium isotope compositions of mid-Proterozoic black shales: Evidence for an episode of increased ocean oxygenation at 1.36 Ga and evaluation of the effect of post-depositional hydrothermal fluid flow. *Precambrian Res.* **298**, 187–201.

Zhang F., Algeo T. J., Cui Y., Shen J., Song H., Sano H., Rowe H. D. and Anbar A. D. (2019a) Global-ocean redox variations across the Smithian-Spathian boundary linked to concurrent climatic and biotic changes. *Earth-Science Rev.* **195**, 147–168.

Zhang F., Algeo T. J., Romaniello S. J., Cui Y., Zhao L., Chen Z.-Q. and Anbar A. D. (2018a) Congruent Permian-Triassic δ238U records at Panthalassic and Tethyan sites: Confirmation of global-oceanic anoxia and validation of the U-isotope paleoredox proxy. *Geology* **46**, 327–330.

Zhang F., Dahl T. W., Lenton T. M., Luo G., Shen S., Algeo T. J., Planavsky N., Liu J., Cui Y. and Qie W. (2020a) Extensive marine anoxia associated with the Late Devonian Hangenberg Crisis. *Earth Planet. Sci. Lett.* **533**, 115976.

Zhang F., Lenton T. M., del Rey Á., Romaniello S. J., Chen X., Planavsky N. J., Clarkson M. O., Dahl T. W., Lau K. V and Wang W. (2020b) Uranium isotopes in marine carbonates as a global ocean paleoredox proxy: A critical review. *Geochim. Cosmochim. Acta*.

Zhang F., Romaniello S. J., Algeo T. J., Lau K. V, Clapham M. E., Richoz S., Herrmann A. D., Smith H., Horacek M. and Anbar A. D. (2018b) Multiple episodes of extensive marine anoxia linked to global warming and continental weathering following the latest Permian mass extinction. *Sci. Adv.* **4**, e1602921.

Zhang F., Shen S., Cui Y., Lenton T. M., Dahl T. W., Zhang H., Zheng Q., Wang W., Krainer K. and Anbar A. D. (2020c) Two distinct episodes of marine anoxia during the Permian-Triassic crisis evidenced by uranium isotopes in marine dolostones. *Geochim. Cosmochim. Acta*.

Zhang F., Xiao S., Kendall B., Romaniello S. J., Cui H., Meyer M., Gilleaudeau G. J., Kaufman A. J. and Anbar A. D. (2018c) Extensive marine anoxia during the terminal Ediacaran Period. *Sci. Adv.* **4**, eaan8983.

Zhang F., Xiao S., Romaniello S. J., Hardisty D., Li C., Melezhik V., Pokrovsky B., Cheng M., Shi W. and Lenton T. M. (2019b) Global marine redox changes drove the rise and fall of the Ediacara biota. *Geobiology* **17**, 594–610.

Zhang J., Dauphas N., Davis A. M., Leya I. and Fedkin A. (2012) The proto-Earth as a significant source of lunar material. *Nature Geoscience* **5**, 251–255.

Zhang J., Dauphas N., Davis A. M. and Pourmand A. (2011) A new method for MC-ICPMS measurement of titanium isotopic composition: Identification of correlated isotope anomalies in meteorites. *Journal of Analytical Atomic Spectrometry* **26**, 2197–2205.

Zhang W., Wang Z., Moynier F., Inglis E., Tian S., Li M., Liu Y. and Hu Z. (2019) Determination of Zr isotopic ratios in zircons using laser-ablation multiple-collector inductively coupled-plasma mass-spectrometry. *Journal of Analytical Atomic Spectrometry* **34**, 1800–1809.

Zhao H., Algeo T. J., Liu Y., Chen Z.-Q., Zhang L., Hu Z. and Li Z. (2020) Lower Triassic carbonate δ238U record demonstrates expanded oceanic anoxia during Smithian Thermal Maximum and improved ventilation during Smithian-Spathian boundary cooling event. *Palaeogeogr. Palaeoclimatol. Palaeoecol.* **539**, 109393.

Zinner E. K., Fahey A. J., Goswami J. N., Ireland T. R. and McKeegan K. D. (1986) Large Ca-48 anomalies are associated with Ti-50 anomalies in Murchison and Murray hibonites. *The Astrophysical Journal* **311**, L103–L107.

2 URANIUM ISOTOPE VARIATIONS TRACING OCEANIC ANOXIA

This chapter is based on: Chen, X., Tissot, F. L. H., Jansen, M. F., Bekker, A., Liu, C. X., Nie, N. X., Halverson, G.P., Veizer, J. and Dauphas, N. (2021). The uranium isotopic record of shales and carbonates through geologic time. *Geochimica et Cosmochimica Acta*, *300*, 164-191.

2.1 Introduction

The variations in non-traditional stable isotopic compositions of marine sediments have been increasingly used to improve our understanding of the oxygenation history of Earth's surface. Among them, the uranium cycle in the modern ocean is relatively well understood and successfully applied to quantify the present extent of ocean anoxia at global scale. In the modern ocean, U reduction and incorporation into anoxic sediments imparts a large isotopic fractionation of approximately +0.6 ‰ that shifts the seawater $\delta^{238}U$ value ($^{238}U/^{235}U$, expressed as $\delta^{238}U$ per mil deviation relative to CRM-112a) relative to continental runoff. Given the long residence time of U in the modern oceans (~400 kyr), the isotopic composition of carbonates (taken as a proxy for seawater) reflects the global balance between anoxic and other sinks. The U isotopic composition of open-marine carbonates has thus emerged as a proxy for reconstructing past changes in the redox state of the global ocean.

Earth's surface oxygenation was marked by two critical transitions known as the Great Oxidation Event (GOE) at ca. 2.43-2.06 Ga and the Neoproterozoic Oxygenation Event (NOE) at ca. 0.68–0.54 Ga (potentially starting as early as 0.8 Ga), which both saw dramatic changes in global surface environments (Holland, 2002; Bekker et al., 2004; Johnston et al., 2012; Thomson et al., 2015; Turner and Bekker, 2016; Gumsley et al., 2017). While most previous studies have focused on specific short intervals of Earth's history when significant change in Earth's surface redox state happened, the aim of the present work is to investigate how U concentrations and isotopic compositions of sediments responded to Earth's progressive oxygenation over the full temporal extent of carbonate sedimentary record and test the tenets of the U isotope paleo-redox

proxy. For that purpose, we use carbonates as they should represent the best archive of the uranium isotopic composition of seawater through time.

Taking clues from the modern U cycle, paleo-redox reconstructions assume a near-constant U isotopic fractionation between oxidized U dissolved in seawater and reduced U deposited under anoxic conditions with organic-rich shales. The validity of this assumption can be directly tested by comparing the $^{238}U/^{235}U$ values in coeval shales and carbonates over broad geological timescales, in a similar manner to what has been done for $\delta^{13}C$ (organic and carbonate carbon) and $\delta^{34}S$ (sulfide and sulfate sulfur) proxies. Here, we report new $\delta^{238}U$ analyses of 95 Precambrian carbonates and combine these results with a compilation of literature data for carbonate and shale to test the assumption that the $\delta^{238}U$ values of shales are indeed fractionated relative to carbonates by a constant offset.

2.2 Materials and Methods

2.2.1 Sample Selections

In order to reconstruct the long-term redox evolution of the ocean, a large suite of marine carbonates (**Table 2.1**) was assembled and the U concentrations and isotopic compositions of 95 carbonate samples spanning the Archean to Neoproterozoic were measured and combined with previously published data (Brennecka et al., 2011; Dahl et al., 2014, 2017, 2019; Azmy et al., 2015; Hood et al., 2016; Lau et al., 2016, 2017; Elrick et al., 2017; Jost et al., 2017; Song et al., 2017; Bartlett et al., 2018; Chen et al., 2018a, b; Clarkson et al., 2018; Herrmann et al., 2018; Phan et al., 2018; White et al., 2018; Zhang et al., 2018a, b, c, 2020c, a, b; F. Zhang et al., 2019b, a; Gilleaudeau et al., 2019; Tostevin et al., 2019; Brüske et al., 2020a; Bura-Nakić et al., 2020; Cao

et al., 2020; Cheng et al., 2020; del Rey et al., 2020; Li et al., 2020; Zhao et al., 2020). The age and detailed description of the geological settings can be found in the references provided in **Table 2.1** and in **Appendix.** Most of the analyzed carbonate samples were deposited in shallow-marine settings above the storm (typically less than 15-40 m depth) and fair-weather-wave base (less than 5-15 m depth), and only two sample sets show no evidence for subaerial emergence and were likely deposited in a deeper environment. We avoided deep-water carbonate depositional settings, sediments with high organic carbon content, and thin carbonate beds and nodules in shales. Most of the sampled carbonate units are tens to hundreds of meters thick, contain little if any detrital material, and have sedimentary textures and structures indicating precipitation from seawater above the fair-weather-wave base. There are several reasons to expect that carbonate deposition in the Precambrian was dominantly restricted to shallow-marine settings and, after the Great Oxidation Event (GOE), was predominantly above the redoxcline:

(*i*) Export of carbonate to deep-water settings requires foraminifera and coccoliths and these did not evolve until the Phanerozoic, resulting in predominantly shallow-water carbonates in early Phanerozoic and Precambrian (*e.g.*, (Holland and Zimmermann, 2000). The only mechanism by which carbonates were transported to deep waters in the Precambrian was through gravity flow deposition, and such slope/deep water deposits were relatively rare.

(*ii*) The carbonate compensation depth in Precambrian oceans was likely shallower due to higher pCO_2.

(*iii*) Once the atmosphere became oxygenated and the shallow portion of the water column contained dissolved oxygen, the steady-state redoxcline could not have been shallower than the well-mixed layer above the fair-weather wave-base where most of our carbonates were deposited.

To summarize, our Precambrian carbonates typically record shallow depositional settings, and those deposited after the GOE likely precipitated above the redoxcline.

The least-altered and best-preserved samples were identified based on a combination of petrographic features and an array of geochemical tracers sensitive to the extent of post-depositional alteration (*i.e.*, Mg/Ca, Mn/Sr, $\delta^{18}O$, and $\delta^{13}C$ values) (Veizer et al., 1989a, b; Banner and Hanson, 1990). When exposed to meteoric waters during sea level lowstands, the oxygen isotopic composition ($\delta^{18}O$) of shallow-marine carbonates evolves towards lower values. The $\delta^{18}O$ values of our samples mostly range between -14 and -4 ‰, which is within the expected range for well-preserved Precambrian carbonates (Shields and Veizer, 2002). The $\delta^{13}C$ values also fall within the range of well-preserved Precambrian carbonates (Shields and Veizer, 2002), characterized by a value close to 0 ‰ during much of the Precambrian with the exception of anomalously high and variable $\delta^{13}C$ values during the early and late Proterozoic (2.35-2.0 Ga and 0.8-0.6 Ga). We did not adopt some of the criteria (*e.g.*, Mn/Sr and Mg/Ca ratios) used in some recent studies on uranium isotope systematics of Phanerozoic carbonates (*e.g.*, (Dahl et al., 2014; Lau et al., 2016; Bartlett et al., 2018)) to screen Precambrian carbonate samples because early in Earth's history most carbonate units were dolomitized shortly after deposition and have high Mn/Sr and Mg/Ca ratios, but preserve primary Sr isotopic values and I content (Veizer et al., 1989a, b, 1990, 1992a, b; Hardisty et al., 2017). Excluding dolomitic units would also leave large gaps in the carbonate archive. Instead, for some intervals, we have analyzed both limestones and dolostones to assess the effect of dolomitization on uranium isotopic ratios (see also the discussions in (Herrmann et al., 2018; Zhang et al., 2020a, b)).

Table 2.1 Sample age and locality, Mn/Sr, Mg/Ca ratios, stable isotopic compositions and U concentrations and isotopic composition for the carbonates measured in this study.

Sample	Rock Type	Age (Ga)	±	Mn/Sr	$\delta^{13}C$ carb (‰ V-PDB)	$\delta^{18}O$ (‰ V-PDB)	Reference*	Total carbonate [a] (wt%)	Mg/Ca [a]	[U] [b] (ppb)	±	$\delta^{238}U$ [c] (‰)	±	$\delta(^{234}U/^{238}U)$ [d] (‰)	±
Fig Tree Group, Barberton Greenstone Belt, Swaziland Supergroup, South Africa															
78-FT-15	Dolostone	3.25	0.02	34.6	1.56	-13.13	1	38.16	0.41	171.6	1.5	-0.21	0.06	728.90	0.35
Woman Lake Group, Uchi Greenstone Belt, Canada															
78-WO-629	Limestone	2.87	0.01	271.2	1.18	-10.19	1	85.54	0.01	113.4	1.0	-0.31	0.03	52.02	0.19
78-WO-617G	Limestone	2.87	0.01	121.3	1.30	-8.80	1	87.24	0.01	108.4	0.9	-0.21	0.03	-6.62	0.24
78-WO-621	Limestone	2.87	0.01	64.8	0.20	-12.70	1	72.84	0.11	383.0	1.7	-0.03	0.04	-11.97	0.33
Confederation Lake	Limestone	2.87	0.01	181.3	1.30	-9.10	1	82.60	0.01	68.0	0.6	-0.69	0.03	175.66	0.37
Mosher Carbonate, Steep Rock Lake Group, Wabigoon Belt, Canada															
1977/43	Limestone	2.79	0.01	8.9	2.50	-9.00	1	84.07	0.02	62.0	0.7	-0.53	0.03	73.74	0.34
1977/43 rep1.										58.4	0.7	-0.54	0.03	65.69	0.34
1977/43 rep2.										67.3	0.7	-0.56	0.03	77.53	0.34
								average		*62.5*	*0.4*	*-0.54*	*0.02*	*72.32*	*0.20*
1977/42	Limestone	2.79	0.01	2.5	2.00	-9.21	1	82.74	0.03	26.9	2.3	-0.42	0.06	290.78	0.38
Tumbiana Formation, Forstescue Group, Australia															
84-F-54.9	Limestone	2.73	0.01	293.0	-4.01	-18.77	2	51.00	0.02	74.3	0.7	-0.21	0.05	368.90	0.57
84-F-106	Limestone	2.73	0.01	140.1	-2.06	-8.34	2	37.23	0.08	162.0	1.5	-0.21	0.05	333.98	0.57
84-F-112.3	Limestone	2.73	0.01	705.6	-2.48	-18.43	2	32.96	0.06	142.3	1.3	-0.08	0.05	503.57	0.57
84-F-158.6	Limestone	2.73	0.01	303.9	-3.23	-18.74	2	37.64	0.03	84.8	0.8	-0.19	0.05	597.36	0.57
Klippan and Bothaville Formations, Vendersdorp Supergroup, South Africa															
79-VE-15	Limestone	2.72	0.01	14.6	-2.10	-19.60	2	34.04	0.05	233.6	2.0	-0.23	0.04	2111.19	0.28
79-VE-11c	Limestone	2.72	0.01	3.2	-3.19	-19.04	2	24.42	0.23	71.3	0.7	-0.01	0.11	3314.56	0.61
Gwanda Greenstone Belt, Zimbabwe															
78-SE-1b	Limestone	2.70	0.00	200.2	0.80	-9.60	1	84.33	0.01	22.8	0.3	-0.26	0.09	215.54	1.00
Yellowknife Supergroup, Slave Province, Canada															
HBA-J-224.2.74	Limestone	2.67	0.01	3.5	-5.70	-18.20	1	28.26	0.16	551.2	5.8	-0.43	0.04	424.08	0.30
HBA-J-147.4.74	Limestone	2.67	0.01	33.9	-14.37	-15.84	1	90.66	0.53	54.6	0.5	-0.18	0.08	10.48	0.43
Carawine Dolomite, Hamersley Group, Australia															

Table 2.1 *continued*

Sample	Rock Type	Age (Ga)	±	Mn/Sr	$\delta^{13}C$ carb (‰ V-PDB)	$\delta^{18}O$ (‰ V-PDB)	Reference*	Total carbonate [a] (wt%)	Mg/Ca [a]	[U] [b] (ppb)	±	$\delta^{238}U$ [c] (‰)	±	$\delta(^{234}U/^{238}U)$ [d] (‰)	±
84-Ca-240	Dolomite	2.63	0.00	627.5	-0.30	-8.70	2	81.01	0.08	23.4	0.2	-0.42	0.06	357.05	0.70
84-Ca-114	Dolomite	2.63	0.00	831.7	-0.77	-5.83	2	77.00	0.47	374.6	1.1	-0.41	0.02	70.36	0.18
84-Ca-118.3	Dolomite	2.63	0.00	647.9	-0.10	-5.25	2	86.08	0.53	256.5	0.9	0.00	0.03	35.70	0.19
Gamohaan Formation, Campbellrand Subgroup, South Africa															
WB98 - 519.33	Calcite	2.52	0.00		-1.24	-8.00	3	74.29	0.01	83.9	0.7	-0.32	0.04	201.03	0.48
WB98 - 515.13	Calcite	2.52	0.00		-1.55	-8.39	3	60.55	0.02	800.4	2.5	-0.12	0.03	139.02	0.25
WB98 - 513.2	Calcite	2.52	0.00		-1.77	-8.46	3	63.56	0.02	361.9	1.9	-0.12	0.04	171.76	0.24
WB98 - 519.63	Calcite	2.52	0.00		-3.32	-7.09	3	66.50	0.04	173.5	1.5	-0.11	0.03	112.86	0.22
WB98 - 509.6	Calcite	2.52	0.00		-1.78	-8.62	3	62.70	0.02	47.6	0.4	-0.23	0.04	255.33	0.47
WB98 - 519.63 white	Calcite	2.52	0.00		-0.48	-6.93	3	66.22	0.01	40.3	0.4	-0.58	0.05	67.94	0.58
WB98 - 522.44	Calcite	2.52	0.00		-1.18	-8.49	3	74.56	0.02	41.9	0.4	-0.36	0.04	149.55	0.47
Itabira Group, Gandarela Formation, Brazil															
GA-2 white	Calcite	2.43	0.00	13.1-15.4	-0.60	-8.80	4	87.62	0.01	71.4	0.7	-0.72	0.05	216.75	0.36
GA-2 white rep1.										82.4	0.8	-0.75	0.04	158.69	0.32
GA-2 white rep2.										93.4	0.9	-0.78	0.04	103.78	0.32
								average		*80.8*	*0.4*	*-0.75*	*0.03*	*155.67*	*0.19*
GA-1	Calcite	2.43	0.00	26.7	-0.40	-8.20	4	86.17	0.02	28.6	0.3	-0.82	0.12	-218.89	0.77
GA-4	Calcite	2.43	0.00	7.5	-1.00	-9.30	4	71.09	0.09	239.2	2.1	-0.76	0.05	193.88	0.35
GA-2 black	Calcite	2.43	0.00	13.1-15.4	-0.60	-8.80	4	76.18	0.05	165.6	1.4	-0.91	0.04	-259.23	0.26
Espanola Formation, lower Huronian Supergroup, Canada															
82-BL-2	Limestone	2.40	0.00	2.1	-1.29	-16.20	5	69.01	0.02	135.5	1.2	-0.29	0.03	1661.30	0.46
82-BL-5	Limestone	2.40	0.00	2.5	-1.24	-16.41	5	70.24	0.03	73.7	0.6	-0.18	0.04	1097.34	0.48
BL-S54-1697	Limestone	2.40	0.00	5.9	-1.46	-16.29	5	68.59	0.05	110.5	0.9	-0.31	0.04	2268.95	0.48
DM1722'	m. calcite	2.40	0.00	22.8	-2.10	-12.90	6	21.23	0.08	626.6	8.6	-0.35	0.04	426.64	0.30
DM2323'3"	Calcite	2.40	0.00	12.6	-1.50	-14.30	6	54.87	0.51	324.5	1.5	-0.33	0.02	373.11	0.19
Gordon Lake Formation, upper Huronian Supergroup, Canada															
PL-SA	Dolomite	2.31	0.00	123.6	6.20	-8.90	7	38.26	0.56	752.0	2.0	-0.27	0.02	305.45	0.18
PL-S	Dolomite	2.31	0.00		5.80	-9.40	7	33.33	0.58	602.1	2.2	-0.25	0.03	631.96	0.19
KN-S	Dolomite	2.31	0.00	4.6	8.20	-10.30	7	75.28	0.55	301.8	1.1	-0.21	0.02	168.53	0.19
Pretoria Group, Silverton Formation, South Africa															
Si-4	Dolostone	2.15	0.00	2.9	9.10	-7.40	8	75.56	0.53	107.3	0.5	-0.28	0.04	580.27	0.25
Mcheka Formation, Lomagundi Group, Zimbabwe															
SLD-11	Dolomite	2.10	0.00		11.60	-4.80	9	78.92	0.61	492.7	1.1	-0.32	0.02	63.71	0.18

Table 2.1 *continued*

Sample	Rock Type	Age (Ga)	±	Mn/Sr	$\delta^{13}C$ carb (‰ V-PDB)	$\delta^{18}O$ (‰ V-PDB)	Reference*	Total carbonate [a] (wt%)	Mg/Ca [a]	[U] [b] (ppb)	±	$\delta^{238}U$ [c] (‰)	±	$\delta(^{234}U/^{238}U)$ [d] (‰)	±
Fecho do Funil Formation, Minas Supergroup, Minas Gerais, Brazil															
PC-5	Dolomite	2.10	0.00	61.3	7.40	-11.00	4	70.20	0.54	146.8	0.7	-0.29	0.04	274.62	0.25
Mistassini Group, Albanel Formation															
MI-10-1	Dolomite	2.10	0.00		0.30	-9.60	10	18.08	1.04	497.1	4.8	-0.35	0.04	277.34	0.25
D2-83-74	Limestone	2.10	0.00	1.1	1.23	-10.93	10	76.77	0.04	166.4	1.5	-0.50	0.03	129.34	0.18
D2-81-74	Limestone	2.10	0.00	0.7	1.46	-11.51	10	34.29	0.47	696.3	3.5	-0.29	0.03	155.90	0.20
D2-72-74	Limestone	2.10	0.00				10	20.53	0.84	273.7	2.4	-0.03	0.05	491.15	0.31
upper Nash Fork Formation, upper Libby Creek Group, USA															
2000-3	Dolomite	2.05	0.00	1.8	1.50	-4.80	11	75.11	0.55	141.3	0.5	-0.55	0.02	57.58	0.20
Roberts Draw Formation and Estes Creek Formation, Black Hills, South Dakota															
B99.14	Calcite	2.00	0.00		-0.20	-9.80	11	79.76	0.51	524.2	0.9	-0.17	0.02	149.25	0.18
B99.11	Dolomite	2.00	0.00		1.30	-9.70	11	75.69	0.52	61.3	0.5	-0.42	0.06	1144.69	0.35
SD99.2-7	Dolomite	2.00	0.00		2.40	-11.70	11	78.85	0.52	193.9	0.5	-0.30	0.02	668.62	0.19
Snare Group, Basler Lake, NWT, Canada															
SN-1	Dolomite	1.97	0.00		2.52	-8.07	12	92.53	0.54	150.3	0.4	-0.42	0.02	182.15	0.18
Aluminium River Formation, Amer Group, Nunavut, Canada															
AMC14	Dolomite	1.93	0.00		4.27	-7.13	13	85.75	0.61	258.2	0.8	-0.44	0.03	-111.11	0.20
Watterson Formation, Hurwitz Group, Nunavut, Canada															
96-16-1	Dolomite	1.93	0.00	15.2	1.40	-9.50	14	83.92	0.57	71.2	0.6	-0.36	0.05	658.93	0.27
Cowles Lake Formation, Coronation Supergroup, NWT, Canada															
84-Co-19	Limestone	1.88	0.00	0.5	1.80	-13.14	5	56.43	0.09	152.1	1.3	-0.32	0.03	149.55	0.42
84-Co-20	Limestone	1.88	0.00	3.2	-1.83	-13.29	5	67.04	0.02	53.3	0.5	-0.32	0.05	504.63	0.57
84-Co-21	Limestone	1.88	0.00	4.4	1.40	-11.28	5	74.67	0.05	60.0	0.5	-0.35	0.04	533.07	0.55
Taltheilei Formation, Pethei Group, NWT, Canada															
TL 12	Dolomite	1.86	0.00		1.37	-8.01	12	58.57	0.56	217.3	1.0	-0.28	0.02	960.23	0.19
George Formation, Muskwa Assemblage, BC, Canada															
MUSQUA		1.60	0.00				15	53.42	0.15	122.3	1.1	-0.36	0.04	1346.94	0.48
Wallace, Helena, and Snowslip Formations, Belt Supergroup, MT, USA															
Base	Limestone	1.45	0.00				12	58.49	0.04	2649.2	4.4	-0.19	0.04	103.79	0.30

Table 2.1 *continued*

Sample	Rock Type	Age (Ga)	±	Mn/Sr	$\delta^{13}C$ carb (‰ V-PDB)	$\delta^{18}O$ (‰ V-PDB)	Reference*	Total carbonate [a] (wt%)	Mg/Ca [a]	[U] [b] (ppb)	±	$\delta^{238}U$ [c] (‰)	±	$\delta(^{234}U/^{238}U)$ [d] (‰)	±
Upper1	Limestone	1.45	0.00				12	73.31	0.03	186.4	1.7	-0.24	0.04	290.59	0.27
B1-5	Limestone	1.45	0.00				12	36.51	0.16	336.9	3.3	-0.29	0.05	504.33	0.35
A1-5	Limestone	1.45	0.00				12	44.16	0.04	219.8	1.9	-0.40	0.04	574.68	0.26
Upper2	Limestone	1.45	0.00				12	71.00	0.06	191.7	1.6	-0.29	0.04	243.39	0.33
RP190	Limestone	1.45	0.00				12	67.45	0.02	77.3	0.9	-0.28	0.03	538.00	0.18
RP10	Limestone	1.45	0.00		-0.68	-10.46	12	62.13	0.02	45.4	0.4	-0.13	0.04	1371.70	0.47
RP 682	Limestone	1.45	0.00		2.08	-9.33	12	79.32	0.01	94.1	0.8	-0.57	0.04	418.22	0.28
RP 711	Limestone	1.45	0.00		1.33	-10.18	12	75.27	0.03	66.5	0.6	-0.51	0.03	492.84	0.37
RP 504	Limestone	1.45	0.00				12	74.70	0.02	205.9	1.5	-0.20	0.03	192.91	0.25
Sukhaya Tunguska Fm., Western Siberia															
GS4-448	Limestone	1.04	0.00		3.50	-6.86	16	87.16	0.01	39.2	0.4	-0.64	0.07	147.08	0.50
GS4-448 rep1.										49.5	0.5	-0.59	0.07	136.65	0.50
GS4-448 rep2.										51.7	0.5	-0.64	0.06	147.90	0.41
								average		*45.4*	*0.3*	*-0.63*	*0.04*	*144.45*	*0.27*
GS4-401	Limestone	1.04	0.00	0.04	1.50	-6.61	16	75.30	0.04	127.6	1.1	-0.82	0.04	127.14	0.34
GS4-490	Limestone	1.04	0.00		3.75	-6.59	16	86.46	0.02	145.9	1.3	-0.79	0.04	76.57	0.27
GS4-478	Limestone	1.04	0.00		3.06	-6.64	16	87.22	0.05	77.7	0.7	-0.64	0.04	163.67	0.28
GS4-383	Limestone	1.04	0.00		1.14	-7.29	16	73.05	0.02	81.8	0.7	-0.61	0.04	217.05	0.55
Ymer Ø Group, Eleonore Supergroup, E. Greenland															
GR9-564	Limestone	0.81	0.01	0.01	5.33	-8.32	17, 18	84.23	0.00	1159.6	2.5	-0.64	0.04	56.45	0.19
GR9-564 rep1.										1216.2	1.3	-0.65	0.04	55.89	0.19
GR9-564 rep2.										1204.3	1.3	-0.65	0.04	56.36	0.19
								average		*1204.2*	*0.9*	*-0.65*	*0.02*	*56.23*	*0.11*
GR9-178.6	Limestone	0.81	0.01		4.34	-9.30	17, 18	53.15	0.12	70.4	0.8	-0.18	0.12	413.28	0.77
GR9-148.3	Limestone	0.81	0.01	1.80			17, 18	65.34	0.05	38.9	0.4	-0.22	0.05	779.74	0.58
GR9-148.3 rep										36.7	0.3	-0.25	0.05	747.24	0.57
								average		*37.6*	*0.3*	*-0.23*	*0.04*	*763.40*	*0.41*
GR9-131	Limestone	0.81	0.01	0.90	-0.86	-9.45	17, 18	73.72	0.02	406.0	1.7	-0.14	0.04	471.83	0.33
GR9-120.3	Limestone	0.81	0.01	0.67	-0.34	-9.98	17, 18	79.62	0.01	34.6	0.4	0.10	0.06	628.04	0.70
GR9-326	Limestone	0.81	0.01	0.02	4.98	-7.66	17, 18	86.78	0.01	132.3	1.0	-0.64	0.03	48.77	0.41
Elbobreen Fm., Polarisbreen Group, Svalbard															
G529-66	Limestone	0.73	0.00	0.64	2.51	-8.85	19, 20	67.20	0.04	289.4	2.6	-0.32	0.03	365.86	0.18
G529-77	Limestone	0.73	0.00	0.47	2.55	-8.71	19, 20	67.57	0.05	18.8	0.3	0.01	0.06	488.39	0.70
G529-68.1	Limestone	0.73	0.00	0.54	2.13	-9.07	19, 20	63.28	0.07	118.9	1.2	-0.18	0.04	402.62	0.48
G529-72.5	Limestone	0.73	0.00	0.36	-1.91	-8.67	19, 20	81.16	0.02	48.6	0.4	-0.11	0.04	431.07	0.55

Table 2.1 *continued*

Sample	Rock Type	Age (Ga)	±	Mn/Sr	$\delta^{13}C$ carb (‰ V-PDB)	$\delta^{18}O$ (‰ V-PDB)	Reference*	Total carbonate [a] (wt%)	Mg/Ca [a]	[U] [b] (ppb)	±	$\delta^{238}U$ [c] (‰)	±	$\delta(^{234}U/^{238}U)$ [d] (‰)	±
Bed-Group 20, E. Greenland															
GR16-70	Limestone	0.73	0.00	0.83	-6.47	-8.25	21	45.73	0.12	293.2	2.5	-0.52	0.06	255.77	0.38
GR16-105.4	Limestone	0.73	0.00		-2.30	-7.26	21	74.57	0.01	127.6	1.1	-0.79	0.03	56.04	0.24
GR16-37.3	Limestone	0.73	0.00		-6.38	-4.24	21	38.89	0.73	373.4	2.3	-0.47	0.02	171.65	0.19
Rasthof Formation, Otavi Group, Namibia															
B036-20.0	Limestone	0.66	0.00		-0.80	-10.30	22	83.93	0.04	237.6	2.9	-0.14	0.03	201.14	0.18
B036-20.0 rep1.										289.3	3.1	-0.17	0.03	199.66	0.18
B036-20.0 rep2.										296.1	3.1	-0.19	0.03	194.75	0.18
								average		*272.4*	*1.7*	*-0.16*	*0.02*	*198.51*	*0.11*
B036-7.9	Limestone	0.66	0.00		-1.80	-8.20	22	85.96	0.08	401.9	1.4	-0.21	0.04	395.52	0.24
B036-35.7	Limestone	0.66	0.00		-1.00	-6.90	22	81.62	0.03	66.1	0.4	-0.34	0.05	110.67	0.34
B036-3.4	Limestone	0.66	0.00		-2.20	-8.40	22	83.21	0.07	485.7	1.5	-0.13	0.04	315.02	0.33
B036-40.0	Limestone	0.66	0.00		-0.40	-6.20	22	84.02	0.04	377.0	1.5	-0.18	0.03	146.29	0.25
B036-12.0	Limestone	0.66	0.00				22	86.49	0.16	109.6	1.2	-0.27	0.03	591.37	0.41
B036-2.5	Limestone	0.66	0.00		-1.80	-6.80	22	85.33	0.16	235.6	1.8	-0.19	0.03	217.76	0.41
Maieberg Formation, Otavi Group, Namibia															
P4017.6.0	Dolostone	0.63	0.00		-2.98	-6.01	22	91.83	0.58	226.5	0.9	-0.33	0.02	251.59	0.19
P4017.16.1	Dolostone	0.63	0.00		-4.51	-7.79	22	76.71	0.55	193.7	0.6	-0.49	0.02	565.51	0.18
P4017.0.63	Dolostone	0.63	0.00		-3.10	-5.84	22	90.29	0.54	29.3	0.3	-0.15	0.08	555.85	0.43
geostandard															
SDO-1	Black Shale	Devonian						*average*		*42237.8*	*17.0*	*-0.07*	*0.01*	*-0.40*	*0.07*

* References for sample description Mn/Sr and stable isotope data: (1) Veizer et al. 1989b; (2) Veizer et al. 1990; (3) Rouxel et al., 2005; (4) Bekker et al., 2003b; (5) Veizer et al., 1992; (6) Bekker et al., 2005; (7) Bekker et al., 2006 ; (8) Bekker et al., 2008; (9) Master et al., 2010; (10) Mirota and Veizer, 1994; (11) Bekker et al., 2003a; (12) Hardisty et al., 2017; (13) Rainbird et al., 2010; Bekker and Eriksson, 2003; (14) Aspler and Chiarenzelli, 2002; (15) Ross et al., 2001; (16) Bartley et al., 2001; (17) Sonderholm and Tirsgaard 1993; (18) Worndle et al. 2019; (19) Fairchild and Hambrey 1995; (20) Halverson et al. 2018a; (21) Herrington and Fairchild 1989; (22) Hoffman and Halverson 2008

[a] estimated from major element abundances determined on compacted powder pellets using scanning electron microscope (SEM)

[b] U concentrations in the digested carbonate fraction

[c] $\delta^{238}U$ (‰)=$[(^{238}U/^{235}U)_{sample} / (^{238}U/^{235}U)_{CRM\text{-}112a}\text{-}1]\times1000$, where CRM-112a is a U standard

[d] $\delta(^{234}U/^{238}U)$ (‰)=$[(^{234}U/^{238})_{sample} / (\lambda_{238}/\lambda_{234})\text{-}1)]\times1000$, where λ_{238} and λ_{234} are the decay constants of ^{238}U and ^{234}U, respectively, $\lambda_{238}/\lambda_{234}=(1.5513\times10^{-10})/(2.8220\times10^{-6})=5.4970\times10^{-5}$(Cheng et al., 2013).

2.2.2 Sample preparation

Samples provided as rock specimens were visually inspected, and veins and non-carbonate component (*e.g.*, sulfides) were trimmed off with a rock saw. The carbonates samples were then crushed into fine powder using an agate mortar and pestle, and the carbonate content was estimated from major element abundances determined on compacted powder pellets using a JEOL JSM-5800LV scanning electron microscope (SEM). The carbonate content was used to calculate the amount of acid to add to each sample to fully digest the carbonate fraction without leaching detrital phases (Tissot et al., 2018; Clarkson et al., 2020; Zhang et al., 2020b).

Approximately 1 g of carbonate powder was used for each sample analysis. We added just enough 1M HCl to digest only 1% of the sample in order to remove the easily mobilized U, which could be of secondary origin ((Kuznetsov et al., 2017). The remaining bulk carbonates were digested using just enough 1 M HCl to digest the carbonate fraction. The centrifuge tubes containing the powdered carbonates were placed on a shaking platform to allow the solids and acid to fully react. Once the reaction was completed, after ~24 hours, the tubes were centrifuged and the supernatants were pipetted out. The remaining insoluble residues were dried in a laminar flow hood using heat lamps for approximately one day. The weight loss was used to estimate the mass of carbonate digested, which is required to calculate U concentrations. In **Table 2.1**, we report U concentrations in the digested carbonate fraction (amount of U in the leachate divided by mass of carbonate dissolved).

2.2.3 Uranium extraction chromatography

After digestion, 20 μL (~0.1%) of the sample solution was taken, diluted 100-fold and used for U concentration measurement on a Neptune MC-ICP-MS. The U concentrations were used to calculate the amount of spike to add before column chemistry. The remaining liquid was then transferred into a clean Teflon beaker and spiked with the IRMM-3636 U double spike (49.51% ^{236}U and 50.46% ^{233}U; (Verbruggen et al., 2008)). Enough spike was added to obtain a U_{spike}/U_{sample} ratio of ~3%. After spiking, the samples were dried completely then redissolved in concentrated HNO_3 before dilution with 3 M HNO_3. Uranium purification was performed on 2 mL cartridges (length = 2.7 cm, diameter = 0.8 cm) of U-TEVA specific resin, following the procedure described in previous publications (Telus et al., 2012; Tissot and Dauphas, 2015; Tissot et al., 2018). In brief, the resin was cleaned with 40 mL of 0.05 M HCl and conditioned with 10 mL of 3 M HNO_3. The digested samples were loaded onto the column in ~5 mL of 3 M HNO_3 and matrix elements were removed with 30 mL of 3M HNO_3. The resin was converted with 5 mL of 10 M HCl. Thorium was eluted in 12 mL of 5 M HCl. Uranium was finally eluted in 32 mL of 0.05 M HCl. All samples were purified twice through the column chemistry to ensure full removal of matrix elements. Following chemical separation, the U cuts were dried down completely, taken back in 0.4 mL of HNO_3-H_2O_2 (1:1), and dried again before being re-dissolved in concentrated HNO_3, evaporated to near dryness, and taken back in 0.3 M HNO_3 for isotopic analysis.

2.2.4 Uranium mass spectrometry

All U isotopic analyses followed the protocol detailed in previous work of our group (Tissot and Dauphas, 2015; Tissot et al., 2017, 2018) and were performed on the ThermoFinnigan

Neptune MC-ICP-MS upgraded to Neptune Plus specifications (*i.e.*, with a jet pump installed) at the Origins Laboratory of the University of Chicago. Jet sample and X-skimmer cones were used in combination with an Aridus II desolvating nebulizer. The measurements were performed in low-resolution mode, using a static cup configuration and comprised 60 cycles of 4.194 s integration time each (see (Tissot and Dauphas, 2015) for details). The measurements were performed on ~8 mL of solution with U concentrations between 20 and 30 ppb. The instrument sensitivity was ~1.5 V/ppb on ^{238}U with a 10^{11} Ω resistance amplifier and a 100 µl/min nebulizer. Baseline and gain calibrations were performed daily. Isotope mass fractionation introduced during chemical separation and mass spectrometry was corrected for using the ^{233}U/^{236}U double-spike IRMM-3636. The data reduction methodology is described in detail in Tissot and Dauphas (2015). The sample measurements were bracketed by measurements of the CRM-112a standard spiked with IRMM-3636 with a spike/standard ratio similar to that of the samples. The ^{238}U/^{235}U ratios are reported using the δ notation in per mil units as,

$$\delta^{238}\mathrm{U}\ (‰) = [(^{238}\mathrm{U}/^{235}\mathrm{U})_{\mathrm{sample}} / (^{238}\mathrm{U}/^{235}\mathrm{U})_{\mathrm{CRM\text{-}112a\text{-}1}}]\times 1000\,, \quad (2.1)$$

The ^{234}U/^{238}U ratio is reported as a departure from secular equilibrium,

$$\delta(^{234}\mathrm{U}/^{238}\mathrm{U}) = [(^{234}\mathrm{U}/^{238})_{\mathrm{sample}} / (\lambda_{238}/\lambda_{234})\text{-}1]]\times 1000\,, \quad (2.2)$$

where λ_{238} and λ_{234} are the decay constants of ^{238}U and ^{234}U, respectively, and $\lambda_{238}/\lambda_{234} = (1.5513 \times 10^{-10})/\ (2.8220 \times 10^{-6}) = 5.4970 \times 10^{-5}$ (Cheng et al., 2013). The uncertainties are calculated based on the reproducibility of the CRM-112a standard measurements that bracketed the sample solution analyses and are reported as 95% confidence intervals.

2.3 Results

We repeatedly processed (n=24) and measured the U isotopic composition of geo-standard SDO-1 (a Devonian black shale) and found an average value of -0.07 ± 0.008 ‰ (2SD, each was measured 4 to 8 times in different sessions), which agrees well with previously published data for the same geo-standard of -0.08 ± 0.03 ‰ (Tissot and Dauphas, 2015). Several samples (with different ages) were replicated multiple times, from sequential dissolution to U isotope analysis. The U concentrations and isotopic compositions agree well between the replicate analyses (see **Table 2.1**). These measurements show that our data are reproducible and do not suffer from any obvious analytical bias.

Using the two-step leaching protocol described in **Section 2.2.2**, we measured U concentrations and isotopic compositions of carbonate samples (n=95) ranging in age from 0.63 to 3.25 Ga. The first leaching step, aimed at removing easily mobilized U, released only 1 % of the total U during digestion of carbonate. Because of the low U concentrations in the Precambrian carbonates, large sample masses were used (typically 1 g) to provide sufficient U (typically ~20 to 200 ng) for $\delta^{238}U$ measurement with a precision of ~±0.05 ‰. The results are presented in **Figs. 2.1 and 2.2**, along with literature data (see references listed in **Section 2.2.1** and **Supplementary Table 1**), and good agreement is observed for samples of similar age. Note that the data for carbonates with ages between 2.72 and 2.6 Ga from (Wang et al., 2018) were excluded from this compilation because these samples display both high U concentrations (1.61 ppm on average) and Al/U ratios that are higher than average Al/U ratios in basalts and granites (Asael et al., 2013), indicating that the U budget in these samples is overwhelmed by detrital U.

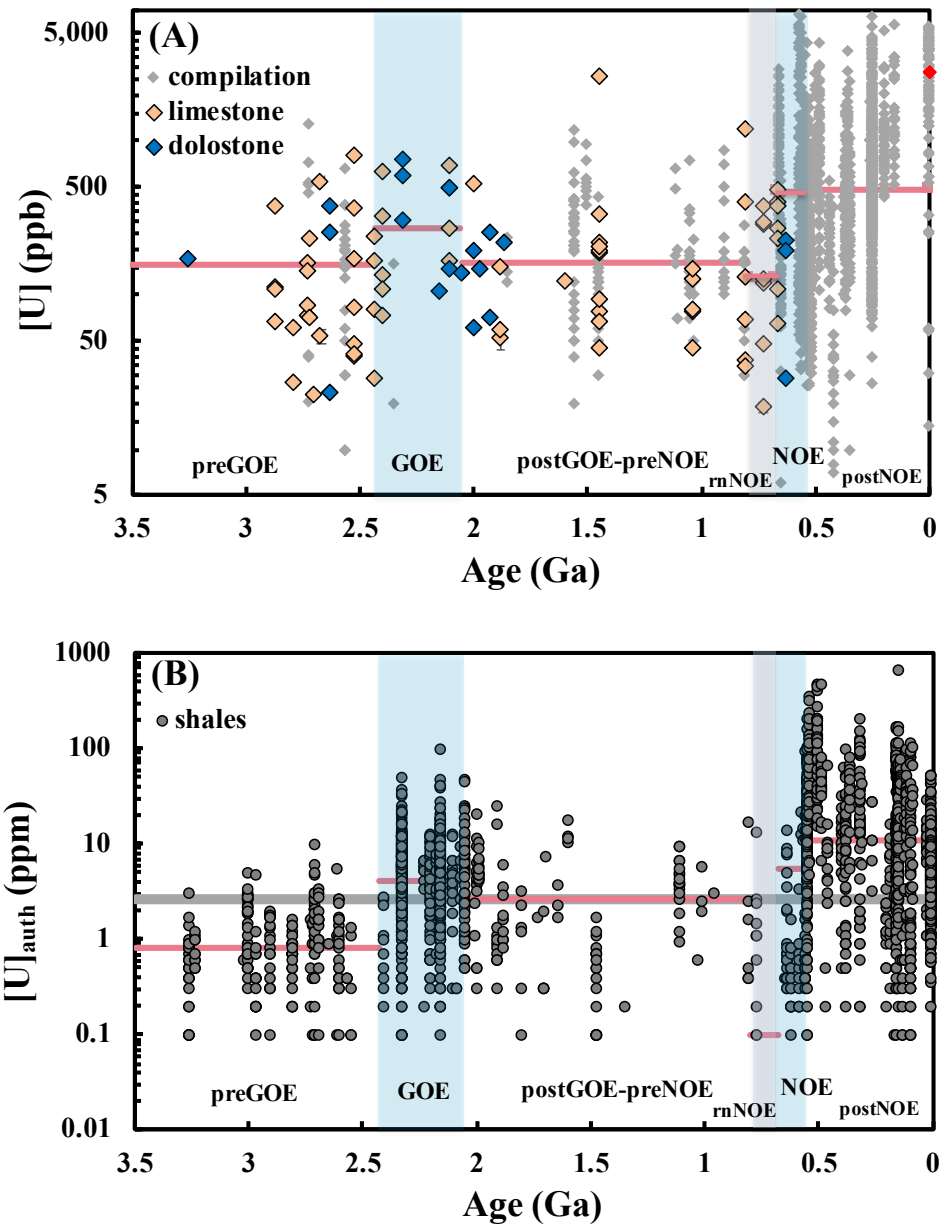

Figure 2.1 (A). [U] in carbonates through time. [U] data measured in this study (orange diamonds = limestones; blue diamonds = dolostones) are for the leached carbonates fractions (U per unit mass of carbonate dissolved; see detail in Section 2.2.2). Grey diamonds are [U] literature data (see compilation in **Supplementary Table 1**). The red bars are the median uranium concentrations of carbonates in the six intervals of 3.25-2.43 Ga (preGOE), 2.43-2.06 Ga (GOE), 2.06-0.8 Ga (postGOE-preNOE), 0.8-0.68 Ga (ruNOE, ramp up to NOE), 0.68-0.54 Ga (NOE), and 0.54 Ga-

Figure 2.1 *continued*
present (postNOE). The large red dot is the median modern value. (B). $[U]_{auth}$ in shales through time ($[U]_{auth} = [U]_{total}$-[Th]/3 with [U] and [Th] in ppm). Note that [U] in carbonates and shales are displayed in different units (ppb vs. ppm). Shale data are from (Partin et al., 2013a). The average [U] in the continental crust is indicated by the grey line at 2.7 ppm ((Taylor and McLennan, 1985b)). The red lines are the medians of the authigenic uranium concentrations in shales during the same six intervals as defined for the carbonate data.

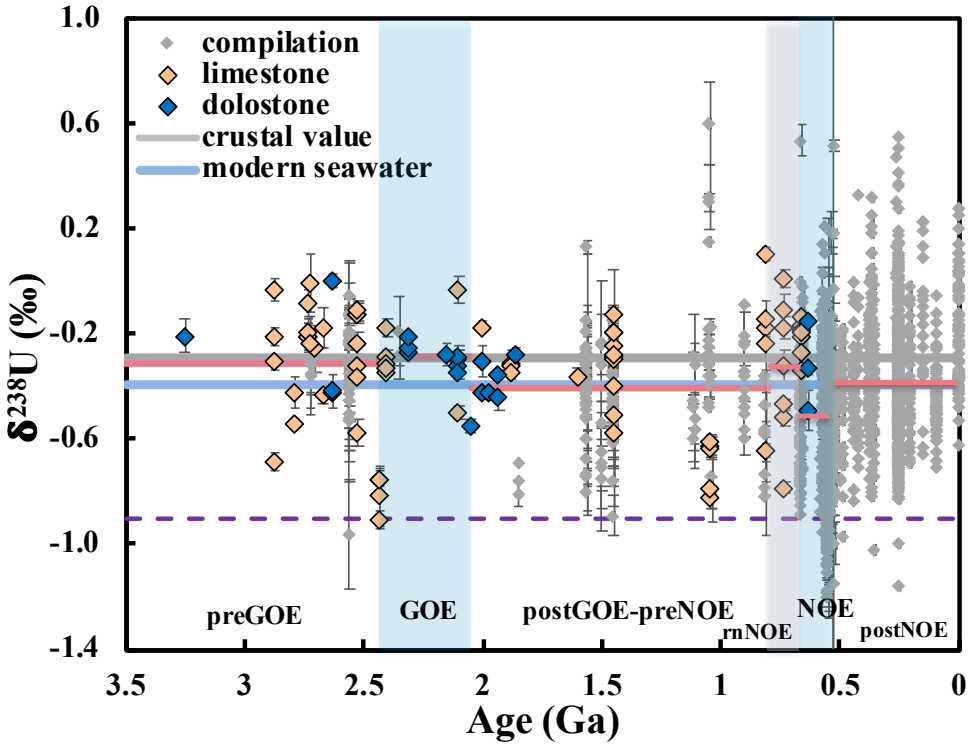

Figure 2.2 $\delta^{238}U$ in carbonates through time. $\delta^{238}U$ data measured in this study on leached carbonates fraction are displayed as orange diamonds for limestones and blue diamonds for dolostones. For both [U] and $\delta^{238}U$, the data shows no systematic difference between dolostones and limestones in the Precambrian. Grey diamonds are literature data (see **Supplementary Table 1**). $\delta^{238}U$ of the continental crust (-0.29 ± 0.03‰) and modern seawater (-0.392 ± 0.005‰, (Tissot and Dauphas, 2015)) are shown for comparison. The red lines are the median uranium isotopic composition of carbonates in the same six intervals as shown in **Fig. 2.1**. The purple dashed line shows the first-order expected $\delta^{238}U$ value (-0.9 ‰) of carbonates and seawater in a steady-state ocean if the uranium oceanic sink is predominantly anoxic (the U fraction going into anoxic sediment is close to 100%). Contrary to expectations, carbonates show $\delta^{238}U$ values similar to

Figure 2.2 *continued*
those of the continental crust and riverine runoff. These results are inconsistent with the view that the U isotopic composition of Precambrian seawater simply reflects the areal extent of anoxic sediments in the past.

We calculated average, median, and mode of U concentrations and $\delta^{238}U$ values of carbonates spanning different time intervals (before 2.43 Ga = preGOE; between 2.43 and 2.06 Ga = GOE; between 2.06 and 0.8 Ga = postGOE-preNOE; between 0.8 and 0.68 Ga = ruNOE = ramp up to NOE; between 0.68 and 0.54 Ga = NOE; 0.54 Ga to present = postNOE) and ran two-sided student *t*-tests to evaluate if these quantities changed significantly across consecutive time intervals. The average U concentration in preGOE carbonates is 209±58 ppb (n=64, median=155 ppb, mode=230 ppb), while the average of carbonates spanning the GOE is 323±123 ppb (n=17, median=274 ppb). Carbonates deposited in postGOE-preNOE have an average [U] of 243±45 ppb (n=159, median=160 ppb, mode=120 ppb) (**Fig. 2.1A**). No significant difference in U concentration is detected for either preGOE and GOE, or GOE and postGOE-preNOE time intervals (*p*-values of 0.09 and 0.21, respectively). Shales show a clear increase in their U concentrations across the GOE (Partin et al. 2013a, see also **Fig. 2.1B**).

Carbonates deposited in ruNOE (0.8-0.68 Ga) have an average [U] of 181±126 ppb (n=7, median=128 ppb). Carbonates deposited during the NOE (0.68-0.54 Ga) show a marked increase in U concentration to an average value of 952±155 ppb (n=410, median=469 ppb, mode=300 ppb). Carbonates deposited after the NOE and through the present have an average [U] of 901±64 ppb (n=1233, median=486 ppb, mode=240 ppb) (**Fig. 2.1A**). Statistical tests show that carbonates deposited before the NOE have significantly lower U concentrations than those deposited during the NOE or after (*p*-values of 0.30, 2×10^{-11}, and 0.55 for 2.06-0.8 Ga postGOE-preNOE *vs*. 0.8-

0.68 Ga ruNOE; ruNOE *vs*. 0.68-0.54 Ga NOE, and NOE *vs*. 0.54-0 Ga postNOE comparisons, respectively). The significantly different average and median U concentrations in carbonates deposited before and after the NOE indicate that the U seawater cycle and reservoir size changed dramatically during the NOE.

There is no clear trend in the $\delta^{238}U$ value of carbonates across the GOE (**Fig. 2.2**) with *t*-tests yielding *p*-values of 0.11, 0.0003 and 0.07 for comparisons between preGOE/GOE, GOE/postGOE-preNOE and preGOE/postGOE-preNOE respectively. The preGOE samples have an average $\delta^{238}U$ value of -0.34 ± 0.06 ‰ (n=59, median= -0.31 ‰, mode= -0.35 ‰), which is within error identical to the crustal value of -0.29 ± 0.03 ‰ (Tissot and Dauphas, 2015). The samples deposited during the GOE give an average $\delta^{238}U$ value of -0.28 ± 0.05 ‰ (n=17, median= -0.29 ‰), and the postGOE-preNOE carbonates give an average $\delta^{238}U$ value of -0.40 ± 0.04 ‰ (n=159, median= -0.41 ‰, mode= -0.36 ‰). Note that the $\delta^{238}U$ values of our Archean and mid-Proterozoic carbonates agree well with the recently published data from (Brüske et al., 2020a), (X. Wang et al., 2020) and (Gilleaudeau et al., 2019). Although the postGOE-preNOE average and median $\delta^{238}U$ values are closer to the modern seawater value of -0.40 ‰ (Tissot and Dauphas 2015) than those of the Archean carbonate samples, the two-sided student *t*-tests *p*-values between preGOE and postGOE-preNOE is 0.07, which shows no significant difference between these two intervals.

The ruNOE carbonates give an average $\delta^{238}U$ value of -0.34 ± 0.25 ‰ (n=7, median= -0.32 ‰), while NOE and postNOE carbonates have average $\delta^{238}U$ values of -0.53 ± 0.03 ‰ (n=393, median= -0.51 ‰, mode= -0.34 ‰) and -0.37 ± 0.01 ‰ (n=1147, median= -0.39 ‰, mode= -0.37 ‰), respectively. The p-values of the statistical tests for comparison between postGOE-

preNOE/ruNOE, ruNOE/NOE and NOE/postNOE are 0.57, 0.12 and 7×10^{-21}, respectively. The statistical test results confirm that the U oceanic cycle and reservoir size before and after NOE (~ 0.54 Ga) are significantly different.

We have also compared the Precambrian dolostone compositions (shown in blue diamonds in **Figs. 2.1 and 2.2**) with those for limestone samples of the same ages (shown in orange diamonds in **Figs. 2.1 and 2.2**). Both [U] and $\delta^{238}U$ values show no significant systematic difference between dolostone and limestone samples (**Figs. 2.1 and 2.2**). In addition, we show in **Fig. 2.3** the histograms of [U] and $\delta^{238}U$ values of shallow-marine and deep-marine carbonates in our sample set, and we find that there is no difference in [U] and $\delta^{238}U$ values between the two groups, with the caveat that the number of deep-marine carbonates measured in the present study is only 5.

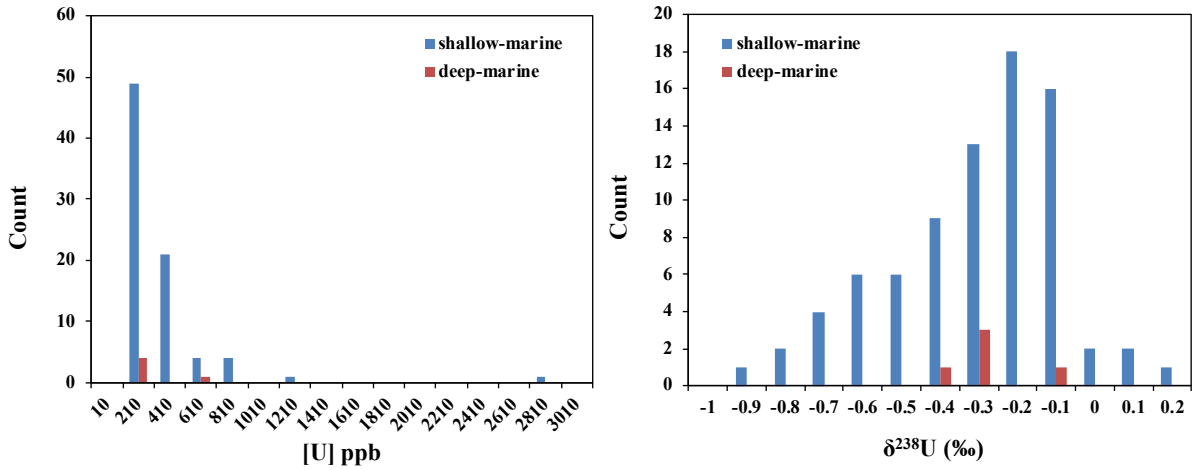

Figure 2.3 Histograms of [U] (left) and $\delta^{238}U$ (right) values in shallow-marine and deep-marine carbonates in our sample set. Most of the samples are shallow-marine carbonates, which were deposited above the storm- and fair-weather-wave base. Two sample sets were inferred to deposited in a deeper environment and are designated in the histogram as "deep-marine". Although the number of deep-marine carbonates is limited, the current dataset shows that there is no difference in [U] and $\delta^{238}U$ values between the two groups.

The [U] and $\delta^{238}U$ values of carbonates are also plotted in **Fig. 2.4A**, color-coded to represent the same six intervals shown in **Figs. 2.1 and 2.2**. The distributions of the U data ([U] and $\delta^{238}U$) also suggest that except for the dramatic change recorded in carbonates spanning the NOE, there is no clear change prior to that time.

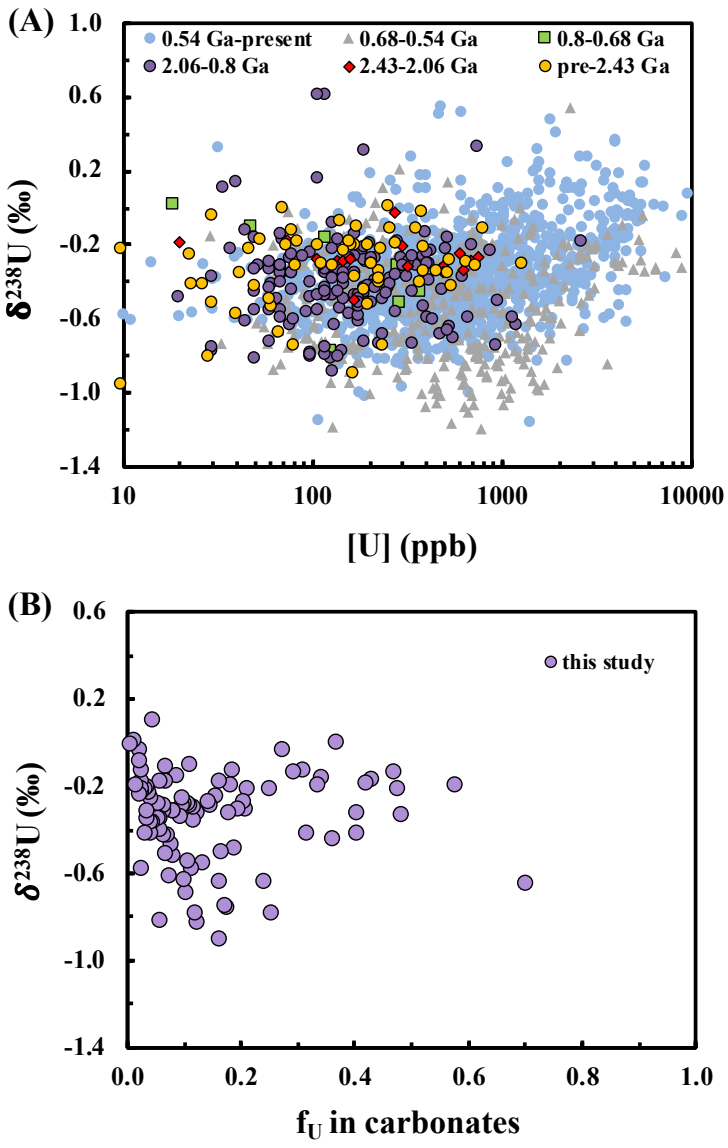

Figure 2.4 (A). $\delta^{238}U$ *vs*. [U] in carbonates. Data are from this study and literature (see **Supplementary Table 1**). The distribution of the U data clearly shows that there are differences in the U oceanic cycle and reservoir size before and after NOE (~ 0.54 Ga), while differences

Figure 2.4 *continued*
among other time intervals are not clear based on the current dataset. (B). $\delta^{238}U$ *vs*. U fraction in carbonates (f_U). Neither $\delta^{238}U$ *vs*. [U], nor $\delta^{238}U$ *vs*. f_U show any correlation that point to contamination by a detrital component.

A possible concern is that given the low authigenic U concentration in Precambrian carbonates, they could be more easily disturbed by the detrital component than those deposited during the Phanerozoic. We find large $\delta(^{234}U/^{238}U)$ excesses in carbonate that do not correlate with $\delta^{238}U$ values (**Fig. 2.6**). As discussed below (**Sect. 4.1**), these ^{234}U excesses are thought to be due to recoil effects from detrital grains into carbonates, and they would be small if significant amounts of detrital U had been digested during leaching. As shown in **Fig. 2.4A**, we also do not see any correlation between [U] and $\delta^{238}U$ values of carbonates. We find no correlation neither between $\delta^{238}U$ values and the fraction of bulk U that is in the carbonate fraction (the rest is in the detrital fraction; assumed to have a composition close to that of the upper continental crust) (**Fig. 2.4B**). If the carbonates were contaminated by detritus through leaching in the laboratory or fluid circulation in sediments, one would expect to find mixing relationships in these diagrams. At lower [U] and higher f_U, $\delta^{238}U$ would tend to be more negative (closer to a putative anoxic ocean value), while at higher [U] and lower f_U, $\delta^{238}U$ would tend to be closer to the crustal value. No such correlations are found. To summarize, the effect of contamination by detrital U is most likely small and cannot account for the fact that most Precambrian carbonates have near-crustal $\delta^{238}U$ values.

We report in **Table 2.1** and **Fig. 2.5** the $\delta(^{234}U/^{238}U)$ values of our old carbonate samples. Most of the $\delta(^{234}U/^{238}U)$ values of our old carbonate samples deviate from secular equilibrium, with one sample displaying a value of ~+3500 ‰.

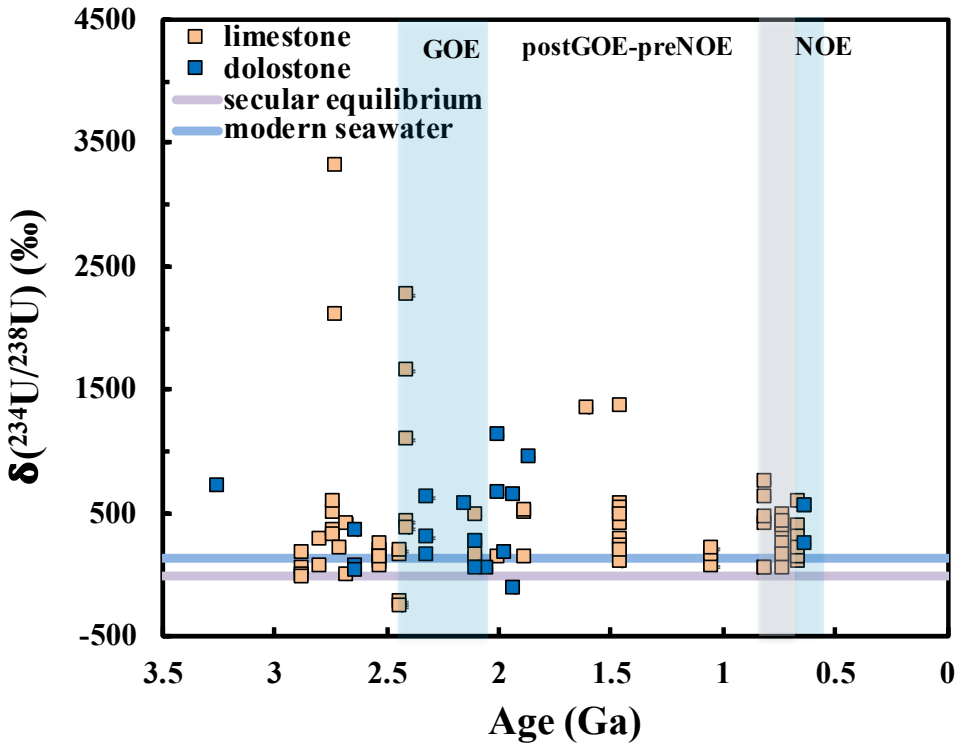

Figure 2.5 $\delta(^{234}U/^{238}U)$ in Precambrian carbonates. Symbol colors as in **Fig. 2.1**. The purple horizontal line shows the secular equilibrium value (0 ‰), and the blue line shows the modern seawater value of ~145‰ (*e.g.* (Ku et al., 1977; Chen et al., 1986; Andersen et al., 2010)). Many of the $\delta(^{234}U/^{238}U)$ values of the carbonates measured in this study are much larger than the seawater value, suggesting that these excesses cannot be simply explained by post-depositional alteration by seawater alone. They most likely reflect recoil of ^{234}U into the carbonate fraction from the detrital fraction (see **Fig. 2.7** and main text for details**)**.

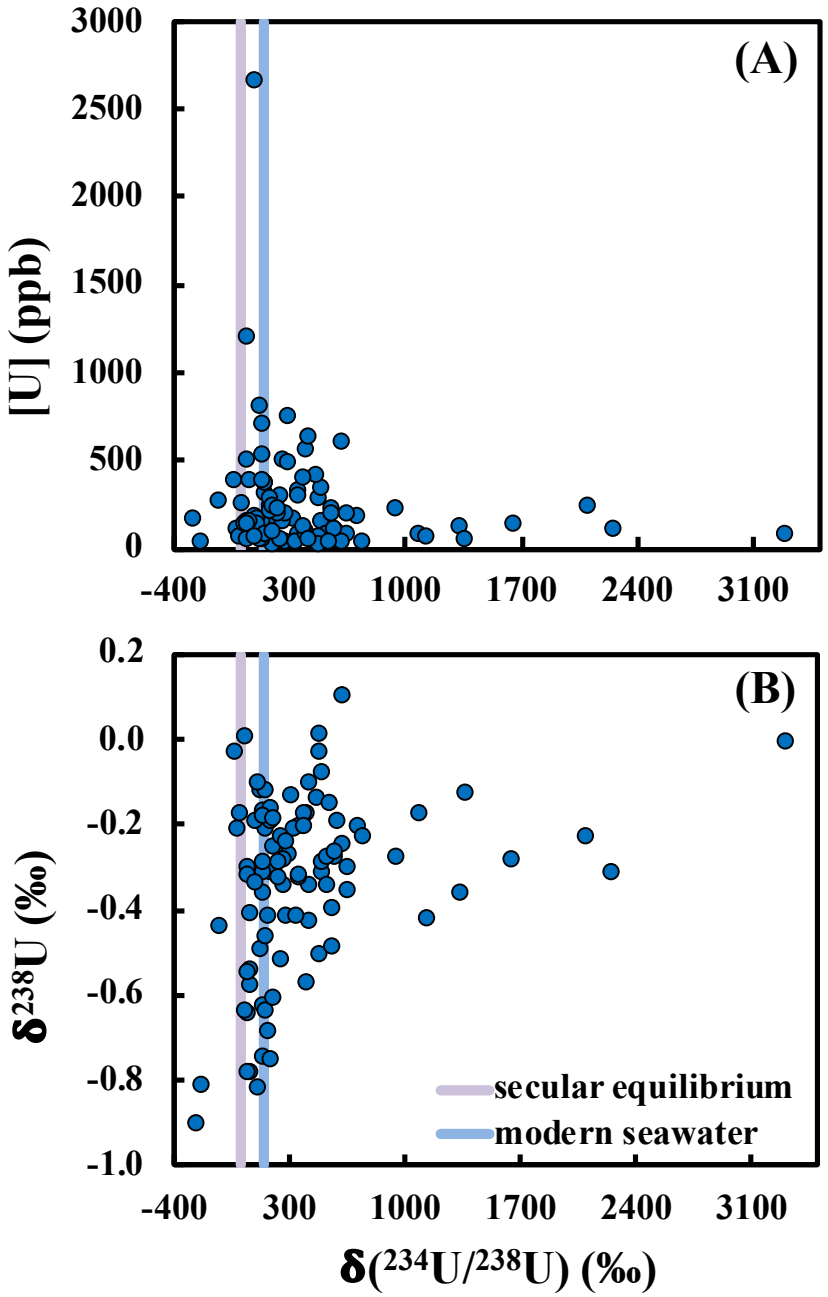

Figure 2.6 (A). [U] *vs*. δ(^{234}U/^{238}U) and (B) δ^{238}U *vs*. δ(^{234}U/^{238}U) in the Precambrian carbonates measured in this study. The lack of correlation between these data suggests that the factor responsible for the δ(^{234}U/^{238}U) excesses in the sample had no impact on their [U] and δ^{238}U values.

2.4 Discussion

2.4.1 Excess $\delta^{234}U$ in ancient carbonates

As ^{234}U is the decay product of ^{238}U, carbonates that behaved as a closed system for more than ~1.5 Myr (six times the half-life of ^{234}U, $t_{1/2} = 245{,}620$ yr; (Cheng et al., 2013)) should be characterized by $\delta(^{234}U/^{238}U)$ value of ~0 (*i.e.*, $^{234}U/^{238}U$ activity ratio of 1) corresponding to secular equilibrium. Deviation from secular equilibrium indicates that some sort of open-system behavior affected the carbonate fraction. In modern marine sediments, and in particular carbonates, deviation from secular equilibrium is the result of incorporation of seawater U, which, in the modern ocean, has a $\delta(^{234}U/^{238}U)$ value of ~+145 ‰ (*e.g.* (Ku et al., 1977; Chen et al., 1986; Andersen et al., 2010)). This process cannot explain the $\delta(^{234}U/^{238}U)$ values of the Precambrian carbonates in this study as they display ^{234}U enrichments that are much greater than the modern seawater value (**Fig. 2.5**). The $\delta(^{234}U/^{238}U)$ values of the Precambrian carbonates show no correlation with either [U] concentration or $\delta^{238}U$ (**Fig. 2.6**), suggesting that the factor causing excess in ^{234}U is unrelated to the processes that control their [U] and $\delta^{238}U$ values.

The excess in ^{234}U observed in old carbonates is most likely caused by alpha-recoil from the detrital fraction (with relatively high U concentration), whereby the daughter nuclides are implanted in the carbonate fraction (with low U concentration) in sedimentary rocks ((Henderson et al., 2001)). For old sedimentary rocks, the rate of gain of ^{234}U due to alpha-recoil will eventually equal the rate of decay of excess ^{234}U; the activity ratio at this equilibrium can be calculated as (modified from (Henderson et al., 1999) for porewater),

$$\left(\frac{^{234}U}{^{238}U}\right) = \frac{r^3-(r-\alpha)^3}{4r^3} \times \frac{U_{detritus} \times f_{detritus}}{U_{carbonate} \times f_{carbonate}} + 1\,, \qquad (2.3)$$

where r is the effective radius of detrital grains in the sediment, α is the alpha-recoil distance of ^{234}Th (initial decay product of ^{238}U that decays in 24.1 day into ^{234m}Pa and then ^{234}U, $\alpha \approx 0.1\ \mu m$, (DePaolo et al., 2003)) in silicates. The first term on the right side of the equation represents the volume fraction of daughter ^{234}U that will be expelled from the detrital grain into another grain (Bourdon et al., 2003). $U_{detritus}$ and $U_{carbonate}$ are the uranium concentrations in detrital and carbonate fractions, respectively; $f_{detritus}$ and $f_{carbonate}$ are the mass fractions of detritus and carbonate in the rock, respectively. The second term on the right side ($U \times f$) is the ratio of the U mass fractions in the detritus and carbonate. Larger excess of ^{234}U can be produced with finer detrital grain sizes (r), larger differences in U concentration ($\frac{U_{detritus}}{U_{carbonate}}$) and/or mass fractions ($\frac{f_{detritus}}{f_{carbonate}}$) between detritus and carbonates in the sediment. We plot the $\delta(^{234}U/^{238}U)$ values of our old carbonates as a function of ($\frac{U_{detritus} \times f_{detritus}}{U_{carbonate} \times f_{carbonate}}$) (**Fig. 2.7**) to check if the excess of $\delta(^{234}U/^{238}U)$ can be explained by the alpha-recoil effect (*i.e.*, a net transfer of ^{234}Th/^{234}U from detrital grains to carbonate in the rocks, (Henderson et al., 2001)). [U] in the continental crust (2.7 ppm; (Taylor and McLennan, 1985b)) is used to represent $U_{detritus}$ and the measured [U] of each Precambrian carbonate in this study is $U_{carbonate}$. The carbonate mass fraction, $f_{carbonate}$, is estimated from major element abundances using a scanning electron microscope (**Table 2.1**). As seen in **Fig. 2.7**, the $\delta(^{234}U/^{238}U)$ value of our Precambrian carbonates broadly correlates with the calculated index ($\frac{U_{detritus} \times f_{detritus}}{U_{carbonate} \times f_{carbonate}}$) of each sample, the predicted correlation being modulated by grain size. This observation strengthens our interpretation that excess ^{234}U observed in ancient carbonates most likely comes from alpha-recoil and implantation from the detrital fraction into the carbonate fraction of ^{234}Th (and its decay product ^{234}U). This also confirms that the leaching

protocol applied only releases U from the carbonate fraction and does not leach the detrital fraction in our rock samples, as any dissolution of the detritus would significantly decrease the $\delta(^{234}U/^{238}U)$ and bring the values closer to the secular equilibrium value of ~0 ‰.

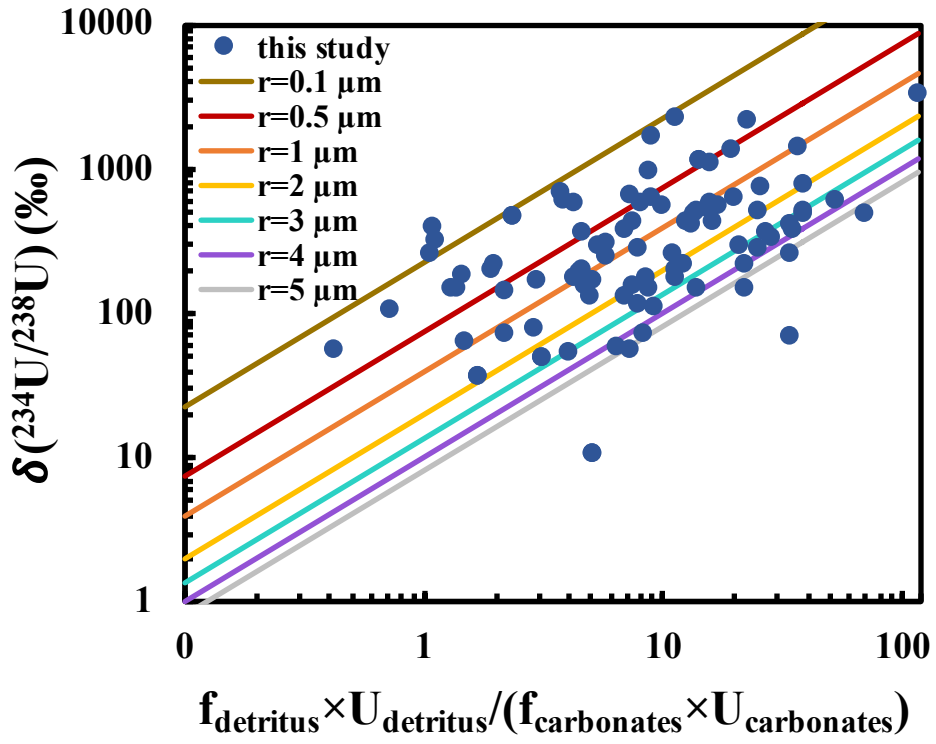

Figure 2.7 $\delta(^{234}U/^{238}U)$ value in the carbonates measured in this study as a function of the ratio of U mass fractions in detritus and carbonate. The different lines correspond to predicted excesses due to alpha-recoil for different effective detritus grain sizes (r) (see **Section 2.4.1** for details). The $\delta(^{234}U/^{238}U)$ value of our Precambrian carbonates show a broad correlation with the calculated index ($\frac{U_{detritus} \times f_{detritus}}{U_{carbonate} \times f_{carbonate}}$) of each sample, and the dispersion in the data can be explained by different detrital grain sizes, suggesting that the ^{234}U excesses observed in the carbonates were most likely caused by the alpha-recoil effect from the detrital fraction of the sediments.

2.4.2 U concentration and isotopic records through time

The basis for using the U isotopic composition of either shales or carbonates to reconstruct seawater paleoredox conditions is that, at steady-state, the overall isotopic composition of U sinks (anoxic and others) must be equal to that of the riverine input, which is similar to that of the continental crust (-0.29 ‰; (Stirling et al., 2007a; Tissot and Dauphas, 2015; Andersen et al., 2016)). At steady-state, the mass balance equation takes the form,

$$\delta U_{Input} = f \times \delta U_{anoxic} + (1 - f) \times \delta U_{non\text{-}anoxic}\ , \quad (2.4)$$

where δU_{Input} is the U isotopic composition of the sources of U to the oceans, typically taken to be the modern river value of -0.26 ‰, f is the fraction of U removed to anoxic sinks (a measure of the extent of oceanic anoxia), and $\delta^{238}U_{non\text{-}anoxic}$ is the U isotopic composition of all non-anoxic sinks generally assumed to be negligibly fractionated from seawater. To calculate f from either carbonate (taken as a proxy for seawater, *i.e.* $\delta^{238}U_{non\text{-}anoxic}$) or organic-rich shale ($\delta^{238}U_{anoxic}$) values, it is usually assumed that the U isotopic composition of the anoxic sink is systematically shifted relative to seawater (SW) by a constant offset of $\Delta_{SW}^{anoxic} \simeq +0.6$ ‰ (the exact magnitude depends on the efficiency of U transport into pore-water and deep-water renewal; (Andersen et al., 2014; Noordmann et al., 2015)),

$$f = \frac{\delta U_{River} - \delta U_{SW}}{\delta U_{anoxic} - \delta U_{SW}} = \frac{\delta U_{River} - \delta U_{Carbonate}}{\Delta_{SW}^{anoxic}} = \frac{\delta U_{River} - \delta U_{Shale} + \Delta_{SW}^{anoxic}}{\Delta_{SW}^{anoxic}}\ , \quad (2.5)$$

If the oceans were completely oxic and the anoxic sink was negligible, seawater would have the isotopic composition of the source (near-crustal), anoxic sediments would be shifted by ~+0.6 ‰ relative to the crust, and carbonates would have a near-crustal U isotopic composition. Conversely, if almost all U went into the anoxic sink, anoxic sediments would have the U isotopic composition of the source (near-crustal), and seawater and carbonates would be shifted by ~ -0.6

‰ relative to the crust. The current dataset of $\delta U_{Carbonate}$ values combined with previously published δU_{Shale} data allow us to evaluate one of the major tenets of the U isotope paleoredox proxy that the fractionation $\Delta_{SW}^{anoxic} \simeq +0.6$ ‰ documented in modern environments is applicable to the past.

In **Figs 2.1 and 2.8**, we compare the U concentrations and $\delta^{238}U$ values of carbonates, shales, and iron-rich rocks. The disappearance of detrital uraninite at the GOE and the drastic change in U concentration of carbonates at the NOE, and of shales during the GOE and NOE imply that the redox cycle of U must have been drastically different in the Archean and Proterozoic relative to the present one. The $\delta^{238}U$ values of carbonates and shales deposited before ~2.43 Ga are largely indistinguishable, both defining averages that correspond to the crustal value (**Fig. 2.8A**). After the GOE, the two records start diverging as many shales display elevated $\delta^{238}U$ values (Asael et al., 2013; Kendall et al., 2015; Yang et al., 2017; Mänd et al., 2020) relative to carbonates of similar age (this study; (Gilleaudeau et al., 2019); **Fig. 2.8A**). According to the isotope mass-balance outlined above and in previous publications (*e.g.*, (Montoya-Pino et al., 2010b)Brennecka et al. 2011; (Tissot and Dauphas, 2015; Lau et al., 2016, 2017; Andersen et al., 2017)), if a steady-state U seawater cycle existed and was dominated by anoxic settings in the Archean, one would expect Archean seawater and therefore carbonates to have a $\delta^{238}U$ value lower than the crust, possibly approaching -0.9 ‰. During the GOE and after the NOE, the $\delta^{238}U$ value of carbonates should have shifted towards the modern $\delta^{238}U$ value of -0.4 ‰ as the areal extent of anoxic settings shrank, and other sinks started to influence the mass-balance (**Fig. 2.8B**). Instead, we find that the U isotopic composition of carbonates did not change significantly through the Precambrian (**Figs. 2 and 2.8A**). Below, we explore two possible explanations as to why Archean and Proterozoic

carbonates have similar U isotopic composition as continental runoff and Archean shales. We first focus on the residence time of U in the Precambrian oceans and ocean mixing timescale and show that they could have been much closer than in the modern ocean. We then discuss non-uniformitarian U isotopic fractionation during deposition of Precambrian black shales that might be responsible for the lack of a clear offset between black shale and carbonate U isotope records.

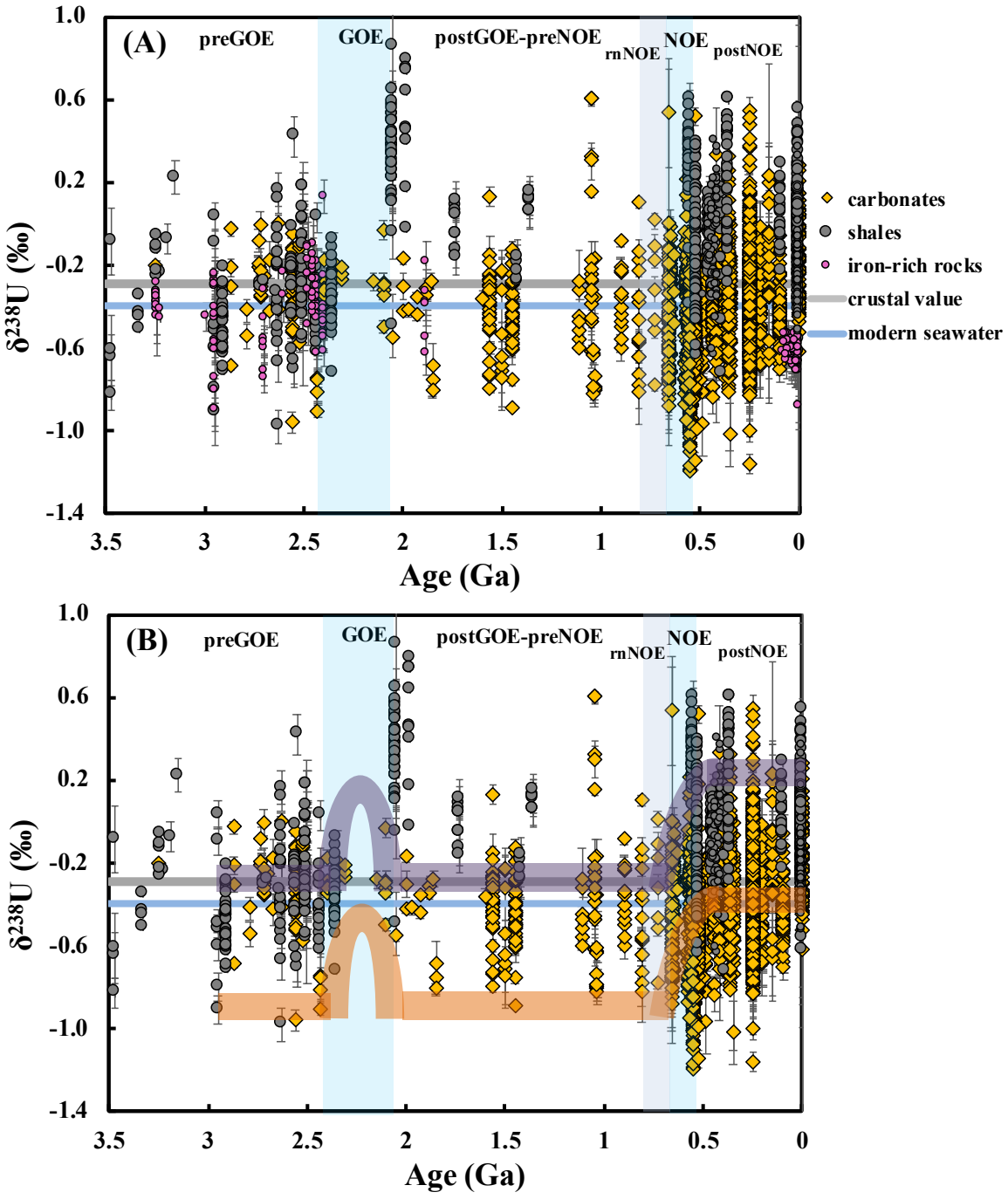

Figure 2.8 (A). $\delta^{238}U$ in carbonates, shales, and iron-rich sedimentary rocks through time. $\delta^{238}U$ in carbonates are from this study and the literature (as in **Figs. 2.1 and 2.2**). $\delta^{238}U$ values for shales and iron-rich sedimentary rocks are from the literature (see compilation in **Supplementary Table 1**). If no $\delta^{238}U_{auth}$ were reported, the data were all corrected for detrital contribution using the method described in (Asael et al., 2013). Samples with Al/U ratio larger than the detrital ratio were

Figure 2.8 *continued*
excluded from this figure. (B). The two broad bands illustrate the expected $\delta^{238}U$ trends in carbonates and shales under the assumption of constant offset between anoxic sinks and seawater (which is based on our current understanding of the modern seawater U cycle). The differences between the observed trends and the expected ones show that the assumption of a constant offset between anoxic sediments and seawater might not be valid for the Precambrian, and great care should be exercised when applying knowledge of the modern U isotopic cycle to periods in Earth's history when the extent of anoxia was much greater than at the present.

2.4.3 Residence time for U in Archean and Proterozoic oceans

In the modern oxic ocean, U is highly soluble as uranyl carbonate complexes (Langmuir, 1978; Dong and Brooks, 2006; Endrizzi and Rao, 2014; Maloubier et al., 2015). Its residence time of ~400 kyr (Ku et al., 1977; Chen et al., 1986; Dunk et al., 2002) greatly exceeds the mixing timescale of the oceans (~1 kyr, (Siberlin and Wunsch, 2011; Khatiwala et al., 2012)), meaning that the U content and isotopic composition of modern seawater is largely uniform and one can reliably assess the global mass-balance of U in the ocean among oxic, suboxic, carbonate, and anoxic sinks. In the Archean, seawater had much lower U concentration than in the modern ocean, and anoxic settings were much more extensive. It is thus likely that the residence time of U dissolved in seawater was much shorter. If the residence time of U was similar to the mixing timescale of the oceans, the U concentration and isotopic composition of the oceans would have been heterogeneous, which would have important consequences for interpretation of the U isotopic mass-balance of ancient carbonates and organic-rich shales.

To get a sense of how the U residence time could have been different in the past oceans compared to the modern value (τ~400 kyr), we have estimated the residence time of uranium for different extent of anoxia. The residence time is given by,

$$\tau = \frac{M_{sw}[U]_{sw,t}}{F_{in}}, \quad (2.6)$$

where, M_{sw} is the mass of the oceans, $[U]_{sw,t}$ is the seawater U concentration at time *t*, and F_{in} is the U input flux into the ocean. The mass of the oceans M_{sw} did not change much since the Archean (presumably within a factor of 2; (Pope et al., 2012; Korenaga et al., 2017)). The input flux and U inventory of seawater could have changed more dramatically, and we examine below how the residence time of U could have been affected. These changes are assessed by examining the composition of chemical sediments, which indirectly record the composition of seawater from which they derive.

We estimate $[U]_{sw,t}$ and F_{in} in Eq. 2.6 based on an oceanic mass-balance model modified from (Reinhard et al., 2013) and (Sheen et al., 2018). At steady-state, the flux of uranium into the ocean F_{in} (μg/yr) is equal to the flux out F_{out} (μg/yr) given by the U burial rate B_i (μg U cm^{-2} yr^{-1}) integrated over the seafloor surface area A_i (cm^2) covered by a particular sink *i*,

$$F_{in} = F_{out} = \sum_i F_i = \sum_i \int_0^{A_i} B_i \, dA \,, \quad (2.7)$$

Splitting the sinks into anoxic (*a*), and non-anoxic (*na*), Eq. 2.7 becomes,

$$F_{in} = \int_0^{A_{na}} B_{na} \, dA + \int_0^{A_a} B_a \, dA \,, \quad (2.8)$$

The U burial rates in the past ocean are related to the modern (m subscript) burial rates in each sink by a dimensionless scaling factor ε,

$$B_{na} = \varepsilon_{na} B_{na,m} \,, \quad (2.9)$$

$$B_a = \varepsilon_a B_{a,m} \,, \quad (2.10)$$

The U burial rates scale with U concentration in seawater at time t $[\mathrm{U}]_{sw,t}$ following a power relationship (Reinhard et al., 2013),

$$\varepsilon_{na} = k_{na}[\mathrm{U}]_{sw,t}{}^{\theta_{na}}, \quad (2.11)$$

$$\varepsilon_{a} = k_{a}[\mathrm{U}]_{sw,t}{}^{\theta_{a}}, \quad (2.12)$$

For the non-anoxic sink, we take k_{na} to be constant and we constrain it from the modern seawater U concentration $[U]_{sw,m}$ ($\varepsilon_{na,m} = 1$),

$$k_{na} = \frac{1}{[U]_{sw,m}{}^{\theta_{na}}}, \quad (2.13)$$

The modern burial rate for the non-anoxic sink is $B_{na,m} = F_{na,m}/A_{na,m}$, so that Eq. 2.9 becomes,

$$B_{na} = \left(\frac{[\mathrm{U}]_{sw,t}}{[\mathrm{U}]_{sw,m}}\right)^{\theta_{na}} \frac{F_{na,m}}{A_{na,m}}, \quad (2.14)$$

As discussed by (Reinhard et al., 2013) and (Sheen et al., 2018), one cannot assume that the anoxic sink scaling factor k_a remained constant as trace metal burial rate also depends on organic carbon burial rate (Algeo and Lyons, 2006). Modern anoxic burial rates are measured in shelf sediments, where organic burial rates are high due to high primary productivity. In the past, anoxia could have expanded into abyssal plains, which are characterized by lower carbon burial rates and presumably lower efficiency of redox metal removal (*e.g.,* U). In order to account for these two effects, we write k_a as a function of the organic carbon burial rate $B_{C_{org}}$ (mmol C cm^{-2} yr^{-1}),

$$k_a = \gamma B_{C_{org}}, \quad (2.15)$$

where γ is a parameter that did not change through time. The scaling factor relating anoxic U burial rate to seawater concentration therefore takes the following form (by combining Eqs. 2.12 and 2.15),

$$\varepsilon_{a} = \gamma B_{C_{org}}[U]_{sw,t}{}^{\theta_{a}}, \quad (2.16)$$

The anoxic burial rate in Eq. 2.10 is therefore,

$$B_a = \gamma B_{C_{org}} [U]_{sw,t}{}^{\theta_a} B_{a,m} \,, \tag{2.17}$$

Integrating the burial rates over the surface area of the sinks, we have from Eq. 2.8,

$$F_{in} = \left(\frac{[\mathrm{U}]_{sw,t}}{[\mathrm{U}]_{sw,m}}\right)^{\theta_{na}} \frac{A_{na}}{A_{na,m}} F_{na,m} + \int_0^{A_a} \gamma [U]_{sw,t}{}^{\theta_a} B_{C_{org}} B_{a,m} \, dA \,, \tag{2.18}$$

Assuming that the oceans were homogeneous and given that $[U]_{sw,m}{}^{\theta_{na}}$, γ, $B_{na,m}$ and $B_{a,m}$ are constant in our model, we can rewrite Eq. 2.18 as,

$$F_{in} = \left(\frac{[\mathrm{U}]_{sw,t}}{[\mathrm{U}]_{sw,m}}\right)^{\theta_{na}} \frac{A_{na}}{A_{na,m}} F_{na,m} + \gamma [U]_{sw,t}{}^{\theta_a} B_{a,m} \int_0^{A_a} B_{C_{org}} \, dA \,, \tag{2.19}$$

We now focus on the anoxic flux (second term on the right side of Eq. 2.19). The carbon burial rate per unit time per unit surface area depends on depth Z (m) following the equation ((Middelburg et al., 1997); we assume that this relationship did not change through time),

$$B_{C_{org}} = \alpha 10^{-\beta Z} \,, \tag{2.20}$$

with $\alpha = 0.63$, $\beta = 0.00062$. Following (Reinhard et al., 2013) and (Sheen et al., 2018), we posit that anoxia expands from the continental shelf to abyssal plains. This is obviously a simplification as in the modern oceans, non-anoxic and anoxic environments coexist laterally at the same bathymetry. With this caveat in mind, we introduce $\zeta(A)$, a function that gives the seawater depth ζ above which seafloor covers a surface area A. The modern function $\zeta_m(A)$ is fitted using a linear function to bathymetric data from the Global Topography V19.1 database ((Smith and Sandwell, 1997); **Fig. 2.9**),

$$\zeta_m(A) \simeq aA + b \,, \tag{2.21}$$

with $\zeta_m(A)$ in m and A in m^2, $a = 1.59 \times 10^{-15}$ and $b = 560$.

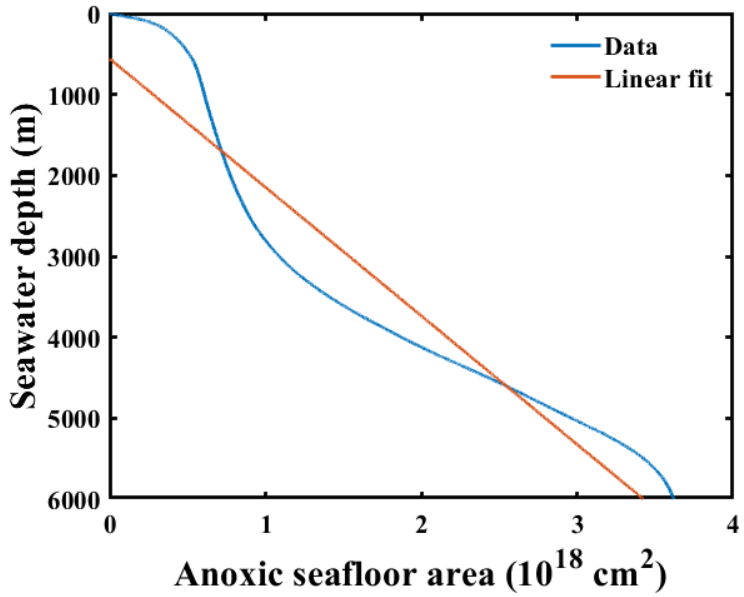

Figure 2.9 Seawater depth *vs*. seafloor area above that depth (ζ_m function in the main text). The blue curve is the modern Global Topography V19.1 database ((Smith and Sandwell, 1997)). The orange line is an approximate best fit line (Eq. 2.21).

Equation 2.19 therefore takes the form,

$$F_{in} = \left(\frac{[\mathrm{U}]_{sw,t}}{[\mathrm{U}]_{sw,m}}\right)^{\theta_{na}} \frac{A_{na}}{A_{na,m}} F_{na,m} + \gamma [U]_{sw,t}{}^{\theta_a} B_{a,m} \int_0^{A_a} \alpha 10^{-\beta \zeta_m(A)} dA \,, \tag{2.22}$$

To constrain γ, we apply the expression for the anoxic sink to the modern ocean,

$$F_{a,m} = \gamma [U]_{sw,m}{}^{\theta_a} B_{a,m} \int_0^{A_{a,m}} \alpha 10^{-\beta \zeta_m(A)} \, dA \,, \tag{2.23}$$

from which we can express γ as,

$$\gamma = \frac{F_{a,m}}{[U]_{sw,m}{}^{\theta_a} B_{a,m} \int_0^{A_{a,m}} \alpha 10^{-\beta \zeta_m(A)} dA} \,, \tag{2.24}$$

We thus have for F_{in} (by combining Eqs. 2.22 and 2.24),

$$F_{in} = \left(\frac{[\mathrm{U}]_{sw,t}}{[\mathrm{U}]_{sw,m}}\right)^{\theta_{na}} \frac{A_{na}}{A_{na,m}} F_{na,m} + \left(\frac{[\mathrm{U}]_{sw,t}}{[\mathrm{U}]_{sw,m}}\right)^{\theta_a} \frac{\int_0^{A_a} 10^{-\beta \zeta_m(A)} dA}{\int_0^{A_{a,m}} 10^{-\beta \zeta_m(A)} dA} F_{a,m} \,, \tag{2.25}$$

We are primarily interested in evaluating how the U residence time could have changed in the past. The residence time τ (kyr) depends on the U input and output fluxes (μg U/yr) and the U inventory of seawater as expressed in Eq. 2.6. Reinhard et al. (2013) showed that for Mo in modern anoxic basins, θ_a was apparently close to 0.25. In our calculation of residence time, we therefore explore θ_a values for U between 0.25 and 1.

Table 2.2 Parameters used in U residence time modelling

Parameter	**Value**	
Global seafloor area (cm^2)	3.62×10^{18}	
Mass of seawater (kg)	1.4×10^{21}	
Modern anoxic U burial rate (μg cm^{-2} yr^{-1}) [a]	0.251	
Sedimentation rates (m/Myr)	33[a,b], 5[c],100[c]	
Modern anoxic sink area fraction (%) [d]	0.11	
Modern U seawater concentration (ppb) [a]	3.3	
Modern U riverine input flux (μg/yr) [b]	1×10^{16}	
	>2.4 Ga	1.9-0.8 Ga
Average $[U]_{bs}$ (ppm) [a]	1.14	2.96
$[U]_{sw,t}$ (ppb) [e]	0.10	0.14
*$[U]_{carb}$ (ppb) [e]	40	90
$[Ca]_{carb}$ (wt%) [e]	29.18	31.07
$[Ca]_{sw,t}$ (ppm) [f]	954	654

[a] Partin et al. (2013a)
[b] Dunk et al. (2002)
[c] Einsele (1992)
[d] Sheen et al. (2018)
[e] This study
[f] Hardie (2003)
*We use here the 25th percentile $[U]_{carb}$ (ppb) of the measured values in the model calculation, which yields realistic $[U]_{sw}$ and U input flux while adopting the mean or median yields no satisfactory solution.

2.4.3.1 Approach 1. Constant U input flux after the GOE

(Reinhard et al., 2013) and (Sheen et al., 2018) applied their mass-balance model to the Proterozoic Eon to constrain the extent of oceanic anoxia based on the concentrations of authigenic

redox metals (Cr, Mo and Re) in shales. For that purpose, they assumed that once the GOE started, the riverine flux of redox-sensitive elements stayed the same and was equal to the modern value. The justification for this assumption is that after the GOE, the atmosphere became oxygenated and redox-sensitive minerals disappeared from detrital sediments, so if crustal weathering was the same as today, riverine delivery of redox-sensitive elements must have been similar to the present levels. As a first approach, we make the same assumption to calculate the residence time of U in the oceans after the GOE (as discussed below, we use other approaches before the GOE). If we keep the influx equal to the modern value $F_{in,m}$, we can use the relation in Eq. 2.25 and the inverse function $[\mathrm{U}]_{sw,t} = \phi^{-1}(F_{in,m})$ to calculate the residence time as a function of anoxia extent,

$$\tau = \frac{M_{sw}\phi^{-1}(F_{in,m})}{F_{in,m}}, \tag{2.26}$$

In **Fig. 2.10**, we plot τ as a function of A_a. The residence time of U in seawater decreases significantly if the anoxic seafloor area exceeds ~4% of the total seafloor. Knowing the influx, we can calculate seawater concentration using Eq. 2.25 (**Fig. 2.11**), as well as the U concentrations in carbonates and black shales (**Fig. 2.12**, the details of the calculations are provided in **Sections 2.4.3.2 and 2.4.3.3**). Some model parameters would yield black shale and carbonate U concentrations that are clearly inconsistent with the rock record, and we highlight with thick solid lines in **Fig. 2.10** the range of values of seafloor anoxia that yield realistic concentrations. As expected, the seawater U residence time decreases with a greater extent of anoxia and it could have reached ~18 kyr for θ_a = 0.75 and around $\geq$ 30 % anoxia. This value for the seawater U residence time is larger than the modern ocean mixing timescale of ~1 kyr but is much lower than the modern seawater U residence time of ~400 kyr.

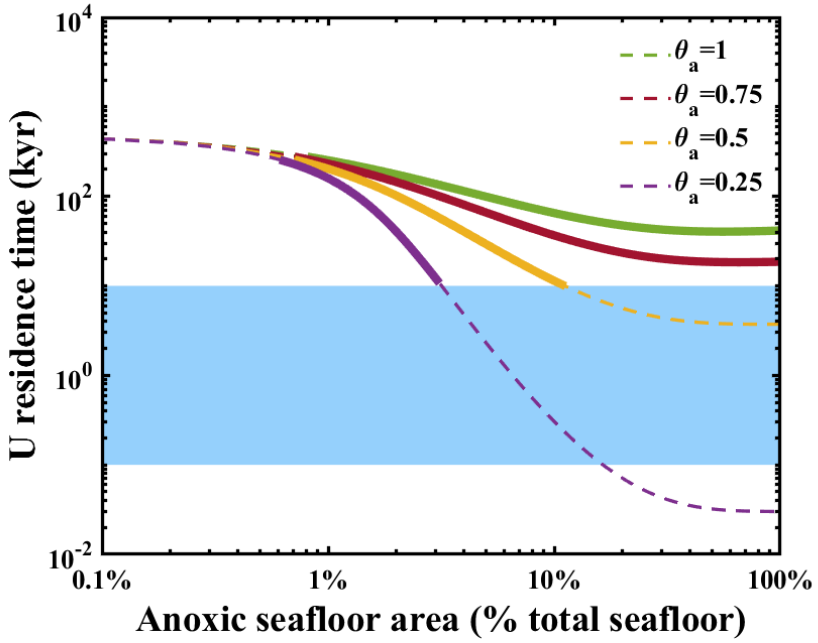

Figure 2.10 Modeled U residence time with increasing seafloor anoxia based on the assumption of constant modern-like U riverine flux after the GOE ((Reinhard et al., 2013) with different θ_a exponents. The blue box shows the probable ocean mixing timescale range in the Precambrian (0.1-10 kyr, see discussion in **Section 2.4.4**). The thick solid lines are those that yield realistic U concentrations in carbonates and shales (see **Fig. 2.12**).

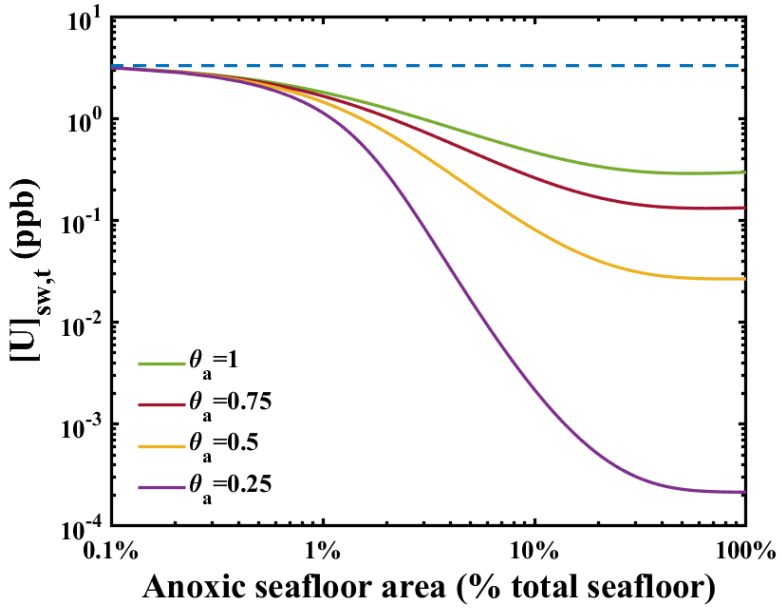

Figure 2.11 U concentration in seawater modeled in method 1 using Eq. 2.25. The blue dashed line is the modern seawater concentration.

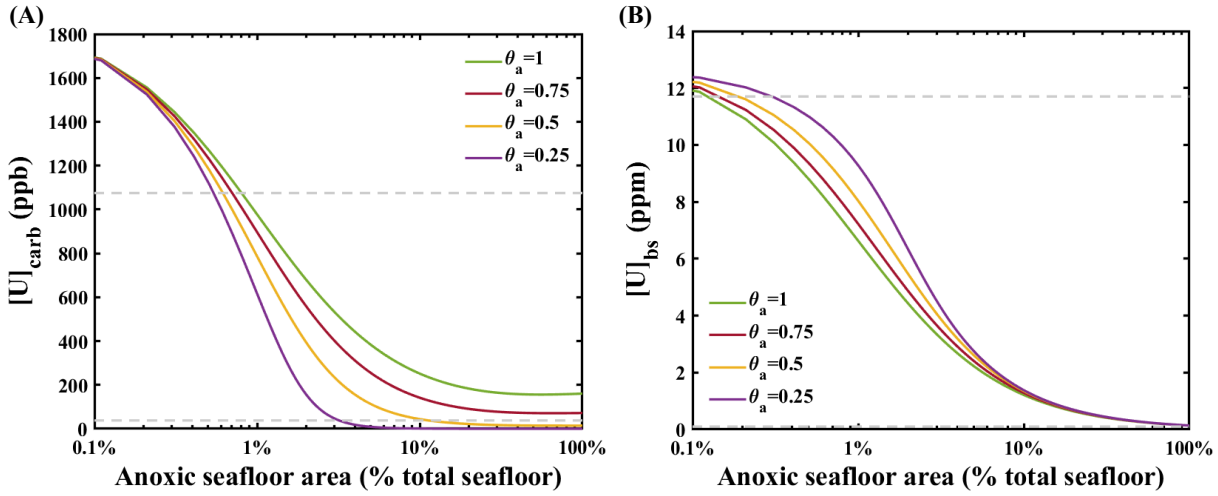

Figure 2.12 U concentrations predicted in carbonates (A) and black shales (B) using modeled $[U]_{sw,t}$ in method 1 and Eqs. 2.28, 2.32. The thick solid lines in **Fig. 2.10** are parameters that yield (*i*) 38 ppb ≤ $[U]_{carb}$ ≤ 1075 ppb for the postGOE-preNOE (see also **Fig. 2.1A**, note that the lower bound of 38 ppb are the 5th percentile $[U]_{carb}$ (ppb) of the measured values, while upper bound of 1075 ppb are the 95th percentile $[U]_{carb}$ (ppb) of the measured values), and (*ii*) yield

Figure 2.12 *continued*
0.1 ppm $\leq [U]_{bs} \leq$ 11.7 ppm for the postGOE-preNOE (see also **Fig. 2.1B**, note that the lower bound of 0.1 ppm are the 5th percentile $[U]_{bs}$ (ppm) of the measured values, while upper bound of 11.7 ppm are the 95th percentile $[U]_{bs}$ (ppm) of the measured values from Partin et al. 2013a).

2.4.3.2 Approach 2. Using authigenic U concentration in shale

The constant input flux assumption used in **Section 2.4.3.1** (this study; Sheen et al. 2018; Reinhard et al. 2013) may be reasonable after the GOE. However, it is invalid before the GOE as detrital uraninite was able to survive weathering under the anoxic atmosphere that prevailed during that time. Below, we explore two approaches that relax the assumption of a constant input flux and use instead sedimentary data to constrain the seawater U residence time, starting with the shale data.

In the framework of our model, we can relate the concentration of authigenic U in black shales $[U]_{bs}$ (ppm) to the concentration of U in seawater. Since shale samples are from continental margins, we integrate the anoxic burial rate B_a over the anoxic area A_a until it reaches the boundary of modern continental margins ($A_a \leq A_{CM} = 1.014 \times 10^{18}$ cm^2, 28% of global seafloor area, (Carleton, 2000)). The total amount of U deposited per unit time in anoxic sediments on the continental margin $F_{a,CM}$ is given by,

$$F_{a,CM} = \int_0^{min(A_a,A_{CM})} B_a \, dA = \left(\frac{[U]_{sw,t}}{[U]_{sw,m}}\right)^{\theta_a} \frac{\int_0^{min(A_a,A_{CM})} 10^{-\beta\zeta m(A)} dA}{\int_0^{A_{a,m}} 10^{-\beta\zeta m(A)} dA} F_{a,m} \,, \tag{2.27}$$

The black shale bulk mass accumulation rate R is calculated using the dry bulk density measured in Cariaco Basin (0.606 g/cm^3 of dry solid per volume of wet sediment; (Sheen et al., 2018), (Peterson et al., 2000)) multiplied by a sedimentation rate S of 5-100 m/Myr (Einsele, 1992). The average modern value is ~33 m/Myr (Partin et al., 2013a) and we explore the range 5-

100 m/Myr to illustrate the sensitivity of the calculation to this parameter. These three sedimentation rates result in bulk mass accumulation rate values of 0.3×10^{-3}, 2.0×10^{-3} and 6.1×10^{-3} g cm^{-2} yr^{-1}, respectively. The predicted authigenic U concentration in anoxic shales $[\mathrm{U}]_{bs}$ (ppm) is obtained by dividing Eq. 2.27 by the total sediment flux in shelf anoxic sediments $R \times min(A_a, A_{CM})$,

$$[\mathrm{U}]_{bs} = \frac{\int_0^{min(A_a,A_{CM})} B_a dA}{R \times min(A_a,A_{CM})} = \frac{1}{R \times min(A_a,A_{CM})} \left(\frac{[\mathrm{U}]_{sw,t}}{[\mathrm{U}]_{sw,m}}\right)^{\theta_a} \frac{\int_0^{min(A_a,A_{CM})} 10^{-\beta\zeta_{m(A)}} dA}{\int_0^{A_{a,m}} 10^{-\beta\zeta_{m(A)}} dA} F_{a,m} \quad (2.28)$$

For a given extent of anoxia A_a, this equation establishes a relationship between the authigenic U enrichment in black shale $[\mathrm{U}]_{bs}$ and the U concentration in seawater $[\mathrm{U}]_{sw,t}$. We take authigenic U concentrations in black shales from (Partin et al., 2013a) (**Table 2.2**) to solve Eq. 2.28 for the concentration of U in seawater as a function of the extent of anoxia,

$$[\mathrm{U}]_{sw,t} = [\mathrm{U}]_{sw,m} \left(\frac{[\mathrm{U}]_{bs} \times R \times min(A_a,A_{CM})}{F_{a,m}} \frac{\int_0^{A_{a,m}} 10^{-\beta\zeta_{m(A)}} dA}{\int_0^{min(A_a,A_{CM})} 10^{-\beta\zeta_{m(A)}} dA} \right)^{1/\theta_a}, \quad (2.29)$$

Injecting Eq. 2.29 to Eq. 2.25, we can calculate the U input flux at any geological time for a given extent of anoxia based on the available black shale record,

$$F_{in} = \left(\frac{[\mathrm{U}]_{bs} \times R \times min(A_a,A_{CM})}{F_{a,m}} \frac{\int_0^{A_{a,m}} 10^{-\beta\zeta_{m(A)}} dA}{\int_0^{min(A_a,A_{CM})} 10^{-\beta\zeta_{m(A)}} dA} \right)^{\theta_{na}/\theta_a} \frac{A_{na}}{A_{na,m}} F_{na,m} + [\mathrm{U}]_{bs} \times R \times$$

$$min(A_a, A_{CM}) \frac{\int_0^{A_{a,m}} 10^{-\beta\zeta_{m(A)}} dA}{\int_0^{min(A_a,A_{CM})} 10^{-\beta\zeta_{m(A)}} dA}, \quad (2.30)$$

The residence time is the inventory in seawater divided by the input flux (Eq. 2.6), which we can calculate by combining Eqs. 2.29 and 2.30,

$$\tau = \frac{M_{SW}[\mathrm{U}]_{sw,m}\left(\frac{[\mathrm{U}]_{bs}\times R\times min(A_a,A_{CM})}{F_{a,m}}\frac{\int_0^{A_{a,m}} 10^{-\beta\zeta m(A)}dA}{\int_0^{min(A_a,A_{CM})} 10^{-\beta\zeta m(A)}dA}\right)^{1/\theta_a}}{\left(\frac{[\mathrm{U}]_{bs}\times R\times min(A_a,A_{CM})}{F_{a,m}}\frac{\int_0^{A_{a,m}} 10^{-\beta\zeta m(A)}dA}{\int_0^{min(A_a,A_{CM})} 10^{-\beta\zeta m(A)}dA}\right)^{\theta_{na}/\theta_a}\frac{A_{na}}{A_{na,m}}F_{na,m}+[\mathrm{U}]_{bs}\times R\times min(A_a,A_{CM})\frac{\int_0^{A_{a,m}} 10^{-\beta\zeta m(A)}dA}{\int_0^{min(A_a,A_{CM})} 10^{-\beta\zeta m(A)}dA}},$$

(2.31)

Fig. 2.13 shows the U residence time calculated using black shale data as a function of the areal extent of anoxic sinks with different sedimentation rates in the Archean (left panel) and mid-Proterozoic (right panel). We also calculate and plot the predicted U concentration in carbonates using the approach described in **Section 2.4.3.3** (**Fig. 2.14**) and the seawater concentration calculated using black shale data and Eq. 2.29 (**Fig. 2.15**). Some model parameters yield U concentrations in carbonates that are clearly inconsistent with the rock record (**Fig. 2.1A**). We also calculate and plot the predicted U input flux using Eq. 2.30 (**Fig. 2.16**), which adds another constraint to the possible residence time, as we can conservatively assume that the flux of dissolved U to the oceans was smaller in the Archean than what it is at present. We highlight with thick solid lines in **Fig. 2.13** the range of values that yield realistic carbonate concentrations and input U flux. In the Archean and mid-Proterozoic, the residence time decreases with a greater extent of anoxia, and it could have reached ~18 kyr for $\theta_a = 0.75$, S = 100 m/Myr and around $\geq$ 20 % anoxia in the Archean, and could have reached ~18 kyr for $\theta_a = 0.75$, S = 33 m/Myr and around $\geq$ 25 % anoxia in the mid-Proterozoic, respectively. These modeled Precambrian seawater U residence times are much shorter than that of the modern ocean.

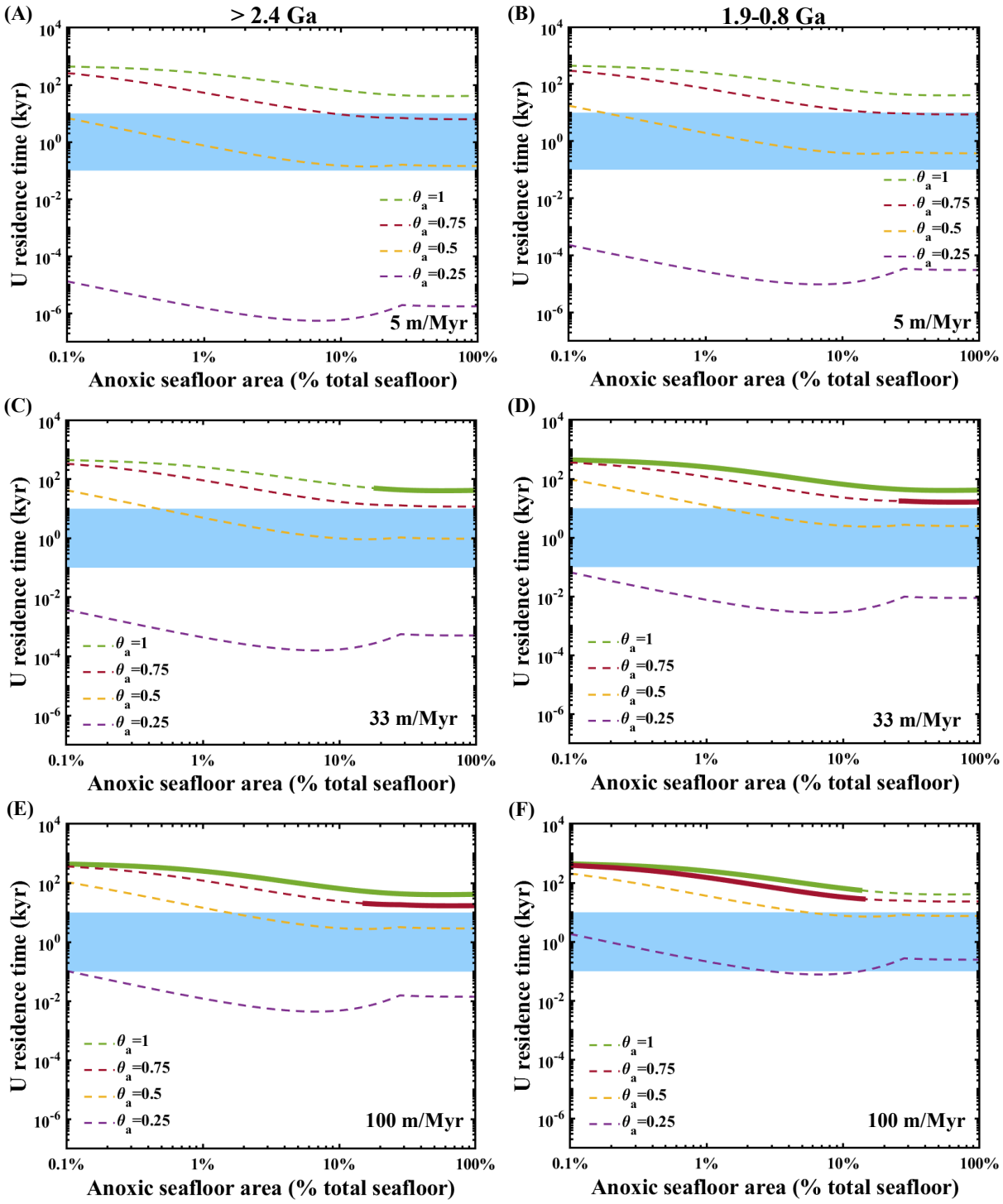

Figure 2.13 Modeled U residence time with increasing seafloor anoxia using authigenic U enrichment in shales with different assumptions for the sedimentation rates (top panels S=5, middle panels S=33, and bottom panels S=100 m/Myr) in the Archean (left) and mid-Proterozoic

Figure 2.13 *continued*
(right) (see text for details). The residence times calculated here relax the assumption of a constant influx of U to the oceans made in plotting **Fig. 2.10**. Different lines correspond to different exponents for the scaling of U burial rates with seawater concentration (Eqs. 2.12, 2.17). The blue box shows the probable ocean mixing timescale range in the Precambrian (0.1-10 kyr, see discussion in **Section 2.4.4**). The thick solid lines are those that yield realistic U concentrations in carbonates (**Fig. 2.14**) and U input flux (**Fig. 2.16**). We can conservatively say that the residence time decreases with a greater extent of anoxia, and in the Archean it could have reached ~18 kyr for $\theta_a = 0.75$, S = 100 m/Myr and around ≥ 20 % anoxia, and in the mid-Proterozoic it could have reached ~18 kyr for $\theta_a = 0.75$, S = 33 m/Myr and around ≥ 25 % anoxia.

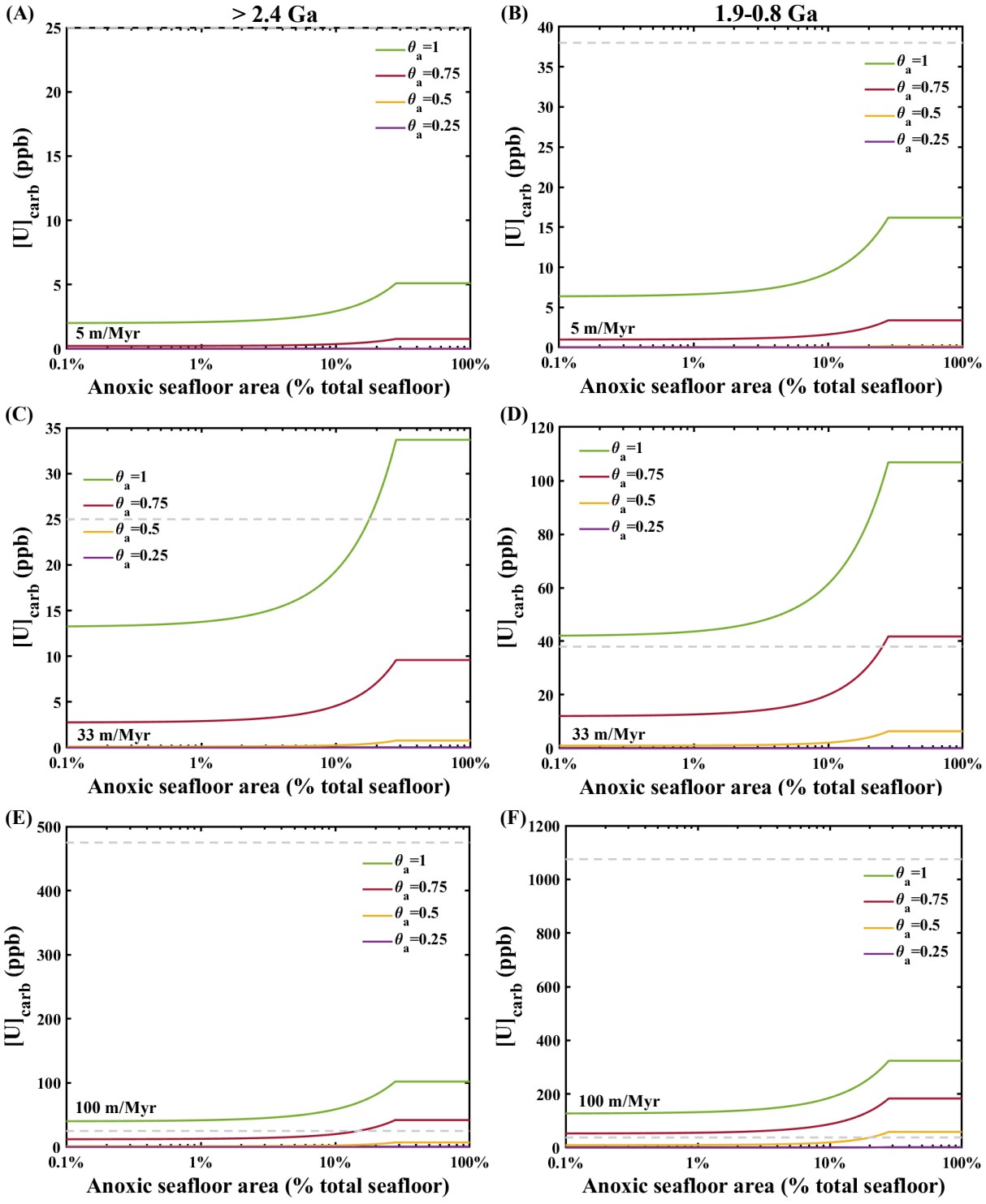

Figure 2.14 U concentrations predicted in carbonates using modeled $[U]_{sw,t}$ in method 2 and Eq. 2.32. Each panel corresponds to the panel in **Fig. 2.13**. The thick solid lines in **Fig. 2.13** correspond to parameters that yield 25 ppb $\leq [U]_{carb} \leq$ 475 ppb in the Archean and 38 ppb $\leq [U]_{carb} \leq$

Figure 2.14 *continued*
1075 ppb in the mid-Proterozoic (see also **Fig. 2.1A**, note that the lower bound of 25, 38 ppb are the 5th percentile $[U]_{carb}$ (ppb) of the measured values, while upper bound of 475, 1075 ppb are the 95th percentile $[U]_{carb}$ (ppb) of the measured values).

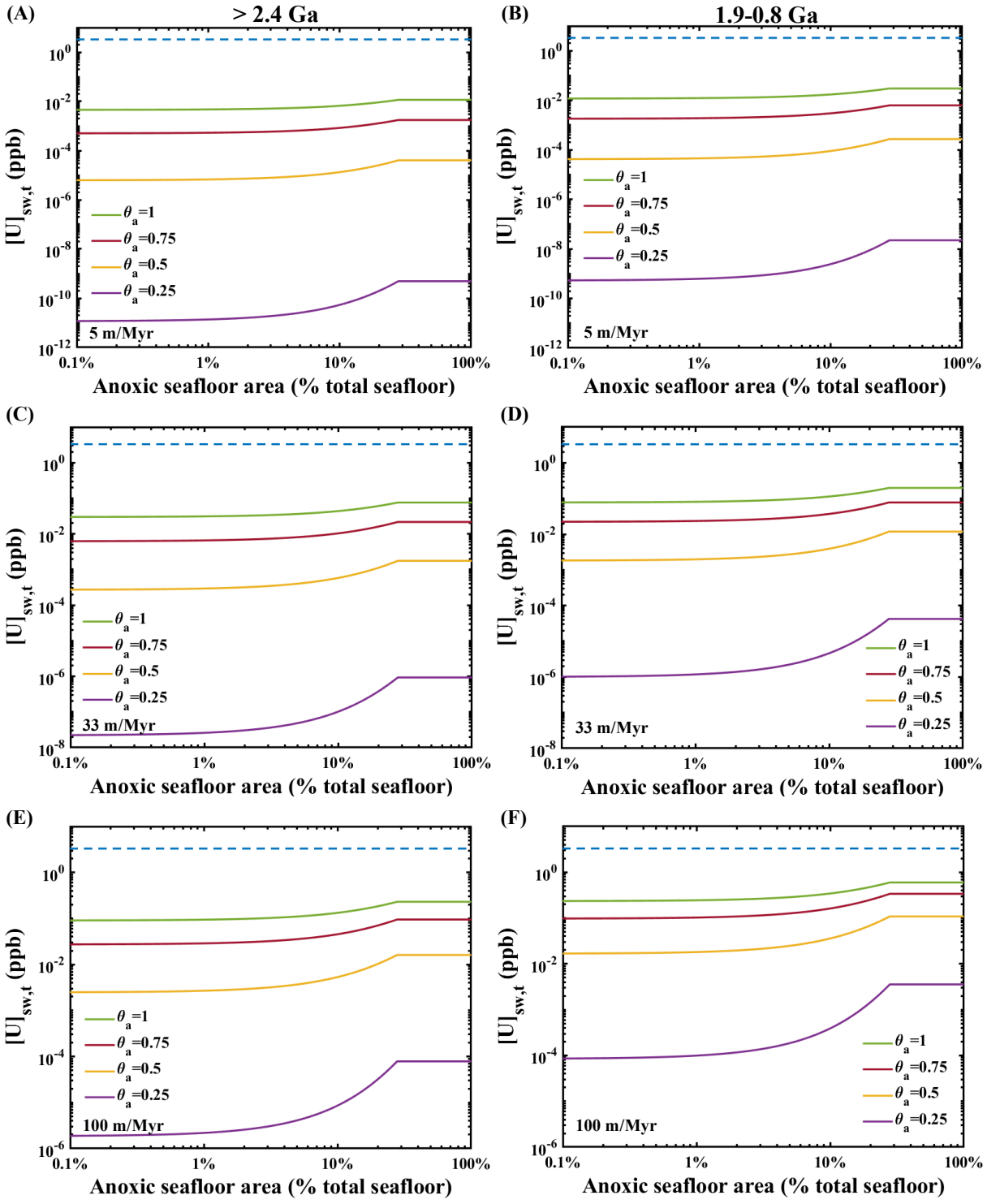

Figure 2.15 U concentration in seawater calculated using black shale data and Eq. 2.29. Each panel corresponds to the panels in **Fig. 2.13**. The blue dashed line is the modern seawater concentration.

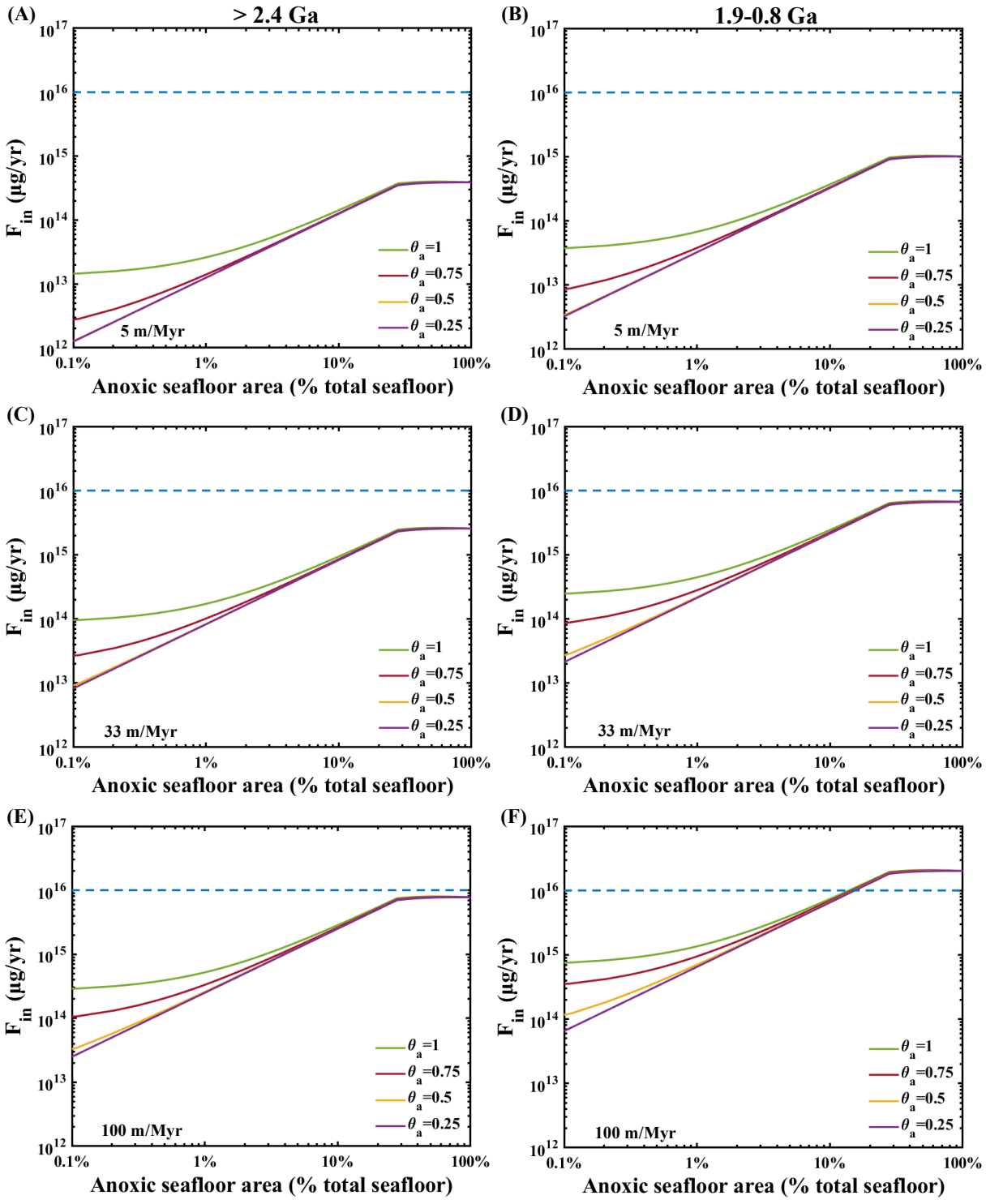

Figure 2.16 U input flux calculated using black shale data and Eq. 2.30. Each panel corresponds to the panel in **Fig. 2.13**. The blue dashed line is the U modern input flux. The thick solid lines in

Figure 2.16 *continued*
Fig. 2.13 correspond to parameters that yield U input flux in the Archean and mid-Proterozoic less than the modern value.

2.4.3.3 Approach 3. Using carbonate U concentration

A third approach for estimating the residence time of U in seawater when holding *flux in* constant is unjustified, is to use carbonates to infer seawater U concentration by using the U/Ca ratio,

$$[U]_{sw,t} = [Ca]_{sw,t} \times \frac{(U/Ca)_{carb,t}}{D_U}, \quad (2.32)$$

where D_U is the U/Ca distribution coefficient between carbonate and seawater, and $[Ca]_{sw,t}$ is the Ca concentration in seawater at time t (11 mmol/kg in modern seawater). For $(U/Ca)_{carb,t}$ (mass ratio), we use our carbonate measurements as well as the data compiled from the literature listed above (see **Supplementary Table 1**). The values of $[Ca]_{sw,t}$ and D_U relevant to the Precambrian are discussed below.

Based on analyses of primary fluid inclusions from marine halite, (Brennan et al., 2004) estimated that $[Ca]_{sw}$ increased from 9.5-18.5 to 33.5-40 mmol/kg at the Neoproterozoic-Cambrian boundary between ~544 Ma and 515 Ma. (Spear et al., 2014) also used the composition of primary fluid inclusions in marine halite to constrain the Ca concentration of ~830 Ma seawater to be between 9 and 12 mmol/kg. (Blättler et al., 2018) provided a range of ~2.5-40 mmol/kg for $[Ca]_{sw}$ at ~2.1 Ga based on the study of a 2.1-billion-year-old marine evaporite succession from the Onega Parametric Hole (OPH), Karelia, Russia. These estimates are also consistent with the modeled secular variations in Precambrian seawater chemistry of (Hardie, 2003). (Hardie, 1996)

modeled the secular $[Ca]_{sw}$ evolution during the Phanerozoic. We use the $[Ca]_{sw}$ value for each time interval from (Hardie, 1996, 2003) for calculation of $[U]_{sw,t}$.

The U/Ca distribution coefficient D_U is highly variable and has been estimated based on culture experiments (*e.g.*, (Russell et al., 1994)), co-precipitation experiments of inorganic aragonite and calcite (*e.g.*, (Meece and Benninger, 1993; DeCarlo et al., 2015)), studies of natural corals (*e.g.*, (Swart and Hubbard, 1982; Gothmann et al., 2019)), measurements of other biogenic carbonates (*e.g.*, (Russell et al., 1994; Keul et al., 2013)) and studies of coexisting porewater and carbonate in drill cores (Teichert et al., 2003; Maher et al., 2006). Although the average distribution coefficient through Earth's history might be expected to vary depending on proportion of aragonite precipitating from seawater, we find no clear correlation between the U concentration of carbonates and the inferred Mg/Ca ratio of coeval seawater (Halevy and Bachan 2017; Hardie 1996, 2003), suggesting minimal influence of primary carbonate mineralogy on U enrichment in the sedimentary carbonate record (see **Fig. 2.17**). We therefore assume a single value of 1.4 as calculated from measurements of uranium concentrations in calcite and pore water from the Ocean Drilling Program site 984 (Maher et al., 2006; Lau et al., 2016). This distribution coefficient might indeed be suitable for modeling U incorporation in Precambrian carbonates before the rise of calcifying organisms.

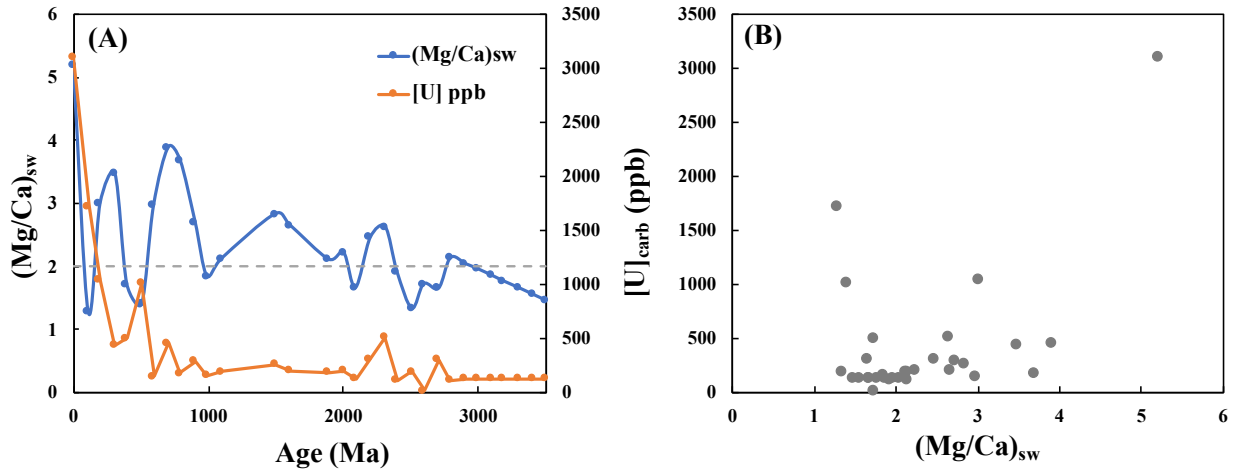

Figure 2.17 (A) Secular evolution of Mg/Ca in seawater (Halevy and Bachan 2017; Hardie 1996, 2003) and U concentrations in carbonates (average values binned in ~100 Ma), the grey dashed line at $(Mg/Ca)_{sw} = 2$, is the divide between aragonite and calcite seas. (B) [U] in carbonates *vs*. Mg/Ca in seawater. Uranium concentration is generally low in Precambrian carbonates and there is no clear correlation between $[U]_{carb}$ and $(Mg/Ca)_{sw}$, suggesting that the influence of primary carbonate mineralogy on U enrichment in old samples is small.

Equation 2.32 allows us to calculate the concentration of U in seawater from carbonate data, which we can then inject in Eq. 2.25 and Eq. 2.6 to calculate the U input flux and residence time,

$$F_{in} = \left(\frac{[Ca]_{sw,t} \times \frac{(U/Ca)_{carb,t}}{D_U}}{[U]_{sw,m}}\right)^{\theta_{na}} \frac{A_{na}}{A_{na,m}} F_{na,m} + \left(\frac{[Ca]_{sw,t} \times \frac{(U/Ca)_{carb,t}}{D_U}}{[U]_{sw,m}}\right)^{\theta_a} \frac{\int_0^{A_a} 10^{-\beta\zeta_{m(A)}} dA}{\int_0^{A_{a,m}} 10^{-\beta\zeta_{m(A)}} dA} F_{a,m}, \quad (2.33)$$

$$\tau = \frac{M_{sw}[Ca]_{sw,t} \times \frac{(U/Ca)_{carb,t}}{D_U}}{F_{in} = \left(\frac{[Ca]_{sw,t} \times \frac{(U/Ca)_{carb,t}}{D_U}}{[U]_{sw,m}}\right)^{\theta_{na}} \frac{A_{na}}{A_{na,m}} F_{na,m} + \left(\frac{[Ca]_{sw,t} \times \frac{(U/Ca)_{carb,t}}{D_U}}{[U]_{sw,m}}\right)^{\theta_a} \frac{\int_0^{A_a} 10^{-\beta\zeta_{m(A)}} dA}{\int_0^{A_{a,m}} 10^{-\beta\zeta_{m(A)}} dA} F_{a,m}}, \quad (2.34)$$

In **Fig. 2.18**, we plot the U residence time as a function of the areal extent of anoxia in the Archean (left) and mid-Proterozoic (right) using estimated U concentrations in seawater (**Table 2.2**) calculated from the measured U concentration in carbonates. We also calculated the predicted

black shale concentration in **Fig. 2.19** using Eq. 2.28. Some model parameters yield U concentrations in black shales that are clearly inconsistent with the rock record (see **Fig. 2.1B**). Some parameters also yield input dissolve U fluxes into the oceans that exceed the modern value, which is unrealistic (**Fig. 2.20**). We highlight with thick solid lines in **Fig. 2.18** the range of values that yield realistic shale U concentrations and U input flux. The residence time decreases with a greater extent of anoxia and it could have reached ~18 kyr for $\theta_a = 0.75$ and around ≥ 30 % anoxia in the Archean and mid-Proterozoic. Again, these modeled Precambrian seawater U residence times are much shorter than that of the modern ocean and are consistent with the modeled results in approach 1 and 2.

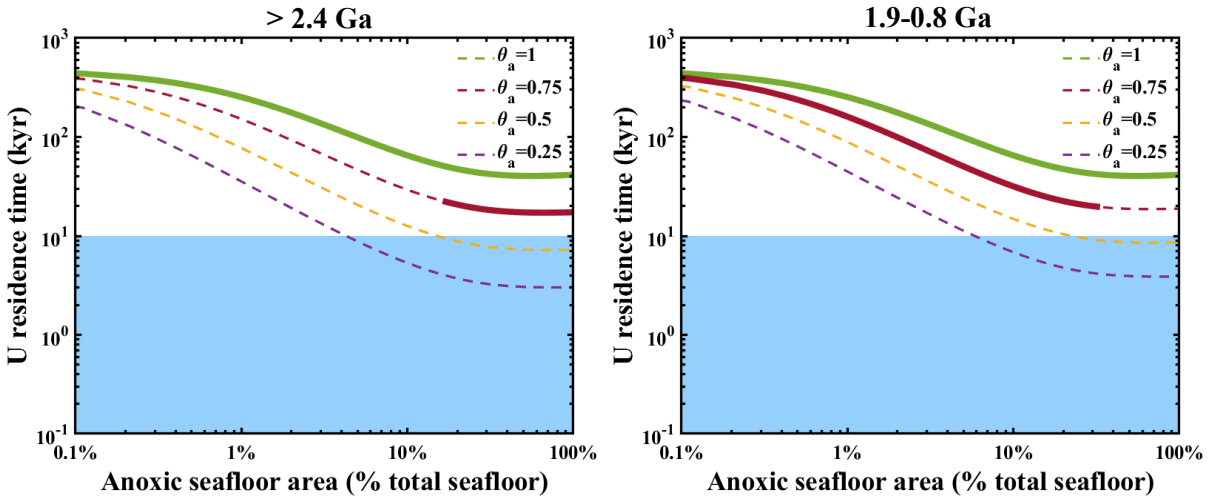

Figure 2.18 Modeled U residence time with increasing seafloor anoxia using U in carbonates in the Archean (left) and mid-Proterozoic (right) (see text for details). Different lines correspond to different θ_a exponents. The residence times calculated here relax the assumption of a constant influx of U to the oceans made in plotting **Fig. 2.10**. The blue box shows the probable ocean mixing timescale range in the Precambrian (0.1-10 kyr, see discussion in **Section 2.4.4**). The thick solid lines correspond to parameters that yield realistic U concentrations in black shales (**Fig. 2.19**) and U input flux (**Fig. 2.20**). As shown, the residence time decreases with a greater extent of anoxia

Figure 2.18 *continued*

and it could have reached ~18 kyr for $\theta_a = 0.75$ and around ≥ 30 % anoxia in the Archean and mid-Proterozoic.

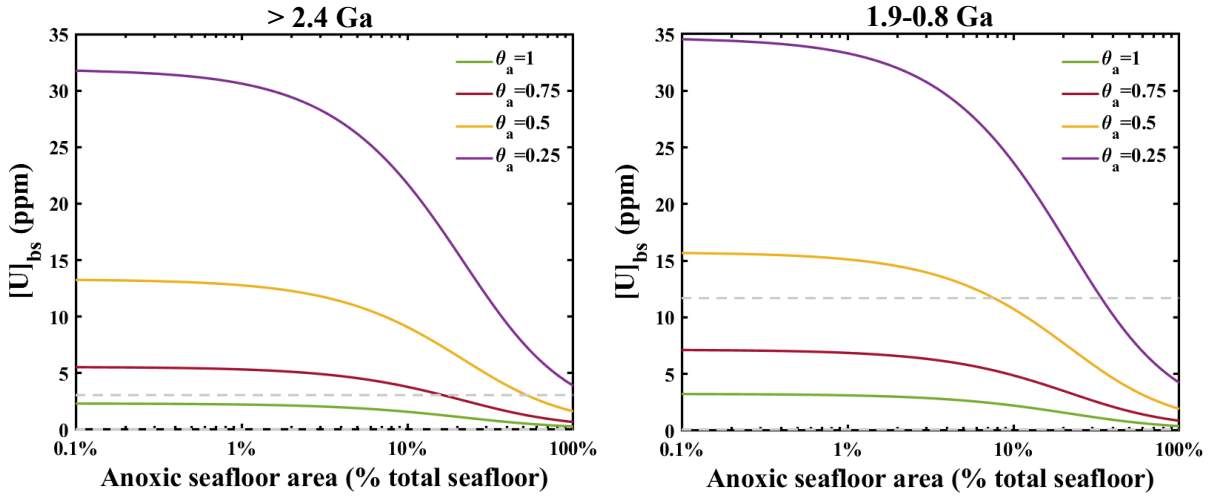

Figure 2.19 U concentrations predicted in shales using modeled $[U]_{sw,t}$ in method 3 and Eq. 2.28. Each panel corresponds to the panels in **Fig. 2.18**. The thick solid lines in **Fig. 2.18** correspond to parameters that yield $0.04\ \text{ppm} \leq [U]_{bs} \leq 3.06\ \text{ppm}$ for Archean, and $0.1\ \text{ppm} \leq [U]_{bs} \leq 11.7\ \text{ppm}$ for mid-Proterozoic (see also **Fig. 2.1B**, note that the lower bound of 0.04, 0.1 ppm are the 5th percentile $[U]_{bs}$ (ppm) of the measured values, while upper bound of 3.06, 11.7 ppm are the 95th percentile $[U]_{bs}$ (ppm) of the measured values from Partin et al. 2013a).

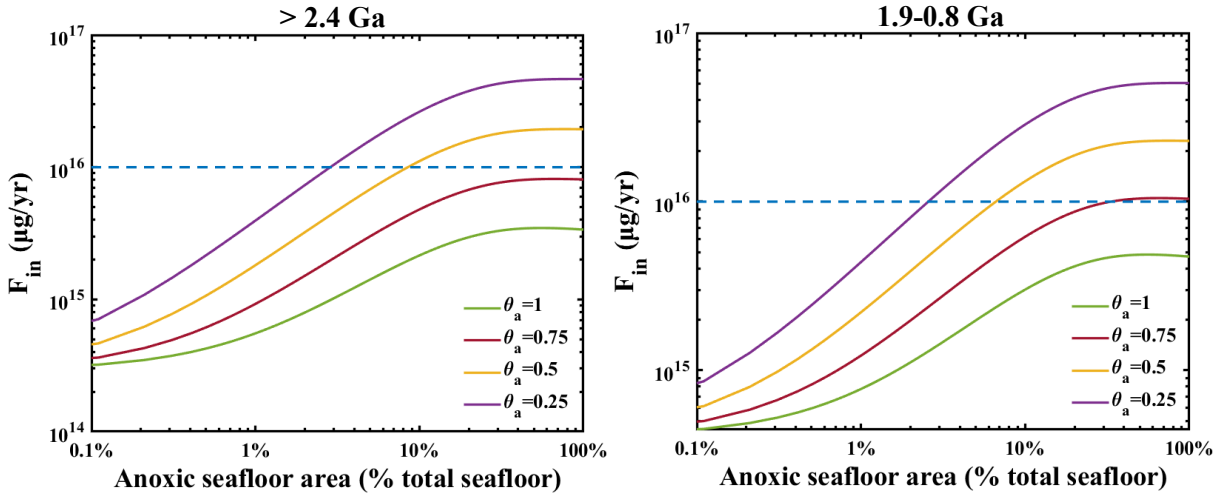

Figure 2.20 U input flux calculated using carbonate data and Eq. 2.33. Each panel corresponds to the panels in **Fig. 2.18**. The blue dashed line is the U modern input flux. The thick solid lines in

Figure 2.20 *continued*
Fig. 2.18 correspond to parameters that yield U input flux in the Archean and mid-Proterozoic less than the modern value.

2.4.4 Mixing time in Archean and Proterozoic oceans

The above estimates indicate that the residence time of U may have been short, and in some cases approached the present-day seawater mixing timescale. However, the ancient ocean mixing timescale could have also differed significantly from that of today, as the oceans were likely characterized by different bathymetry, atmospheric forcing and tides. Highlighting the role of sea ice in Antarctic bottom-water formation, (Lowe, 1994) speculated that deep-ocean mixing timescale during the Archean may have been hundreds of thousands, or even millions of years, if the climate was warm enough for the Earth to be ice free. However, our current understanding of the deep-ocean circulation suggests that, while the location of bottom-water formation may change, the deep-ocean overturning circulation could remain active even with ice-free climates (*e.g.*, (Enderton and Marshall, 2009; Jansen, 2017)). Moreover, turbulent mixing processes ventilate the abyssal ocean even in the absence of a large-scale overturning circulation (*e.g.*, (Burke et al., 2015)).

To estimate whether the ocean mixing timescale would have differed substantially from the modern value during the Late Archean and Early Proterozoic, it is useful to consider the energy sources for ocean dynamics. The deep-ocean circulation and mixing processes derive their energy primarily from winds and tides (*e.g.*, (Wunsch and Ferrari, 2004)). Winds affect the circulation both directly by driving divergent currents that pull waters from the deep ocean to the surface (*e.g.*, (Nikurashin and Vallis, 2012)) and indirectly via the generation of ocean turbulence. Tides also lead to the generation of small-scale turbulence in the ocean's interior and are likely to be the

dominant source of energy for diapycnal mixing (*i.e.*, mixing across density surfaces), which in turn is fundamental to the maintenance of the deep-ocean overturning circulation and stratification (Wunsch and Ferrari, 2004).

Winds in the Archean may have differed from those today due to possible differences in the global mean temperature, Earth's rotation rate, continental area and configuration and/or atmospheric pressure. The climate of the Archean is poorly constrained, such that a wide range of global mean temperatures is possible based on empirical constraints (*e.g.*, (Feulner, 2012)). Modeling by (O'Gorman and Schneider, 2008) suggests that atmospheric eddy kinetic energy varies non-monotonically by about a factor of two across a wide range of climate states with global mean temperatures between -10 and +45 °C, with the highest energy obtained at a temperature similar to that of the present day. The planetary rotation rate in the Archean was likely faster, perhaps by about a factor of two (*e.g.* (Webb, 1982)). While (Jenkins et al., 1993) found that this could have led to a significant reduction in mean tropospheric winds, (Olson et al., 2020) showed that the surface wind stress, which governs the energy input into the oceans, was not very sensitive to rotation rate, with a halving of the day length leading to about a 15% decrease in the surface wind stress over the ocean. Surface pressure during the Archean remains uncertain, but most data point towards a lower surface pressure, perhaps around half of the present-day value (Catling and Zahnle, 2020). Olson et al. (2020) find that a halving of surface pressure leads to a reduction in surface wind stress of about 25%. Assuming that ocean surface currents are themselves proportional to the wind stress magnitude (as expected for the major ocean gyres - *e.g.,* (Vallis, 2006) the energy input is proportional to the square of the wind stress, such that a 25% reduction in wind stress would amount to about a 45% decrease in wind-driven energy input. We conclude

that the wind energy input to the Archean and Early Proterozoic oceans was probably somewhat lower than today, but within the same order of magnitude.

Tides during the Archean were affected by two compensating effects: the closer proximity of the moon would result in stronger tides, but the shorter day-length would lead to reduced tidal dissipation as oceanic normal modes become less efficiently excited by the tidal forcing (Webb, 1982; Bills and Ray, 1999). Modeling by (Webb, 1982) suggests that the average tidal energy dissipation in the ocean ~2 Ga was roughly similar to that today, while it may have been about twice as large at ~3 Ga. However, estimates of Archean tides remain highly uncertain, and the models at best provide only a rough estimate of the *average* tidal dissipation rates. Tidal resonances, which modulate energy dissipation, are affected by ocean basin geometry, adding further uncertainty to tidal dissipation in the Archean (*e.g.*, (Bills and Ray, 1999)).

A number of additional factors that are difficult to constrain can affect how efficiently the energy input of winds and tides is converted into motion that contributes to deep-ocean mixing. These factors include the continental configuration, which shapes deep-ocean overturning circulation (*e.g.*, (Enderton and Marshall, 2009)), as well as various parameters that influence the relationship between tidal energy dissipation and diapycnal mixing rates (such as sea-floor topography and ocean stratification; *e.g.* (Garrett and Kunze, 2007; Mashayek et al., 2017)). Substantial uncertainties therefore remain with regards to the ocean mixing timescale during the Late Archean and Early Proterozoic, but we do not expect a systematic difference beyond an order-of-magnitude from the present ocean mixing timescale, so a range of 0.1-10 kyr appears reasonable for much of Earth's history.

When Earth was dominated by anoxic bottom water, our calculations (**Figs. 2.13 and 2.18**) show that the residence time of U would have been much lower than present, possibly reaching ~18 kyr. It is thus conceivable that the deep-ocean mixing timescale and residence time of U in the Archean oceans may have been of similar order. Consequently, the isotopic composition of U in carbonates and shales may not necessarily reflect the global redox state of the oceans, but instead may only provide information about the regional redox conditions under which the carbonates and shales were deposited. In particular, we cannot exclude a substantial gradient in U concentration and isotopic composition between the upper layer of the oceans (where carbonates are deposited) and the deep-waters overlying anoxic sediments. It is even possible that ocean mixing itself governed the residence time of U in the oceans by limiting its supply to the sediments. This scenario offers a possible explanation for the observed similarity in $\delta^{238}U$ values of Archean carbonates and shales. Carbonates would have precipitated from surface waters whose U isotopic composition resembled the riverine source, while shales would have formed in deep waters where quantitative U removal under anoxic conditions would again record the U isotopic composition of the input flux, while leaving abyssal seawater depleted in ^{238}U (**Fig. 2.21**).

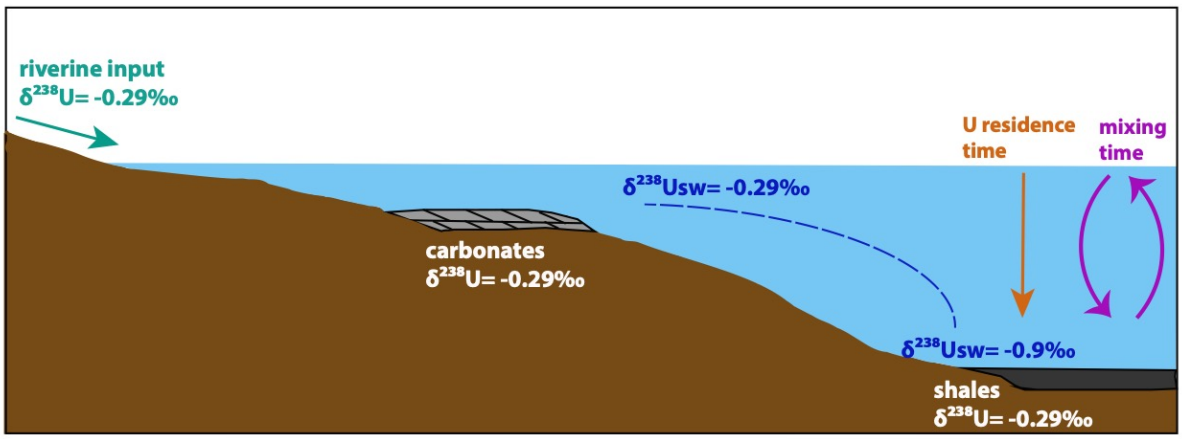

Figure 2.21 Cartoon showing the possible scenario for the observed U isotopic composition in Precambrian carbonates and shales. Due to the similar magnitudes of the U residence time in ancient seawater and ocean mixing timescale, $\delta^{238}U$ values in carbonates and shales may not necessarily reflect the global redox state of the ocean, but instead only provide information about the provenance of U where the carbonates or shales were deposited.

2.4.5 Non-uniformitarian U isotopic fractionation during deposition of Precambrian black shales

The mass balance of U isotopic composition of anoxic and other sinks assumes that our knowledge of the U cycle in the modern ocean is transferrable to deep times, as it uses empirical isotopic fractionation factors between sinks and seawater that are constrained based on analyses of recent sediments. Another conceivable explanation as to why Archean and Proterozoic carbonates have the same isotopic composition as continents is that the inferred U isotopic fractionation between U in anoxic sediments (black shales) and seawater constrained based on the modern ocean (Weyer et al., 2008a; Montoya-Pino et al., 2010a; Andersen et al., 2014, 2016; Holmden et al., 2015; Tissot and Dauphas, 2015) is not applicable to the Archean world. In organic-rich sediments of the modern ocean, $\delta^{238}U$ values are shifted by ~+0.6 ‰ relative to U

dissolved in seawater. If this fractionation factor was smaller in the Archean oceans, the removal of U with anoxic shales would not necessarily have induced a shift in the U isotopic composition of seawater and thus carbonates. If the isotopic fractionation during U uptake to carbonates was different than the modern, this would also affect our interpretations of the U sedimentary record. Uranium isotopic fractionation during removal to sediment can be affected by both equilibrium and kinetic processes, which are in turn affected by U speciation in seawater (Chen et al., 2016, 2017). We therefore start by calculating U speciation in ancient seawater (**Fig. 2.22A**). Chen et al. (2017) had calculated U speciation in the Phanerozoic and we extend that work to the Archean.

The geochemical modeling of aqueous U speciation follows (Chen et al., 2017) and uses the PHREEQC program (Parkhurst and Appelo, 2013). The four most important aqueous U(VI) species (their total concentration accounts for >99% of U in solution) are $Ca_2UO_2(CO_3)_3(aq)$, $CaUO_2(CO_3)_3^{2-}$, $MgUO_2(CO_3)_3^{2-}$ and $UO_2(CO_3)_3^{4-}$. In (Chen et al., 2017), $Ca_2UO_2(CO_3)_3(aq)$, $CaUO_2(CO_3)_3^{2-}$, and $MgUO_2(CO_3)_3^{2-}$ were added into the sit.dat database for the speciation calculation, with equilibrium constants from (Dong and Brooks, 2006). The species $Ca_2UO_2(CO_3)_3(aq)$ and $CaUO_2(CO_3)_3^{2-}$ are in the sit.dat database of the latest PHREEQC (version 3), so only $MgUO_2(CO_3)_3^{2-}$ and its equilibrium constant from (Dong and Brooks, 2006) were added to the sit.dat database in our simulation. The major element seawater chemistry from the Archaean to the present is from (Hardie, 1996, 2003; Halevy and Bachan, 2017). Specifically, the simulation uses major ion concentrations (Cl^-, Na^+, K^+ and Mg^+) in seawater given by (Hardie, 1996, 2003; Halevy and Bachan, 2017), as well as PCO_2, pH and Ca concentrations constrained by (Hardie, 1996, 2003; Halevy and Bachan, 2017). Uranium concentration in seawater is estimated in this study based on carbonate concentrations (see **Section 2.4.3.2**). Using these

parameters, we find that the fraction of the neutral U(VI) species $Ca_2UO_2(CO_3)_3(aq)$ in seawater is dominantly affected by Ca concentration in seawater. The dominant species are always $Ca_2UO_2(CO_3)_3(aq)$ and $CaUO_2(CO_3)_3^{2-}$. The modern ocean comprises ~44% $Ca_2UO_2(CO_3)_3$ and ~33% $CaUO_2(CO_3)_3^{2-}$, while the ocean older than ~0.7 Ga would have comprised a larger fraction of neutral U species (~51% $Ca_2UO_2(CO_3)_3$ and ~32% $CaUO_2(CO_3)_3^{2-}$). Uranium aqueous speciation could have affected U isotopic fractionation in two manners: (1) During U(VI) removal to carbonates, U isotopic fractionation is affected by the U speciation in seawater as the equilibrium fractionation between $Ca_2UO_2(CO_3)_3$ and U in $CaCO_3$ is larger than the fractionation between $CaUO_2(CO_3)_3^{2-}$ and U in $CaCO_3$ (Chen et al. 2017). (2) During U removal to black shales, U is reduced from U(VI) to U(IV) and this can be affected by kinetic isotope effects that again are controlled by U speciation in seawater (Brown et al. 2018).

Based on our speciation calculation and the equilibrium isotopic fractionation factor given by Chen et al. (2017), we have calculated the equilibrium fractionation of U between U(VI) in carbonate and U(VI) in seawater and we find that in the Archean the isotopic fractionation could have been ~0.16-0.21 ‰ for $\delta^{238}U$ compared to ~0.1 ‰ at present (**Fig. 2.22B**). This is a small change and it is insufficient to explain the fact that carbonates have the same isotopic composition as black shales in the Archean and much of the Proterozoic.

Brown et al. (2018) studied experimentally the effect of reduction kinetics on U isotopic fractionation. They found that abiotic U reduction was associated with a larger isotopic fractionation when the dissolved species were dominated by neutrally charged aqueous Ca-U-CO_3 species. Conversely, the fractionation was smaller when the fraction of neutral dissolved species was low, and the reduction rate was high. Changes in U aqueous speciation through time could

have affected the magnitude of U isotopic fractionation during U-reduction and removal to black shales. (Brown et al., 2018) found a correlation between the fraction of the neutral species $Ca_2UO_2(CO_3)_3(aq)$ and the isotope fractionation between reduced and oxidized U ($\Delta^{238}U_{IV\text{-}VI} = 0.854 \times fU_{neutral} + 0.2$). Using this relationship and our speciation calculation, we calculate the predicted isotopic fractionation between reduced U in sediments (black shales) and seawater (**Fig. 2.22B**). As shown in **Fig. 2.22A**, the larger fraction of neutral species in the Archean should have been associated with larger isotopic fractionation between black shales and seawater (carbonates) and this cannot explain the similar isotopic fractionation recorded by shales and carbonates from that Eon. This is also shown in **Fig. 2.22B,** where we plot the predicted fractionation between carbonate and shales, only considering changes in U speciation.

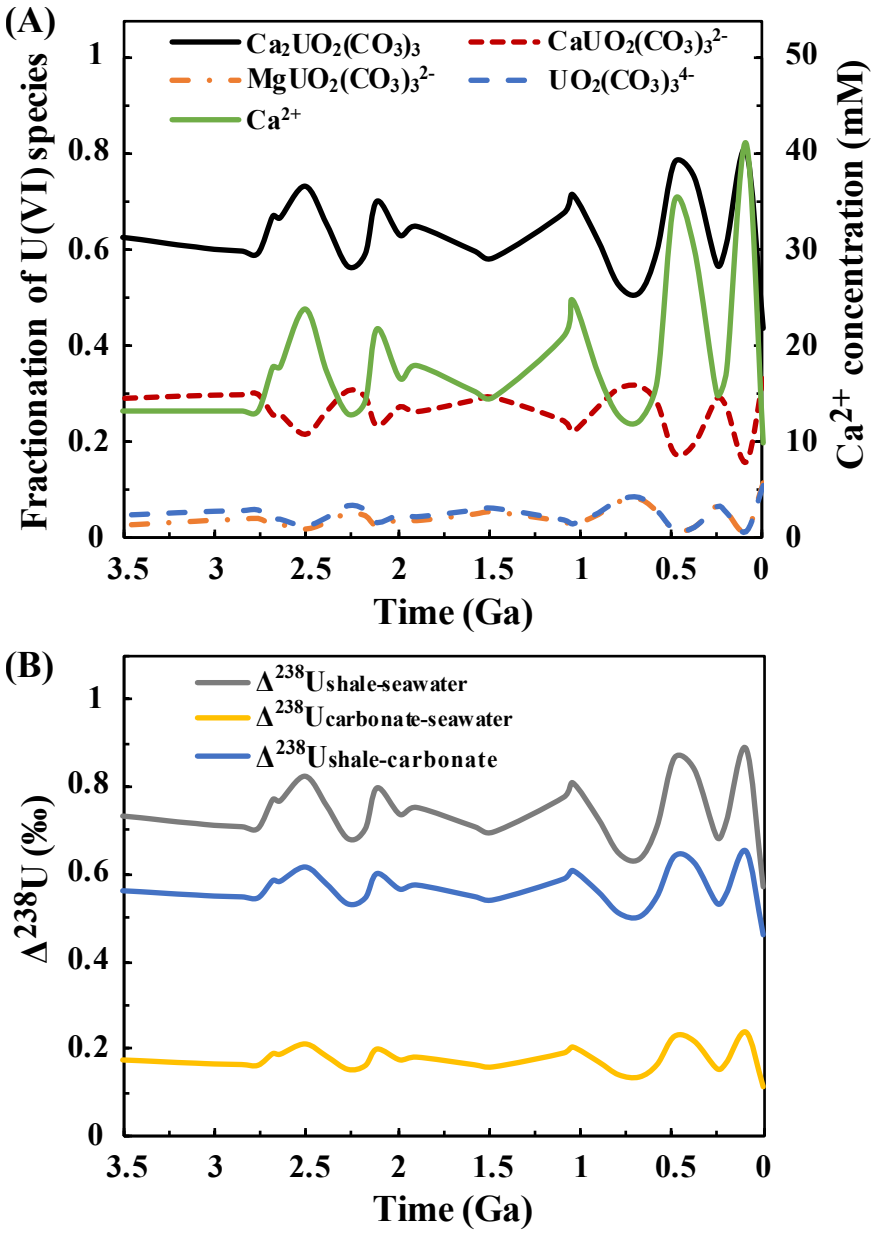

Figure 2.22 U-speciation-induced secular variations of U isotopic fractionation factors. Panel (A) shows the U speciation through geologic time calculated using the PHREEQC program. Panel (B) shows the predicted influence of speciation on carbonate-seawater (Chen et al. 2016, 2017), shale-seawater (Brown et al. 2018), and carbonate-shale $\delta^{238}U$ values using the calculated proportions of U species.

As discussed above, changes in the U speciation in seawater cannot explain our observation that both carbonates and black shales have $\delta^{238}U$ isotopic compositions similar to the crust during the Archean. Other processes may have been at play however, especially concerning U removal to black shales. Indeed, the pathway by which U(IV) is scavenged into reduced sediments is not fully resolved; it could involve both precipitation of uraninite in pore waters and adsorption onto organic matter and organic matter-coated clays (Anderson et al., 1989; Klinkhammer and Palmer, 1991; Cochran, 1992; Barnes and Cochran, 1993; Morford and Emerson, 1999; Bone et al., 2017). As discussed by (Bone et al., 2017), the role of adsorption could be critical in aqueous systems with low U concentrations, as adsorption could lower the dissolved U(IV) concentration below the level required for uraninite precipitation. Based on studies of U concentrations in Precambrian BIFs (Partin et al., 2013b), shales (Partin et al., 2013a), and carbonates (this study; (Gilleaudeau et al., 2019; Brüske et al., 2020a)), it is likely that the U concentrations in the Archean and Proterozoic oceans were factors of 10 to 100 lower than they are in today's oceans. In this context, the pathway for U removal into anoxic sediments could have been very different compared to the modern oceans, where both precipitation and adsorption are involved. It is thus conceivable that the U isotopic fractionation associated with U removal into anoxic sediments was different in the Archean and Proterozoic oceans compared to modern oceans where the ratio of dissolved uranium to organic carbon was presumably lower than in the modern oceans and the nature of organic matter was different (*i.e.*, mainly bacterial in origin; also comprising mature kerogen recycled from older sedimentary successions; (Bekker and Holland, 2012)). These suggestions are highly speculative and call for more field and experimental studies to better understand the controls on U removal and isotopic fractionation in shales. Interestingly,

a recent study investigated the U isotopic composition of the modern and Silurian-Devonian shales, which were deposited in ferruginous settings and found that $\delta^{238}U$ values were highly variable with a muted fractionation factor on average (Cole et al., 2020). The authors also explored the effects on the mass balance model resulting from different reduction pathways with various apparent fractionation factors as well as different U mass accumulation rates. Their preferred interpretation is that the fractionation factors associated with ferruginous sinks are small (~ 0.1 ‰) and similar to the oxic sinks. If correct, $\delta^{238}U$ values may actually constrain the extent of euxinic sinks, which could be associated with larger fractionation factors (Gilleaudeau et al., 2019; Stockey et al., 2020). The anoxic but non-sulfidic conditions are thought to be extensive and dominant in the Precambrian oceans (cf. (Planavsky et al., 2011; Poulton and Canfield, 2011) and if the results of Cole et al. (2020) are confirmed, their implication would support our interpretation that the U fractionation factor during reduction and burial in Precambrian black shales may have been different compared to that documented in modern euxinic ocean basins. A muted fractionation factor during U removal in Precambrian black shales would not shift the $\delta^{238}U$ value of seawater and carbonates away from the riverine source value, which could possibly explain our observations.

2.5 Conclusions

Uranium isotopic analyses of black shales and carbonates are increasingly used to reconstruct the extent of anoxia in critical periods of Earth's history. The applicability of this system relies on our understanding of the modern U cycle indicating that anoxic sediments tend to be enriched in the heavy isotopes of U relative to seawater by ~+0.6 ‰ in $\delta^{238}U$. If this U isotopic

fractionation is applicable to the Precambrian sedimentary records, we should expect that once an oceanic U redox cycle was established, carbonates precipitated in the predominantly anoxic oceans would have their $\delta^{238}U$ values fractionated by -0.6 ‰ relative to the crustal value. We have measured the U isotopic compositions of 95 carbonates ranging in age from 3.25 to 0.63 Ga and our results reveal that on a long timescale, the U isotopic composition of carbonates did not significantly evolve over the Precambrian and was always close to that of continental runoff. This suggests that some of the assumptions used to reconstruct ocean paleo-redox conditions from U isotope composition of carbonates and organic-rich shales may be invalid. In particular, we show that when oceanic anoxia increases significantly, the U residence time may decrease to a level comparable to the mixing timescale for the oceans. If correct, this implies that the common assumption that the U isotopic composition of Precambrian sediments reflects global ocean redox conditions might be flawed. Alternatively, the isotopic fractionation during U removal into Precambrian anoxic sediments could have been smaller than the modern value if the mechanism for U removal in shales was different. For example, anoxic and Fe-rich deep-ocean conditions, which have been inferred to be extensive in the early oceans, might have induced smaller fractionation to U uptake in these settings compared to the modern, anoxic and sulfidic, aerially restricted marine settings. If this interpretation is correct, it would imply a different operation of the U cycle, until the seawater sulfate reservoir dramatically increased in the late Neoproterozoic. More importantly, it would point to the limitation of U isotope proxy to constrain Precambrian seawater redox state. Coupled carbonate and black shales studies in the same succession might help better constrain the underlying reason for muted U isotope fractionations in Precambrian carbonates and organic-rich shales.

2.6 Appendix

Tissot, Bekker, Halverson and Veizer made the sample selections. Groups 1-8, 11, 16 and 22 were from Veizer. Groups 9-15, 17-21, 23-25 were from Bekker. Groups 28-30 were from Halverson.

2.6.1 Geological Settings of Samples

1. Fig Tree Group, Barberton Greenstone Belt, Swaziland Supergroup, South Africa, ~3.26-3.23 Ga (Veizer et al. 1989b)

The depositional setting is considered to be marine deepening from south to north from shallow-platformal to deep-water facies (Lowe 1980, 1982; Paris et al. 1985; Brandl et al. 2006). The middle part of the 3.26-3.23 Ga Fig Tree Group (the Mapepe Formation; Armstrong et al. 1990; Byerly et al. 1996; Kröner et al. 1991) contains a section of interbedded dolomite and chert 30 to 50 m thick in the Barite Syncline (Heinrichs and Reimer 1977) at the southern edge of farm Heemstede 378JU. The sequence contains unquestionable sedimentary textures and structures, which have been described in Lowe and Knauth (1977; locality 5), Heinrichs and Reimer (1977), and Bao et al. (2007), indicating deposition above the fair-weather-wave base.

2. Woman Lake Assemblage, Uchi Greenstone Belt, Ontario, Canada, ~2.87-2.86 Ga (Veizer et al. 1989b)

The geology of the Woman Lake area of the Uchi Greenstone Belt has been summarized in Hofmann et al. (1985). Grey siliceous, stromatolitic limestones from SE Shabu Lake, Woman Lake, and Confideration Lake that experienced greenschist facies metamorphism and cap the mafic to felsic volcanic cycle were analyzed. The ~2600 m thick cycle starts with amygdaloidal pillowed

basaltic flows grading to subaqueous, intermediate pumice flows, felsic tuffs, lapilli-tuffs, and finally felsic tuff, indicating local subaerial volcanism in a caldera setting (Hofmann et al. 1985). Stromatolitic limestone, up to 60 m in thickness, contains stratiform structures with corrugated laminae; 2) small hemispheroidal mounds; and 3) columnar structures; all indicating shallow-water setting within the photic zone. Geochronological and geological considerations constrain the age of carbonates to ~2870-2860 Ma (Nunes and Thurston 1980; Corfu and Andrews 1987; Ayres and Thurston 1985; Sanborn-Barrie et al. 2004).

3. Mosher Carbonate, Steep Rock Lake Group, Wabigoon Belt, Canada, ~2.80-2.78 Ga (Veizer et al. 1989b)

The geology of the lower-greenschist metamorphic facies Steep Rock Lake Group and of its stromatolitic carbonates (Mosher Carbonate) has been summarized in Shklanka (1972), Hofmann (1981), Wilks and Nisbet (1984, 1988), and Fralick and Riding (2015). The age of this group is bracketed by the youngest detrital zircon (2779 ± 22 Ma) from the underlying Wagita Formation and by the 2780 ± 1 Ma volcanic zircon in the overlying Dismal Ashrock (Fralick and Riding, 2015). The Mosher Carbonate, up to 500 m thick, consists almost entirely of limestones and shows sedimentary structures and stromatolites, indicating deposition on the carbonate platform above the fair-weather-wave base (Fralick and Riding 2015)

4. Tumbiana Formation, Forstescue Group, Australia, ~2.73-2.72 Ga (Veizer et al. 1990)

The stromatolitic carbonate units of the Tumbiana Formation have been described by Grey (1979), Buick (1992), Awramik and Buchheim (2009) and Coffey et al. (2013). The U-Pb SHRIMP zircon ages bracket the depositional age of the unit between 2720 and 2730 Ma (Arndt et al. 1991; Blake et al. 2004). The sampled core (SVI, Sherlock River Valley) yielded only impure

silicified carbonates from an interbedded siltstone-shale-dolostone sequence. Trendall (1983), Blake (1984a,b), Blake and Groves (1987), Buick (1992), Blake et al. (2004) and Awramik and Buchheim (2009) considered the sequence was deposited in an extensional, rift-related, lacustrine, shallow basin with episodic exposure and evaporite facies.

5. Klippan and Bothaville formations, Vendersdorp Supergroup, South Africa, ~2.73-2.71 Ga (Veizer et al. 1990)

The stromatolitic carbonates of the Klippan and Bothaville formations, collected in the Welkom goldfield area (drill-holes WZ2 and SAP4), have been described by Buck (1980). The U-Pb SHRIMP age of the underlying Makwassie quartz porphyry are given as 2709 ± 4 Ma (Armstrong et al. 1991) and the correlative underlying units Hartswater Group yielded age of 2732.9 ± 3.2 Ma and 2724.3 ± 5.8 Ma (de Koch et al. 2012). The carbonates are interpreted as non-marine playa lake sediments deposited upon the surfaces of alluvial fans in a rift system (Buck 1980; Tankard et al. 1982; Wilmeth et al. 2019).

6. Gwanda Greenstone Belt, Zimbabwe, ~2.70 Ga (Veizer et al. 1989b)

The grey, crystalline marble has been collected from the south-central part of the Gwanda greenstone belt (Tyndale-Biscoe 1940) in the vicinity of Thornwood asbestos mine (21°01’09.64”N; 29°03’11.28’’E) in Zimbabwe. Regional correlation with the thick carbonate succession (Cheshire Formation) in the better geologically and geochronologically constrained and understood Belingwe Greenstone Belt provide a ~2700 Ma age for this carbonate unit (Wilson et al. 1995; Jelsma and Dirks 2002; Bolhar et al. 2002; Hofmann et al. 2004).

7. Yellowknife Supergroup, Slave Province, Canada, ~2.68-2.66 Ga (Veizer et al. 1989b)

The Archean supracrustal rocks of the Slave Province have high proportion of metagreywacke-mudstone to volcanic rock in the preserved record (Henderson 1981). The sampled carbonates, closely associated with felsic volcaniclastic rocks, were collected from the Point and Agricola lake areas in the central Slave Province from the ~2.66 Ga Contwoy Formation of the Cogead Group (chlorite grade of greenschist metamorphic facies) and ~2.69 Ga Ignerit Formation of the Hackett River Group, respectively (Frith 1987; Henderson 1998). U-Pb zircon geochronological data constrain the age of these units between ~2.68 and 2.66 Ga based on felsic volcanic units (Frith and Loveridge 1982; Mortensen et al. 1988; Northrup et al. 1999). Carbonates were deposited in association with turbidites and volcanogenic massive sulfide deposits below the photic zone, but in a relatively shallow part of the basin close to a marginal or continental, shallow-water to emerged arc-related volcanic caldera (Bleeker and Hall 2007).

8. Carawine Dolomite, Hamersley Group, Australia, ~2.63 Ga (Veizer et al. 1990)

The Carawine Dolomite contains stromatolites, oolites, pisolites, oncolites, evaporite facies, and wave ripples, indicating deposition on a shallow-marine carbonate platform within the photic zone with episodic exposure (Simonson et al., 1993). The age of the Carawine Dolomite is 2630 ± 6 Ma, based on U-Pb SHRIMP zircon age for the tuff. The Carawine Dolomite samples are from the drill hole RHDHZA (21°17’S, 120°49’E; Nullagine 1:250,000 Sheet; Kriewaldt and Ryan 1967; see also Hickman 1983 for the general geology of the area).

9. Gamohaan Formation, Campbellrand Subgroup, South Africa, ~2.52 Ga (Rouxel et al. 2005)

The Gamahaan Formation is the uppermost unit of the Campbellrand Subgroup immediately below the ca. 2465 Ma Kuruman Iron Formation. The age of the Gamohaan

Formation is well-constrained by the TIMS U-Pb zircon age for the ash bed within this unit at 2521 ± 3 Ma (Summer and Bowring 1996). The formation was deposited on the open continental margin of the Kaapvaal Craton and consists of peritidal, subtidal, and basinal siliciclastic and carbonate rocks with various microbialite assemblages and abundant inorganic precipitates, carbonaceous shale with pyrite nodules, tuff, chert, and chert and dolostone breccia (Summer 1997). Carbonaceous shale is particularly abundant near the top of the formation and contains uncompacted laminated mats and it is interpreted to be formed in deep subtidal environment (Summer 1997). Samples were collected from the drill hole WB-98 from the Kuruman area.

10. Itabira Group, Gandarela Formation, Brazil, ~2.43 Ga (Bekker et al. 2003b)

The Gandarela Formation has a gradational contact with the Caue Iron Formation and includes dolostones, limestones, dolomitic phyllite, a dolomitic iron formation, and phyllite (Dorr 1969). Carbonates in the middle part of the Gandarela Formation contain well-preserved domal and LLH-type (laterally-linked hemispheroids of Logan et al. 1964) stromatolites and oncolites (Souza and Muller 1984), indicating deposition in high-energy intertidal to shallow subtidal environments. Intraformational dolostone and chert flat-pebble conglomerates, which range in thickness from few centimeters to more than 1 meter, occur in the upper part of this unit (Dorr 1969). Dark-colored dolostones contain up to 1.2 percent Mn (Moore 1969). A minimum age constraint for the Itabira Group is provided by the 2420 ± 19 Ma Pb-Pb carbonate age of the Gandarela Formation (Babinski el al. 1995).

11. Espanola Formation, lower Huronian Supergroup, Ontario, Canada, ~2.40 Ga (Veizer et al. 1992; Bekker et al. 2005)

The Huronian Supergroup is subdivided by unconformities into four groups; the upper three are climatically controlled cycles with basal glacial diamictites overlain by deltaic shale or carbonate and thick fluvial sandstones (Young et al. 2001). The only thick and extensive carbonate unit of the Huronian Supergroup, the Espanola Formation, occurs directly above the middle glacial diamictite (Bruce Formation) and is overlain by fluvial sandstones of the Serpent Formation. Interlayered mafic volcanic rocks and intrusive contacts with the Murray and Creighton granites constrain the age of the basal Huronian Supergroup to 2.49–2.45 Ga (Krogh et al. 1984, 1996; Smith and Heaman 1999), whereas the whole Huronian Supergroup is cut by the 2217.5 ± 1.6 Ma Nipissing sills and dikes (Andrews et al. 1986). The Gordon Lake Formation of the upper Huronian Supergroup was deposited at 2308 ± 8 Ma, based on the U-Pb SHRIMP zircon age for the tuff (Rasmussen et al., 2013). The age of the Espanola Formation is thus estimated to be around 2.40 Ga.

The Bruce “Limestone” Member is the lowermost unit of the Espanola Formation. At the outcrop in the Quirke Lake area, the sequence is a thin-bedded grey siltstone and recrystallized limestone with 1.5–3.0 m thick shale at the base. Limestone beds are thinly laminated and contain soft-sediment deformation structures. Stromatolites are conspicuously missing in the Esponala Formation, with the exception of one locality on Quirke Lake (Hoffmann et al. 1980). The dolostone member consists of interlayered ferruginous dolostone, calcareous siltstone, and limestone. The member contains flat-pebble conglomerate beds that resemble “beach rosettes” suggesting deposition in oscillatory flow. The uppermost part of the member contains mudcracks, symmetrical and ladder ripples, and wave ripples indicating a shallow-water depositional setting

(Bekker et al. 2005). The area has been subjected to lower greenschist facies metamorphism (Card 1978).

Samples were collected from the S-54 and Kerr-McGee Corp. 150/1 drill-holes and from the outcrop near the shaft 1 on the north side of creek to Quirke Lake.

12. Gordon Lake Formation, upper Huronian Supergroup, Ontario, Canada, ~2.31 Ga (Bekker et al. 2006)

The ca. 2.31 Ga Gordon Lake Formation is 300–700 m thick and consists of well-bedded, variegated mudstone and siltstone; chert; and minor fine-grained quartz sandstone that contains rare beds and nodules of dolostone (Hofmann et al. 1980; Bennett et al. 1991; Young 1991; Jackson 1994; Bekker et al. 2006). The unit is subdivided into three members: a lower member consisting of red sandstone and siltstone with chert and anhydrite/gypsum nodules (Chandler 1988); a middle member composed of green siltstone and mudstone with minor sandstone; and an upper member made up of red siltstone, mudstone, and chert. Chamosite and glauconite are present in the middle part of the formation indicating marine environment (Wood 1973; Chandler 1986). The lower part of the formation was deposited in a sabkha tidal-flat setting; the middle part represents transgressive storm-influenced marine environment below tidal current influence; and the upper part is the regressive section grading towards tidal-flat setting of the overlying Bar River Formation (Chandler 1986). The age of the Gordon Lake Formation is constrained at 2308 ± 8 Ma, based on the U-Pb SHRIMP zircon age for the tuff (Rasmussen et al., 2013).

Carbonates of the Gordon Lake Formation are restricted to the base of the formation and occur in several localities (Bekker et al., 2006). Thin laminated dolostone beds with fenestral fabrics were sampled at Plummer Township (Hofmann et al. 1980). The most extensive outcrop

of the dolostone unit is in Fenwick Township and consists of pink dolomicrite; pale-grey doloarenite with quartz grains, oolites, intraformational flat-pebble conglomerate, and stratiform copper deposit; 20–30 cm thick lenses of pale-pink to grey barite; and chert (Bennett et al. 1989). The carbonate unit is at least 30 m thick in this area (Bennett et al. 1989).

13. Pretoria Group, Silverton Formation, South Africa, ~2.15 Ga (Bekker et al. 2008)

The Silverton Formation belongs to the Paleoproterozoic Pretoria Group deposited in the open-marine Transvaal Basin in South Africa. The formation is bracketed in age by the underlying ca. 2.22 Ga Hekpoort Lava and the overlying or intruding 2.06–2.05 Ga Rooiberg Felsite Group and Bushveld Complex, respectively (Walraven 1997; Buick et al. 2001; Dorland 2004). Further indirect age constraints might be inferred from the ca. 2.14–2.12 Ga U–Pb ages of authigenic metamorphic monazite in metashales, metasiltstones, and quartzites of the Chuniespoort Group and the older Central Rand Group of the Witwatersrand Supergroup, reflecting recently recognized tectonic event in the Transvaal Basin (cf. Rasmussen et al. 2007). This pre-Bushveld compressional event folded the upper part of the Pretoria Group including the Silverton Formation in the far western part of the Transvaal Basin (Hartzer 1995, 2000; Bumby et al. 1998). Furthermore, units in the upper part of the Pretoria Group, above the Silverton Formation, are less mature with respect to the lower part of the Pretoria Group deposited on the passive continental margin, indicating transition to an active tectonic regime and a sediment provenance to the north of the Kaapvaal craton (Button 1973, 1986; Schreiber et al. 1992). The Silverton Formation records the 2.22–2.1 Ga Lomagundi carbon isotope excursion and was most likely deposited shortly before the 2.14–2.12 Ga tectonic event. We therefore assume a ca. 2.15 Ga age for deposition of the Silverton Formation.

The Silverton Formation contains carbonates, interlayered with shales that are partially dolomitized, laminated, and rarely display the features of a shallow-water depositional environment such as wave ripples, domal stromatolites, silicified nodules, soft-sediment deformation structures, water and gas escape structures, and small-scale cross-bedding (Bekker et al. 2008).

14. Mcheka Formation, Lomagundi Group, Zimbabwe, ~2.10 Ga (Master et al. 2010)

The Mcheka Formation was defined by Tennick and Phaup (1976) and is the lowermost unit of the Paleoproterozoic Lomagundi Group in Zimbabwe. It overlies the Paleoproterozoic Deweras Group unconformably, and in places it lies with a structural (thrust) contact on Archaean basement rocks. It comprises basal pebbly grits (Basal Conglomerate Member) overlain by the Lower Dolomite, Phyllite, Quartzite, Upper Dolomite, and Sandy Argillite members. A basal conglomerate grades laterally into a grit and contains clasts of Deweras Group and Archaean greenstone belt lithologies (Stagman 1961; Tennick and Phaup 1976; Stowe 1978). Thin bands of dolostone interbedded with the grits are indistinguishable from the main dolostone intervals in the Mcheka Formation, and indicate an interfingering of facies in the gradation to the overlying Lower Dolomite (Stagman 1961).

The Lower Dolomite consists of whitish-pink mottled dolostone, with thin argillaceous and arenaceous interbeds and is discontinuous along the strike. The Upper Dolomite shows great variation in texture, crystallinity and color, and contains bands of biotite-rich phyllite and sericitic and feldspathic grits and chloritic quartzite. It contains two bands of stromatolites, which include both domical and columnar varieties (Jacobsen 1962; Bond 1973; Tennick and Phaup 1976; Stowe

1978). An oolitic horizon is present in the upper dolomite (Stowe 1978), and has also been found in the Mawiru Hills area (Tennick and Phaup 1976).

Both the Lomagundi and Deweras groups record the Lomagundi carbon isotope excursion and therefore we estimate the age of the Mcheka Formation to be close to ca. 2.1 Ga.

15. Fecho do Funil Formation, Minas Supergroup, Minas Gerais, Brazil, ~2.10 Ga (Bekker et al. 2003b)

The Fecho do Funil Formation contains phyllite, siltstone, ferruginous quartz arenite, and lenses of argillaceous dolostone. Phyllite is more abundant in the lower part of the formation and dolostone content increases upsection. Dolostone lenses are up to 30 meters thick, contain long columnar and domal stromatolites (Dardenne and Campos Neto 1975; Garcia et al. 1988), and lack siliciclastic detritus, indicating a subtidal to intertidal depositional setting. A 2110 ± 110 Ma Pb-Pb carbonate date of the Fecho do Funil Formation was related to a metamorphic overprint due to the Transamazonian event (Babinski et al. 1995). Since the Fecho do Funil Formation was likely deposited in a foreland basin corresponding to the Transamazonian Orogeny and records the Lomagundi carbon isotope excursion, the date provides the estimate for the age of this unit.

16. Mistassini Group, Albanel Formation, ~2.10 Ga (Mirota and Veizer 1994)

The Paleoproterozoic Mistassini Group encompasses in stratigraphic succession, the following formations (Kouassi 1979): Papasquasati (sandstone and conglomerate), Chemo (sandstone and dolostone), Lower Albanel (carbonates and shale), Upper Albanel (dolostones), Temiscamie (iron formation), and Kallio (slate and greywacke). The carbonate sequence of the Lower Albanel Formation is essentially dolomitic, with limestones abundant only in the deeper water intervals, the Lower Black Shale complex (Unit II) and the lower portion of the Banded

Dolostone Unit (Unit III). The above sequence evolves gradationally into the Upper Albanel Formation (Wahl 1953), consisting of a grey to pink, commonly cross-bedded Sandy Dolostone Member (Unit VI) at the base, overlain by the greyish laminated to stromatolitic Banded Dolostone Member (Unit VII). The carbonates were deposited in a generally warm, shallow-marine environment of normal to slightly elevated salinities. The Lower Albanel Formation is devoid of any petrographic evidence as to the nature of its precursor carbonate minerals. The Upper Albanel Formation contains textures indicative of former aragonite as well as high-Mg calcite.

The sample MI-10-1 was collected from the basal part of the Unit I of the Lower Albanel Formation and record the Lomagundi carbon isotope excursion, whereas the overlying Lower Black Shale complex (Unit II) straddles the end of the Lomagundi carbon isotope excursion between ca. 2.11 and 2.06 Ga. We thus assign ca. 2.10 Ga age to the Unit I. Model Pb ages for diagenetic galena in the Lower Albanel Formation of 2.07-2.13 Ga (Roscoe 1984) are consistent with this age.

17. upper Nash Fork Formation, Upper Libby Creek Group, Wyoming, USA, ~2.05 Ga (Bekker et al. 2003a)

The Nash Fork Formation is the lowermost unit in the upper Libby Creek Group (Karlstrom and Houston 1984). The lower contact is structural along the Lewis Lake Fault and the upper contact is not exposed but is considered to be comformable with the Towner Greenstone. The Nash Fork Formation is separated by two carbonaceous shales, interpreted as drowning events into lower, middle, and upper units.

The upper Nash Fork Formation above the upper carbonaceous shale (M3 member) consists of a massive dolostone facies association (U1 member) and contains a prominent karstic

surface overlain by fluvial quartzite dividing the member into two parts. This facies association consists of upward-shallowing parasequences of organic-rich dolostone, gray dolostone, dolosiltite, and brown dolostone that reflects deposition in outer shelf to subaerial environments. The presence of facies indicative of tidal flat, lagoonal, inner and outer shelf, and drowned platform environments and the sequence architecture (Bekker and Eriksson 2003) suggest that the Nash Fork Formation developed entirely in open-marine settings on a mature passive margin along the southern edge of the Wyoming Craton. The boundary between the upper and lower Nash Fork formations corresponds to the end of the Lomagundi carbon isotope excursion, providing the ca. 2.05 Ga age for this unit.

18. Roberts Draw Formation and Estes Creek formations, Black Hills, South Dakota, USA, ~2.0 Ga (Bekker et al. 2003a)

The oldest unit of the Paleoproterozoic succession in the Black Hills--the Boxelder Creek Formation belongs to the older rift sequence. A younger rift succession (Estes Formation) unconformably overlies the Benchmark Iron Formation and Boxelder Formation and consists of conglomerate overlain by quartzite (Redden 1981). Siliceous fine- to medium-grained dolostone and phyllite occur in the middle part of the formation. Carbonate samples were collected at the intersection of Estes Creek Road and Estes Creek (SD-series; Bekker et al. 2003a). The Roberts Draw Formation, conformably overlying the Estes Formation, consists of dolostone gradationally overlain by limestone with interbedded dolostone and capped by graphitic, gray phyllite (Redden 1981). Samples were collected along the South Boxelder Creek (B99-series; Bekker et al. 2003a). Based on chemostratigraphic and geochronologic age constraints, Bekker et al. (2003a) inferred ca. 2.0-2.06 Ga age for these two units.

19. Snare Group, Basler Lake, NWT, Canada, ~1.97 Ga (Hardisty et al. 2017)

The greenschist metamorphic facies, Paleoproterozoic Snare Group is developed east of the Wopmay fault zone and includes quartz arenite and stromatolitic and clastic dolostone unconformably overlying the Slave craton and considered correlative with the ~1969 Ma passive margin sequence (Epworth Group) in the northern part of the Wopmay Orogen (Bowring and Grotzinger 1992; Hoffman et al. 1970; Jackson et al. 2013; McGlynn et al. 1972). It is divided into two members at Mattberry Lake: the lower siliciclastic member that contains conglomerate, arenite, siltstone, and mudstone and the upper carbonate member that contains dolostone and calc-arenite with rare stromatolites, intraformational breccia, imbricated clasts, and ripple marks (Jackson 2008; Lord 1963; Saylor and Grotzinger 1992). The carbonate member is a upward-shallowing sequence of rhythmite, stromatolotic bioherms, and irregularly laminated, cherty dolostone with tepee structures deposited in carbonate shelf and slope setting (Saylor and Grotzinger 1992).

20. Aluminium River Formation, Amer Group, Nunavut, Canada, ~1.93 Ga (Rainbird et al. 2010)

The Amer Group outcrop underlies the late Paleoproterozoic Thelon Basin and overlies mainly Neoarchean granites and lesser supracrustal rocks of the Woodburn Lake Group (e.g. Patterson 1986). It records initial terrestrial (mainly fluvial) sedimentation followed by marine or lacustrine reworking with development of a thick succession of ultra-mature sandstone (Ayagaq Lake Formation). The volcanic rocks (Five-Mile Lake volcanics) and carbonates are locally developed within the Ayagaq Lake Formation. The basin then rapidly subsided as recorded by abruptly overlying carbonaceous shale and fine-grained sandstone of the Resort Lake Formation,

which pass gradationally upward into shallow-water deposits of massive, cherty carbonate of the Aluminium River Formation, which was sampled in this study. The succeeding Three Lakes Formation, composed of siltstone and mudstone, the Oora Lake Formation, composed of quartzarenite and interbedded carbonate, and the Showing Lake Formation, composed of rhythmically interbedded feldspathic sandstone and mudstone are interpreted as an upward-shallowing sequence and are probably, in part, facies equivalents recording a regional regressive depositional episode. The uppermost unit, the Itza Lake Formation, is a cross-bedded, subarkosic sandstone of marine origin. The base of the formation is marked by a coarse-grained conglomerate, interpreted as a submarine fan deposit, and some thin units of shallow-marine, stromatolitic dolostone. The conglomerate contains large rounded clasts derived from the Ayagaq Lake Formation. These clasts suggest local tectonic uplift during deposition of the Itza Lake Formation (Rainbird et al. 2010). Based on regional correlation and detrital zircon geochronologic age constraints, the Assemblage 3, including the Aluminium River Formation, has depositional age of ca. 1.93 Ga (Rainbird et al., 2010).

21. Watterson Formation, Hurwitz Group, Nunavut. Canada, ~1.93 Ga

The Watterson Formation (Eade and Chandler 1975; Hofmann and Davidson, 1998; Aspler and Chiarenzelli, 2002) is a regionally extensive succession of dolostones and siliciclastic rocks. Four principal facies assemblages are recognized in the Watterson Formation. The domal stromatolite, stratiform stromatolite and arkosic facies assemblages constitute inner-ramp environments, and the pelitic facies assemblage represents the mid-ramp to outer-ramp setting (Aspler and Chiarenzelli, 2002). Virtually all of the carbonate rocks have been altered to dolomicrite (<0.004 mm) and xenotopic to hypidiotopic dolomicrospar (0.004 – 0.05 mm). Aspler

and Chiarenzelli (2002) interpreted that the Watterson Formation was deposited on a storm-dominated, microtidal mixed siliciclastic-carbonate ramp.

Sm–Nd and Pb–Pb isotopic data (Aspler et al. 2001) and detrital zircon geochronologic data (Davis et al. 2000) document a depositional break (at least 200 Myr) within the Hurwitz Group, and show that the Watterson Formation was deposited after 1960 ± 22 Ma (Pb-Pb SHRIMP age of youngest detrital zircon; Davis et al., 2000). Based on regional correlation and detrital zircon geochronologic age constraints, the Assemblage 3 of the Rae Domain in Nunavut, Canada, including the Watterson Formation, has depositional age of ca. 1.93 Ga (Rainbird et al., 2010).

22. Cowles Lake Formation, Coronation Supergroup, NWT, Canada, ~1.88 Ga (Veizer et al. 1992)

The Coronation Supergroup of the Wopmay Orogen in northwestern Canada includes one of the oldest well-developed passive margin sequences in the world, the Epworth Group (Grotzinger 1986a,b, 1989a,b). Subsequent to deposition of the passive margin sequence, the foreland basin developed with an eastward migrating foredeep filled by the sediments of the Recluse Group (Hoffman and Bowring 1984). The latter includes a linear subtidal stromatolite buildup on the outer trench slope of the basin, the Cowles Lake Reef (Jackson 1989). The sequence contains limestone/argillite rhythmites, intraclast grainstones, slope breccias, and slump deposits. In contrast to the Epworth Group carbonates, this facies shows no evidence for subaerial emergence and has likely been deposited in a deep-water environment. Dolomitization is lacking and the rocks contain pervasive pressure solution phenomena, such as stylolites. Samples 84-CO-19 to 21 are from the Cowles Lake Formation. Based on U-Pb zircon ages of volcanic ash beds at

the base of the Recluse Group, the studied sequence is dated at 1882 ± 4 Ma (Bowring and Grotzinger, 1992).

23. Taltheilei Formation, Pethei Group, NWT, Canada, ~1.86 Ga (Hardisty et al. 2017)

The Taltheilei Formation of the Pethei Group was deposited along the southeastern margin of the Slave craton and belongs to the platform facies. It contains shallow-water, marine stromatolitic dolostone of two facies: 1) laterally-continuous, stromatolitic, laminated, and massive dolostone with oncolites, edgewise conglomerates, and desiccation cracks of back-reef, intertidal lagoonal setting, and 2) stromatolitic bioherms consisting of branching stromatolites with elliptical plan view surrounded by coarse-grained, clastic carbonate of barrier-reef setting (Hoffman 1968, 1974). Recent and ongoing geochronologic studies bracket this unit between ~1.88-1.85 Ga in age (Kjarsgaard et al. 2013; van Breemen et al. 2013).

24. George Formation, Muskwa Assemblage, BC, Canada, ~1.6 Ga (Ross et al. 2001)

The exposed, deformed, but sub-greenschist metamorphic facies Muskwa Assemblage has been divided into seven formations (Bell 1966, 1968; Taylor and Stott 1973; Long et al. 1999; Bellefroid et al. 2019). The lower 3.4 km consist predominantly of fine-grained siliciclastic strata and carbonates deposited in a marine environment. It has been suggested that the George Formation was deposited in an extensional to transtensional basin (Long et al., 1999). Sedimentary structures include hummocky cross-stratified carbonates, and wavy-bedded dololutite with soft-sediment deformation structures in the lower, progressively shallowing from a storm-influenced, mid- to outer shelf settings to an inner shelf facies of thick-bedded, parallel laminated carbonate mudstones with stromatolites, abundant molar tooth structures, ripples, flat-pebble conglomerates, and molar-tooth structures (Long et al. 1999; Pratt 2017). Therefore, water depths where above

storm wave base. The depositional age and stratigraphic affinities of this succession are uncertain, and the best age estimate for deposition based on detrital zircons is ca. 1.6 Ga, though an age closer to 1.4 Ga is possible (Ross et al. 2001; Pratt and Long, 2017; Bellefroid et al., 2019).

25. Wallace, Helena, and Snowslip formations, Belt Supergroup, MT, USA, ~1.45 Ga (Hardisty et al. 2017)

The middle Belt carbonate in the middle part of the Belt Supergroup contains the Wallace Formation in the western part of the intracratonic Belt Basin interfingering with the Helena Formation in its eastern part (Glacier National Park), where it is overlain by the predominantly fine-grained, siliciclastic Snowslip Formation. The lower part of the Helena Formation contains ~10 m thick cyclic intervals of siliciclastic to carbonate rocks representing shallowing and deepening sequences and transitions to stromatolitic and oolitic facies in the middle and upper portions of the formation (Winston, 2006). The Wallace Formation contains oolitic dolomitic carbonate and coarse-grained quartz sandstone at the base grading to mudcracked argillite-carbonate cycles with large domal stromatolites at the top. The Snowslip Formation consists of alternating mudcracked red argillite and tabular sand beds that grade to the north to green argillite and carbonate. Evidences for shallow-marine or possibly lacustrine deposition include mudcracks and other dessication features, stromatolites, storm-lag deposits, and cross-bedding (Winston and Lyons 1993).

Oolitic carbonate from near the base of the Wallace Formation was sampled at Logan Pass near the Going-to-the-Sun Road. The cross-bedded, oolitic limestone of the Snowslip Formation, underlying domal stromatolites with flat-pebble conglomerates and mudcracked argillite was sampled near Highway 37 close to Rexford, Idaho.

The ca. 1.45 Ga age for these units is constrained by U-Pb ages of 1454 ± 9 Ma from a tuff bed in the upper part of the Helena Formation at Logan Pass and 1443 ± 7 Ma for the overlying Purcell Lava at the base of the directly overlying Missoula Group, including the Snowslip Formation (Aleinikoff et al. 2015; Evans et al. 2000).

26. Sukhaya Tunguska Fm., Western Siberia, ~1.04 Ga (Bartley et al. 2001)

The Turukhansk region is an uplifted margin along the northwestern edge of the Siberian Craton. Within the uplift, unmetamorphosed Riphean carbonates and siliciclastic rocks, up to 4.5 km thick, are exposed in three north–south trending, east-transported, thrust-bounded blocks (Semikhatov and Serebryakov 1983; Petrov and Semikhatov 1997, 1998). The Sukhaya Tunguska Formation is the uppermost Middle Riphean unit in this region. Limestones and dolostones of the Sukhaya Tunguska Formation (560 – 680 m) accumulated in shallow subtidal to intertidal settings (Petrov et al. 1995; Sergeev et al. 1997; Sergeev 1999).

Radiometric data from the Turukhansk Riphean succession are limited, but broadly constrain the age of deposition. A 16-point Pb–Pb isochron on carbonates from the middle Sukhaya Tunguska Formation yielded an age of 1035 ± 60 Ma (Ovchinnikova et al. 1995). Correlation with other upper Middle Riphean sections on the Siberian craton are consistent with this age assignment, although no correlative unit has been precisely dated.

27. Ymer Ø Group, Eleonore Supergroup, E. Greenland, ~ 0.81 Ga (Sønderholm and Tirsgaard, 1993; Worndle et al. 2019)

The Ymer Ø Group is part of the Tonian Eleonore Bay Supergroup within the Caledonides of East Greenland (Katz, 1961; Sønderholm and Tirsgaard, 1993). The Eleonore Bay Supergroup is overlain by the Tillite Group, which includes a pair of Cryogenian glacial units that correlate

unambiguously with Cryogenian glacial units in northeastern Svalbard (Fairchild and Hambrey 1984, 1995; Hoffman et al.., 2012). Close lithological similarities also are found between the Eleonore Bay Supergroup and the Veteranen and Akademikerbreen groups in northeastern Svalbard, leading many researchers to conclude that the Neoproterozoic strata of East Greenland and northeastern Svalbard were deposited in a single, contiguous, basin. The Ymer Ø Group (also referred to as the Brogetdal Formation or Multicoloured series; Katz, 1961; Haller, 1971), occurs near the top of the Eleonore Bay Group, and comprises up to 1200 m of mixed red to brown mudstone and sandstone, yellow and red dolostone, and grey to black limestone deposited in offshore–slope to inner carbonate platform environments (Sønderholm and Tirsgaard, 1990).

Samples analyzed in this study were collected from the type section on Ymer Ø, where the logged section begins in blue-grey to grey, medium bedded limestone capped by a thin pale dolostone bed, the top of which is a subaerial unconformity (Worndle et al. 2019). The lower part of the overlying (Bed-group 10) consists of green silt, grading upward into interbedded, thin and wavy pink and white limestone and dolomitic limestone beds and red, marly shale and silt, inferred to have been deposited primarily in a shallow subtidal setting.

No direct radiometric ages have been obtained on the Ymer Ø Group. However, the logged logged section on Ymer Ø record the so-called Bitter Springs negative carbon isotope anomaly (BSA), which has been dated elsewhere globally (e.g. Macdonald et al., 2010; Maclennan et al., 2018), indicating an age of ca. 810–800 Ma for the rocks collected for this study.

28. Elbobreen Fm., Polarisbreen Group, Svalbard, ~0.73 Ga (Fairchild and Hambrey 1995; Halverson et al. 2018a)

The late Tonian–early Ediacaran Polarisbreen Group is exposed in a north-south trending belt that extends from southern Olav V Land in Spitsbergen to western Nordaustlandet in the Svalbard Archipelago of the Barents Shelf. The Polarisbreen Group comprises the mixed siliciclastic-carbonate Elbobreen, Wilsonbreen and Dracoisen formations in the uppermost Neoproterozoic of the Hecla Hoek Succession of northeastern Spitsbergen (Wilson and Harland 1964; Fairchild and Hambrey 1984), widely accepted to correlate with the Tillite Group in East Greenland. These include two distinct glacial units correlated with the global Sturtian and Marinoan glaciations. Precise ages from the Neoproterozoic of Svalbard are lacking, but an age model can be found in Halverson et al. (2018b). This age model implies that the latest Tonian, lower Polarisbreen Group rocks analyzed for this study (from the Russøya Member of the Elbobreen Formation) are ca. 740-730 Ma. The Russøya Member comprises up to 220 m of mixed carbonates and siliciclastics but is predominantly carbonate in Nordaustlandet, where it was sampled. Here the carbonates include black limestones with abundant molar tooth structures, wavy laminated and fine-bedded ribbonite facies, and abundant grainstone, some of which is oolitic. Collectively these carbonates were deposited in a mid-shelf to intertidal environment (Halverson et al. 2018a).

29. Bed-Group 20, E. Greenland, ~0.73 Ga (Herrington and Fairchild 1989)

The upper André Land Group represents the latest Tonian stratigraphy within the thick Neoproterozoic Eleonore Bay Supergroup in the East Greenland Caledonies (Sønderholm and Tirsgaard 1993). It comprises three informal formations, Bed-Groups 18–20 (Herrington and Fairchild 1989), the upper two of which broadly correlate with the lower Polarisbreen Group in NE Svalbard (see above; Fairchild and Hambrey 1995), implying an age of ca. 740–730 Ma

(Halverson et al., 2018a). Bed-Group 20, which was sampled for this study, occurs only on Ella Ø, where it is >131 m-thick. It consists of laminated dolostone and shale with interbedded floatstone (debrites) that transitions upward into organic-rich limestones with dense molar tooth structure, representing deposition in a slope to mid-shelf environment (Herrington and Fairchild, 1989; Hoffman et al. 2012). Bed-Group 20 is disconformably overlain by the glaciogenic (early Cryogenian) Ulvesø Formation.

30. Otavi Group, Rasthof Formation ~0.66 Ga, Maieberg Formation ~0.63 Ga, Namibia (Hoffman and Halverson 2008)

The Otavi Group lies on the southwestern margin of the Congo craton where it is well exposed in the Kaoko and central Damara fold-and-thrust belts in northwestern and north-central Namibia (Hoffman and Halverson 2008). The Otavi Group comprises the Ombombo, Ugab, Abenab, and Tsumeb subgroups, the latter two of which are floored by the glaciogenic Chuos (Sturtian) and Ghaub (Marinoan) formations (Hoffmann and Prave 1996).

The Chuos Formation is highly variable in thickness, heterolithic, and, typical of (but not unique to) Sturtian glacial deposits, contains banded iron-formation (BIF) and is overlain by a cap-carbonate sequence (Rasthof Fm.) with a negative $\delta^{13}C$ anomaly (Hoffmann et al. 2007). The Rasthof Formation is the lower of three formations (along with the Gruis and Ombaatjie formations), which together comprise the Cryogenian non-glacial interval of the Abenab Subgroup. The Rasthof Formation represents a single, thick (ca. 200 m) shoaling-upward sequence, with abundant sub-tidal microbial buildups, overlain by dolomitic grainstones. The global chronological framework for the Cryogenian implies an age of ca. 660–655 Ma for the Rasthof Formation (Rooney et al. 2020).

The basal Ediacaran Maieberg Formation is the cap-carbonate to the (Marinoan) Ghaub glacials (Hoffman et al. 1998a,b). A pair of precise U–Pb zircon ages from tuffs Ghaub Formation, along with early Ediacaran ages globally, provide a tight age estimate of ca. 635 Ma for the base of the Maieberg Formation (Prave et al., 2016). The ~300–400 m-thick Maieberg Formation records a single transgressive-regressive sequence, which includes the Keilberg Mb. cap dolostone at its base (Hurtgen et al. 2006). Above the cap dolostone, the Maieberg Formation comprises mainly finely laminated rhythmite, dololutite and dolarenites deposited in outer-mid-shelf to inner platform (intertidal) environments. Based on global correlations and radiometric ages, it is inferred that the entire Maieberg Formation was deposited in ca. 3 Ma.

2.7 References

Abe M., Suzuki T., Fujii Y., Hada M. and Hirao K. (2008) An ab initio molecular orbital study of the nuclear volume effects in uranium isotope fractionations. *J. Chem. Phys.* **129**, 164309.

Abshire M. L., Romaniello S. J., Kuzminov A. M., Cofrancesco J., Severmann S. and Riedinger N. (2020) Uranium isotopes as a proxy for primary depositional redox conditions in organic-rich marine systems. *Earth Planet. Sci. Lett.* **529**, 115878.

Aleinikoff, J. N., Lund, K., & Fanning, C. M. (2015). SHRIMP U–Pb and REE data pertaining to the origins of xenotime in Belt Supergroup rocks: evidence for ages of deposition, hydrothermal alteration, and metamorphism. *Canadian Journal of Earth Sciences*, *52*(9), 722-745.

Algeo T. J. and Lyons T. W. (2006) Mo–total organic carbon covariation in modern anoxic marine environments: Implications for analysis of paleoredox and paleohydrographic conditions. *Paleoceanography* **21**.

Anbar A. D., Duan Y., Lyons T. W., Arnold G. L., Kendall B., Creaser R. A., Kaufman A. J., Gordon G. W., Scott C. and Garvin J. (2007) A whiff of oxygen before the great oxidation event? *Science (80-.).* **317**, 1903–1906.

Andersen M. B., Matthews A., Vance D., Bar-Matthews M., Archer C. and de Souza G. F. (2018) A 10-fold decline in the deep Eastern Mediterranean thermohaline overturning circulation during the last interglacial period. *Earth Planet. Sci. Lett.* **503**, 58–67.

Andersen M. B., Romaniello S., Vance D., Little S. H., Herdman R. and Lyons T. W. (2014) A modern framework for the interpretation of 238U/235U in studies of ancient ocean redox. *Earth Planet. Sci. Lett.* **400**, 184–194.

Andersen M. B., Stirling C. H. and Weyer S. (2017) Uranium isotope fractionation. *Rev. Mineral. Geochemistry* **82**, 799–850.

Andersen M. B., Stirling C. H., Zimmermann B. and Halliday A. N. (2010) Precise determination of the open ocean 234U/238U composition. *Geochemistry, Geophys. Geosystems* **11**.

Andersen M. B., Vance D., Morford J. L., Bura-Nakić E., Breitenbach S. F. M. and Och L. (2016) Closing in on the marine 238U/235U budget. *Chem. Geol.* **420**, 11–22.

Anderson R. F., Fleisher M. Q. and LeHuray A. P. (1989) Concentration, oxidation state, and particulate flux of uranium in the Black Sea. *Geochim. Cosmochim. Acta* **53**, 2215–2224.

Andrews A.J., Masliwec A., Morris W.A., Owsiacki L., York D. (1986) The silver deposits at Cobalt and Gowganda, Ontario. II: An experiment in age determinations employing radiometric and paleomagnetic measurements. *Can. J. Earth Sci*. 23, 1507– 1518.

Armstrong, R.A., Compston, W., Dewit, M.J., Williams, I.S., 1990. The Stratigraphy of the 3.5-3.2-Ga Barberton Greenstone-Belt Revisited - a Single Zircon Ion Microprobe Study. Earth and Planetary Science Letters, 101(1): 90-106.

Armstrong, R. A., Compston, W., Retief, E. A., Williams, I. T., & Welke, H. J. (1991). Zircon ion microprobe studies bearing on the age and evolution of the Witwatersrand triad. *Precambrian Research*, *53*(3-4), 243-266.

Arndt, N. T., Nelson, D. R., Compston, W., Trendall, A. F., & Thorne, A. M. (1991). The age of the Fortescue Group, Hamersley Basin, Western Australia, from ion microprobe zircon U-Pb results. *Australian Journal of Earth Sciences*, *38*(3), 261-281.

Asael D., Tissot F. L. H., Reinhard C. T., Rouxel O., Dauphas N., Lyons T. W., Ponzevera E., Liorzou C. and Chéron S. (2013) Coupled molybdenum, iron and uranium stable isotopes as oceanic paleoredox proxies during the Paleoproterozoic Shunga Event. *Chem. Geol.* **362**, 193–210.

Aspler, L. B., & Chiarenzelli, J. R. (2002). Mixed Siliciclastic–Carbonate Storm-Dominated Ramp in a Rejuvenated Palaeoproterozoic Intracratonic Basin: Upper Hurwitz Group, Nunavut, Canada. *Precambrian sedimentary environments: a modern approach to ancient depositional systems*, 293-321.

Aspler L.B., Chiarenzelli J.R., Cousens B.L., McNicoll V.J. & Davis W.J. (2001) Paleoproterozoic intracratonic basin processes, from breakup of Kenorland to assembly of Laurentia: Hurwitz Basin, Nunavut, Canada. *Sediment. Geol.*, **141–142**, 287–318.

Awramik, S. M., and Buchheim, H. P. (2009). A giant, late archean lake system: the meentheena member (tumbiana formation; fortescue group), Western Australia. *Precambrian Research*, *174*(3-4), 215-240.

Ayres L.D. and Thurston P.C. (1985) Archean supracrustal sequences in the Canadian Shield: An overview. *Geol. Assoc. Can. Special Paper* 28, 344-380.

Azmy K., Kendall B., Brand U., Stouge S. and Gordon G. W. (2015) Redox conditions across the Cambrian–Ordovician boundary: Elemental and isotopic signatures retained in the GSSP carbonates. *Palaeogeogr. Palaeoclimatol. Palaeoecol.* **440**, 440–454.

Babinski M., Chemale F. Jr. and Van Schmus W.R. (1995) The Pb/Pb age of the Minas Supergroup carbonate rocks, Quadrilatero Ferrıfero, Brazil. *Precambrian Research*, v. 72, p. 235–245.

Banner J. L. and Hanson G. N. (1990) Calculation of simultaneous isotopic and trace element variations during water-rock interaction with applications to carbonate diagenesis. *Geochim. Cosmochim. Acta* **54**, 3123–3137.

Bao, H., Rumble III, D., Lowe, D.R., 2007. The five stable isotope compositions of Fig Tree barites: Implications on sulfur cycle in ca. 3.2 Ga oceans. Geochim. Cosmochim. Acta, 71: 4868-4879.

Barnes C. E. and Cochran J. K. (1993) Uranium geochemistry in estuarine sediments: controls on removal and release processes. *Geochim. Cosmochim. Acta* **57**, 555–569.

Bartlett R., Elrick M., Wheeley J. R., Polyak V., Desrochers A. and Asmerom Y. (2018) Abrupt global-ocean anoxia during the Late Ordovician–early Silurian detected using uranium isotopes of marine carbonates. *Proc. Natl. Acad. Sci.* **115**, 5896–5901.

Bartley, J. K., Semikhatov, M. A., Kaufman, A. J., Knoll, A. H., Pope, M. C., & Jacobsen, S. B. (2001). Global events across the Mesoproterozoic–Neoproterozoic boundary: C and Sr isotopic evidence from Siberia. *Precambrian Research*, *111*(1-4), 165-202.

Bekker A. and Holland H. D. (2012) Oxygen overshoot and recovery during the early Paleoproterozoic. *Earth Planet. Sci. Lett.* **317**, 295–304.

Bekker A., Holland H. D., Wang P.-L., Rumble D., Stein H. J., Hannah J. L., Coetzee L. L. and Beukes N. J. (2004) Dating the rise of atmospheric oxygen. *Nature* **427**, 117–120.

Bekker A., Karhu J.A., Eriksson K.A., Kaufman A.J. (2003a) Chemostratigraphy of Paleoproterozoic carbonate successions of the Wyoming Craton: tectonic forcing of biogeochemical change? *Precambrian Res*. 120, 279–325.

Bekker, A., Sial, A. N., Karhu, J. A., Ferreira, V. P., Noce, C. M., Kaufman, A. J., ... & Pimentel, M. M. (2003b). Chemostratigraphy of carbonates from the Minas Supergroup, Quadrilátero Ferryífero (Iron Quadrangle), Brazil: A stratigraphic record of early proterozoic

atmospheric, biogeochemical and climactic change. *American Journal of Science*, *303*(10), 865-904.

Bekker A., Eriksson K.A. (2003) Paleoproterozoic drowned carbonate platform on the southeastern margin of the Wyoming Craton: a record of the Kenorland breakup. *Precambrian Res*. 120, 327–364.

Bekker A., Kaufman A.J., Karhu J.A., Eriksson K.A. (2005) Evidence for Paleoproterozoic cap carbonates in North America. *Precambrian Res*. 137, 167–206.

Bekker, A., Karhu, J. A., & Kaufman, A. J. (2006). Carbon isotope record for the onset of the Lomagundi carbon isotope excursion in the Great Lakes area, North America. *Precambrian Research*, *148*(1-2), 145-180.

Bekker, A., Holmden, C., Beukes, N. J., Kenig, F., Eglinton, B., & Patterson, W. P. (2008). Fractionation between inorganic and organic carbon during the Lomagundi (2.22–2.1 Ga) carbon isotope excursion. *Earth and Planetary Science Letters*, *271*(1-4), 278-291.

Bell R.T. (1966) Precambrian rocks of the Tuchodi Lakes map-area, northeastern British Columbia. Unpublished Ph.D. thesis, Princeton University. 138 pp.

Bell R.T. (1968) Proterozoic Stratigraphy of Northeastern British Columbia. *Geol. Surv. Can. Pap*. 67-68, 75.

Bellefroid, E. J., Planavsky, N. J., Hood, A. V., Halverson, G. P., & Spokas, K. (2019). Shallow water redox conditions of the mid-Proterozoic Muskwa Assemblage, British Columbia, Canada. *American Journal of Science*, *319*(2), 122-157.

Bennett G., Dressler B.O., Robertson J.A. (1991) The Huronian Supergroup and associated intrusive rocks. In: Thurston P.C., Williams H.R., Sutcliffe R.H., Stott G.M. (Eds.), Geology of Ontario. *Ontario Geological Survey Special Volume* 4, Part 1, Toronto, pp. 549–591.

Bennett G., Born P., Hatfield K. (1989) A report on a recently identified dolostone unit in Fenwick Township, Goulais Bay area, District of Algoma. In: Fenwick K.G., Giblin P.E., Pitts A.E. (Eds.), Report of activities 1988. Resident Geologists, *Ontario Geological Survey Miscellaneous Paper* 142, pp. 211–215.

Bigeleisen J. (1996) Nuclear size and shape effects in chemical reactions. Isotope chemistry of the heavy elements. *J. Am. Chem. Soc.* **118**, 3676–3680.

Bills B. G. and Ray R. D. (1999) Lunar orbital evolution: A synthesis of recent results. *Geophys. Res. Lett.* **26**, 3045–3048.

Blake T.S. (1984a) The lower Fortescue Group of the northern Pilbara craton: Stratigraphy and paleogeography. In *Archean and Proterozoic basins of‘ the Pilbara, Western Australia:*

Evolution and Mineralization Potential (eds. J.R. Muhling et al.): *Univ. W. Australia. Dept. and Univ. Ext. Publ*. 9, pp. 123-143.

Blake T.S. (1984b) Evidence for stabilization of the Pilbara Block. Australia. *Nature* 307, 72l-723.

Blake T.S. and Groves D.I. (1987) Continental rifting and the Archean-Proterozoic transition. *Geology* 15, 229-232.

Blake, T. S., Buick, R., Brown, S. J. A., & Barley, M. E. (2004). Geochronology of a Late Archaean flood basalt province in the Pilbara Craton, Australia: constraints on basin evolution, volcanic and sedimentary accumulation, and continental drift rates. *Precambrian Research*, *133*(3-4), 143-173.

Blättler C. L., Claire M. W., Prave A. R., Kirsimäe K., Higgins J. A., Medvedev P. V, Romashkin A. E., Rychanchik D. V, Zerkle A. L. and Paiste K. (2018) Two-billion-year-old evaporites capture Earth's great oxidation. *Science (80-.).* **360**, 320–323.

Bleeker, W., and Hall, B. (2007). The Slave Craton: geological and metallogenic evolution. *Mineral deposits of Canada: a synthesis of major deposit-types, district metallogeny, the evolution of geological provinces, and exploration methods. Edited by WD Goodfellow. Geological Association of Canada, Mineral Deposits Division, Special Publication*, *5*, 849-879.

Bolhar, R., Hofmann, A., Woodhead, J., Hergt, J., & Dirks, P. H. G. M. (2002). Pb-and Nd-isotope systematics of stromatolitic limestones from the 2.7 Ga Ngezi Group of the Belingwe Greenstone Belt: constraints on timing of deposition and provenance. *Precambrian Research*, *114*(3-4), 277-294.

Bond G. (1973) The palaeontology of Rhodesia. *Rhod. Geol. Surv. Bull*. 70.

Bone S. E., Dynes J. J., Cliff J. and Bargar J. R. (2017) Uranium (IV) adsorption by natural organic matter in anoxic sediments. *Proc. Natl. Acad. Sci.* **114**, 711–716.

Bourdon B., Turner S., Henderson G. M. and Lundstrom C. C. (2003) Introduction to U-series geochemistry. *Rev. Mineral. geochemistry* **52**, 1–21.

Bowring S.A., Grotzinger J.P. (1992) Implications of new chronostratigraphy for tectonic evolution of Wopmay Orogen, northwest Canadian Shield. *American Journal of Science* 292, 1-20.

Brandl, G., Cloete, M., Anhaeusser, C.R., 2006. Archean greenstone belts. In: Johnson, M.R., Anhaeusser, C.R., Thomas, R.J. (Eds.), The Geology of South Africa. Geological Society of South Africa, Johannesburg and Council for Geoscience, Pretoria, pp. 9-56.

Brennan S. T., Lowenstein T. K. and Horita J. (2004) Seawater chemistry and the advent of biocalcification. *Geology* **32**, 473–476.

Brennecka G. A., Herrmann A. D., Algeo T. J. and Anbar A. D. (2011) Rapid expansion of oceanic anoxia immediately before the end-Permian mass extinction. *Proc. Natl. Acad. Sci.* **108**, 17631–17634.

Brown S. T., Basu A., Ding X., Christensen J. N. and DePaolo D. J. (2018) Uranium isotope fractionation by abiotic reductive precipitation. *Proc. Natl. Acad. Sci.* **115**, 8688–8693.

Brüske A., Martin A. N., Rammensee P., Eroglu S., Lazarov M., Albut G., Schuth S., Aulbach S., Schoenberg R. and Beukes N. (2020a) The onset of oxidative weathering traced by uranium isotopes. *Precambrian Res.* **338**, 105583.

Brüske A., Weyer S., Zhao M.-Y., Planavsky N. J., Wegwerth A., Neubert N., Dellwig O., Lau K. V and Lyons T. W. (2020b) Correlated molybdenum and uranium isotope signatures in modern anoxic sediments: Implications for their use as paleo-redox proxy. *Geochim. Cosmochim. Acta* **270**, 449–474.

Buck S.G. (1980) Stromatolite and ooid deposits within the fluvial and lacustrine sediments of the Precambrian Ventersdorp Supergroup of South Africa. *Precambrian Res.* 12, 311-330.

Buick I.S., Maas R., Gibson R. (2001) Precise U–Pb titanite age constraints on the emplacement of the Bushveld Complex, South Africa. *J. Geol. Soc.* (Lond.) 158, 3–6.

Buick, R. (1992). The antiquity of oxygenic photosynthesis: evidence from stromatolites in sulphate-deficient Archaean lakes. *Science*, *255*(5040), 74-77.

Bumby, A. J., Eriksson, P. G., & Van der Merwe, R. (1998). Compressive deformation in the floor rocks to the Bushveld Complex (South Africa): evidence from the Rustenburg Fault Zone. Journal of African Earth Sciences, 27(3-4), 307-330.

Bura-Nakić E., Andersen M. B., Archer C., de Souza G. F., Marguš M. and Vance D. (2018) Coupled Mo-U abundances and isotopes in a small marine euxinic basin: constraints on processes in euxinic basins. *Geochim. Cosmochim. Acta* **222**, 212–229.

Bura-Nakić E., Sondi I., Mikac N. and Andersen M. B. (2020) Investigating the molybdenum and uranium redox proxies in a modern shallow anoxic carbonate rich marine sediment setting of the Malo Jezero (Mljet Lakes, Adriatic Sea). *Chem. Geol.* **533**, 119441.

Burke A., Stewart A. L., Adkins J. F., Ferrari R., Jansen M. F. and Thompson A. F. (2015) The glacial mid-depth radiocarbon bulge and its implications for the overturning circulation. *Paleoceanography* **30**, 1021–1039.

Button, A. (1973). The stratigraphic history of the Malmani dolomite in the eastern and north-eastern Transvaal. South African Journal of Geology, 76(3), 229-247.

Button, A. (1986). The Transvaal sub-basin of the Transvaal Sequence. In Mineral deposits of southern Africa (pp. 811-817).

Byerly, G. R., Kröner, A., Lowe, D. R., Todt, W., & Walsh, M. M. (1996). Prolonged magmatism and time constraints for sediment deposition in the early Archean Barberton greenstone belt: evidence from the Upper Onverwacht and Fig Tree groups. Precambrian Research, 78(1-3), 125-138.

Cao M., Daines S. J., Lenton T. M., Cui H., Algeo T. J., Dahl T. W., Shi W., Chen Z.-Q., Anbar A. and Zhou Y.-Q. (2020) Comparison of Ediacaran platform and slope δ238U records in South China: Implications for global-ocean oxygenation and the origin of the Shuram Excursion. *Geochim. Cosmochim. Acta*.

Card K.D. (1978) Metamorphism of the middle Precambrian (Aphebian) rocks of the eastern Southern Province. *Geol. Surv. Canada Pap.* 78-10,269-282.

Carleton P. J. C. C. (2000) *Continental shelf limits: the scientific and legal interface*., Oxford University Press on Demand.

Catling D. C. and Zahnle K. J. (2020) The Archean atmosphere. *Sci. Adv.* **6**, eaax1420.

Chandler F.W. (1988) Diagenesis of sabkha-related, sulphate nodules in the Early Proterozoic Gordon Lake Formation, Ontario, Canada. *Carbonate Evaporite* 3 (1), 75–94.

Chandler F.W. (1986) Sedimentology and paleoclimatology of the Huronian (Early Aphebian) Lorrain and Gordon Lake Formations and their bearing on models for sedimentary copper mineralization, Current Research, Part A. *Geological Survey of Canada*, Paper 86- 1A, pp. 121–132.

Chen J. H., Edwards R. L. and Wasserburg G. J. (1986) 238U, 234U and232Th in seawater. *Earth Planet. Sci. Lett.* **80**, 241–251.

Chen X., Romaniello S. J. and Anbar A. D. (2017) Uranium isotope fractionation induced by aqueous speciation: Implications for U isotopes in marine CaCO3 as a paleoredox proxy. *Geochim. Cosmochim. Acta* **215**, 162–172.

Chen X., Romaniello S. J., Herrmann A. D., Hardisty D., Gill B. C. and Anbar A. D. (2018a) Diagenetic effects on uranium isotope fractionation in carbonate sediments from the Bahamas. *Geochim. Cosmochim. Acta* **237**, 294–311.

Chen X., Romaniello S. J., Herrmann A. D., Samankassou E. and Anbar A. D. (2018b) Biological effects on uranium isotope fractionation (238U/235U) in primary biogenic carbonates. *Geochim. Cosmochim. Acta* **240**, 1–10.

Chen X., Romaniello S. J., Herrmann A. D., Wasylenki L. E. and Anbar A. D. (2016) Uranium isotope fractionation during coprecipitation with aragonite and calcite. *Geochim. Cosmochim. Acta* **188**, 189–207.

Cheng H., Edwards R. L., Shen C.-C., Polyak V. J., Asmerom Y., Woodhead J., Hellstrom J., Wang Y., Kong X. and Spötl C. (2013) Improvements in 230Th dating, 230Th and 234U half-life values, and U–Th isotopic measurements by multi-collector inductively coupled plasma mass spectrometry. *Earth Planet. Sci. Lett.* **371**, 82–91.

Cheng K., Elrick M. and Romaniello S. J. (2020) Early Mississippian ocean anoxia triggered organic carbon burial and late Paleozoic cooling: Evidence from uranium isotopes recorded in marine limestone. *Geology* **48**, 363–367.

Clarkson M. O., Müsing K., Andersen M. B. and Vance D. (2020) Examining pelagic carbonate-rich sediments as an archive for authigenic uranium and molybdenum isotopes using reductive cleaning and leaching experiments. *Chem. Geol.* **539**, 119412.

Clarkson M. O., Stirling C. H., Jenkyns H. C., Dickson A. J., Porcelli D., Moy C. M., von Strandmann P. A. E. P., Cooke I. R. and Lenton T. M. (2018) Uranium isotope evidence for two episodes of deoxygenation during Oceanic Anoxic Event 2. *Proc. Natl. Acad. Sci.* **115**, 2918–2923.

Cochran J. K. (1992) The oceanic chemistry of the uranium-and thorium-series nuclides. In *Uranium-series disequilibrium: applications to earth, marine, and environmental sciences. 2. ed*

Coffey, J. M., Flannery, D. T., Walter, M. R., & George, S. C. (2013). Sedimentology, stratigraphy and geochemistry of a stromatolite biofacies in the 2.72 Ga Tumbiana Formation, Fortescue Group, Western Australia. *Precambrian Research*, *236*, 282-296.

Cole D. B., Planavsky N. J., Longley M., Böning P., Wilkes D., Wang X., Swanner E. D., Wittkop C., Loydell D. and Busigny V. (2020) Uranium isotope fractionation in non-sulfidic anoxic settings and the global uranium isotope mass balance. *Global Biogeochem. Cycles*, e2020GB006649.

Corfu F. and Andrews A.J. (1987) Geochronological constraints on the timing of magmatism, deformation, and gold mineralization in the Red Lake greenstone belt, northwestern Ontario. *Can. J. Earth Sci*. 24, 1302-1320.

Dahl T. W., Boyle R. A., Canfield D. E., Connelly J. N., Gill B. C., Lenton T. M. and Bizzarro M. (2014) Uranium isotopes distinguish two geochemically distinct stages during the later Cambrian SPICE event. *Earth Planet. Sci. Lett.* **401**, 313–326.

Dahl T. W., Connelly J. N., Kouchinsky A., Gill B. C., Månsson S. F. and Bizzarro M. (2017) Reorganisation of Earth's biogeochemical cycles briefly oxygenated the oceans 520 Myr ago.

Dahl T. W., Connelly J. N., Li D., Kouchinsky A., Gill B. C., Porter S., Maloof A. C. and Bizzarro M. (2019) Atmosphere–ocean oxygen and productivity dynamics during early animal radiations. *Proc. Natl. Acad. Sci.* **116**, 19352–19361.

Dardenne M.A. and Campos Neto M.C. (1975) Estromatolitos colunares na Serie Minas (MG). *Revista Brasileira de Geociencias*, v. 5, n. 2, p. 99 –105.

Davis W.J., Aspler L.B., Rainbird R.H. & Chiarenzelli J.R. (2000) Detrital zircon geochronology of the Proterozoic Hurwitz and Kiyuk groups: a revised post-1.92 Ga age for deposition of the upper Hurwitz Group. *GeoCanada 2000 Conference CD*. Iron Leaf Communications, Calgary.

DeCarlo T. M., Gaetani G. A., Holcomb M. and Cohen A. L. (2015) Experimental determination of factors controlling U/Ca of aragonite precipitated from seawater: Implications for interpreting coral skeleton. *Geochim. Cosmochim. Acta* **162**, 151–165.

De Kock, M. O., Beukes, N. J., & Armstrong, R. A. (2012). New SHRIMP U–Pb zircon ages from the Hartswater Group, South Africa: Implications for correlations of the Neoarchean Ventersdorp Supergroup on the Kaapvaal craton and with the Fortescue Group on the Pilbara craton. *Precambrian Research*, *204*, 66-74.

DePaolo D. J., Maher K. and Christensen J. N. (2003) Measuring the timescales of sediment production, transport, and deposition-U-234 sediment comminution ages. *AGUFM* **2003**, V11H-07.

Dong W. and Brooks S. C. (2006) Determination of the formation constants of ternary complexes of uranyl and carbonate with alkaline earth metals (Mg2+, Ca2+, Sr2+, and Ba2+) using anion exchange method. *Environ. Sci. Technol.* **40**, 4689–4695.

Dorland H.C. (2004) Provenance ages and timing of sedimentation of selected Neoarchean and Paleoproterozoic successions on the Kaapvaal Craton. Ph.D. Thesis, Rand Afrikaans University, Johannesburg, South Africa, 326 pp.

Dorr J.V.N.d. (1969) Physiographic, stratigraphic and structural development of the Quadrilatero Ferrıfero, Minais Gerais, Brazil. *United States Geological Survey Professional Paper* 641-A, 110 p.

Dunk R. M., Mills R. A. and Jenkins W. J. (2002) A reevaluation of the oceanic uranium budget for the Holocene. *Chem. Geol.* **190**, 45–67.

Eade K.E. & Chandler F.W. (1975) Geology of Watterson Lake (west half) map-area, District of Keewatin. *Paper 74-64*, 10 pp. Geological Survey of Canada, Ottawa.

Einsele G. (1992) *Sedimentary basins: evolution, facies, and sedimentary budget*., Springer-Verlag.

Elrick M., Polyak V., Algeo T. J., Romaniello S., Asmerom Y., Herrmann A. D., Anbar A. D., Zhao L. and Chen Z.-Q. (2017) Global-ocean redox variation during the middle-late Permian through Early Triassic based on uranium isotope and Th/U trends of marine carbonates. *Geology* **45**, 163–166.

Enderton D. and Marshall J. (2009) Explorations of atmosphere–ocean–ice climates on an aquaplanet and their meridional energy transports. *J. Atmos. Sci.* **66**, 1593–1611.

Endrizzi F. and Rao L. (2014) Chemical Speciation of U (VI) in Marine Environments: Complexation of Ca2+ and Mg2+ with (UO2)(CO3) 3 4-and the Effect on the Extraction of Uranium from Seawater.

Evans, K. V., Aleinikoff, J. N., Obradovich, J. D., & Fanning, C. M. (2000). SHRIMP U-Pb geochronology of volcanic rocks, Belt Supergroup, western Montana: evidence for rapid deposition of sedimentary strata. *Canadian Journal of Earth Sciences*, *37*(9), 1287-1300.

Fairchild I.J. and Hambrey M.J. (1984) The Vendian succession of northeastern Spitsbergen: petrogenesis of a dolomite-tillite association. *Precambrian Res*., 26, 111-167.

Fairchild I.J. and Hambrey M.J. (1995) Vendian basin evolution in East Greenland and NE Svalbard. *Precambrian Res*. 73, 217-233.

Farquhar J., Zerkle A. L. and Bekker A. (2014) Geologic and geochemical constraints on Earth's early atmosphere.

Farquhar J., Zerkle A. L. and Bekker A. (2011) Geological constraints on the origin of oxygenic photosynthesis. *Photosynth. Res.* **107**, 11–36.

Feulner G. (2012) The faint young Sun problem. *Rev. Geophys.* **50**.

Fralick, P., Riding, R., 2015. Steep Rock Lake: Sedimentology and geochemistry of an Archean carbonate platform. Earth-Science Reviews, 151: 132-175.

Frith, R. A., and Loveridge, W. D. (1982). Ages of Yellowknife Supergroup volcanic rocks, granitoid rocks and regional metamorphism in the northeastern Slave province. *Geological Survey of Canada Current Research, Part A*, 225-237.

Frith, R. A. (1987). *Precambrian geology of the Hackett River area, District of Mackenzie, NWT* (Vol. 417). Geological Survey of Canada, Energy, Mines and Resources Canada.

Garcia A.J.V., Fonseca M.A., Bernardi A.V. and Januzzi A. (1988) Contribuicao ao reconhecimento dos paleoambientes deposicionais do grupo Piracicaba na regiao de Dom Bosco - SW de Ouro Preto, Quadrilatero Ferrıfero-MG. *Acta Geologica Leopoldensia*, v. 11, n. 27, p. 83–108.

Garrett C. and Kunze E. (2007) Internal tide generation in the deep ocean. *Annu. Rev. Fluid Mech.* **39**, 57–87.

Gilleaudeau G. J., Romaniello S. J., Luo G., Kaufman A. J., Zhang F., Klaebe R. M., Kah L. C., Azmy K., Bartley J. K. and Zheng W. (2019) Uranium isotope evidence for limited euxinia in mid-Proterozoic oceans. *Earth Planet. Sci. Lett.* **521**, 150–157.

Gothmann A. M., Higgins J. A., Adkins J. F., Broecker W., Farley K. A., McKeon R., Stolarski J., Planavsky N., Wang X. and Bender M. L. (2019) A Cenozoic record of seawater uranium in fossil corals. *Geochim. Cosmochim. Acta* **250**, 173–190.

Grey K. (1979) Preliminary results of biostratigraphic studies of Proterozoic stromatolites in Western Australia. *Geol. Surv. West Australia Rec.* 1979(2), 1-26.

Grotzinger J.P. (1986a) Evolution of Early Proterozoic passive margin carbonate platform, Rocknest Formation, Wopmay Orogen, Northwest Territories. *Canada. J. Sediment. Petrol*. 56, 831- 847.

Grotzinger J.P. (1986b) Cyclicity and paleoenvironmental dynamics, Rocknest platform, northwest Canada. *GSA Bull*. 97, 1208-1231.

Grotzinger J.P. (1989a) Construction of Early Proterozoic (1.9 Ga) barrier reef complex, Rocknest platform, Northwest Territories. *Canada Soc. Petrol. Geol. Memoir* 13, 30-37.

Grotzinger J.P. (1989b) Facies and evolution of Precambrian carbonate depositional systems: Emergence of the modem platform archetype. *SEPM Spec. Publ*. 44, 89-106.

Gumsley A. P., Chamberlain K. R., Bleeker W., Söderlund U., de Kock M. O., Larsson E. R. and Bekker A. (2017) Timing and tempo of the Great Oxidation Event. *Proc. Natl. Acad. Sci.* **114**, 1811–1816.

Halevy I. and Bachan A. (2017) The geologic history of seawater pH. *Science (80-.).* **355**, 1069–1071.

Haller J. (1971) *Geology of the East Greenland Caledonides*. Interscience Publishers (New York). 413 pp.

Halverson G.P., Kunzmann M., Strauss J.V., Maloof A.C., 2018a. The Tonian-Cryogenian transition in Svalbard. *Precambrian Res*. 319, 79–95.

Halverson G.P., Porter S.M., Gibson T.M., 2018b. Dating the late Proterozoic stratigraphic record. *Emerging Topics in Life Science* 2 (137-147).

Hardie L. A. (1996) Secular variation in seawater chemistry: An explanation for the coupled secular variation in the mineralogies of marine limestones and potash evaporites over the past 600 my. *Geology* **24**, 279–283.

Hardie L. A. (2003) Secular variations in Precambrian seawater chemistry and the timing of Precambrian aragonite seas and calcite seas. *Geology* **31**, 785–788.

Hardisty D. S., Lu Z., Bekker A., Diamond C. W., Gill B. C., Jiang G., Kah L. C., Knoll A. H., Loyd S. J. and Osburn M. R. (2017) Perspectives on Proterozoic surface ocean redox from iodine contents in ancient and recent carbonate. *Earth Planet. Sci. Lett.* **463**, 159–170.

Hardisty D. S., Lu Z., Planavsky N. J., Bekker A., Philippot P., Zhou X. and Lyons T. W. (2014) An iodine record of Paleoproterozoic surface ocean oxygenation. *Geology* **42**, 619–622.

Hartzer, F. J. (1995). Transvaal Supergroup inliers: geology, tectonic development and relationship with the Bushveld Complex, South Africa. *Journal of African Earth Sciences*, *21*(4), 521-547.

Hartzer, F. J. (2000). Geology of Transvaal inliers in the Bushveld Complex. *Memoir- geological survey(Pretoria)*.

Heinrichs T.K. and Reimer T.O. (1977) A sedimentary barite deposit from the Archean Fig Tree Group of the Barberton Mountain Land (South Africa). *Econ. Geol*. 72, 1426-1441.

Henderson G. M., Slowey N. C. and Fleisher M. Q. (2001) U-Th dating of carbonate platform and slope sediments. *Geochim. Cosmochim. Acta* **65**, 2757–2770.

Henderson G. M., Slowey N. C. and Haddad G. A. (1999) Fluid flow through carbonate platforms: Constraints from 234U/238U and Cl− in Bahamas pore-waters. *Earth Planet. Sci. Lett.* **169**, 99–111.

Henderson J.B. (1981) Archean basin evolution in the Slave Province, Canada. In *Precambrian Plate Tectonics* (ed. A. KRONER), pp. 213-235.Elsevier.

Henderson, J. B. (1998). *Geology of the Keskarrah Bay Area, District of Mackenzie, Northwest Territories* (Vol. 527). Geological Survey of Canada.

Herrington P.M. and Fairchild I.J. (1989) Carbonate shelf and slope facies evolution prior to Vendian glaciation, central East Greenland. In: The Caledonide Geology of Scandinavia (Ed. by R.A. Gayer), pp. 285-297. Graham Trotman, London.

Herrmann A. D., Gordon G. W. and Anbar A. D. (2018) Uranium isotope variations in a dolomitized Jurassic carbonate platform (Tithonian; Franconian Alb, Southern Germany). *Chem. Geol.* **497**, 41–53.

Hickman A. (1983) Geology of the Pilbana Block and its environs. *Geol. Surv. West. Australia Bull*. 127, 1-268.

Hofmann H.J., Pearson D.A.B. and Wilson B.H. (1980) Stromatolites and fenestral fabric in Early Proterozoic Huronian Supergroup, Ontario. *Canadian .J. Earth Sci*. 17, 1351-1357.

Hofmann H.J. (1981) Precambrian fossils in Canada-the 1970 in retrospect. *Geol. Surv. Can. Spec. Paper* 81-10, pp. 419-443.

Hofmann, H. J., & Davidson, A. (1998). Paleoproterozoic stromatolites, Hurwitz Group, Quartzite Lake area, Northwest Territories, Canada. *Canadian Journal of Earth Sciences*, *35*(3), 280-289.

Hoffmann K.-H., Prave A. (1996) A preliminary note on a revised subdivision and regional correlation of the Otavi Group based on glaciogenic diamictites and associated cap dolostones, Communications of the Geological Survey of Namibia 11, 81–86.

Hoffmann K.-H., Condon D., Bowring S., Crowley J. (2004) A U–Pb zircon date from the Neoproterozoic Ghaub Formation, Namibia: constraints on Marinoan glaciation, *Geology* 32, 817–820.

Hofmann M.J., Thurston P.C. and Wallace H. (1985) Archean stromatolites from Uchi greenstone belt, northwestern Ontario. *Geol. Assoc. Can. Spec. Paper* 28, pp. 125-132.

Hoffman P. (1968) Stratigraphy of the Lower Proterozoic (Aphebian), Great Slave Supergroup, East Arm of Great Slave Lake, District of Mackenzie. Department of Energy, Mines and Resources.

Hoffman P., Fraser J., McGlynn J. (1970) The Coronation geosyncline of Aphebian age, district of Mackenzie, Symposium on Basins and Geosynclines of the Canadian Shield: *Geological Survey of Canada, Paper*, pp. 70-40.

Hoffman P. (1974) Shallow and Deepwater Stromatolites in Lower Proterozoic Platform--to--Basin Facies Change, Great Slave Lake, Canada. AAPG Bulletin 58, 856-867.

Hofmann P.F. and Bowring S.A. (1984) Short-lived 1.9Ga continental margin and its destruction, Wopmay Orogen, northwest Canada. *Geology* 12,68-72.

Hoffman, P. F., Halverson, G. P., Domack, E. W., Husson, J. M., Higgins, J. A., & Schrag, D. P. (2007). Are basal Ediacaran (635 Ma) post-glacial "cap dolostones" diachronous?. *Earth and Planetary Science Letters*, *258*(1-2), 114-131.

Hoffman P.F., Halverson G. P. (2008) The Otavi Group of the Northern Platform and the Northern Margin Zone. In: Miller, R. M. (Ed.), T*he Geology of Namibia. Vol. 2*. Geological Survey of Namibia, Windhoek.

Hoffman P., Kaufman A., Halverson G., Schrag D. (1998a) A Neoproterozoic snowball Earth, Science 281, 1342–1346.

Hoffman P., Kaufman A., Halverson G. (1998b) Comings and goings of global glaciations on a Neoproterozoic tropical platform in Namibia, GSA Today 8, 1–9.

Hoffman P., Halverson G.P., Domack E.W., Maloof A.C., Swanson-Hysell N.L., Cox G.M. (2012) Cryogenian glaciations on the southern tropical paleomargin of Laurentia (Ne Svalbard and East Greenland), and a primary origin for the Russøya (Islay) carbon isotope anomaly. Precambrian. Res. 206–207, p. 137–158.

Holland H. D. (2006) The oxygenation of the atmosphere and oceans. *Philos. Trans. R. Soc. B Biol. Sci.* **361**, 903–915.

Holland H. D. (2002) Volcanic gases, black smokers, and the Great Oxidation Event. *Geochim. Cosmochim. Acta* **66**, 3811–3826.

Holland H. D. and Zimmermann H. (2000) The dolomite problem Revisited1. *Int. Geol. Rev.* **42**, 481–490.

Holmden C., Amini M. and Francois R. (2015) Uranium isotope fractionation in Saanich Inlet: A modern analog study of a paleoredox tracer. *Geochim. Cosmochim. Acta* **153**, 202–215.

Hood A. vS, Planavsky N. J., Wallace M. W., Wang X., Bellefroid E. J., Gueguen B. and Cole D. B. (2016) Integrated geochemical-petrographic insights from component-selective δ238U of Cryogenian marine carbonates. *Geology* **44**, 935–938.

Hurtgen M.T., Halverson G.P., Arthur M.A., Hoffman P.F. (2006) Sulfur cycling in the aftermath of a Neoproterozoic (Marinoan) snowball glaciation: Evidence for a syn-glacial sulfidic deep ocean. *Earth Planet. Sci. Letts*. 245, 551–570.

Jackson M.J. (1989) Lower Proterozoic Cowles Lake foredeep reef, N.W.T., Canada. *Canadian Soc. Petrol. Geol. Memoir* 13, 64-71.

Jackson S.L. (1994) Geology of the Aberdeen Area. Open File Report 5903, *Ontario Geological Survey*, 69 pp.

Jackson V. (2008) Preliminary geologic map of part of the southern Wopmay Orogen (parts of NTS 86B and 86C; 2007 updates); descriptive notes to accompany 1: 100,000 scale map. NWT Geosci Office, NWT Open Rep 7.

Jackson V., van Breemen O., Ootes L., Bleeker W., Bennett V., Davis W., Ketchum J., Smar L., McFarlane C. (2013) U–Pb zircon ages and field relationships of Archean basement and Proterozoic intrusions, south-central Wopmay Orogen, NWT: implications for tectonic assignments 1, 2. *Canadian Journal of Earth Sciences* 50, 979-1006.

Jacobsen J.B.E. (1962) The Geology of the Lomagundi District. M.Sc. thesis (unpubl.), University of the Witwatersrand, Johannesburg.

Jansen M. F. (2017) Glacial ocean circulation and stratification explained by reduced atmospheric temperature. *Proc. Natl. Acad. Sci.* **114**, 45–50.

Jelsma, H. A., and Dirks, P. H. (2002). Neoarchaean tectonic evolution of the Zimbabwe Craton. *Geological Society, London, Special Publications*, *199*(1), 183-211.

Jenkins G. S., Marshall H. G. and Kuhn W. R. (1993) Precambrian climate: The effects of land area and Earth's rotation rate. *J. Geophys. Res. Atmos.* **98**, 8785–8791.

Johnston D. T., Poulton S. W., Goldberg T., Sergeev V. N., Podkovyrov V., Vorob'Eva N. G., Bekker A. and Knoll A. H. (2012) Late Ediacaran redox stability and metazoan evolution. *Earth Planet. Sci. Lett.* **335**, 25–35.

Jost A. B., Bachan A., van de Schootbrugge B., Lau K. V, Weaver K. L., Maher K. and Payne J. L. (2017) Uranium isotope evidence for an expansion of marine anoxia during the end-Triassic extinction. *Geochemistry, Geophys. Geosystems* **18**, 3093–3108.

Karlstrom K.E., Houston, R.S. (1984) The Cheyenne belt: analysis of a Proterozoic suture in southern Wyoming. *Precambrian Res*. 25, 415-446.

Katz H.R. (1961) Late Precambrian to Cambrian stratigraphy in East Greenland. In: Raasch, G.O. (Ed.), Geology of the Arctic 1. Toronto University Press, Toronto, pp. 299–328.

Kendall B., Brennecka G. A., Weyer S. and Anbar A. D. (2013) Uranium isotope fractionation suggests oxidative uranium mobilization at 2.50 Ga. *Chem. Geol.* **362**, 105–114.

Kendall B., Komiya T., Lyons T. W., Bates S. M., Gordon G. W., Romaniello S. J., Jiang G., Creaser R. A., Xiao S. and McFadden K. (2015) Uranium and molybdenum isotope evidence for an episode of widespread ocean oxygenation during the late Ediacaran Period. *Geochim. Cosmochim. Acta* **156**, 173–193.

Kendall B., Wang J., Zheng W., Romaniello S. J., Over D. J., Bennett Y., Xing L., Kunert A., Boyes C. and Liu J. (2020) Inverse correlation between the molybdenum and uranium isotope compositions of Upper Devonian black shales caused by changes in local depositional conditions rather than global ocean redox variations. *Geochim. Cosmochim. Acta*.

Keul N., Langer G., de Nooijer L. J., Nehrke G., Reichart G. and Bijma J. (2013) Incorporation of uranium in benthic foraminiferal calcite reflects seawater carbonate ion concentration. *Geochemistry, Geophys. Geosystems* **14**, 102–111.

Khatiwala S., Primeau F. and Holzer M. (2012) Ventilation of the deep ocean constrained with tracer observations and implications for radiocarbon estimates of ideal mean age. *Earth Planet. Sci. Lett.* **325**, 116–125.

Kjarsgaard B.A., Pearson D.G., DuFrane A. and Heaman L. (2013) Proterozoic geology of the East Arm Basin with emphasis on Paleoproterozoic magmatic rocks, Thaidene Nene MERA study area. Chapter 3 in Mineral and Energy Resource Assessment for the Proposed Thaidene Nene National Park Reserve in the Area of the East Arm of Great Slave Lake, Northwest Territories, (eds.) D.F. Wright, E.J. Ambrose, D. Lemkow, and G.F. Bonham-Carte; Geological Survey of Canada Open File 7196, 77-117.

Klinkhammer G. P. and Palmer M. R. (1991) Uranium in the oceans: where it goes and why. *Geochim. Cosmochim. Acta* **55**, 1799–1806.

Korenaga J., Planavsky N. J. and Evans D. A. D. (2017) Global water cycle and the coevolution of the Earth's interior and surface environment. *Philos. Trans. R. Soc. A Math. Phys. Eng. Sci.* **375**, 20150393.

Kouassi F. (1979) Etude stratigraphique et analyse de la dispersion des elements traces dans le membre inferieur de la Formation d'Albane1, du groupe de Mistassini, region du Lac Mistassini, Quebec, Canada, M.Sc. thesis, Universite du Quebec-Chicoutimi.

Kriewaldt M.J.B. and Ryan G.R. (1967) Pyramid, W.A. *West. Australia Geol. Surv. 1:250,000 Geol. Ser. Expl. Notes.*

Krogh T.E., Davis D.W., Corfu F. (1984) Precise U-Pb zircon and badelleyite ages for the Sudbury area. In: Pye, E.G., Naldrett, A.J., Giblin, P.E. (Eds.), The Geology and Ore Deposits of the Sudbury Structure. *Ontario Geol. Surv. Spec*. 1, pp. 431– 446.

Krogh T.E., Kamo S.L., Bohor B.F. (1996) Shock metamorphosed zircons with correlated U–Pb discordance and melt rocks with concordant protolith ages indicate an impact origin for the Sudbury structure. Earth Processes: Reading the isotopic code. *Geophys. Monograph 95. Am. Geophys. Union*, pp. 343–353.

Kröner, A., Byerly, G.R., Lowe, D.R., 1991. Chronology of Early Archean Granite-Greenstone Evolution in the Barberton Mountain Land, South-Africa, Based on Precise Dating by Single Zircon Evaporation. Earth and Planetary Science Letters, 103(1-4): 41-54.

Ku T.-L., Knauss K. G. and Mathieu G. G. (1977) Uranium in open ocean: concentration and isotopic composition. *Deep Sea Res.* **24**, 1005–1017.

Kuznetsov A. B., Bekker A., Ovchinnikova G. V, Gorokhov I. M. and Vasilyeva I. M. (2017) Unradiogenic strontium and moderate-amplitude carbon isotope variations in early Tonian seawater after the assembly of Rodinia and before the Bitter Springs Excursion. *Precambrian Res.* **298**, 157–173.

Langmuir D. (1978) Uranium solution-mineral equilibria at low temperatures with applications to sedimentary ore deposits. *Geochim. Cosmochim. Acta* **42**, 547–569.

Lau K. V, Macdonald F. A., Maher K. and Payne J. L. (2017) Uranium isotope evidence for temporary ocean oxygenation in the aftermath of the Sturtian Snowball Earth. *Earth Planet. Sci. Lett.* **458**, 282–292.

Lau K. V, Maher K., Altiner D., Kelley B. M., Kump L. R., Lehrmann D. J., Silva-Tamayo J. C., Weaver K. L., Yu M. and Payne J. L. (2016) Marine anoxia and delayed Earth system recovery after the end-Permian extinction. *Proc. Natl. Acad. Sci.* **113**, 2360–2365.

Li Z., Cao M., Loyd S. J., Algeo T. J., Zhao H., Wang X., Zhao L. and Chen Z.-Q. (2020) Transient and stepwise ocean oxygenation during the late Ediacaran Shuram Excursion: Insights from carbonate δ238U of northwestern Mexico. *Precambrian Res.*, 105741.

Livermore B. D., Dahl T. W., Bizzarro M. and Connelly J. N. (2020) Uranium isotope compositions of biogenic carbonates–Implications for U uptake in shells and the application of the paleo-ocean oxygenation proxy. *Geochim. Cosmochim. Acta* **287**, 50–64.

Logan B.W., Rezak R. and Ginsburg R.N. (1964) Classification and environmental significance of algal stromatolites. *Journal of Geology* 72, p. 68 – 83.

Long D.G.F., Devaney J.R., Pratt B.R. (1999) Tectonostratigraphic framework of the Mesoproterozoic Muskwa assemblage, northern British Columbia. In: Cook, F., Erdmer, P. (Eds.), *Lithoprobe Rept,* vol. 69, pp. 112–119.

Lord C.S. (1963) Snare River and Ingray Lake map-areas, Northwest Territories. R. Duhamel, Queen's Printer and Controller of Stationery.

Lowe D. R. (1994) Early environments: constraints and opportunities for early evolution. *Early life Earth*, 25–35.

Lowe D. R. (1980) Archean sedimentation. *Ann. Rev. Earth Planet. Sci*. 8, 145-167.

Lowe D. R. (1982) Comparative sedimentology of the principal volcanic sequences of Archean greenstone belts in South Africa, Western Australia and Canada. Implications for crustal evolution. *Precambrian Res.* 17, l-29.

Lowe D. R. and Knauth L.P. (1977) Sedimentology of the Onverwacht Group (3.4 billion years), Transvaal, South Africa, and its bearing on the characteristics and evolution of the early Earth. *J. Geol*. 85, 699-723.

Lu X., Kendall B., Stein H. J., Li C., Hannah J. L., Gordon G. W. and Ebbestad J. O. R. (2017) Marine redox conditions during deposition of Late Ordovician and Early Silurian organic-rich mudrocks in the Siljan ring district, central Sweden. *Chem. Geol.* **457**, 75–94.

Lyons T. W., Reinhard C. T. and Planavsky N. J. (2014) The rise of oxygen in Earth's early ocean and atmosphere. *Nature* **506**, 307–315.

Macdonald, F. A., Smith, E. F., Strauss, J. V., Cox, G. M., Halverson, G. P., Roots, C. F., ... & Relf, C. (2010). Neoproterozoic and early Paleozoic correlations in the western Ogilvie Mountains, Yukon. *Yukon Exploration and Geology*, 161-182.

MacLennan, S., Park, Y., Swanson-Hysell, N., Maloof, A., Schoene, B., Gebreslassie, M., ... & Haileab, B. (2018). The arc of the Snowball: U-Pb dates constrain the Islay anomaly and the initiation of the Sturtian glaciation. *Geology*, *46*(6), 539-542.

Maher K., Steefel C. I., DePaolo D. J. and Viani B. E. (2006) The mineral dissolution rate conundrum: Insights from reactive transport modeling of U isotopes and pore fluid chemistry in marine sediments. *Geochim. Cosmochim. Acta* **70**, 337–363.

Maloubier M., Solari P. L., Moisy P., Monfort M., Den Auwer C. and Moulin C. (2015) XAS and TRLIF spectroscopy of uranium and neptunium in seawater. *Dalt. Trans.* **44**, 5417–5427.

Mänd K., Lalonde S. V, Robbins L. J., Thoby M., Paiste K., Kreitsmann T., Paiste P., Reinhard C. T., Romashkin A. E. and Planavsky N. J. (2020) Palaeoproterozoic oxygenated oceans following the Lomagundi–Jatuli Event. *Nat. Geosci.* **13**, 302–306.

Mashayek A., Salehipour H., Bouffard D., Caulfield C. P., Ferrari R., Nikurashin M., Peltier W. R. and Smyth W. D. (2017) Efficiency of turbulent mixing in the abyssal ocean circulation. *Geophys. Res. Lett.* **44**, 6296–6306.

Master, S., Bekker, A., & Hofmann, A. (2010). A review of the stratigraphy and geological setting of the Palaeoproterozoic Magondi Supergroup, Zimbabwe–Type locality for the Lomagundi carbon isotope excursion. *Precambrian Research*, *182*(4), 254-273.

McGlynn J., Glass D.J., Fraser J.A. (1972) Archean and Proterozoic Geology of the Yellowknife and Great Bear Areas, Northwest Territories: Excursion A27. 24th International Geological Congress.

Meece D. E. and Benninger L. K. (1993) The coprecipitation of Pu and other radionuclides with CaCO3. *Geochim. Cosmochim. Acta* **57**, 1447–1458.

Middelburg J. J., Soetaert K. and Herman P. M. J. (1997) Empirical relationships for use in global diagenetic models. *Deep Sea Res. Part I Oceanogr. Res. Pap.* **44**, 327–344.

Mirota, M. D., & Veizer, J. (1994). Geochemistry of precambrian carbonates: VI. Aphebian albanel formations, Quebec, Canada. *Geochimica et cosmochimica acta*, *58*(7), 1735-1745.

Montoya-Pino C., Weyer S., Anbar A. D., Pross J., Oschmann W., van de Schootbrugge B. and Arz H. W. (2010) Global enhancement of ocean anoxia during Oceanic Anoxic Event 2: A quantitative approach using U isotopes. *Geology* **38**, 315–318.

Moore S.L. (1969) Geology and ore deposits of the Antonio dos Santos, Gongo Soco and Conceicao do Rio Acima Quadrangles, Minas Gerais, Brazil. *United States Geological Survey Professional Paper* 341-I, 50 p.

Morford J. L. and Emerson S. (1999) The geochemistry of redox sensitive trace metals in sediments. *Geochim. Cosmochim. Acta* **63**, 1735–1750.

Mortensen, J. K., Thorpe, R. I., Padgham, W. A., King, J., & Davis, W. J. (1988). U–Pb zircon ages for felsic volcanism in the Slave Province, NWT. *Radiogenic age and isotopic studies: Report*, *2*, 88-2.

Nikurashin M. and Vallis G. (2012) A theory of the interhemispheric meridional overturning circulation and associated stratification. *J. Phys. Oceanogr.* **42**, 1652–1667.

Noordmann J., Weyer S., Montoya-Pino C., Dellwig O., Neubert N., Eckert S., Paetzel M. and Böttcher M. E. (2015) Uranium and molybdenum isotope systematics in modern euxinic basins: Case studies from the central Baltic Sea and the Kyllaren fjord (Norway). *Chem. Geol.* **396**, 182–195.

Northrup, C. J., Isachsen, C., & Bowring, S. A. (1999). Field relations, U-Pb geochronology, and Sm-Nd isotope geochemistry of the Point Lake greenstone belt and adjacent gneisses, central Slave craton, NWT, Canada. *Canadian Journal of Earth Sciences*, *36*(7), 1043-1059.

Nunes P.D. and Thurston P.C. (1980) Two hundred and twenty million years of Archean evolution: A zircon U-Pb age stratigraphic study of the Uchi-Confederation Lakes greenstone belt, north- western Ontario. *Can. J. Earth Sci*. 17. 710-721.

O'Gorman P. A. and Schneider T. (2008) Energy of midlatitude transient eddies in idealized simulations of changed climates. *J. Clim.* **21**, 5797–5806.

Olson S. L., Jansen M. and Abbot D. S. (2020) Oceanographic Considerations for Exoplanet Life Detection. *Astrophys. J.* **895**, 19.

Ovchinnikova G.V., Semikhatov M.A., Gorokhov I.M., Belyatskii B.V., Vasilieva I.M., Levskii L.K. (1995) U–Pb systematics of Pre-Cambrian carbonates: the Riphean Sukhaya Tunguska Formation in the Turukhansk Uplift, Siberia. *Lithology Min. Resour*. 30, 525–536.

PARIS I., STANISTREET I.G. and HUGHES M.J. (1985) Cherts of the Barberton greenstone belt interpreted as products of submarine exhalative activity. J. Geol. 93, 111-129.

Parkhurst D. L. and Appelo C. A. J. (2013) *Description of input and examples for PHREEQC version 3: a computer program for speciation, batch-reaction, one-dimensional transport, and inverse geochemical calculations*., US Geological Survey.

Partin C. A., Bekker A., Planavsky N. J., Scott C. T., Gill B. C., Li C., Podkovyrov V., Maslov A., Konhauser K. O. and Lalonde S. V (2013a) Large-scale fluctuations in Precambrian atmospheric and oceanic oxygen levels from the record of U in shales. *Earth Planet. Sci. Lett.* **369**, 284–293.

Partin C. A., Lalonde S. V, Planavsky N. J., Bekker A., Rouxel O. J., Lyons T. W. and Konhauser K. O. (2013b) Uranium in iron formations and the rise of atmospheric oxygen. *Chem. Geol.* **362**, 82–90.

Patterson J.G. (1986) The Amer Belt; remnant of an Aphebian foreland fold and thrust belt. *Canadian Journal of Earth Sciences* 23 (12), 2012–2023.

Peterson L. C., Haug G. H., Murray R. W., Yarincik K. M., King J. W., Bralower T. J., Kameo K., Rutherford S. D. and Pearce R. B. (2000) Late Quaternary stratigraphy and sedimentation

at site 1002, Cariaco Basin (Venezuela). In *Proceedings of the Ocean Drilling Program, Scientific Results* Ocean Drilling Program College Station, Texas, USA. pp. 85–99.

Petrov P.Y., Semikhatov M.A., Sergeev V.N. (1995) Development of the Riphean carbonate platform and distribution of silicified microfossils: the Sukhaya Tunguska Formation, Turukhansk Uplift, Siberia. *Stratigr. Geol. Correl*. 3, 602–620.

Petrov P.Y., Semikhatov M.A. (1997) Structure and environ- mental conditions of a transgressive Upper Riphean com- plex: Miroedikha Formation of the Turukhansk Uplift, Siberia. *Lithology Min. Resour*. 32, 11–29.

Petrov P.Y., Semikhatov M.A. (1998) The upper Riphean stromatolitic reefal complex; Burovaya Formation of the Turukhansk region, Siberia. *Lithology Min. Resour*. 33, 539 – 560.

Phan T. T., Gardiner J. B., Capo R. C. and Stewart B. W. (2018) Geochemical and multi-isotopic (87Sr/86Sr, 143Nd/144Nd, 238U/235U) perspectives of sediment sources, depositional conditions, and diagenesis of the Marcellus Shale, Appalachian Basin, USA. *Geochim. Cosmochim. Acta* **222**, 187–211.

Planavsky N. J., McGoldrick P., Scott C. T., Li C., Reinhard C. T., Kelly A. E., Chu X., Bekker A., Love G. D. and Lyons T. W. (2011) Widespread iron-rich conditions in the mid-Proterozoic ocean. *Nature* **477**, 448–451.

Pope E. C., Bird D. K. and Rosing M. T. (2012) Isotope composition and volume of Earth's early oceans. *Proc. Natl. Acad. Sci.* **109**, 4371–4376.

Poulton S. W. and Canfield D. E. (2011) Ferruginous conditions: a dominant feature of the ocean through Earth's history. *Elements* **7**, 107–112.

PRATT, B. R. (2017). SEDIMENTATION AND DEFORMATION OF THE GEORGE FORMATION, A PALEOPROTEROZOIC CARBONATE PLATFORM IN THE MUSKWA ASSEMBLAGE OF NORTHEASTERN BRITISH COLUMBIA. In *Geological Society of America Abstracts with Programs* (Vol. 49, No. 5).

Prave A.R., Condon D. J., Hoffmann K.-H., Tapster S., Fallick A.E. (2016) Duration and nature of the end-Cryogenian (Marinoan) glaciation. *Geology* 44, 631–634.

Rainbird, R. H., Davis, W. J., Pehrsson, S. J., Wodicka, N., Rayner, N., & Skulski, T. (2010). Early Paleoproterozoic supracrustal assemblages of the Rae domain, Nunavut, Canada: Intracratonic basin development during supercontinent break-up and assembly. *Precambrian Research*, *181*(1-4), 167-186.

Ramdohr P. (1958) New observations of the ores of the Witwatersrand in South Africa and their genetic significance. *Geol. Soc. South Africa Trans.* **61**, 1–50.

Rasmussen B. and Buick R. (1999) Redox state of the Archean atmosphere: evidence from detrital heavy minerals in ca. 3250–2750 Ma sandstones from the Pilbara Craton, Australia. *Geology* **27**, 115–118.

Rasmussen B., Fletcher I.R., Muhling J.R., Mueller A.G., Hall G.C. (2007) Bushveld-aged fluid flow, peak metamorphism, and gold mobilization in the Witwatersrand basin, South Africa: constraints from in situ SHRIMP U–Pb dating of monazite and xenotime. *Geology* 35, 931–934.

Rasmussen, B., Bekker, A., & Fletcher, I. R. (2013). Correlation of Paleoproterozoic glaciations based on U–Pb zircon ages for tuff beds in the Transvaal and Huronian Supergroups. *Earth and Planetary Science Letters*, *382*, 173-180.

Redden J.A. (1981) Summary of the geology of the Nemo area. In: Rich F.J. (Ed.), Geology of the Black Hills, South Dakota and Wyoming. *Geol. Soc. Am. Guidebook. Rocky Mountain Section, Annual Meeting*, Rapid City, SD, 1981, pp. 193-210.

Reinhard C. T., Planavsky N. J., Robbins L. J., Partin C. A., Gill B. C., Lalonde S. V, Bekker A., Konhauser K. O. and Lyons T. W. (2013) Proterozoic ocean redox and biogeochemical stasis. *Proc. Natl. Acad. Sci.* **110**, 5357–5362.

del Rey Á., Havsteen J. C., Bizzarro M. and Dahl T. W. (2020) Untangling the diagenetic history of uranium isotopes in marine carbonates: a case study tracing the δ238U composition of late Silurian oceans using calcitic brachiopod shells. *Geochim. Cosmochim. Acta*.

Romaniello S. J., Herrmann A. D. and Anbar A. D. (2013) Uranium concentrations and 238U/235U isotope ratios in modern carbonates from the Bahamas: Assessing a novel paleoredox proxy. *Chem. Geol.* **362**, 305–316.

Rooney A.D., Yang C., Condon D.J., Zhu M., Macdonald F.A. (2020) U-Pb and Re-Os geochronology tracks stratigraphic condensation in the Sturtian snowball Earth aftermath. *Geology* 48, 625–629.

Roscoe S.M. (1984) Lead isotope dating of galena-bearing veins in dolomite at Artillery Lake, N.W.T. and Mistassini Lake, Quebec. *Geol. Assoc. Canada Mineral. Assoc. Canada Ann. Mtg.. Prog. Abstr*. 9, 101.

Ross, G. M., Villeneuve, M. E., & Theriault, R. J. (2001). Isotopic provenance of the lower Muskwa assemblage (Mesoproterozoic, Rocky Mountains, British Columbia): New clues to correlation and source areas. *Precambrian Research*, *111*(1-4), 57-77.

Rouxel, O. J., Bekker, A., & Edwards, K. J. (2005). Iron isotope constraints on the Archean and Paleoproterozoic ocean redox state. *Science*, *307*(5712), 1088-1091.

Russell A. D., Emerson S., Nelson B. K., Erez J. and Lea D. W. (1994) Uranium in foraminiferal calcite as a recorder of seawater uranium concentrations. *Geochim. Cosmochim. Acta* **58**, 671–681.

Sahoo S. K., Planavsky N. J., Kendall B., Wang X., Shi X., Scott C., Anbar A. D., Lyons T. W. and Jiang G. (2012) Ocean oxygenation in the wake of the Marinoan glaciation. *Nature* **489**, 546–549.

Sanborn-Barrie M., Rogers N., Skulskl T., Parker J., McNicoll V. and Devaney J. (2004) Geology and Tectonostratigraphic Assemblages, East Uchi Subprovince, Red Lake and Birch-Uchi belts, Ontario; Geological Survey of Canada, Open File 4256; Ontario Geological Survey, Preliminary Map P. 3460, scale 1:250 000.

Saylor B., Grotzinger J. (1992) Reconnaissance of the structure and stratigraphy of the Basler Lake area, southern Wopmay Orogen, Northwest Territories. Current research, part C. *Geological Survey of Canada, Paper*, 259-268.

Schauble E. A. (2007) Role of nuclear volume in driving equilibrium stable isotope fractionation of mercury, thallium, and other very heavy elements. *Geochim. Cosmochim. Acta* **71**, 2170–2189.

Schreiber, U. M., Eriksson, P. G., Van der Neut, M., & Snyman, C. P. (1992). Sedimentary petrography of the early Proterozoic Pretoria Group, Transvaal sequence, South Africa: implications for tectonic setting. *Sedimentary geology*, *81*(1-2), 89-103.

Scott C., Lyons T. W., Bekker A., Shen Y., Poulton S. W., Chu X. and Anbar A. D. (2008) Tracing the stepwise oxygenation of the Proterozoic ocean. *Nature* **452**, 456–459.

Scott C., Wing B. A., Bekker A., Planavsky N. J., Medvedev P., Bates S. M., Yun M. and Lyons T. W. (2014) Pyrite multiple-sulfur isotope evidence for rapid expansion and contraction of the early Paleoproterozoic seawater sulfate reservoir. *Earth Planet. Sci. Lett.* **389**, 95–104.

Semikhatov M.A. and Serebryakov S.N. (1983) Sibirskii gipostratotip rifeya (The Siberian Hypostratotype of the Riphean). Trudy, Geologicheskogo Instituta, Akademii Nauk SSSR, 367. Nauka, Moscow (in Russian).

Sergeev V.N., Knoll A.H., Petrov P.Y. (1997) Paleobiology of the Mesoproterozoic–Neoproterozoic transition: the Sukhaya Tunguska Formation, Turukhansk Uplift, Siberia. *Precambrian Res*. 85, 201–239.

Sergeev V.N. (1999) Silicified microfossils from the transitional Meso–Neoproterozoic deposits of the Turukhansk Uplift, Siberia. *Societa Paleontol. Ital. Bull. Spec. Issue* 38, 287– 295.

Sheen A. I., Kendall B., Reinhard C. T., Creaser R. A., Lyons T. W., Bekker A., Poulton S. W. and Anbar A. D. (2018) A model for the oceanic mass balance of rhenium and implications for the extent of Proterozoic ocean anoxia. *Geochim. Cosmochim. Acta* **227**, 75–95.

Shields G. and Veizer J. (2002) Precambrian marine carbonate isotope database: Version 1.1. *Geochemistry, Geophys. Geosystems* **3**, 1-of.

Shklanka R. (1972) Geology of the Steep Rock Lake area, district of Rainy River. *Ont. Dept. Mines and North. Aflairs, Geol. Rept*. 93, 1-l 14.

Siberlin C. and Wunsch C. (2011) Oceanic tracer and proxy time scales revisited.

Simonson, B. M., Schubel, K. A., & Hassler, S. W. (1993). Carbonate sedimentology of the early Precambrian Hamersley Group of western Australia. *Precambrian Research*, *60*(1-4), 287-335.

Smith W. H. F. and Sandwell D. T. (1997) Global sea floor topography from satellite altimetry and ship depth soundings. *Science (80-.).* **277**, 1956–1962.

Smith M.D., Heaman L.M. (1999) Constraints on the timing of felsic magmatism associated with the Matachewan igneous events: preliminary results for the Creighton granite, Ontario. *Geol. Ass. Canada, Min. Ass. Canada Joint Ann. Meeting Abstract* 24, p. 119.

Sønderholm M. and Tirsgaard H. (1990) Sedimentological investigations of the Multicoloured 'series' (Eleonore Bay Group, Late Precambrian) in the Scoresby Land — Andrée Land region, North-East Greenland. *Rapport Grønlands Geologiske Undersøgelse* 148, 38 pp.

Sønderholm M. and Tirsgaard H. (1993) Lithostratigraphic framework of the Upper Proterozoic Eleonore Bay Supergroup of East and North-East Greenland. *Grønlands Geolgiske Undersøgelsen* 167, 38 oo.

Song Huyue, Song Haijun, Algeo T. J., Tong J., Romaniello S. J., Zhu Y., Chu D., Gong Y. and Anbar A. D. (2017) Uranium and carbon isotopes document global-ocean redox-productivity relationships linked to cooling during the Frasnian-Famennian mass extinction. *Geology* **45**, 887–890.

Souza P.C. and Muller G. (1984) Primeiras Estruturas Algais Comprovadas na Formacao Gandarela, Quadrilatero Ferrıfero. *Revista Escola de Minas Ouro Preto*, v. 2, p. 13–21.

Spear N., Holland H. D., Garcia-Veígas J., Lowenstein T. K., Giegengack R. and Peters H. (2014) Analyses of fluid inclusions in Neoproterozoic marine halite provide oldest measurement of seawater chemistry. *Geology* **42**, 103–106.

Stagman J.G. (1961) The geology of the country around Sinoia and Banket, Lomagundi District. *Bull. Geol. Surv. S. Rhod*. 49, 107 pp.

Stirling C. H., Andersen M. B., Potter E.-K. and Halliday A. N. (2007) Low-temperature isotopic fractionation of uranium. *Earth Planet. Sci. Lett.* **264**, 208–225.

Stockey R. G., Cole D. B., Planavsky N. J., Loydell D. K., Frýda J. and Sperling E. A. (2020) Persistent global marine euxinia in the early Silurian. *Nat. Commun.* **11**, 1–10.

Stowe C.W. (1978) Structure of the Lomagundi Group in the Sinoia area, Rhodesia. *Spec. Publ. Geol. Soc. S. Afr*. 4, 449–459.

Sumner D.Y. and Bowring S.A. (1996) U-Pb geochronologic constraints on deposition of the Campbellrand Subgroup, Transvaal Supergroup, South Africa. *Precambrian Res*. 79, 25-35.

Sumner D.Y. (1997) Carbonate precipitation and oxygen stratification in late Archean seawater as deduced from facies and stratigraphy of the Gamohaan and Frisco formations, Transvaal Supergroup, South Africa. *Am. J. Sci.* 297, 455.

Swanner E. D., Planavsky N. J., Lalonde S. V, Robbins L. J., Bekker A., Rouxel O. J., Saito M. A., Kappler A., Mojzsis S. J. and Konhauser K. O. (2014) Cobalt and marine redox evolution. *Earth Planet. Sci. Lett.* **390**, 253–263.

Swart P. K. and Hubbard J. (1982) Uranium in scleractinian coral skeletons. *Coral Reefs* **1**, 13–19.

Tankard A.J., Jackson M.P.A., Eriksson K.A., Hobday D.K., Hunter D.R. and Minter W.E.L. (1982) *Crustal Evolution of Southern Africa: 3.8 Billion Years of Earth History*. Springer.

Taylor G.C., Stott D.F. (1973) Tuchodi Lakes map-area, British Columbia. *Geol. Surv. Can. Mem*. 373, 37.

Taylor S. R. and McLennan S. M. (1985) The continental crust: its composition and evolution.

Teichert B. M. A., Eisenhauer A., Bohrmann G., Haase-Schramm A., Bock B. and Linke P. (2003) U/Th systematics and ages of authigenic carbonates from Hydrate Ridge, Cascadia Margin: recorders of fluid flow variations. *Geochim. Cosmochim. Acta* **67**, 3845–3857.

Telus M., Dauphas N., Moynier F., Tissot F. L. H., Teng F.-Z., Nabelek P. I., Craddock P. R. and Groat L. A. (2012) Iron, zinc, magnesium and uranium isotopic fractionation during continental crust differentiation: The tale from migmatites, granitoids, and pegmatites. *Geochim. Cosmochim. Acta* **97**, 247–265.

Teng F.-Z., Dauphas N. and Watkins J. M. (2017) Non-traditional stable isotopes: retrospective and prospective. *Rev. Mineral. geochemistry* **82**, 1–26.

Tennick F.P., Phaup A.E. (1976) The geology of the country around Magondi, Lomagundi, Hartley and Gatooma Districts. *Bull. Geol. Surv. Rhod*. 65, 314 pp.

Thomson D., Rainbird R. H., Planavsky N., Lyons T. W. and Bekker A. (2015) Chemostratigraphy of the Shaler Supergroup, Victoria Island, NW Canada: A record of ocean composition prior to the Cryogenian glaciations. *Precambrian Res.* **263**, 232–245.

Tissot F. L. H., Chen C., Go B. M., Naziemiec M., Healy G., Bekker A., Swart P. K. and Dauphas N. (2018) Controls of eustasy and diagenesis on the 238U/235U of carbonates and evolution of the seawater (234U/238U) during the last 1.4 Myr. *Geochim. Cosmochim. Acta* **242**, 233–265.

Tissot F. L. H. and Dauphas N. (2015) Uranium isotopic compositions of the crust and ocean: Age corrections, U budget and global extent of modern anoxia. *Geochim. Cosmochim. Acta* **167**, 113–143.

Tissot F. L. H., Dauphas N. and Grove T. L. (2017) Distinct 238U/235U ratios and REE patterns in plutonic and volcanic angrites: Geochronologic implications and evidence for U isotope fractionation during magmatic processes. *Geochim. Cosmochim. Acta* **213**, 593–617.

Tostevin R., Clarkson M. O., Gangl S., Shields G. A., Wood R. A., Bowyer F., Penny A. M. and Stirling C. H. (2019) Uranium isotope evidence for an expansion of anoxia in terminal Ediacaran oceans. *Earth Planet. Sci. Lett.* **506**, 104–112.

Trendall A.F. (1983) The Hamersley Basin. *In Banded Iron Formations: Facts and Problems* (eds. A.F. Trendall and R.C. Morris), pp.69-123. Elsevier.

Turner E. C. and Bekker A. (2016) Thick sulfate evaporite accumulations marking a mid-Neoproterozoic oxygenation event (Ten Stone Formation, Northwest Territories, Canada). *GSA Bull.* **128**, 203–222.

Tyndale-Biscoe, R. M. (1940). *The Geology of the Country Around Gwanda...* Rhodesian Printing & Publishing Company.

Vallis G. K. (2006) Atmospheric and Oceanic Fluid Dynamics: Fundamentals and Large-Scale Circulation, Cambridge Univ.

van Breemen O., Kjarsgaard B.A., Tella S., Lemkow D. and Aspler L. (2013) U-Pb detrital zircon geochronology of clastic sedimentary rocks of the Paleoproterozoic Nonacho and East Arm basins, Thaidene Nene MERA study area. Chapter 4 in Mineral and Energy Resource Assessment for the Proposed Thaidene Nene National Park Reserve in the Area of the East Arm of Great Slave Lake, Northwest Territories, (eds.) D.F. Wright, E.J. Ambrose, D. Lemkow, and G.F. Bonham-Carter; Geological Survey of Canada Open File 7196, 119-143.

Veizer J., Clayton R. N. and Hinton R. W. (1992a) Geochemistry of Precambrian carbonates: IV. Early Paleoproterozoic (2.25±0.25 Ga) seawater. *Geochim. Cosmochim. Acta* **56**, 875–885.

Veizer J., Clayton R. N., Hlnton R. W., Von Brunn V., Mason T. R., Buck S. G. and Hoefs J. (1990) Geochemistry of Precambrian carbonates: 3-shelf seas and non-marine environments of the Archean. *Geochim. Cosmochim. Acta* **54**, 2717–2729.

Veizer J., Hoefs J., Ridler R. H., Jensen L. S. and Lowe D. R. (1989) Geochemistry of Precambrian carbonates: I. Archean hydrothermal systems. *Geochim. Cosmochim. Acta* **53**, 845–857.

Veizer J., Plumb K. A., Clayton R. N., Hinton R. W. and Grotzinger J. P. (1992b) Geochemistry of Precambrian carbonates: V. late Paleoproterozoic seawater. *Geochim. Cosmochim. Acta* **56**, 2487–2501.

Verbruggen A., Alonso A., Eykens R., Kehoe F., Kuhn H., Richter S. and Aregbe Y. (2008) Preparation and certification of IRMM-3636, IRMM-3636a and IRMM-3636b. *JRC Sci. Tech. Reports*.

Wahl W.C. (1953) Geological report on the Temiscamie River area. *Ministhre Mines, Rapt. Geol*. 54, l-37.

Walraven F. (1997) Geochronology of the Rooiberg Group, Transvaal Supergroup, South Africa. Inf. Circ. 316. Economic Geology Research Unit, University of the Witwatersrand, Johannesburg, South Africa, 21 pp.

Wang X., Ossa F. O., Hofmann A., Agangi A., Paprika D. and Planavsky N. J. (2020) Uranium isotope evidence for Mesoarchean biological oxygen production in shallow marine and continental settings. *Earth Planet. Sci. Lett.* **551**, 116583.

Wang X., Planavsky N. J., Hofmann A., Saupe E. E., De Corte B. P., Philippot P., LaLonde S. V, Jemison N. E., Zou H. and Ossa F. O. (2018) A Mesoarchean shift in uranium isotope systematics. *Geochim. Cosmochim. Acta* **238**, 438–452.

Wang X., Planavsky N. J., Reinhard C. T., Hein J. R. and Johnson T. M. (2016) A Cenozoic seawater redox record derived from 238U/235U in ferromanganese crusts. *Am. J. Sci.* **316**, 64–83.

Webb D. J. (1982) Tides and the evolution of the Earth—Moon system. *Geophys. J. Int.* **70**, 261–271.

Wei G.-Y., Planavsky N. J., Tarhan L. G., Chen X., Wei W., Li D. and Ling H.-F. (2018) Marine redox fluctuation as a potential trigger for the Cambrian explosion. *Geology* **46**, 587–590.

Wei G.-Y., Planavsky N. J., Tarhan L. G., He T., Wang D., Shields G. A., Wei W. and Ling H.-F. (2020) Highly dynamic marine redox state through the Cambrian explosion highlighted by authigenic δ238U records. *Earth Planet. Sci. Lett.* **544**, 116361.

Weyer S., Anbar A. D., Gerdes A., Gordon G. W., Algeo T. J. and Boyle E. A. (2008) Natural fractionation of 238U/235U. *Geochim. Cosmochim. Acta* **72**, 345–359.

White D. A., Elrick M., Romaniello S. and Zhang F. (2018) Global seawater redox trends during the Late Devonian mass extinction detected using U isotopes of marine limestones. *Earth Planet. Sci. Lett.* **503**, 68–77.

Wilks M.E. and Nisbet E.G. (1984) Archean stromatolites from the Steep Rock Group, northwestern Ontario, Canada. *Can. J. Earth Sci*. 22, 792-799.

Wilks, M. E. and Nisbet, E. G. (1988). Stratigraphy of the Steep Rock Group, northwest Ontario: a major Archaean unconformity and Archaean stromatolites. *Canadian Journal of Earth Sciences*, *25*(3), 370-391.

Wilmeth, D. T., Corsetti, F. A., Beukes, N. J., Awramik, S. M., Petryshyn, V., Spear, J. R., & Celestian, A. J. (2019). Neoarchean (2.7 Ga) lacustrine stromatolite deposits in the Hartbeesfontein Basin, Ventersdorp Supergroup, South Africa: Implications for oxygen oases. *Precambrian Research*, *320*, 291-302.

Wilson C.B. and Harland W.B. (1964) The Polarisbreen Series and other evidences of late Pre-Cambrian ice ages in Spitsbergen. *Geol. Mag*., 101, 198-219.

Wilson, J. F., Nesbitt, R. W., & Fanning, C. M. (1995). Zircon geochronology of Archaean felsic sequences in the Zimbabwe craton: a revision of greenstone stratigraphy and a model for crustal growth. *Geological Society, London, Special Publications*, *95*(1), 109-126.

Winston D., Lyons T. (1993) Sedimentary cycles in the St. Regis, Empire and Helena formations of the Middle Proterozoic Belt Supergroup, northwestern Montana, Geologic Guidebook to the Belt-Purcell Supergroup, Glacier National Park and vicinity, Montana and adjacent Canada: Belt Symposium III Field Trip Guidebook, Belt Association, c/o PK Link, Dept. of Geology, Idaho State University, Pocatello, ID, pp. 21-51.

Winston, D. (2006). Revised Stratigraphy and Depositional History of the Helena and Wallace Formations, Mid-Proterozoic Piegan Group, Belt Supergroup Montana and Idaho. *SPECIAL PUBLICATION-SEPM*, *86*, 65.

Wood J. (1973) Stratigraphy and depositional environments of upper Huronian rocks of the Rawhide Lake–Flack Lake area, Ontario. In: Young G.M. (Ed.), Huronian Stratigraphy and Sedimentation. *Geol. Assn. Can. Spec. Paper* 12, pp. 73–95.

Wörndle S., Crockford P.W., Kunzmann M., Bui T.H., Halverson G.P., 2019. Linking the Bitter Springs carbon isotope anomaly and early Neoproterozoic oxygenation through I/[Ca+Mg] ratios. Chemical Geology, 524, 119–135.

Wunsch C. and Ferrari R. (2004) Vertical mixing, energy, and the general circulation of the oceans. *Annu. Rev. Fluid Mech.* **36**, 281–314.

Yang S., Kendall B., Lu X., Zhang F. and Zheng W. (2017) Uranium isotope compositions of mid-Proterozoic black shales: Evidence for an episode of increased ocean oxygenation at 1.36

Ga and evaluation of the effect of post-depositional hydrothermal fluid flow. *Precambrian Res.* **298**, 187–201.

Young G.M. (1991) Stratigraphy, sedimentology and tectonic setting of the Huronian Supergroup. In: Proceedings of the Joint Annual Meeting, Toronto'91, Field trip B5: Guidebook, Geological Association of Canada, Mineralogical Association of Canada, Society of Economic Geologists, 34 pp.

Young G.M., Long D.G.F., Fedo C.M., Nesbitt H.W. (2001) Paleoproterozoic Huronian basin: product of a Wilson cycle punctuated by glaciations and a meteorite impact. *Sed. Geol*. 141–142, 233–254.

Zhang F., Algeo T. J., Cui Y., Shen J., Song H., Sano H., Rowe H. D. and Anbar A. D. (2019a) Global-ocean redox variations across the Smithian-Spathian boundary linked to concurrent climatic and biotic changes. *Earth-Science Rev.* **195**, 147–168.

Zhang F., Algeo T. J., Romaniello S. J., Cui Y., Zhao L., Chen Z.-Q. and Anbar A. D. (2018a) Congruent Permian-Triassic δ238U records at Panthalassic and Tethyan sites: Confirmation of global-oceanic anoxia and validation of the U-isotope paleoredox proxy. *Geology* **46**, 327–330.

Zhang F., Dahl T. W., Lenton T. M., Luo G., Shen S., Algeo T. J., Planavsky N., Liu J., Cui Y. and Qie W. (2020a) Extensive marine anoxia associated with the Late Devonian Hangenberg Crisis. *Earth Planet. Sci. Lett.* **533**, 115976.

Zhang F., Lenton T. M., del Rey Á., Romaniello S. J., Chen X., Planavsky N. J., Clarkson M. O., Dahl T. W., Lau K. V and Wang W. (2020b) Uranium isotopes in marine carbonates as a global ocean paleoredox proxy: A critical review. *Geochim. Cosmochim. Acta*.

Zhang F., Romaniello S. J., Algeo T. J., Lau K. V, Clapham M. E., Richoz S., Herrmann A. D., Smith H., Horacek M. and Anbar A. D. (2018b) Multiple episodes of extensive marine anoxia linked to global warming and continental weathering following the latest Permian mass extinction. *Sci. Adv.* **4**, e1602921.

Zhang F., Shen S., Cui Y., Lenton T. M., Dahl T. W., Zhang H., Zheng Q., Wang W., Krainer K. and Anbar A. D. (2020c) Two distinct episodes of marine anoxia during the Permian-Triassic crisis evidenced by uranium isotopes in marine dolostones. *Geochim. Cosmochim. Acta*.

Zhang F., Xiao S., Kendall B., Romaniello S. J., Cui H., Meyer M., Gilleaudeau G. J., Kaufman A. J. and Anbar A. D. (2018c) Extensive marine anoxia during the terminal Ediacaran Period. *Sci. Adv.* **4**, eaan8983.

Zhang F., Xiao S., Romaniello S. J., Hardisty D., Li C., Melezhik V., Pokrovsky B., Cheng M., Shi W. and Lenton T. M. (2019b) Global marine redox changes drove the rise and fall of the Ediacara biota. *Geobiology* **17**, 594–610.

Zhao H., Algeo T. J., Liu Y., Chen Z.-Q., Zhang L., Hu Z. and Li Z. (2020) Lower Triassic carbonate δ238U record demonstrates expanded oceanic anoxia during Smithian Thermal Maximum and improved ventilation during Smithian-Spathian boundary cooling event. *Palaeogeogr. Palaeoclimatol. Palaeoecol.* **539**, 109393.

3 ZIRCONIUM AND HAFNIUM ISOTOPE VARIATIONS TRACING PLANETARY DIFFERENTIATION PROCESS

Adapted with permission from: Chen, X., Wang, W., Zhang, Z., Nie, N. X., and Dauphas, N. (2020). Evidence from Ab initio and transport modeling for diffusion-driven zirconium isotopic fractionation in igneous rocks. *ACS Earth and Space Chemistry*, *4*(9), 1572-1595.

3.1 Introduction

High field strength elements have been widely used in geochemistry and cosmochemistry because of their multiple characteristics and they have proven to be extremely useful to record important information regarding major questions of planetary evolutions. Among them the zirconium and hafnium stable isotope systematics are relatively new fields mainly due to the recent improvements in instruments and the corresponding analytical methods. Currently available Zr isotope data and their interpretations among different lab groups are controversial which limit the further developments of this potential geochemical tracer. Before hastily reaching some Earth science "big findings" using this newly developed proxy, we start to address some fundamental questions on Zr and Hf isotope systematics from the theoretical point of view.

We use density functional theory (DFT) to calculate the equilibrium isotopic fractionation factors of zirconium (Zr) in a variety of minerals including zircon, baddeleyite, Ca-catapleiite, ilmenite, geikielite, magnetite, apatite, K-feldspar, quartz, olivine, clinopyroxene, orthopyroxene, amphibole, and garnet. We also report equilibrium isotopic fractionation factors for Hf in zircons, Ca-catapleiite, and ilmenite. These calculations show that coordination environment is an important control on Zr and Hf isotopic fractionation, with minerals with Zr and Hf in low coordinations predicted to be enriched in the heavy isotopes of Zr and Hf, relative to those with Zr and Hf in high coordinations. At equilibrium, zircon, which hosts Zr and Hf in 8-fold coordination, is predicted to have low $^{94}Zr/^{90}Zr$ and $^{179}Hf/^{177}Hf$ ratios compared to silicate melt, which hosts Zr and Hf in 6-fold coordination. However, our modeling results indicate that little equilibrium isotopic fractionation for Zr is expected during magmatic differentiation and zircon crystallization.

We show through isotopic transport modeling that the Zr isotopic variations that were documented in igneous rocks are likely due to diffusion-driven kinetic isotopic fractionation. The two settings where this could take place are (*i*) diffusion-limited crystallization of zircon (DLC model) and (ii) diffusion-triggered crystallization of zircon (DTC model) in the boundary layer created by the growth of Zr-poor minerals. Fractional crystallization of zircons enriched in light Zr isotopes by diffusion can drive residual magmas towards heavy Zr isotopic compositions. Our diffusive transport model gives the framework to interpret Zr isotope data and gain new insights into the cooling history of igneous rocks and the setting of zircon crystallization.

3.2 Methods

3.2.1 Equilibrium mass-dependent isotopic fractionation

Equilibrium mass-dependent isotopic fractionation arises from changes in vibrational frequencies caused by isotopic substitution of an element in a given system (Bigeleisen and Mayer, 1947a; Urey, 1947). Following Bigeleisen and Mayer (1947a), the reduced partition function ratio β_A of an element X in Phase A, which represents the isotope fractionation factor between Phase A and an ideal gas of X atoms, can be expressed within the quasi-harmonic approximation as,

$$\beta_A = \frac{Q_h}{Q_l} = \prod_i^{3N} \frac{u_{ih}}{u_{il}} \frac{e^{-\frac{1}{2}u_{ih}}}{1-e^{-u_{ih}}} \frac{1-e^{-u_{il}}}{e^{-\frac{1}{2}u_{il}}} , \quad (3.1)$$

where *h* and *l* represent the heavy and light isotopes respectively, *i* is a running index of vibrational frequency mode, *N* is the number of atoms in the unit cell, and Q_h and Q_l refer to the vibrational partition function for the heavy and light isotopes, respectively. A phase with *N* atoms has *3N* vibrational modes and thus the product runs over all *3N* phonon modes. u_{ih} and u_{il} are defined as,

$$u_i = \hbar\omega_i / k_B T\,, \tag{3.2}$$

where $\hbar$ and k_B is the reduced Planck constant and Boltzmann constant, respectively, T is temperature in Kelvin, and ω_i is the vibrational frequency of the i^{th} mode. Equilibrium isotopic fractionation between two phases A and B in the δ-notation is readily calculated from the reduced partition function ratio using the following formula,

$$\Delta_{A-B} \simeq 10^3 ln\alpha_{A-B} = 10^3 ln\beta_A - 10^3 ln\beta_B\,, \tag{3.3}$$

For a given phase, $10^3 ln\beta$ can be expressed as a polynomial expansion of even powers of the inverse of the temperature (Polyakov et al., 2005; Dauphas et al., 2012),

$$10^3 \ln\beta = \frac{A_1}{T^2} + \frac{A_2}{T^4} + \frac{A_3}{T^6}\,, \tag{3.4}$$

where the coefficients A_1, A_2, and A_3 can be calculated from the even moments of the phonon density of states (Dauphas et al., 2012). The first term in this equation is proportional to the mean force constant $\langle F \rangle$ (in N/m) of the chemical bonds that the element of interest forms with the coordination atoms,

$$A_1 = 1000 \left(\frac{1}{m_l} - \frac{1}{m_h}\right) \frac{\hbar^2}{8{k_B}^2} \langle F \rangle\,, \tag{3.5}$$

At the high temperatures relevant to igneous systems, this term is the dominant control on equilibrium isotopic fractionation (Herzfeld and Teller, 1938; Bigeleisen and Mayer, 1947b; Dauphas et al., 2012). For the $^{94}Zr/^{90}Zr$ and $^{179}Hf/^{177}Hf$ ratios, we have,

$$1000 \ln\beta(^{94}\mathrm{Zr}/^{90}\mathrm{Zr}) \simeq 2081 \langle F \rangle / T^2\,, \tag{3.6}$$

$$1000 \ln\beta(^{179}\mathrm{Hf}/^{177}\mathrm{Hf}) \simeq 278 \langle F \rangle / T^2\,, \tag{3.7}$$

We follow Dauphas et al. (2012, 2018) and use the mean force constant $\langle F \rangle$ to discuss equilibrium isotopic fractionation factors. The virtues of this approach for non-traditional stable isotopes are:

(1) It is a number that is usually easy to remember when reported in SI unit (the same units as a spring constant), typically spanning the range 0 to ~1000 N/m.

(2) It does not depend on the choice of isotopes used to define isotopic fractionation, so one can compare values from different publications regardless of the choice that are made in reporting isotopic fractionation.

(3) It allows easy comparison of isotopic fractionation between different elements. For example, when comparing Zr and Hf equilibrium isotope fractionations, the difference could result from a difference in the masses of the isotopes of the two elements, and/or from a difference in the nature of the bonds (force constant).

(4) Bond strength is the governing factor for equilibrium isotopic fractionation, especially at high temperature. We use Eq. 3.4 to calculate equilibrium fractionation factors at all temperatures and recommend that this equation be used in future studies, but the truncated Eqs. 3.5 to 3.7 are adequate above ~300 °C.

For the reasons outlined above, we have used the mean force constant $\langle F \rangle$ in a number of publications discussing equilibrium isotopic fractionation (Dauphas et al., 2012, 2018; Blanchard et al., 2015; Yang et al., 2019; Zeng et al., 2019; Roskosz et al., 2020) and we encourage the community to use this quantity more broadly in non-traditional stable isotope geochemistry.

3.2.2 First-principle calculations

We performed first-principle calculations based on density functional theory (DFT) using VASP (Vienna Ab Initio Simulation Package) with the projector-augmented wave (PAW) method (Blöchl, 1994). The generalized-gradient approximation (GGA) (Perdew et al., 1996) for the

exchange-correlation functional was adopted and the PAW-PBE pseudopotentials were used. The energy cutoff for all calculations was 600 eV. All mineral structures, including cell parameters and atomic positions, were well relaxed at ambient pressure. The Brillouin zone summations over the electronic states were performed at different k-point grids according to their unit cell sizes (**Table 3.1**). For all structure optimizations, the residual forces converge within 10^{-3} eV/Å. In order to estimate the β factors of $^{94}Zr/^{90}Zr$ for all phases, we performed full calculations of phonon vibration frequencies using the finite displacement method as implemented in the open-source code PHONOPY (Togo and Tanaka, 2015).

Table 3.1 The k-point mesh used to calculate Brillouin zone summations over electronic states.

clinopyroxene	**Chemical composition**	**k-point mesh**
$Si^{4+}\leftrightarrow Zr^{4+}$	$Mg_{24}Ca_{24}Si_{47}ZrO_{144}$	1×1×1
	$Mg_{32}Ca_{32}Si_{63}ZrO_{192}$	1×1×1
$^{VI}Mg^{2+}+^{VIII}Ca^{2+}\leftrightarrow Zr^{4+}{}_{Mg}+\square$	$Mg_7ZrCa_7Si_{16}O_{48}$	1×1×1
	$Mg_{15}ZrCa_{15}Si_{32}O_{96}$	1×1×1
$^{VI}Mg^{2+}+^{VI}Mg^{2+}\leftrightarrow Zr^{4+}{}_{Mg}+\square$	$Mg_6ZrCa_8Si_{16}O_{48}$	1×1×1
orthopyroxene		
$Si^{4+}\leftrightarrow Zr^{4+}$	$Mg_{32}Si_{31}ZrO_{96}$	1×1×1
	$Mg_{64}Si_{63}ZrO_{192}$	1×1×1
$^{VI}Mg^{2+}(M1)+^{VI}Mg^{2+}(M2)\leftrightarrow{}^{VI}Zr^{4+}+\square$	$Mg_{30}ZrSi_{32}O_{96}$	1×1×1
	$Mg_{62}ZrSi_{64}O_{192}$	1×1×1
olivine		
$Si^{4+}\leftrightarrow Zr^{4+}$	$Mg_{32}Si_{15}ZrO_{64}$	1×1×1
	$Mg_{64}Si_{31}ZrO_{128}$	1×1×1

Table 3.1 *continued*

$^{VI}Mg^{2+}(M2) + {}^{VI}Mg^{2+}(M1) \leftrightarrow {}^{VI}Zr^{4+} + \square$	$Mg_{30}ZrSi_{16}O_{64}$	1×1×1
	$Mg_{62}ZrSi_{32}O_{128}$	1×1×1
quartz		
$Si^{4+} \leftrightarrow Zr^{4+}$	$Si_{80}ZrO_{162}$	1×1×1
	$Si_{95}ZrO_{192}$	1×1×1
K-feldspar		
$^{IV}Al^{3+} + {}^{VIII}K^{+} \leftrightarrow Zr^{4+}{}_{Al} + \square$	$K_7Al_7Si_{24}O_{64}$	1×1×1
	$K_{15}Al_{15}ZrSi_{48}O_{128}$	1×1×1
apatite		
$^{IX}Ca^{2+} + {}^{VII}Ca^{2+} \leftrightarrow Zr^{4+} + \square$	$Ca_{38}ZrP_{24}O_{96}F_8$	1×1×1
	$Ca_{78}ZrP_{48}O_{192}F_{16}$	1×1×1
geikielite		
$Ti^{4+} \leftrightarrow Zr^{4+}$	$Mg_{24}Ti_{23}ZrO_{72}$	1×1×1
	$Mg_{48}Ti_{47}ZrO_{144}$	1×1×1
ilmenite		
$Ti^{4+} \leftrightarrow Zr^{4+}$	$Fe_{24}Ti_{23}ZrO_{72}$	1×1×1
	$Fe_{48}Ti_{47}ZrO_{144}$	1×1×1
$MgFe_2O_4$ magnetite		
$^{VI}Fe^{3+} + {}^{IV}Fe^{3+} \leftrightarrow {}^{VI}Zr^{4+} + {}^{IV}Mg^{2+}$	$Mg_{17}ZrFe_{30}O_{64}$	1×2×2
	$Mg_{33}ZrFe_{62}O_{128}$	1×1×1
tremolite		
$Si^{4+} \leftrightarrow Zr^{4+}$	$Mg_{40}Ca_{16}Si_{63}ZrH_{16}O_{192}$	1×1×1
$^{VI}Mg^{2+}(M2) + {}^{VI}Mg^{2+}(M1) \leftrightarrow Zr^{4+}{}_{M2} + \square$	$Mg_{18}ZrCa_8Si_{32}H_8O_{96}$	1×1×1
	$Mg_{38}ZrCa_{16}Si_{64}H_{16}O_{192}$	1×1×1
pyrope		
$^{IV}Si^{4+} \leftrightarrow Zr^{4+}$	$Mg_{24}Al_{16}Si_{23}ZrO_{96}$	1×1×1

Table 3.1 *continued*		
$^{VI}Al^{3+}+{}^{IV}Si^{4+}\leftrightarrow Zr^{4+}+Al^{3+}$	$Mg_{24}Al_{16}Si_{23}ZrO_{96}$	1×1×1
$^{VIII}Mg^{2+}+{}^{VIII}Mg^{2+}\leftrightarrow Zr^{4+}+\square$	$Mg_{22}ZrAl_{16}Si_{24}O_{96}$	1×1×1
zircon	$Zr_2Si_2O_8$	8×8×8
baddeleyite	Zr_4O_8	6×6×6
Ca catapleiite	$Ca_4Zr_4Si_{12}H_{16}O_{44}$	2×1×1

□ represents the vacancy.

3.2.3 Mineral structures

The DFT approach is better suited to calculate the equilibrium isotopic fractionation for periodic crystals or small molecules. DFT can in principle tackle liquids but it is computationally challenging to run such calculations (Alfe et al., 1999; Stixrude and Karki, 2005; Huang et al., 2019; Solomatova and Caracas, 2019; Zeng et al., 2019), and while there are good constraints to ground truth calculations involving ions in water, the structure of silicate melts remains poorly known. For those reasons, we have decided to use knowledge from X-ray Absorption Fine Structure (EXAFS) spectroscopy on the local structure of Zr in silicate melts to select a model crystal composition to simulate Zr dissolved in silicate liquid. Farges et al. (1991) found that regardless of the glass investigated, Zr^{4+} at a trace level of ~2000 ppm in silicate glass was mainly in 6-coordinated sites and had a local structural environment similar to that in the mineral catapleiite (with a similar Zr-O bond length of ~2.07-2.10 Å) (Farges et al., 1991), a 3-tetrahedra zirconium cyclosilicate (the synthetic sodium zirconium cyclosilicate Lokelma is used to treat hyperkalemia in patients (Stavros et al., 2014; Keyser and Guillem, 2014)). The atomic positions of H atoms in catapleiite ($Na_2ZrSi_3O_9\cdot 2H_2O$) have not been reported, and cannot be properly

modeled by DFT. We have therefore selected the similar Ca-catapleiite ($CaZrSi_3O_9 \cdot 2H_2O$) in which all atomic positions are well known, to use as the model structure for Zr in silicate melt.

The calculated minerals in this study include zircon, baddeleyite, Ca-catapleiite, geikielite, ilmenite, magnetite, apatite, K-feldspar, quartz, olivine, clinopyroxene, orthopyroxene, amphibole and garnet. Zirconium is a trace element in these minerals except for zircon, baddeleyite, and Ca-catapleiite.

In spinel-facies lherzolite and harzburgite, the inventories of Zr and Hf are dominated by clinopyroxene and to a lesser extent orthopyroxene (Eggins et al., 1998). In garnet lherzolite, the inventories of Zr and Hf are dominated by garnet and clinopyroxene, with again orthopyroxene playing a lesser role (Ionov, 2004). Although major element sites in these minerals are well known, the substitution mechanisms for Zr incorporation as a minor element remain unclear. In olivine, clinopyroxene, and orthopyroxene, there are two possible Zr substitution mechanisms. One is that Zr^{4+} directly occupies the tetrahedral Si site ($^{IV}Si^{4+} \leftrightarrow Zr^{4+}$), and the other one is that Zr substitutes in the octahedral Mg site or the dodecahedral Ca site (in clinopyroxene) with charge balanced by nearby Mg vacancies ($^{VI}Mg^{2+}/^{VIII}Ca^{2+} + {}^{VI}Mg^{2+} \leftrightarrow Zr^{4+}_{Mg/Ca} + \square$).

Olivine has one equivalent tetrahedral Si site and two nonequivalent octahedral Mg sites (M1 and M2) with M2 site being larger than M1 site. For the substitution $^{IV}Si^{4+} \leftrightarrow Zr^{4+}$, we constructed a Zr-doped olivine by replacing one Si atom with one Zr atom in a supercell of forsterite. For the substitution $^{VI}Mg^{2+} + {}^{VI}Mg^{2+} \leftrightarrow Zr^{4+} + \square$, the nearest neighbor $[^{VI}Mg^{2+}]$-$[^{VI}Mg^{2+}]$ pair is replaced by Zr^{4+} and a vacancy ($\square$). There are four different possible configurations for this substitution: $[^{VI}Mg^{2+}]_{M1}$-$[^{VI}Mg^{2+}]_{M1}$, $[^{VI}Mg^{2+}]_{M1}$-$[^{VI}Mg^{2+}]_{M2}$, $[^{VI}Mg^{2+}]_{M2}$-$[^{VI}Mg^{2+}]_{M1}$, and $[^{VI}Mg^{2+}]_{M2}$-$[^{VI}Mg^{2+}]_{M2}$, where we substitute the first $^{VI}Mg^{2+}$ of each pair by Zr^{4+} and the second is

replaced by a vacancy. Our calculations show that the Zr-doped olivine with Zr^{4+} occupying the M2 Mg site and the charge balanced by the nearest M1 Mg vacancy ($[^{VI}Mg^{2+}]_{M2}$-$[^{VI}Mg^{2+}]_{M1}$) has the lowest total energy among all nonequivalent configurations. This configuration with the lowest energy was used for the calculation.

Orthopyroxene also has two nonequivalent Mg sites (M1 and M2) and two nonequivalent Si sites (SiA and SiB). Our calculations show that the energy difference between Zr^{4+} in the SiA and SiB sites is large, 7.6 eV for $Mg_{32}Si_{31}ZrO_{96}$ orthopyroxene, suggesting that Zr^{4+} prefers the SiB site. Thus, orthopyroxene with Zr^{4+} occupying the SiB site was used for the substitution $^{IV}Si^{4+}\leftrightarrow Zr^{4+}$. Similar to the substitution $^{VI}Mg^{2+}+{}^{VI}Mg^{2+}\leftrightarrow Zr^{4+}+\square$ in olivine, we also considered four configurations for the $Zr^{4+}+\square$ substitution: $[^{VI}Mg^{2+}]_{M1}$-$[^{VI}Mg^{2+}]_{M1}$, $[^{VI}Mg^{2+}]_{M1}$-$[^{VI}Mg^{2+}]_{M2}$, $[^{VI}Mg^{2+}]_{M2}$-$[^{VI}Mg^{2+}]_{M1}$, and $[^{VI}Mg^{2+}]_{M2}$-$[^{VI}Mg^{2+}]_{M2}$. The Zr-doped orthopyroxene, in which Zr^{4+} occupies the M1 Mg site with the charge balanced by the nearest M2 Mg vacancy ($[^{VI}Mg^{2+}]_{M1}$-$[^{VI}Mg^{2+}]_{M2}\leftrightarrow Zr^{4+}+\square$) has the lowest total energy and was used in the calculations.

Diopside, the $CaMgSi_2O_6$ end-member of clinopyroxene, contains four equivalent Ca atoms, four equivalent Mg atoms, and eight equivalent Si atoms. A Zr-doped clinopyroxene with the substitution $^{IV}Si^{4+}\leftrightarrow Zr^{4+}$ can be produced by replacing one Si atom with one Zr atom. We also investigated the Zr-doped clinopyroxene with the substitution $^{VIII}Ca^{2+}/{}^{VI}Mg^{2+}+{}^{VI}Mg^{2+}\leftrightarrow Zr^{4+}_{Ca/Mg}+\square$, in which $Zr^{4+}+\square$ can substitute for any pair $[^{VIII}Ca^{2+}]$-$[^{VI}Mg^{2+}]$, $[^{VII}Mg^{2+}]$-$[^{VIII}Ca^{2+}]$, or $[^{VI}Mg^{2+}]$-$[^{VI}Mg^{2+}]$. Our calculations show that the Zr-doped diopside with Zr^{4+} occupying the Mg site and the charge balanced by a vacancy in the nearest Ca site ($[^{VII}Mg^{2+}]$-$[^{VIII}Ca^{2+}]\leftrightarrow Zr^{4+}+\square$) has a lower total energy than the configuration with $[^{VIII}Ca^{2+}]$-$[^{VI}Mg^{2+}]\leftrightarrow Zr^{4+}+\square$ (*i.e.*, -2.3 eV for $Ca_7Mg_7ZrSi_{16}O_{48}$), indicating that Zr^{4+} preferentially enters

the Mg site in diopside. This is consistent with the experimental finding that Zr is located in the M1 (Mg) site in clinopyroxene (Farges et al., 1994).

Tremolite has three nonequivalent Mg sites (M1, M2, and M3) and two nonequivalent Si sites (SiT1 and SiT2). The volume of Mg-O octahedron increases in the order of M3 < M1 < M2. For the substitution $^{IV}Si^{4+}\leftrightarrow Zr^{4+}$, the configuration with Zr^{4+} occupying the larger SiT2 site has a lower energy and was used for the calculation. For the substitution $^{VI}Mg^{2+}+{}^{VI}Mg^{2+}\leftrightarrow Zr^{4+}+\square$, tremolite has six different $[^{VI}Mg^{2+}]$-$[^{VI}Mg^{2+}]$ pairs: $[^{VI}Mg^{2+}]_{M1}$-$[^{VI}Mg^{2+}]_{M1}$ (3.17 Å), $[^{VI}Mg^{2+}]_{M2}$-$[^{VI}Mg^{2+}]_{M2}$ (5.59 Å), $[^{VI}Mg^{2+}]_{M3}$-$[^{VI}Mg^{2+}]_{M3}$ (10.27 Å), $[^{VI}Mg^{2+}]_{M1}$-$[^{VI}Mg^{2+}]_{M2}$ (3.08 Å), $[^{VI}Mg^{2+}]_{M1}$-$[^{VI}Mg^{2+}]_{M3}$ (3.08 Å), and $[^{VI}Mg^{2+}]_{M2}$-$[^{VI}Mg^{2+}]_{M3}$ (3.18 Å). Here we only consider $[^{VI}Mg^{2+}]$-$[^{VI}Mg^{2+}]$ pairs where the two Mg sites are in close proximity, corresponding to seven different configurations ($[^{VI}Mg^{2+}]_{M1}$-$[^{VI}Mg^{2+}]_{M1}$, $[^{VI}Mg^{2+}]_{M1}$-$[^{VI}Mg^{2+}]_{M2}$, $[^{VI}Mg^{2+}]_{M2}$-$[^{VI}Mg^{2+}]_{M1}$, $[^{VI}Mg^{2+}]_{M1}$-$[^{VI}Mg^{2+}]_{M3}$, $[^{VI}Mg^{2+}]_{M3}$-$[^{VI}Mg^{2+}]_{M1}$, $[^{VI}Mg^{2+}]_{M2}$-$[^{VI}Mg^{2+}]_{M3}$, and $[^{VI}Mg^{2+}]_{M3}$-$[^{VI}Mg^{2+}]_{M2}$) that could be replaced by $Zr^{4+}+\square$. Our calculations show that the structure with Zr^{4+} occupying the largest M2 Mg site with the charge balanced by the nearest M1 Mg vacancy ($[^{VI}Mg^{2+}]_{M2}$-$[^{VI}Mg^{2+}]_{M1}\leftrightarrow Zr^{4+}+\square$) has the lowest energy and was therefore used in the calculations. This choice is consistent with spectroscopic evidence indicating that in arfvedsonite (a sodium amphibole mineral), Zr is in the M2 site (Farges et al., 1994).

The initial structure of Zr-doped quartz was constructed through the substitution $^{IV}Si^{4+}\leftrightarrow Zr^{4+}$, while the Zr-doped structure for K-feldspar was constructed by substituting Zr^{4+} for K^{+}/Al^{3+} with the charge balanced by a tetrahedral Al^{3+}/K^{+} vacancy ($^{VIII}K^{+}+{}^{IV}Al^{3+}\leftrightarrow Zr^{4+}{}_{K}+\square$ and $^{IV}Al^{3+}+{}^{VIII}K^{+}\leftrightarrow Zr^{4+}{}_{Al}+\square$). Our calculations show that the configuration with

$^{IV}Al^{3+}+{}^{VIII}K^{+}\leftrightarrow Zr^{4+}{}_{Al}+\square$ has a lower energy than $^{VIII}K^{+}+{}^{IV}Al^{3+}\leftrightarrow Zr^{4+}{}_{K}+\square$ (*i.e.*, -4.7 eV for $K_7Al_7ZrSi_{24}O_{64}$). The former was therefore used in the calculations.

Previous work suggested that Zr could substitute for Ca in apatite (Smirnov et al., 2017), we generated the initial structure of Zr-doped apatite by substituting one Zr atom for one nine-coordinated Ca atom, with the charge balanced by the vacancy in the nearest seven-coordinated Ca site ($^{IX}Ca^{2+}+{}^{VII}Ca^{2+}\leftrightarrow Zr^{4+}{}_{IX\text{-}Ca}+\square$).

For geikielite ($MgTiO_3$) and ilmenite ($FeTiO_3$), the Zr-doped structures were generated by the substitution $^{VI}Ti^{4+}\leftrightarrow Zr^{4+}$ due to the similarity between Ti^{4+} and Zr^{4+}. For $MgFe_2O_4$ magnetite, Zr^{4+} occupies the octahedral Fe^{3+} site with charge balanced by the nearest tetrahedral Fe^{3+} replaced by Mg^{2+} ($^{VI}Fe^{3+}+{}^{IV}Fe^{3+}\leftrightarrow Zr^{4+}{}_{VI\text{-}Fe}+Mg^{2+}{}_{IV\text{-}Fe}$).

Pyrope, the Mg endmember of garnet, contains 160 atoms in its conventional cell with space group Ia-3d. Here we consider three possible substitution mechanisms: (1) $^{IV}Si^{4+}\leftrightarrow Zr^{4+}$, where Zr^{4+} occupies the tetrahedral Si site, (2) $^{VI}Al^{3+}+{}^{IV}Si^{4+}\leftrightarrow Zr^{4+}+Al^{3+}$, where Zr^{4+} occupies the octahedral Al site and the original Al^{3+} occupies the nearest Si site, and (3) $^{VIII}Mg^{2+}+{}^{VIII}Mg^{2+}\leftrightarrow Zr^{4+}+\square$, where Zr^{4+} occupies the dodecahedral Mg site with the charge balanced by replacement of the nearest Mg site with a vacancy. Spectroscopic data seems to support the presence of Zr in 6-fold coordination in garnet (Farges et al., 1994), which would be support of the second substitution mechanism $^{VI}Al^{3+}+{}^{IV}Si^{4+}\leftrightarrow Zr^{4+}+Al^{3+}$.

Zirconium is present as trace element in many of these minerals. We modelled various levels of Zr dilution in olivine, orthopyroxene, clinopyroxene, tremolite, quartz, geikielite, ilmenite, apatite, K-feldspar, and magnetite by incorporating Zr into their supercells, which were generated by expanding the primitive cell along different directions. For example, the 112-atom

and 224-atom supercells of olivine were obtained by expanding the primitive cell twice along the *a* and *c* directions and twice simultaneously along *a*, *b*, and *c* directions, respectively. Substituting one Si atom with one Zr atom in those supercells can produce olivine structures with Zr/(Zr+Si) of 1/16 and 1/32, respectively. The same approach was used to simulate dilution in other minerals (**Table 3.2**). For the calculations of Hf equilibrium isotopic fractionation, we investigated Ca-catapleiite and zircon (Hf substituting Zr) as well as ilmenite (Hf substituting Ti). For zircon and Ca-catapleiite, we calculated the mineral structures and β-factors for different Zr/Hf ratios using a supercell approach (**Table 3.2**).

The relaxed cell parameters and volumes of zircon, baddeleyite, and Ca-catapleiite are compared with experimental measurements at 300 K in **Table 3.3**. Our calculations with GGA overestimate the volumes of these minerals by ~3-4%, which is typical of GGA calculations, as already noticed in previous studies (Schauble, 2011; Huang et al., 2013; Wang et al., 2017, 2019). In general, the local density approximation (LDA) tends to underestimate the volume, while GGA tends to give a larger volume than experimental data. DFT calculations will also give different β factors when different exchange-correlation functionals are used. However, the differences in $10^3\ln\beta$ (*i.e.*, $10^3\ln\alpha$ or equilibrium isotope fractionation factors between minerals), are less sensitive to the approximation adopted for the change-correlation functional (Schauble, 2011; Huang et al., 2013; Wang et al., 2017, 2019). We compare the calculated frequencies of zircon and baddeleyite with experimental data in **Fig. 3.1**. Our results agree with experimental measurements, with a slope between calculated and measured frequencies of 0.97±0.04. Following the uncertainty analysis presented by Meheut *et al*. (2009), we estimate that the uncertainties of our calculated lnβ and lnα values at high temperature are ~6 and 8% relative, respectively.

Table 3.2 Average Zr-O and Hf-O bond lengths, coordination numbers (CN), force constant of Zr and Hf in relaxed mineral structures, and polynomial expansion coefficients of the reduced partition function ratios ($10^3 \ln\beta$) of $^{94}Zr/^{90}Zr$ and $^{179}Hf/^{177}Hf$ of the studied minerals.

clinopyroxene	Chemical composition	Average Zr-O bond length (Å)	CN	Zr Force constant (N/m)	Polynomial expansion coefficients[#]		
					$\mathbf{A_1}$	$\mathbf{A_2}$	$\mathbf{A_3}$
$\mathbf{Si^{4+} \leftrightarrow Zr^{4+}}$	$Mg_{24}Ca_{24}Si_{47}ZrO_{144}$ (2b, 3c)	1.985	4	524.3	1.09201	-5.903E-03	1.004E-04
	$Mg_{32}Ca_{32}Si_{63}ZrO_{192}$ (2a, 2b, 2c)	1.989	4	522.4	1.08785	-5.880E-03	1.000E-04
$\mathbf{*^{VI}Mg^{2+} + {}^{VIII}Ca^{2+} \leftrightarrow Zr^{4+}_{Mg} + \square}$	$Mg_7ZrCa_7Si_{16}O_{48}$ (2c)	2.124	6	390.2	0.80773	-4.366E-03	7.472E-05
	$Mg_{15}ZrCa_{15}Si_{32}O_{96}$ (2b, 2c)	2.125	6	395.8	0.81756	-3.778E-03	4.405E-05
$\mathbf{*^{VI}Mg^{2+} + {}^{VI}Mg^{2+} \leftrightarrow Zr^{4+}_{Mg} + \square}$	$Mg_6ZrCa_8Si_{16}O_{48}$ (2c)	2.117	6	371.5	0.77325	-5.224E-03	9.424E-05
orthopyroxene							
$\mathbf{Si^{4+} \leftrightarrow Zr^{4+}}$	$Mg_{32}Si_{31}ZrO_{96}$ (2c)	1.976	4	538.2	1.12083	-6.059E-03	1.031E-04
	$Mg_{64}Si_{63}ZrO_{192}$ (2b, 2c)	1.975	4	540.0	1.12450	-6.078E-03	1.034E-04

Table 3.2 *continued*

$^{VI}Mg^{2+}$ (M1)+ $^{VI}Mg^{2+}$ (M2)	$Mg_{30}ZrSi_{32}O_{96}$ (2c)	2.131	6	409.0	0.85185	-4.604E-03	7.833E-05
$\leftrightarrow Zr^{4+}+\square$	$Mg_{62}ZrSi_{64}O_{192}$ (2b, 2c)	2.130	6	-			
olivine							
$Si^{4+}\leftrightarrow Zr^{4+}$	$Mg_{32}Si_{15}ZrO_{64}$ (2a, 2c)	1.970	4	562.3	1.17094	-6.329E-03	1.077E-04
	$Mg_{64}Si_{31}ZrO_{128}$ (2a, 2b, 2c)	1.969	4	566.4	1.17947	-6.376E-03	1.085E-04
$^{VI}Mg^{2+}$ (M2) + $^{VI}Mg^{2+}$ (M1)	$Mg_{30}ZrSi_{16}O_{64}$ (2a, 2c)	2.124	6	378.7	0.78861	-4.263E-03	7.252E-05
$\leftrightarrow Zr^{4+}+\square$	$Mg_{62}ZrSi_{32}O_{128}$ (2a, 2b, 2c)	2.123	6	380.1	0.79152	-4.278E-03	7.279E-05
quartz							
$Si^{4+}\leftrightarrow Zr^{4+}$	$Si_{80}ZrO_{162}$ (3a, 3b, 3c)	1.961	4	561.0	1.16823	-6.315E-03	1.074E-04
	$Si_{95}ZrO_{192}$ (4a, 4b, 2c)	1.960	4	-			
K-feldspar							
$^{IV}Al^{3+}+^{VIII}K^{+}\leftrightarrow Zr^{4+}{}_{Al}+\square$	$K_7Al_7Si_{24}O_{64}$ (2c)	1.969	4	540.1	1.12488	-8.154E-03	1.529E-04
	$K_{15}Al_{15}ZrSi_{48}O_{128}$ (2a, 2c)	1.968	4	544.3	1.13321	-8.215E-03	1.530E-04
apatite							

Table 3.2 *continued*

$^{IX}Ca^{2+}+{}^{VII}Ca^{2+}\leftrightarrow Zr^{4+}+\square$	$Ca_{38}ZrP_{24}O_{96}F_8$ (2a, 2b)	2.183	6	297.1	0.61798	-2.856E-03	3.330E-05
	$Ca_{78}ZrP_{48}O_{192}F_{16}$ (2a, 2b, 2c)	2.179	6	-			
geikielite							
$Ti^{4+}\leftrightarrow Zr^{4+}$	$Mg_{24}Ti_{23}ZrO_{72}$ (2a, 2b)	2.117	6	407.6	0.84873	-4.588E-03	7.805E-05
	$Mg_{48}Ti_{47}ZrO_{144}$ (2a, 2b, 2c)	2.116	6	410.0	0.85581	-4.626E-03	7.870E-05
ilmenite							
$Ti^{4+}\leftrightarrow Zr^{4+}$	$Fe_{24}Ti_{23}ZrO_{72}$ (2a, 2b)	2.129	6	279.6	0.58224	-3.147E-03	5.354E-05
	$Fe_{48}Ti_{47}ZrO_{144}$ (2a, 2b, 2c)	2.128	6	283.4	0.59015	-3.190E-03	5.427E-05
$MgFe_2O_4$ magnetite							
$^{VI}Fe^{3+}+{}^{IV}Fe^{3+}\leftrightarrow Zr^{4+}{}_{VI\text{-}Fe}+$	$Mg_{17}ZrFe_{30}O_{64}$ (2a)	2.111	6	294.4	0.61306	-3.314E-03	5.638E-05
$Mg^{2+}{}_{IV\text{-}Fe}$	$Mg_{33}ZrFe_{62}O_{128}$ (2a, 2b)	2.110	6	-			
tremolite							
$Si^{4+}\leftrightarrow Zr^{4+}$	$Mg_{40}Ca_{16}Si_{63}ZrH_{16}O_{192}$ (2a, 2c)	1.978	4	533.6	1.11117	-6.006E-03	1.0218E-04

Table 3.2 *continued*

$^{*VI}Mg^{2+}$ (M2) + $^{VI}Mg^{2+}$ (M1)↔Zr^{4+}_{M2}+□	$Mg_{18}ZrCa_8Si_{32}H_8O_{96}$ (2c)	2.113	6	383.3	0.79930	-4.320E-03	7.350E-05
	$Mg_{38}ZrCa_{16}Si_{64}H_{16}O_{192}$ (2a, 2c)	2.112	6	-			
pyrope							
$^{IV}Si^{4+}$↔Zr^{4+}	$Mg_{24}Al_{16}Si_{23}ZrO_{96}$	1.979	4	512.7	1.06679	-9.705E-03	1.902E-04
$^{*VI}Al^{3+}$+ $^{IV}Si^{4+}$↔Zr^{4+}+ Al^{3+}	$Mg_{24}Al_{16}Si_{23}ZrO_{96}$	2.074	6	433.5	0.90215	-7.151E-03	1.354E-04
$^{VIII}Mg^{2+}$+ $^{VIII}Mg^{2+}$↔Zr^{4+}+□	$Mg_{22}ZrAl_{16}Si_{24}O_{96}$	2.240	8	345.7	0.71955	-4.862E-03	8.769E-05
zircon	$Zr_2Si_2O_8$	2.228	8	334.7	0.69698	-3.767E-03	6.409E-05
baddeleyite	Zr_4O_8	2.187	7	323.4	0.67268	-3.109E-03	3.624E-05
Ca-catapleiite	$Ca_4Zr_4Si_{12}H_{16}O_{44}$	2.114	6	369.2	0.77571	-5.704E-03	1.226E-04
	Chemical composition	**Average Hf-O bond length (Å)**	**CN**	**Hf Force constant (N/m)**	**Polynomial expansion coefficients[#]**		
					A_1	**A_2**	**A_3**
zircon	**$Zr_{15}HfSi_{16}O_{64}$ (2a, 2b, 2c)	2.140	8	327.3	0.09094	-4.01E-04	7.49E-06
	$Zr_{31}HfSi_{32}O_{128}$ (2a, 2b, 2c)	2.140	8	326.4	0.09067	-4.00E-04	7.46E-06

Table 3.2 *continued*

ilmenite	**$Fe_{16}Ti_{15}HfO_{48}$ (2a, 2b, 2c)	2.092	6	297.1	0.08254	-3.64E-04	6.79E-06
	$Fe_{24}Ti_{23}HfO_{72}$ (2a, 2b)	2.092	6	294	0.08167	-3.60E-04	6.72E-06
Ca-catapleiite	$Ca_4Zr_3HfSi_{12}H_{16}O_{44}$	2.081	6	393.3	0.10928	-4.82E-04	8.99E-06
	$Ca_8Zr_7HfSi_{24}H_{32}O_{88}$ (2a)	2.082	6	394.1	0.10951	-4.83E-04	9.01E-06

□ represents vacancy.

#The polynomial expansion equation is: $10^3 \ln\beta = A_1 x + A_2 x^2 + A_3 x^3$, where $x = 10^6/T^2$. T is temperature in Kelvin.

Abbreviations after chemical formulas refer to the expansion way of primitive cells to generate supercells and investigate the effect of dilution. For instance, "2a, 2b, 2c" represents the supercell is generated by expanding the primitive cell twice along a, b, and c directions.

*These substitutions are favored by spectroscopic observations (Farges et al., 1994).

**The primitive cells of zircon ($Zr_2Si_2O_8$) and ilmenite ($Fe_2Ti_2O_6$) are used to construct the supercell.

Table 3.3 Calculated cell parameters and volumes of zircon, baddeleyite, and Ca catapleiite under static conditions.

Minerals	a (Å)	b (Å)	c (Å)	α (º)	β (º)	γ (º)	Volume (Å^3)	
zircon	6.7056	6.7056	6.0390	90.00	90.00	90.00	271.5441	This study
	6.6102	6.6102	5.9860	90.00	90.00	90.00	261.5567	Exp. 1
baddeleyite	5.2188	5.2797	5.4052	90.00	99.67	90.00	146.8201	This study
	5.15050	5.21160	5.31730	90.00	99.23	90.00	140.8808	Exp. 2
Ca	7.5060	12.8808	10.1933	89.31	89.52	89.84	985.4147	This study
catapleiite	7.378	12.779	10.096	90.00	90.00	90.00	951.89	Exp. 3

Data sources: Exp. 1(Finch et al., 2001); Exp. 2(Howard et al., 1988); Exp. 3(Merlino et al., 2004).

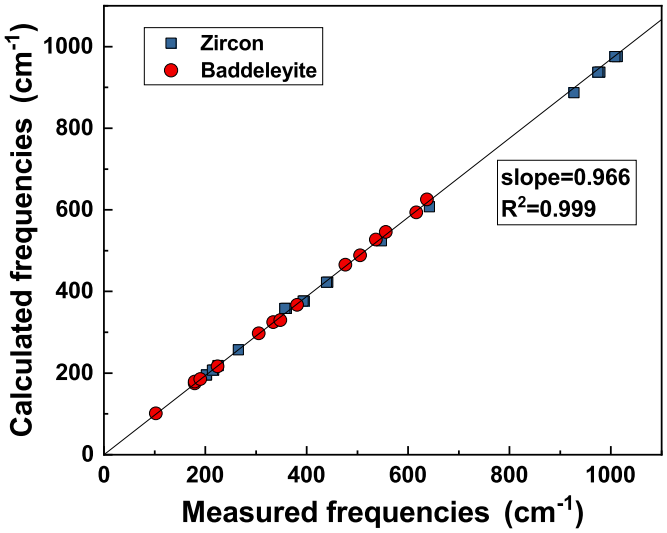

Figure 3.1 Comparison of the calculated vibrational frequencies with experimental data (Raman spectra) with the same vibrational modes. Experimental data sources: zircon (Syme et al., 1977; Gucsik et al., 2004); baddeleyite (Quintard et al., 2004).

3.3 Results

The average Zr-O bond lengths and Zr coordination numbers (CNs) in all calculated minerals are listed in **Table 3.2**. The average Zr-O bond length and Zr CN depend on the threshold adopted for Zr-O bond lengths. In all calculated minerals, the Zr-O distances form two populations, ranging from 1.9 Å to 2.4 Å, or greater than 3.0 Å. Here we adopted a value of 2.4 Å as the cutoff to determine Zr-O bond lengths and Zr CNs. The Zr CN ranges from 4 in silicate minerals with the substitution $Si^{4+}\leftrightarrow Zr^{4+}$ to 8 in zircon, and the average Zr-O bond length ranges from 1.960 Å in olivine with the substitution $Si^{4+}\leftrightarrow Zr^{4+}$ to 2.228 Å in zircon. In addition, within the explored compositional space (**Table 3.2**), there is no significant Zr concentration effect on the average Zr-O bond lengths in Zr-doped minerals.

As discussed in Section 3.2.1 and references therein, the main control on equilibrium isotopic fractionation is the bond strength or force constant, and at high temperature $1000\ln\beta$ is directly proportional to $\langle F \rangle$. The Zr force constants vary from 280 to 566 N/m in the calculated minerals (**Table 3.2**). In all minerals, Zr is primarily coordinated with oxygen and as expected (Schauble, 2004), the main control on the bond strength (force constant) is coordination (**Fig. 3.2A**), which is also manifested as a correlation between force constant with bond length (**Fig. 3.2B**). The average Zr force constants of minerals in 4, 6, 7, and 8 coordination are 540, 366, 323, 340 N/m respectively. Among them, ilmenite (6-fold coordination), magnetite (6), apatite (6), baddeleyite (7) and zircon (8) have weaker Zr-O bonds than that of 6-fold coordination Ca-catapleiite, the silicate melt proxy mineral. Geikielite (6-fold coordination) and most of the silicate minerals with Zr in mostly 4- and 6-fold coordination have stronger Zr-O bonds than that of 6-fold

coordinated Ca-catapleiite. Pyrope with the substitution $^{VIII}Mg^{2+}+{}^{VIII}Mg^{2+}\leftrightarrow Zr^{4+}+\square$ is the only silicate mineral calculated with a weaker Zr-O bond strength than the melt.

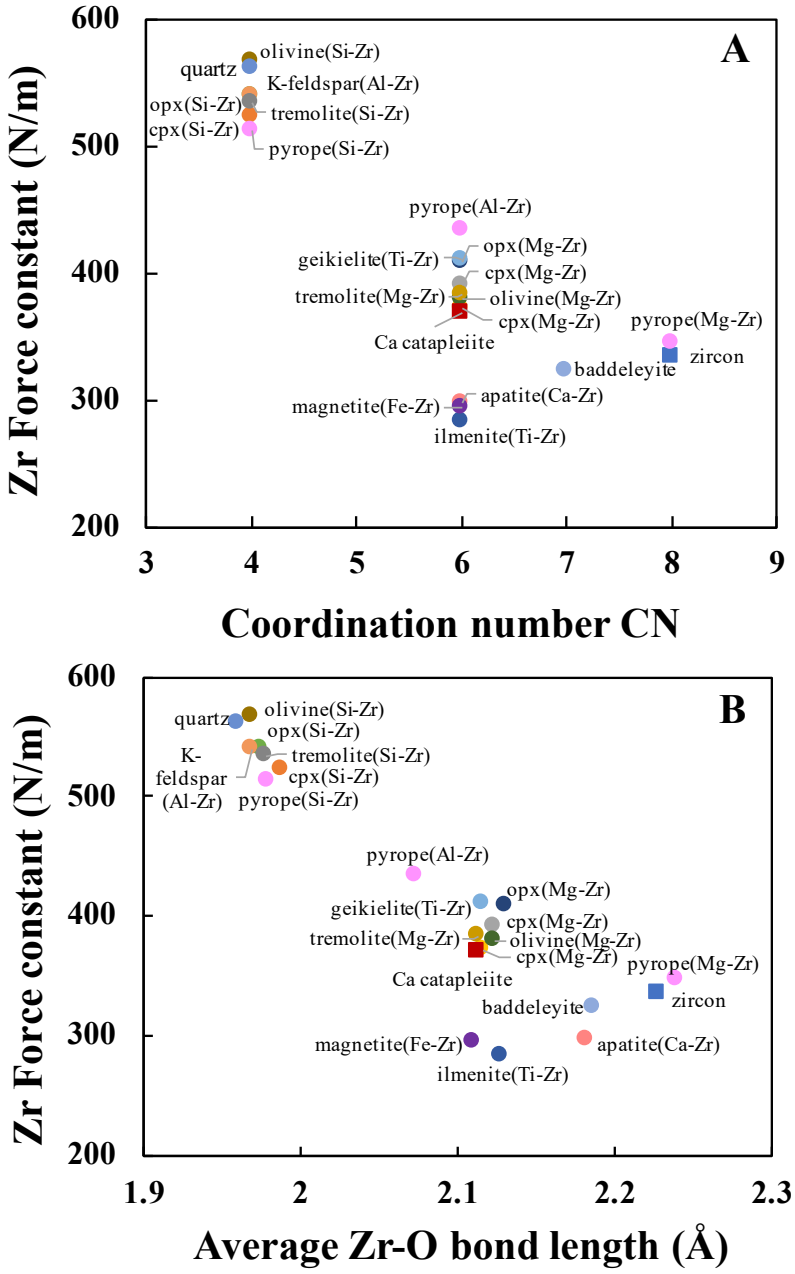

Figure 3.2 (A) Zr mean force constant (N/m) as a function of Zr coordination number in minerals calculated in this study. Lower coordination number generally corresponds to higher force constant

Figure 3.2 *continued*
(stronger bond). (B) Zr mean force constant (N/m) as a function of Zr-O bond length (Å). Shorter Zr-O bond length generally corresponds to stronger bond.

The $1000\ln\beta$ values of $^{94}Zr/^{90}Zr$ of all calculated minerals can be expressed as a function of temperature ($10^3\ln\beta = A_1x + A_2x^2 + A_3x^3$, where $x = 10^6/T^2$ and T is temperature in Kelvin; Eq. 3.4). The coefficients of this polynomial expansion are listed in **Table 3.2**. For many non-traditional stable isotope systems, one can relate equilibrium fractionation at any temperature to an expansion in the even powers of $\langle F \rangle$ (Dauphas et al., 2017, 2018). For a Debye phonon density of states (PDOS), we would have,

$$1000\ln\beta \simeq 1000\left(\frac{m_h}{m_l} - 1\right)\left(\frac{\gamma}{8}\frac{\langle F\rangle}{T^2} - \frac{5\gamma^2}{2016}\frac{\langle F\rangle^2}{T^4} + \frac{25\gamma^3}{326592}\frac{\langle F\rangle^3}{T^6}\right), \quad (3.8)$$

with $\gamma = \hbar^2/(k_B^2 m_h)$. Phonon density of states of naturally occurring minerals rarely follow a Debye profile and we can improve on this formula by writing a more general, semi-empirical equation,

$$1000\ln\beta \simeq B_1\langle F\rangle/T^2 - B_2\langle F\rangle^2/T^4 + B_3\langle F\rangle^3/T^6, \quad (3.9)$$

with $B_1 = 1000(1/m_l - 1/m_h)\,\hbar^2/(8{k_B}^2)$, and B_2 and B_3 constants that depend on the element and isotopes considered (and to some extent the particular PDOS, although these are second order corrections and the exact shape of the PDOS does not matter too much). We have calculated the values of B_2 and B_3 by regressing A_2 *vs.* $\langle F\rangle^2$ and A_3 *vs.* $\langle F\rangle^3$ (**Fig. 3.3)** for the purpose of evaluating the validity of the high-temperature approximation. Note that the equivalent regressions of A_2 *vs.* ${A_1}^2$ and A_3 *vs.* ${A_1}^3$ provide a rapid means of assessing the consistency of the polynomial expansion as an erroneous reporting of the coefficients would show up as an outlier in these diagrams. We find the approximate formula,

$$1000\ln\beta(^{94}Zr/^{90}Zr) \simeq 2081\langle F\rangle/T^2 - 2.5\times10^4\langle F\rangle^2/T^4 + 8.5\times10^5\langle F\rangle^3/T^6, \quad (3.10)$$

In **Fig. 3.4A** (also see **Fig. 3.5**), we use this formula to calculate the extent to which the high-temperature approximation (truncating the polynomial to the first order; Eq. 3.6, 3.9, and 3.10) can approximate the true value of $1000\ln\beta$ (Eq. 3.4) as a function of T and $\langle F\rangle$ (see Fig. 3 of Dauphas et al. (2012) for a similar figure for iron). As shown, given that the force constants of Zr bonds in all calculated minerals are between 280 and 566 N/m, we find that provided that the temperature is higher than ~300-500 °C, truncating the expansion to the first order gives a $1000\ln\beta$ value that is within 1% of the value given by the whole expansion. For most high-temperature applications in metamorphic and igneous geochemistry and petrology, the high-temperature approximation $1000\ln\beta \simeq 2081\langle F\rangle/T^2$ is therefore valid.

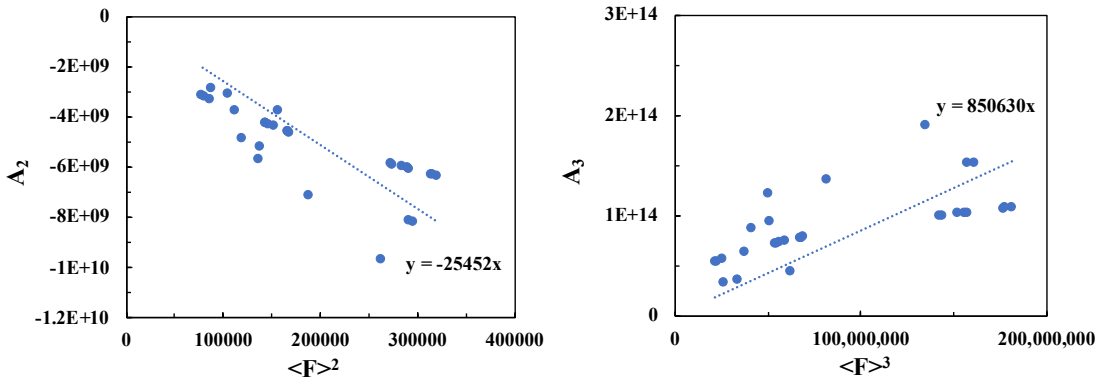

Figure 3.3 Polynomial expansion coefficient (left) A_2 vs $\langle F\rangle^2$ and (right) A_3 vs $\langle F\rangle^3$ for $1000\ln\beta(^{94}Zr/^{90}Zr)$. The regressions give the estimated values of B_2 and B_3 in the one-parameter approximate formula (see eq. 3.9 and 3.10).

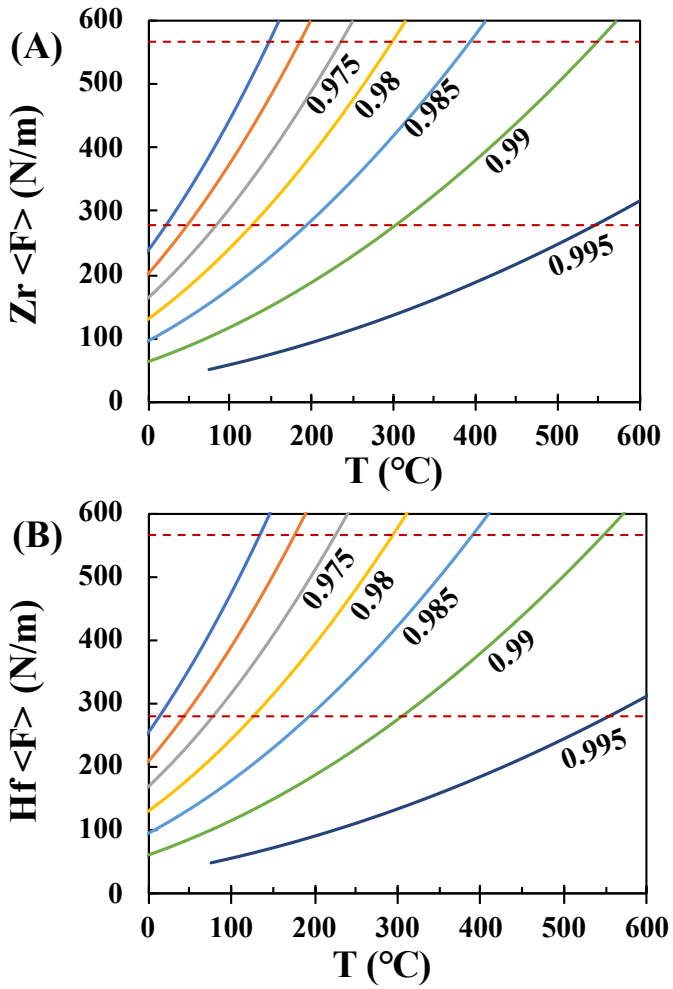

Figure 3.4 Relative error in the high temperature approximation $1000ln\beta = \mathrm{B}_1\langle \mathrm{F}\rangle/\mathrm{T}^2$ (Eqs. 3.6, 3.7) calculated using the 1-parameter 3-term expansion $1000\ln\beta = \mathrm{B}_1\langle \mathrm{F}\rangle/\mathrm{T}^2 + \mathrm{B}_2\langle \mathrm{F}\rangle^2/\mathrm{T}^4 + \mathrm{B}_3\langle \mathrm{F}\rangle^3/\mathrm{T}^6$ (Eqs. 3.10, 3.12). The curves were calculated following Dauphas et al. (2012) for different values of T and $\langle F\rangle$. (A) Relative departure from Eq. (3.10) when truncating the polynomial to the first order for Zr. The force constants of Zr bonds in all calculated minerals are between 280 and 566 N/m (red dashed lines). When the temperature is higher than ~300-500 ℃, truncating the expansion to the first order (Eq. 3.6) will give a $1000\ln\beta$ value that is within 1% of the value given by the whole expansion (Eq. 3.4). (B) Relative departure from Eq. (3.12) when truncating the polynomial to the first order for Hf. When the temperature is higher than ~300-500 ℃, truncating the expansion to the first order (Eq. 3.7) will give a $1000\ln\beta$ value that is within 1% of the value given by the whole expansion (Eq. 3.4). The high temperature approximation can be applied to calculate equilibrium Zr and Hf isotopic fractionation in igneous and metamorphic geochemistry/petrology without compromising accuracy.

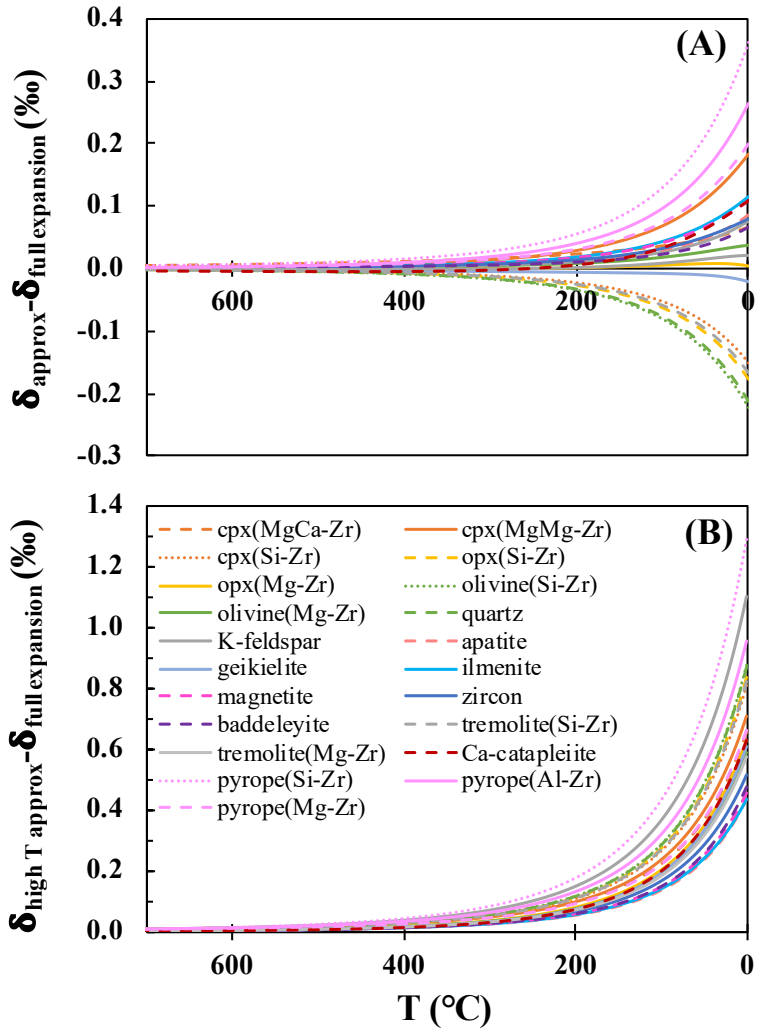

Figure 3.5 Differences of Zr 1000lnβ between (A) the 1-parameter 3-term expansion (eq. 3.9) and the full polynomial expansion equation (eq. 3.4), and (B) the 1-parameter 1-term high-temperature approximation (eq. 3.9 truncated to the first term) and the full polynomial expansion equation (eq. 3.4).

The Zr-doped silicate minerals with the substitution $Si^{4+} \leftrightarrow Zr^{4}$ have significantly larger β factors than other species. This is mainly because Zr in these silicate minerals form stiffer bonds due to the incorporation of Zr into the low-coordination (IV) tetrahedral Si site. At 1000 K, the

$1000\ln\beta$ values range from 1.17 ‰ in Zr-doped olivine (substituting Si) to 0.58 ‰ in Zr-doped ilmenite (substituting Ti). It decreases in the order of Zr-doped olivine (substituting Si), quartz, orthopyroxene, K-feldspar (substituting Al) ~ tremolite (substituting Si) ~ clinopyroxene (substituting Si) ~ pyrope (substituting Si) > pyrope (substituting Al) > geikielite (substituting Ti) ~ orthopyroxene, clinopyroxene, tremolite, and olivine (substituting Mg) > Ca-catapleiite > pyrope (substituting Mg) > zircon ~ baddeleyite > apatite (substituting Ca) ~ $MgFe_2O_4$ magnetite (substituting Fe) > ilmenite (substituting Ti). The temperature dependence of the reduced partition function ratio ($1000\ln\beta$), as well as the equilibrium fractionation factors between minerals and melt ($1000ln\alpha_{mineral-melt}$; taking Ca-catapleiite as a silicate melt proxy) are shown in **Fig. 3.6**. As expected, they scale linearly with $1/T^2$.

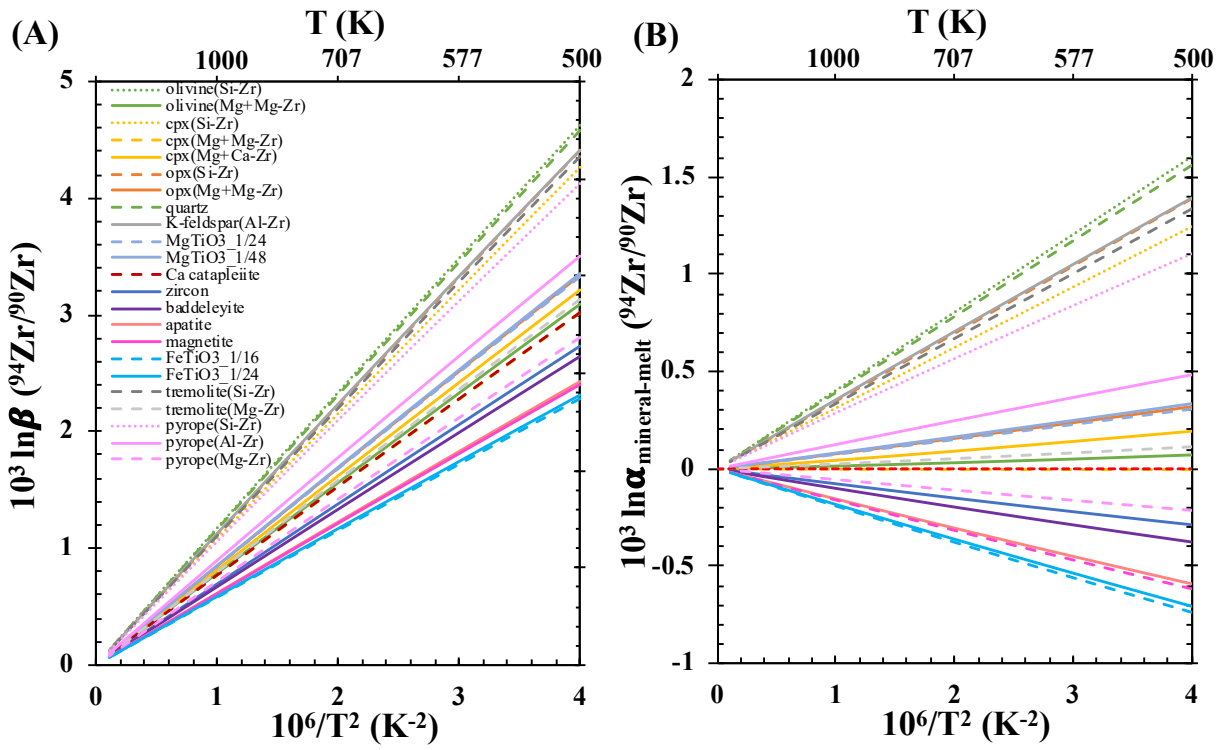

Figure 3.6 (A) Temperature-dependent 1000lnβ for Zr isotopes in minerals investigated in this study. (B) Temperature-dependent $1000\ln\alpha_{\mathrm{mineral-melt}}$ for Zr isotopes in the same set of minerals. The fractionation factors between minerals and melt are calculated by taking the difference between each mineral and Ca-catapleiite (which we use as silicate melt proxy). The calculation results for minerals with different Zr substitution mechanisms as well as different Zr concentrations are also shown in the figure. See main text and Table 3.2 for details.

We have also performed some *ab initio* calculations substituting Hf for Zr in several minerals showing a wide range of Zr bond strengths: zircon, Ca-catapleiite, and ilmenite (**Fig. 3.7**). The force constants of Hf bonds are very similar to those of Zr (**Table 3.2** and **Fig. 3.8**), defining a linear correlation,

$$\langle F_{\mathrm{Hf}}\rangle = (1.032 \pm 0.021)\langle F_{\mathrm{Zr}}\rangle \ , \qquad (3.11)$$

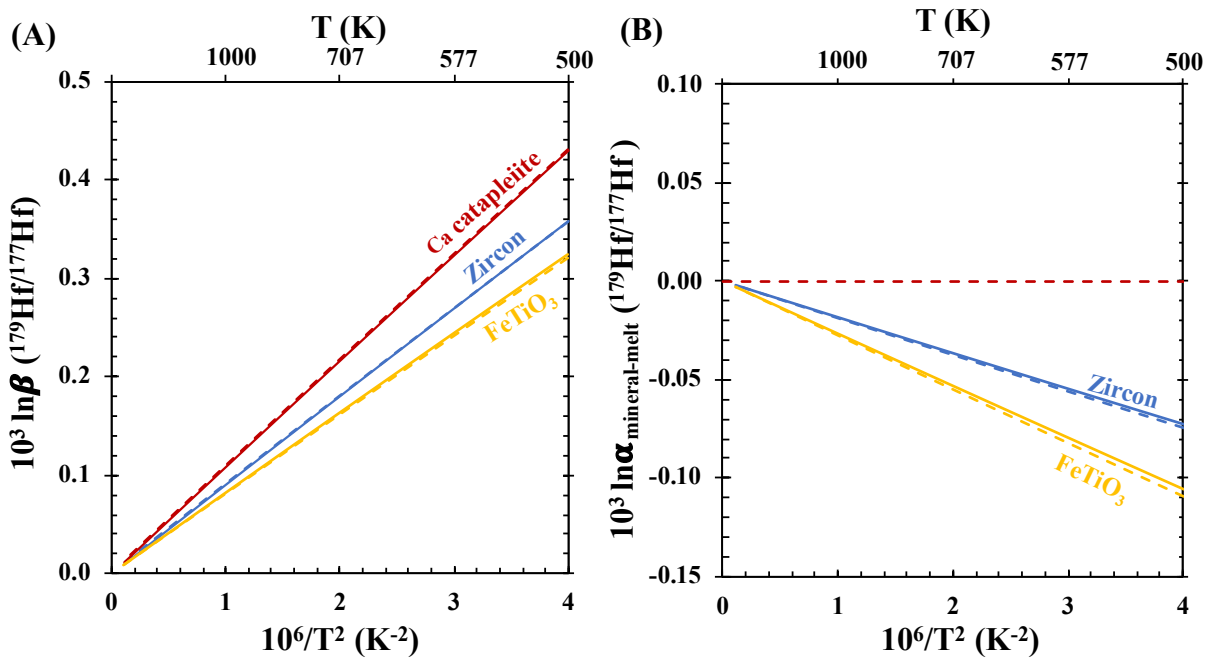

Figure 3.7 (A) Temperature-dependent 1000lnβ for Hf isotopes in zircon, ilmenite and Ca-catapleiite investigated in this study. (B) Temperature-dependent $1000\ln\alpha_{\mathrm{mineral-melt}}$ for Hf isotopes in zircon and ilmenite. As with Zr isotopes, the fractionation factors between minerals and melt are calculated by taking the difference between each mineral and Ca-catapleiite (which we use as silicate melt proxy). Solid and dash lines are calculation results for minerals with different Hf concentrations (see Table 3.2 for details). Our results show that Hf stable isotope fractionation during equilibrium process is very limited.

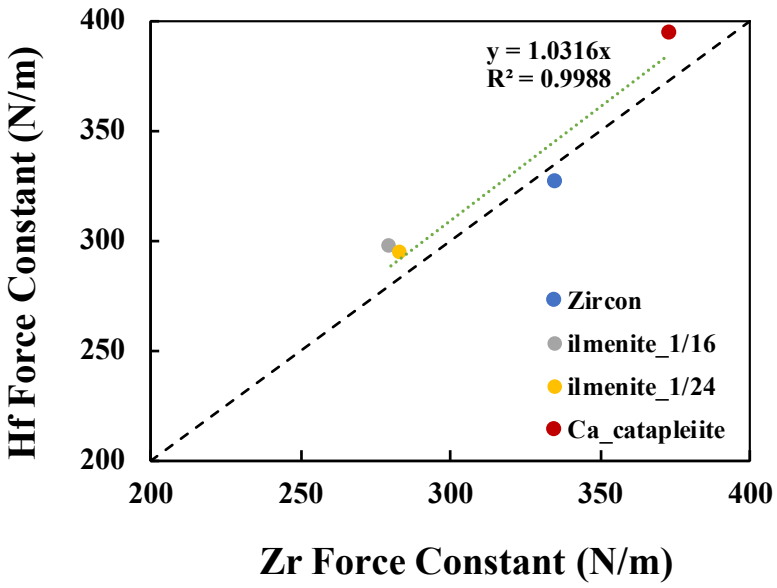

Figure 3.8 Zr and Hf mean force constants in several minerals (zircon, ilmenite with two concentrations, Ca-catapleiite). The current calculation results indicate that in minerals, Zr and Hf form bonds with nearly identical bond strengths. The black dashed line is the 1:1 line and the green dotted line is a regression through the data.

By regressing A_2 *vs.* $\langle F\rangle^2$ and A_3 *vs.* $\langle F\rangle^3$ (**Fig. 3.9**), we derive a one-parameter approximate equation for the $1000\ln\beta$ value of Hf,

$$1000\ln\beta(^{179}\mathrm{Hf}/^{177}\mathrm{Hf}) \simeq 278\langle F\rangle/T^2 - 3464\langle F\rangle^2/T^4 + 175551\langle F\rangle^3/T^6, \qquad (3.12)$$

As with Zr (**Fig. 3.4A**; also see **Fig. 3.5**) and Fe (Dauphas et al., 2012), we use this formula to calculate the extent to which truncating the formula to the first term $1000\ln\beta(^{179}\mathrm{Hf}/^{177}\mathrm{Hf}) \simeq 278\langle F\rangle/T^2$ (Eq. 3.7) provides an adequate approximation of the $1000\ln\beta$ value (Eq. 3.4; **Fig. 3.4B** and **Fig. 3.10**). We find that provided that the temperature is higher than ~300-500 ℃, truncating the expansion to the first order gives a $1000\ln\beta$ value that is within 1% of the value given by the whole expansion. As with Zr, the first term of the polynomial gives an adequate

description of equilibrium Hf isotopic fractionation for applications in igneous and metamorphic geochemistry/petrology.

Given the near-identical force constants of Zr and Hf, the ratio of equilibrium fractionation factors is directly related to the mass of the isotopes involved through (combine Eqs. 3.6 and 3.7),

$$\frac{1000\ln\alpha(^{94}\mathrm{Zr}/^{90}\mathrm{Zr})}{1000\ln\alpha(^{179}\mathrm{Hf}/^{177}\mathrm{Hf})} = \frac{2081}{278} = 7.5\,, \tag{3.13}$$

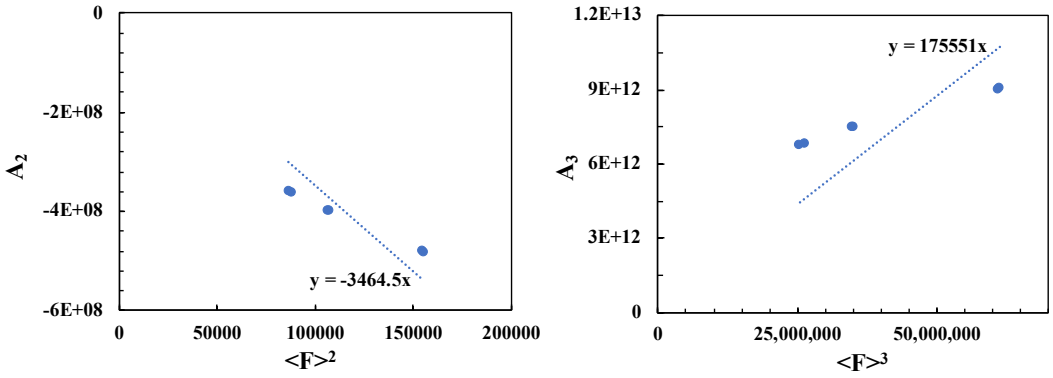

Figure 3.9 Polynomial expansion coefficient (left) A_2 vs $\langle F\rangle^2$ and (right) A_3 vs $\langle F\rangle^3$ for $1000\ln\beta(^{179}\mathrm{Hf}/^{177}\mathrm{Hf})$. The regressions give the estimated values of B_2 and B_3 in the one-parameter approximate formula (see eq. 3.9 and 3.12).

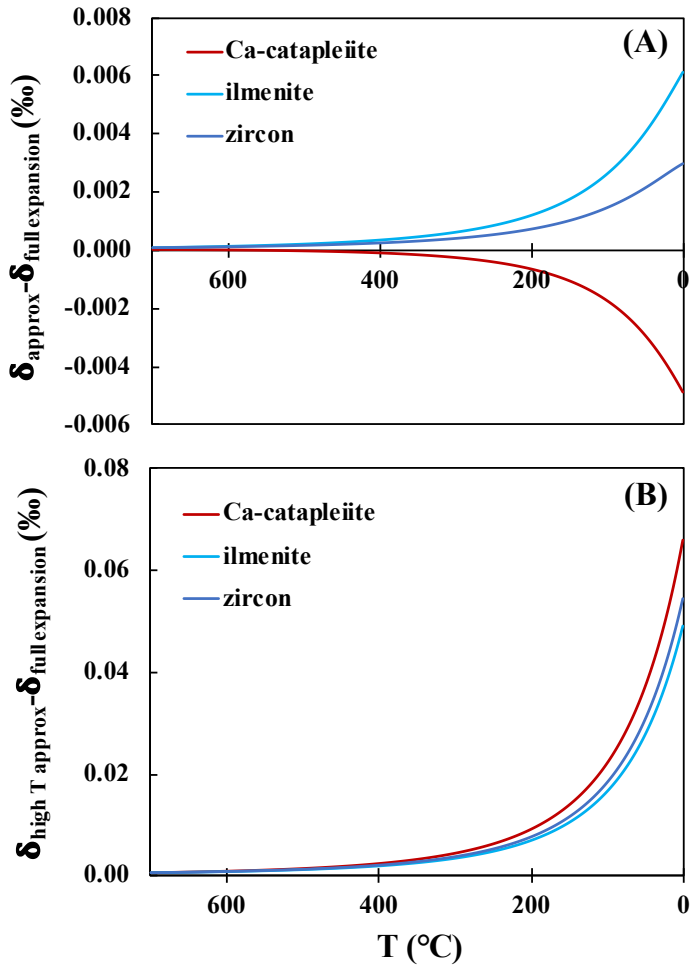

Figure 3.10 Same as Figure 3.5 but for Hf rather than Zr.

3.4 Discussion

As we mentioned in the introduction, the use of Zr isotopic fractionation as a petrogenetic tracer of zircon formation is hampered by our lack of understanding of what controls this fractionation.

Zirconium isotopic analyses reported thus far on bulk rocks and individual zircons (Inglis et al., 2018, 2019; Ibañez-Mejia and Tissot, 2019; W. Zhang et al., 2019; Feng et al., 2020; Guo et al., 2020; Tian et al., 2020; Tompkins et al., 2020) yield contradictory evidence with regard to

what controls the observed Zr isotopic variations, and whether zircons are enriched in the light or heavy isotopes of Zr relative to coexisting magma. Below we use the newly established fractionation factors to show that equilibrium zircon-melt fractionation cannot account for the large Zr isotopic variations that have been documented. These fractionations are most likely explained by diffusion-driven kinetic isotopic fractionation.

3.4.1 Equilibrium Zr isotopic fractionation during zircon crystallization from silicate melts

Zircon is an important carrier of Zr and Hf in igneous rocks, so we start by focusing on the effects of the equilibrium crystallization of this mineral on the behavior of Zr and Hf stable isotopes during magmatic differentiation. Following Inglis et al. (2019) and Ibanez-Meija and Tissot (2019), we model Zr isotopic fractionation during zircon crystallization using a Rayleigh distillation model,

$$\delta'^{94}\mathrm{Zr}_{\mathrm{melt}} = \delta'^{94}\mathrm{Zr}_0 + \Delta_{\mathrm{Zr}}^{\text{zircon-melt}} \ln f_{\mathrm{Zr}}\,, \tag{3.14}$$

where $\delta'^{94}\mathrm{Zr}_{\mathrm{melt}}$ and $\delta'^{94}\mathrm{Zr}_0$ are the Zr isotopic compositions of the residual and starting melt respectively, expressed as $\delta'^{94}\mathrm{Zr} = 10^3 \ln\left[(^{94}\mathrm{Zr}/^{90}\mathrm{Zr})_{\mathrm{sample}}/(^{94}\mathrm{Zr}/^{90}\mathrm{Zr})_{\mathrm{std}}\right]$, f_{Zr} is the fraction of Zr remaining in the melt, and $\Delta_{\mathrm{Zr}}^{\text{zircon-melt}} = 1000 \ln \alpha_{\mathrm{Zr}}^{\text{zircon-melt}}$ is the instantaneous isotopic fractionation factor of Zr between zircon and melt. The Zr isotopic composition of the instantaneous zircon crystallized from the melt can be calculated as,

$$\delta'^{94}\mathrm{Zr}_{\mathrm{i,zircon}} = \delta'^{94}\mathrm{Zr}_0 + \Delta_{\mathrm{Zr}}^{\text{zircon-melt}} (1 + \ln f_{\mathrm{Zr}})\,, \tag{3.15}$$

The zirconium isotopic composition of the cumulative zircon is obtained by mass-balance with the residual melt and initial composition,

$$\delta'^{94}\mathrm{Zr}_{\mathrm{c,zircon}} = \delta'^{94}\mathrm{Zr}_0 - \Delta_{\mathrm{Zr}}^{\text{zircon-melt}} \frac{f_{\mathrm{Zr}}}{1 - f_{\mathrm{Zr}}} \ln f_{\mathrm{Zr}}\,, \tag{3.16}$$

Both Inglis et al. (2019) and Ibanez-Meija and Tissot (2019) derived apparent $\Delta_{Zr}^{zircon\text{-}melt}$ values from their measurements. The $\Delta_{Zr}^{zircon\text{-}melt}$ values that they calculated have opposite directions and different magnitudes. Inglis et al. (2019) found that Zr in the melt becomes isotopically heavy in the course of magmatic differentiation of the Hekla volcano, meaning that zircon must be enriched in the light Zr isotopes. They were able to fit their data with an instantaneous fractionation $\Delta_{Zr}^{zircon\text{-}melt} = -0.5$ ‰. Ibanez-Meija and Tissot (2019) measured many zircons from an anorthositic gabbro (FC-1) and found that the statistical distribution of these δ'^{94}Zr values extended to very negative values, which they argue is more readily explained if zircon crystallizing from the melt was enriched in the heavy isotopes of Zr, and the most negative δ'^{94}Zr values resulted from crystallization from a melt that has experienced extensive distillation. By fitting their statistical distribution, they obtain $\Delta_{Zr}^{zircon\text{-}melt} = +1.06$ ‰. These two studies focused on different materials (bulk rocks sampling a magmatic differentiation trend in the case of Inglis et al. (2019); individual zircons sampling fractional crystallization within a single rock in the case of Ibanez-Meija and Tissot (2019)). Based on available data, it is impossible to tell what is the cause of the discrepancy between these two studies and whether the measurements reflect equilibrium or diffusion-driven kinetic isotopic fractionation, as has been demonstrated previously for Mg and Fe in igneous rocks (Dauphas et al., 2010; Teng et al., 2011; Sio et al., 2013; Oeser et al., 2015; Kin I Sio and Dauphas, 2017).

We have calculated Zr force constants of 335 and 369 N/m for zircon and Ca-catapleiite (the silicate melt proxy), respectively (**Table 3.2**). The slightly higher force constant of Ca-catapleiite relative to zircon is consistent with its lower coordination number (6 for catapleiite *vs*.

8 for zircon). The equilibrium Zr isotopic fractionation between zircon and melt is given by the formula,

$$\Delta^{94}\mathrm{Zr}^{\mathrm{eq}}_{\text{zircon-melt}} = -\frac{7.87\times10^{4}}{T^{2}} + \frac{1.94\times10^{9}}{T^{4}} - \frac{5.85\times10^{13}}{T^{6}}, \quad (3.17)$$

At the temperatures relevant to igneous zircon crystallization of ~700-1000 °C, the equilibrium fractionation would only be -0.048 to -0.081 ‰ (**Fig. 3.11**). The lower δ'^{94}Zr value of zircon relative to silicate melt at equilibrium is due to differences in coordination numbers. The equilibrium fractionation is opposite in sign to the inferred instantaneous zircon-melt fractionation of Ibanez-Meija and Tissot (2019) and is much smaller in magnitude than the values given by both Inglis et al. (2019) and Ibanez-Meija and Tissot (2019). Taken at face value, this would suggest that the instantaneous Zr isotopic fractionations measured in these two studies do not reflect equilibrium. A caveat to this comparison is that we used Zr in 6-fold coordination in Ca-catapleiite ($\langle F \rangle = 369$ N/m) as a proxy for Zr in silicate melt. As shown in **Table 3.2** and **Fig. 3.2A**, Zr in 6-fold coordination in other minerals has force constants that range between 280 and 433 N/m. Using these values for Zr in melt and 335 N/m for zircon would result in zircon-melt equilibrium fractionations in the range -0.12 to +0.21 ‰ above 700 °C. These values are again much smaller than the values inferred by Inglis et al. (2019) and Ibanez-Meija and Tissot (2019), strengthening the case that the values given in these two studies do not reflect zircon-melt equilibrium.

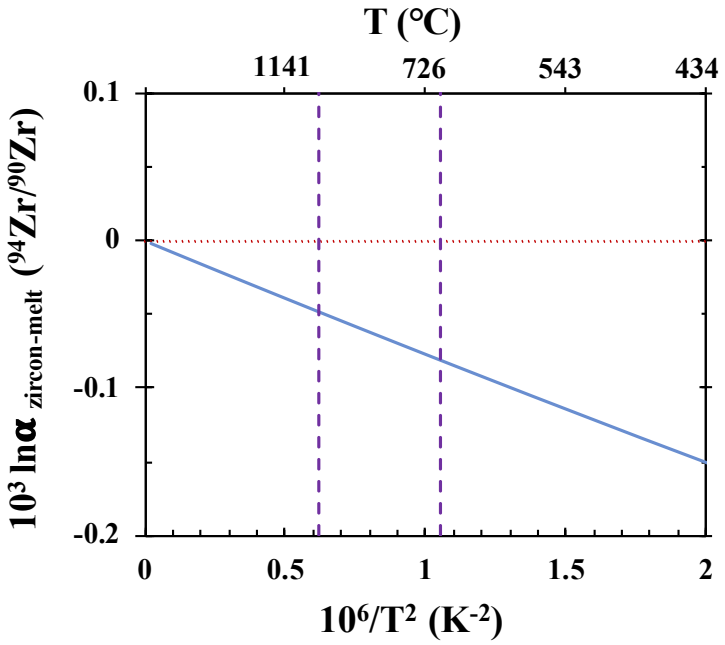

Figure 3.11 Zr isotope equilibrium fractionation factor between zircon and melt as a function of temperature. The two vertical dash lines bracket the temperatures relevant to igneous zircon crystallization of around 700-1000 °C.

We further evaluate below how combining Zr isotopic compositions with Zr/Hf ratios can help identify zircons that grew in equilibrium with the melt. By equilibrium, we mean that zircon growth increments were in equilibrium with the bulk melt but distillation effects can still be present if Zr self-diffusion was too slow for the zircon interior to equilibrate with its rim, or if zircons were sequestered from the melt. The degree of isotopic fractionation in the instantaneous fraction of zircon crystallizing in equilibrium with the melt is given by (combining Eqs. 3.15 and 3.17),

$$\delta'^{94}\mathrm{Zr}_{\mathrm{i,zircon}} = \delta'^{94}\mathrm{Zr}_0 - \frac{7.87\times10^4}{T^2}(1+\ln f_{\mathrm{Zr}})\,, \tag{3.18}$$

In **Fig. 3.12**, we plot the value of $\delta'^{94}\mathrm{Zr}_{\mathrm{i,zircon}}$ for different Zr fractions in zircon $(1-f_{\mathrm{Zr}})$ and two temperatures of 700 and 1000 °C. As shown, at equilibrium the slightly lower δ'^{94}Zr value of zircon relative to the melt can drive the melt to evolve toward heavy δ'^{94}Zr values,

reaching +0.25 ‰ (at 700 °C) and +0.14 ‰ (at 1000 °C) at 95% crystallization. One way to assess whether the data can be explained by equilibrium is to combine $\delta'^{94}\mathrm{Zr}$ with Zr/Hf analyses. Indeed, these two observables should correlate in a predictable manner during equilibrium zircon crystallization as they both depend on T and f_{Zr}. Zircon is a solid solution of zircon ($\mathrm{ZrSiO_4}$) and hafnon ($\mathrm{HfSiO_4}$), and Hf zoning is often observed due to zircon growth while the melt composition evolves by fractional crystallization. Zirconium is more compatible than Hf in zircon, resulting in a decrease of the Zr/Hf ratio during fractional crystallization of zircon. Such Zr/Hf fractionations have been documented within zircon grains (from core to margin) and in bulk rocks (Claiborne et al., 2006, 2010; Padilla et al., 2016). Similar to $\delta'^{94}\mathrm{Zr}$, we can model Zr/Hf fractionation using a Rayleigh distillation equation:

$$(\mathrm{Zr/Hf})_{\mathrm{melt}} = (\mathrm{Zr/Hf})_0 \, f_{\mathrm{Zr}}^{1-1/K_d} \ , \tag{3.19}$$

where $(\mathrm{Zr/Hf})_{melt}$ is the ratio in the melt, $(\mathrm{Zr/Hf})_0$ is the initial melt ratio, f_{Zr} is the fraction of the remaining Zr in melt, and K_d is the $\mathrm{Zr/Hf}$ exchange coefficient between zircon and melt,

$$\frac{(\mathrm{Zr/Hf})_{\mathrm{zircon,inst}}}{(\mathrm{Zr/Hf})_{\mathrm{melt}}} = K_d \ , \tag{3.20}$$

We thus have,

$$(\mathrm{Zr/Hf})_{\mathrm{zircon,inst}} = K_d \, (\mathrm{Zr/Hf})_0 \, f_{\mathrm{Zr}}^{1-1/K_d} \ , \tag{3.21}$$

The zircon $\mathrm{Zr/Hf}$ ratio is not only a function of the extent of fractional crystallization but also a function of temperature. Aranovich and Bortnikov (2018) proposed the following formula for K_d,

$$K_d = e^{1531/T - 0.883} \ , \tag{3.22}$$

In **Fig. 3.13**, we plot the calculated trends of Zr/Hf and δ'^{94}Zr variations in growth increments of zircon crystallized from silicate melt. The free parameters are the fraction of Zr remaining in melt (f_{Zr} from 0.99 to 0.01) and the crystallization temperature, which we keep fixed for simplicity (T from 870 to 600 ℃; calculations are done using equations 3.15 and 3.17, 3.21 and 3.22). We use an initial Zr/Hf ratio of 31.1, initial δ'^{94}Zr value of -0.086 ‰ (Ibañez-Mejia and Tissot, 2019), and the equilibrium isotopic fractionation factor inferred here $\Delta^{94}\mathrm{Zr}^{\mathrm{eq}}_{\text{zircon-melt}} = -\frac{7.87\times10^4}{T^2}$ (Eq. 3.17). We also plot the current analytical uncertainties of Zr/Hf ratio ($\pm1\%$) and δ'^{94}Zr isotopic composition (±0.01‰). The δ'^{94}Zr value is mostly sensitive to the extent of crystallization, while Zr/Hf ratio depends on both temperature and extent of crystallization. By plotting Zr/Hf and δ'^{94}Zr values in zircons, ideally measured along depth profiles (Zhang et al., 2019; Tompkins et al., 2020; Guo et al., 2020), one will be able to compare the results with theoretical predictions, test whether zircon grew in increments in equilibrium with coexisting melt, and assess the temperature (T) and extent (f_{Zr}) of zircon crystallization.

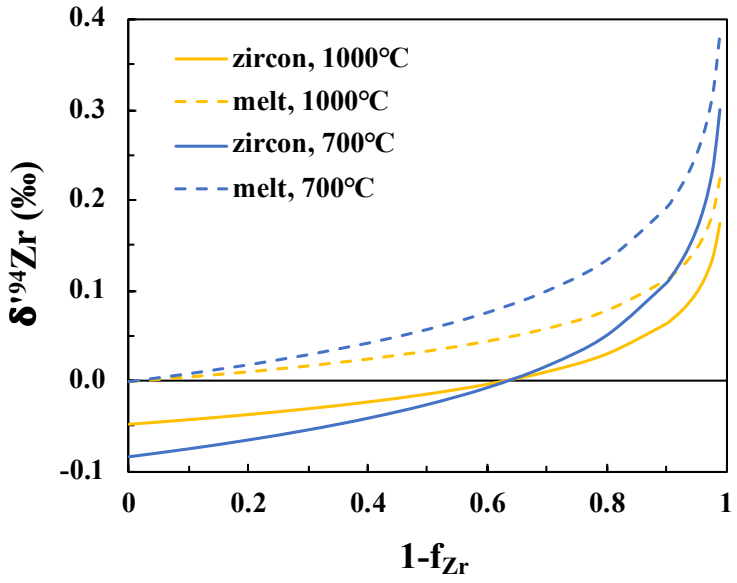

Figure 3.12 $\delta'^{94}Zr$ in the instantaneous zircon and melt during Rayleigh distillation process at two temperatures of 700 and 1000 °C. f_{Zr} is the fraction of Zr remaining in the melt (see Eq. 3.18). $1 - f_{Zr}$ is the fraction of Zr in zircon.

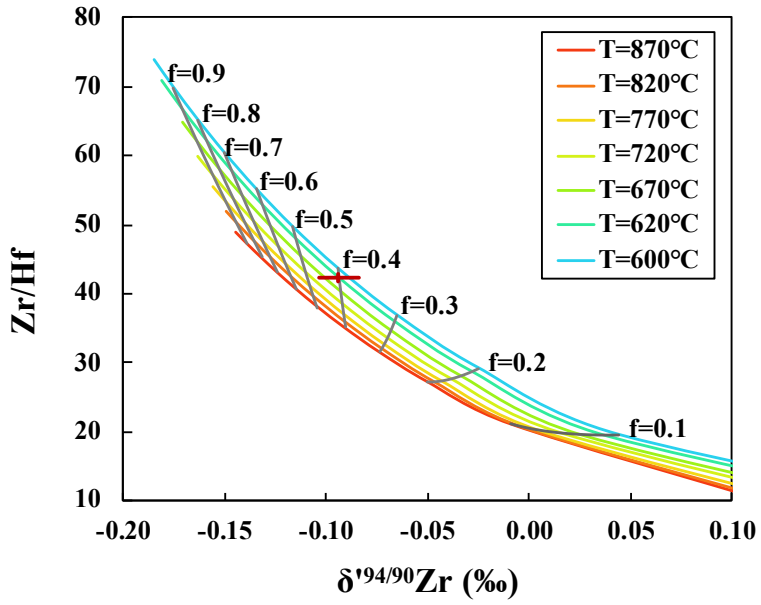

Figure 3.13 Calculated trends of Zr/Hf and $\delta'^{94}Zr$ variations in instantaneous zircon assuming melt-zircon equilibrium at each step of a distillation. The free parameters are the fraction of Zr remaining in melt (f_{Zr} from 0.99 to 0.01) and the crystallization temperature. The calculations are

Figure 3.13 *continued*
done using equations 3.15 and 3.17, 3.21 and 3.22, with an initial Zr/Hf ratio of 31.1 and initial $\delta'^{94}Zr$ value of -0.086 ‰ (Ibañez-Mejia and Tissot, 2019). The zircon-melt equilibrium isotopic fractionation factor is $\Delta^{94}Zr^{eq}_{zircon\text{-}melt} = -\frac{7.87\times10^4}{T^2}$ (Sect. 3.4.1, Eq. 3.17). The red data point shows the current analytical uncertainties of Zr/Hf ratio ($\pm1\%$) and $\delta'^{94}Zr$ isotopic composition (±0.01‰). This figure can help test if zircon grew under equilibrium conditions.

3.4.2 Equilibrium Zr isotopic fractionation before the onset of zircon crystallization in melts

Within the magmatic temperature range of zircon crystallization, our *ab initio* calculation results show limited equilibrium isotopic fractionation between zircon and melt (see **Fig. 3.11**). This can explain the homogenous Zr isotope compositions of those reference zircons reported in Zhang et al. (2019) and Tompkins et al. (2020), but it fails to explain the observations made at the Hekla volcano (Inglis et al., 2019) and zircons and baddeleyites from the FC-1 anorthositic gabbro (Ibañez-Mejia and Tissot, 2019). This implies that the current observed $\delta'^{94}Zr$ variations cannot be simply explained by the mechanism of equilibrium mass-dependent Zr isotopic fractionation between zircon and melt.

Below, we investigate whether equilibrium crystallization of other phases could have controlled Zr isotopic fractionation during magmatic differentiation. We used the Rhyolite-MELTS program (Gualda et al., 2012) to calculate the evolution of Zr concentration and isotopic composition during magmatic differentiation before the onset of zircon crystallization. The melt major-element compositions and temperature at each step in the Rhyolite-MELTS run were used as input in the zircon saturation models of Watson and Harrison (1983) and Boehnke et al. (2013) to check if zircon was saturated, as we were primarily interested here in evaluating the influence

of the crystallization of non-zircon phases on the isotopic composition of Zr during magmatic differentiation (see **Fig. 3.14**).

Two starting melt compositions were used to represent calc-alkaline and tholeiitic magmatic series (Helz et al., 1994; Millet et al., 2016). Both crystallization processes start at the calculated liquidus temperatures and at 1 kbar for calc-alkaline and 0.6 kbar for tholeiitic magma, respectively. For every 5℃ temperature decrease, the major element compositions and mass of melt and crystallizing minerals are calculated using Rhyolite-MELTS. At each step the program gives the proportions of every mineral crystallizing. As a trace element, Zr is not incorporated in Rhyolite-MELTS program, but its distribution among the phases can be calculated based on partition data (**Fig. 3.15**). The Zr partition coefficients ($K_{mineral/melt}$) of each mineral in different rock matrix were compiled from the GERM database (https://kdd.earthref.org/KdD). The compiled values vary in a wide range, due in part to the dependence of partition coefficients on melt composition and temperature. We use the geometric mean of the partition coefficients as fiducial values, and also consider the maxima and minima to assess uncertainties associated with partition data. Knowing the mass fractions of minerals that crystallize, the Zr partition coefficients between bulk rock and melts are calculated at each step, and mass balance between melt and bulk crystallizing solids is then used to calculate the Zr concentration in melt at each step. We also track the evolution of the Zr/Hf ratio and Hf concentration, using literature data for the Zr/Hf exchange coefficients between minerals and melt.

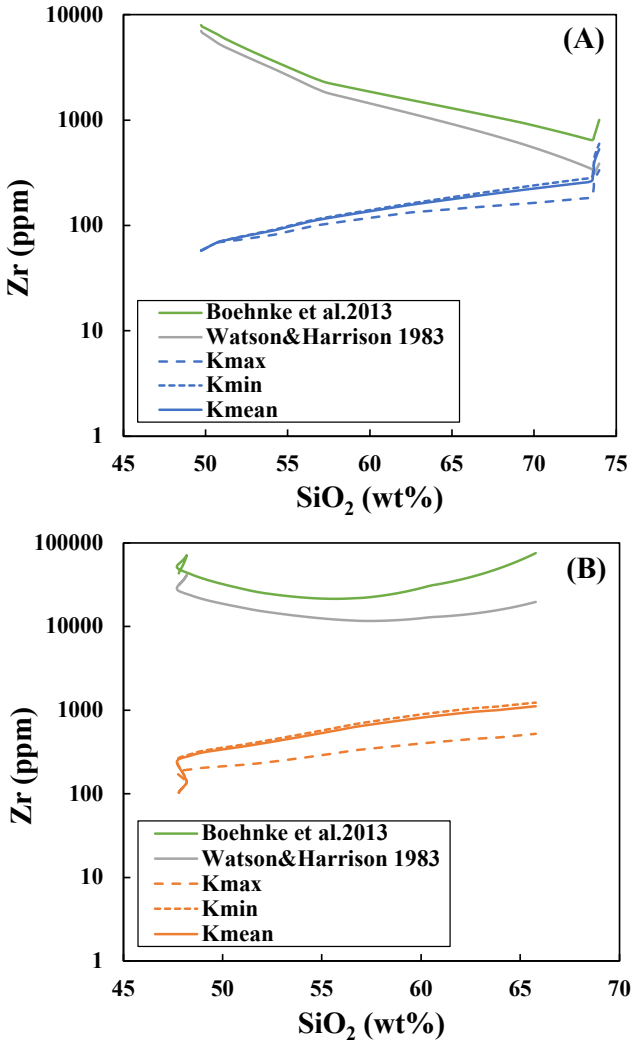

Figure 3.14 Evolution of Zr concentration remaining in the melt (blue and orange curves) and zircon saturation during fractional crystallization of a (A) calc-alkaline and (B) tholeiitic magmas. Calculations are done with different bulk partition coefficients (K) using the modeled mineral assemblage results of the Rhyolite-MELTS program (i.e., **Fig. 3.15**). The zircon saturation curves (green and gray lines) were calculated using Watson and Harrison (1983) and Boehnke et al. (2013) and taking the melt major-element compositions and temperature from the Rhyolite-MELTS program as input. The initial compositions used in Rhyolite-MELTS modeling are (A) calc-alkaline (Millet et al., 2016) (in wt%) SiO_2: 49.7; TiO_2: 0.99; Al_2O_3: 18.39; Fe_2O_3: 2.13; Cr_2O_3: 0; FeO: 9.00; MnO: 0.19; MgO: 5.46; CaO: 8.94; Na_2O: 2.49; K_2O: 0.69; P_2O_5: 0.19; H_2O: 1.78; P: 1 kbar; (B) tholeiitic (Helz et al., 1994) (in wt%) SiO_2: 47.78; TiO_2: 1.98; Al_2O_3: 17.31; Fe_2O_3: 1.22; Cr_2O_3: 0.04; FeO: 7.66; MnO: 0; MgO: 8.92; CaO: 12.2; Na_2O: 2.58; K_2O: 0.02; P_2O_5: 0.07; H_2O: 0.2; P: 0.6 kbar.

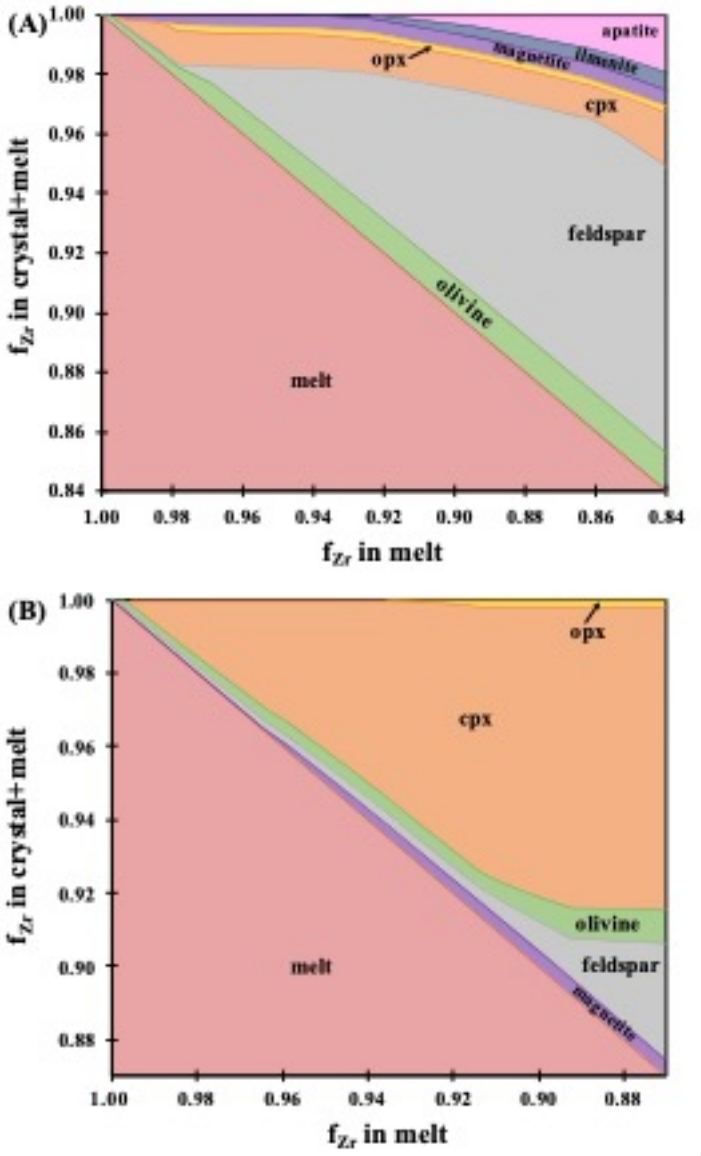

Figure 3.15 Mass fractions of Zr in crystallized minerals and melt as a function of the mass fraction of Zr remaining in melt for (A) calc-alkaline and (B) tholeiitic magmas. Before zircon crystallization, only a small fraction of Zr is removed from the melt (mostly in clinopyroxene and feldspar), and here we use the geometric mean of the partition coefficients for each mineral. These calculations were run before zircon saturation (see **Fig. 3.14**).

As expected, Zr and Hf concentrations in the melt increase during fractional crystallization before zircon saturation (**Fig. 3.16**). In calc-alkaline magmas, about 16% of the total zirconium and 10% of the total hafnium are removed by crystallizing solids before zircon saturation. In tholeiitic magmas, about 13% of total zirconium and 10% of total hafnium are removed (**Figs. 3.17** and **3.18**). These removal fractions ($1 - f_{\mathrm{Zr}}$; $1 - f_{\mathrm{Hf}}$) depend on the values of the partition coefficients that are used and they range from 6 to 47% for Zr, and 3 to 32% for Hf in calc-alkaline magma (**Fig. 3.17**), and from 4 to 60% for Zr and 2 to 52% for Hf in tholeiitic magma (**Fig. 3.18**). In **Fig. 3.16**, we compare the modeling results for Zr and Hf concentrations with compilations of igneous rock compositions from the Andes and Iceland (compiled from GEOROC database, http://georoc.mpch-mainz.gwdg.de/georoc/, see also Fig. S1 in Ptacek et al. (2020)), which typically follow calc-alkaline and tholeiitic magma series, respectively (**Fig. 3.16**). The expected different trends of [Zr] *vs*. SiO_2 (or [Hf] *vs*. SiO_2) between calc-alkaline and tholeiitic series can be explained by the earlier crystallization of SiO_2-rich plagioclase in tholeiitic series compared with calc-alkaline series melts (Grove and Baker, 1984; Juster et al., 1989; Sisson and Grove, 1993; Grove et al., 2003). Overall, all partition data (minimum, geometric mean, and maximum) reproduce well the trends seen in natural calc-alkaline Andes samples, while only the maximum partition data reproduce the tholeiitic Iceland samples. The bulk solid-liquid Zr partition coefficient values are mainly affected by clinopyroxene and feldspar (**Fig. 3.15**).

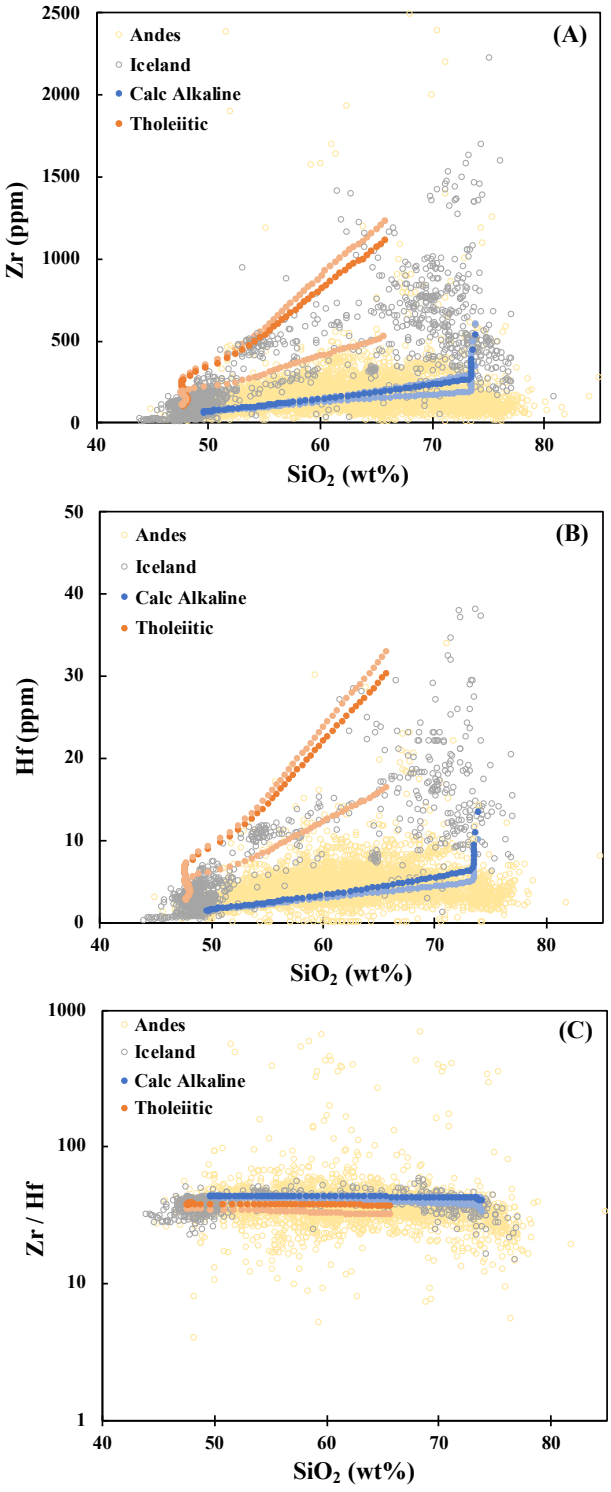

Figure 3.16 (A) Zr and (B) Hf concentration and (C) Zr/Hf (weight ratio) evolutions during magmatic differentiation along calc-alkaline and tholeiitic series. Modeling was done using Rhyolite-MELTS and the results are compared with Andes (calc-alkaline) and Iceland (tholeiitic)

Figure 3.16 *continued*
rocks (compiled from the GEOROC database). The darker color trends were calculated using the geometric mean of the partition coefficients compiled in GERM database, while the bracketing lighter color trends correspond to minimum and maximum partition coefficients.

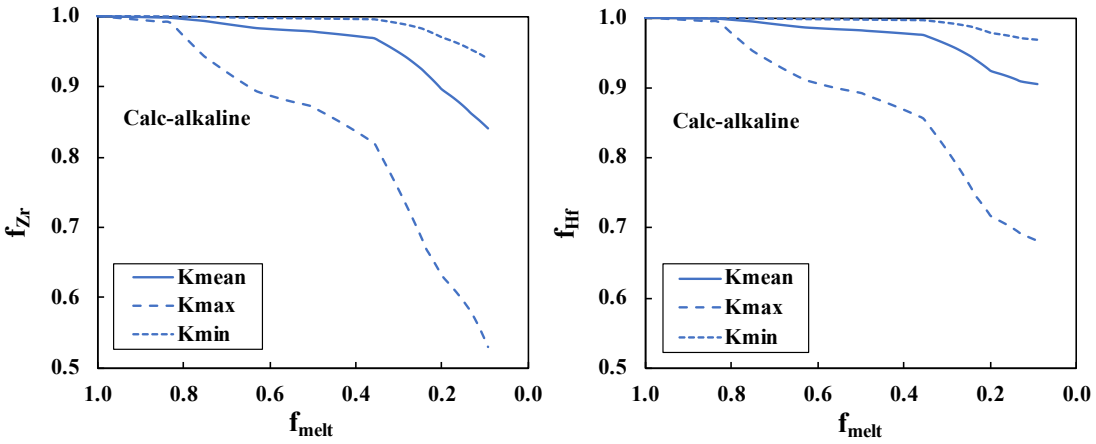

Figure 3.17 Fractions of Zr (left) and Hf (right) remaining in the melt as a function of the mass fraction of the residual melt for calc-alkaline magma during fractional crystallization before zircon starts to crystallize. These curves were calculated with the Rhyolite-MELTS program (see Section 3.4.2. for details).

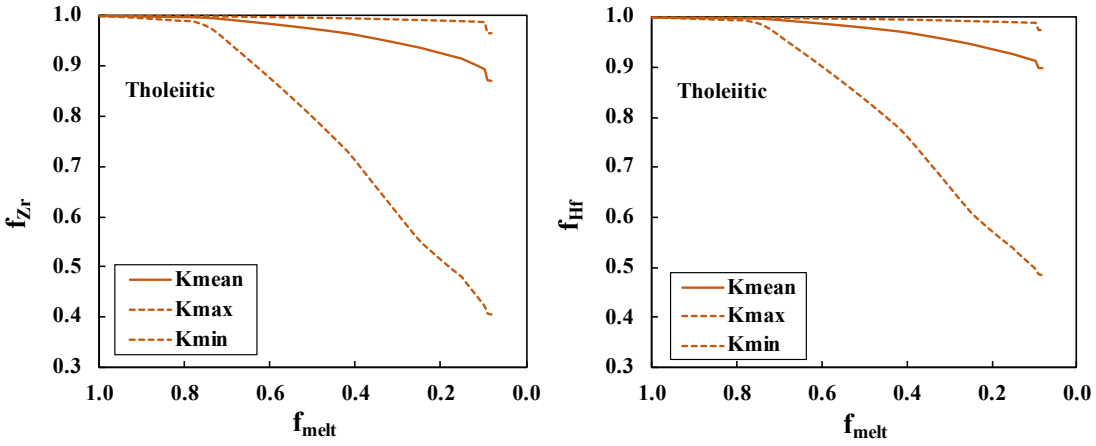

Figure 3.18 Same as **Fig. 3.17** but for a tholeiitic magma.

With the same mass-balance rationale, we model the Zr isotopic evolution trends using the fractionation factors between minerals and melt from our *ab initio* calculation results. Although feldspar and clinopyroxene have the most leverage on Zr concentration, we find that iron-titanium oxides (ilmenite and magnetite) have the potential to produce non-negligible mass-dependent fractionation of Zr isotopes before the onset of zircon crystallization (see **Fig. 3.6B**). The modeling trends in **Fig. 3.19** show that both for calc-alkaline and tholeiitic magma, the δ'^{94}Zr value of the melt evolves towards light values before zircon starts to crystallize (**Fig. 3.19**). The magnitudes of the isotopic fractionations are small, ranging from -0.005 to -0.160 ‰ for tholeiitic series and from -0.016 to -0.165 ‰ for calc-alkaline series. These values are conservative estimates because we considered all possible substitution mechanisms (see **Table 3.2**) and the fractionations would have been smaller if we had solely used the substitution favored by spectroscopic observations for clinopyroxene (Farges et al., 1994). Our modeling results thus show that before the onset of zircon crystallization, magmatic differentiation is not expected to impart large Zr isotopic fractionation in the magma if equilibrium prevails.

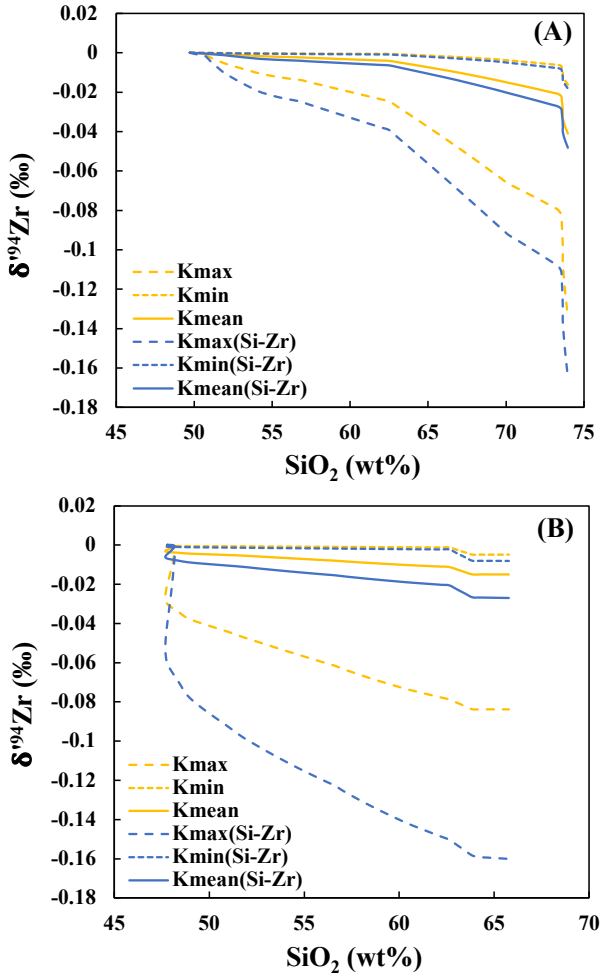

Figure 3.19 Modelled evolution of the Zr isotopic composition of residual melt before zircon crystallization for (A) calc-alkaline and (B) tholeiitic magmas. The Zr isotopic fractionation factors between minerals and melt from our *ab initio* calculations were used in the modeling, using results from Rhyolite-MELTS as input (**Fig. 3.15**). The different trends are mainly caused by two factors: (i) the various bulk Zr partition coefficients used in our calculations and (ii) the different isotopic fractionation factors calculated using different substitution mechanisms for Zr in several silicate minerals. The blue lines labelled Si-Zr are calculated using 1000lnβ values for olivine, cpx and opx using the $^{IV}Si^{4+} \leftrightarrow Zr^{4+}$ substitution with minimum, mean, and maximum mineral/melt K values. The yellow lines are calculated using 1000lnβ values in olivine, cpx and opx using the $^{VI}Mg^{2+} + {}^{VI}Mg^{2+} \leftrightarrow Zr^{4+} + \square$ substitution with minimum, mean, and maximum mineral/melt K values. In all cases, the Zr isotopic compositions of the melts evolve towards lighter values before zircon starts to crystallize but the magnitude of this fractionation is relatively small given the current analytical precision on $\delta'^{94}Zr$ measurements (~±0.01 to ±0.04 ‰, Ibañez-Mejia and Tissot 2019).

3.4.3 Diffusion-driven kinetic isotopic fractionations during crystal growth from silicate melt

The discussions in the previous two sections show that magmatic differentiation processes are unlikely to be associated with significant equilibrium Zr isotopic fractionation. This suggests that the large Zr isotopic fractionations measured in bulk volcanic rocks (Inglis et al., 2019) and igneous zircons and baddeleyites (Ibañez-Mejia and Tissot, 2019) are more likely the product of kinetic isotope effects.

While equilibrium isotopic fractionation decreases rapidly with increasing temperature, kinetic effects associated with diffusion can remain significant at magmatic temperature (Richter et al., 2009). Such diffusive fractionations have been documented in natural magmatic systems for Mg and Fe in olivine (Dauphas et al., 2010; Teng et al., 2011; Sio et al., 2013; Oeser et al., 2015; Sio and Dauphas, 2017) and Mg in melts (Chopra et al., 2012). Such non-equilibrium variations in natural systems can result from diffusion-limited transport in both melts (Jambon, 1980; Dauphas and Rouxel, 2006; Watson and Müller, 2009) and crystals (Dauphas et al., 2010; Teng et al., 2011; Sio et al., 2013; Oeser et al., 2015; Sio and Dauphas, 2017). In the case of zircon, Ibanez-Mejia and Tissot (2019) pointed out that Zr diffusivity in zircon is extremely slow. If any kinetic isotopic fractionation is present in zircon and other non-zircon minerals, it is most likely due to diffusion in the melt (Jambon, 1980; Dauphas and Rouxel, 2006; Watson and Müller, 2009).

We examine below two models of kinetic fractionation of Zr isotopes resulting from diffusion in melts (**Fig. 3.20**) that can explain the Zr isotopic variations that have been documented in igneous rocks: (i) diffusion-limited growth of zircon in a supersaturated magma and (ii)

diffusion in the boundary layer formed during the growth of a Zr-poor mineral. Several studies have examined diffusive isotopic fractionation during crystal growth. Jambon (1980) presented the first model of isotopic fractionation of major and trace elements in magmas associated with crystal growth. They assumed a constant growth rate ($dr/dt = v$, with v constant) and examined a planar geometry. Watson and Muller (2009) also assumed a constant growth rate, but examined a spherical geometry and allowed for advective transport outside of a boundary layer. Dauphas and Rouxel (2006) presented analytical equations for diffusion-limited concretion/crystal growth for both planar and spherical geometries. The main difference with Jambon (1980) and Watson and Muller (2009) is that the growth rate of the crystal is assumed to be limited by diffusion and therefore varies with time ($dr/dt \propto 1/\sqrt{t}$). DePaolo (2011) examined Ca and Mg isotopic fractionation during carbonate formation.

The reason why isotopes can be fractionated by diffusion in magmatic systems is that light (L) isotopes tend to diffuse faster than the heavy ones (H), which is often parameterized as (Richter et al., 2003, 2008, 2009; Watkins et al., 2009, 2011, 2014),

$$\frac{D_H}{D_L} = \left(\frac{m_L}{m_H}\right)^{\beta}, \tag{3.23}$$

where D and m stand for diffusivity and mass of the isotopes, and β is an empirical factor. No data is available documenting Zr or Hf isotopic fractionation during diffusion in silicate melts. However, Watkins et al. (2017) recognized that β exponents correlate with the ratio of the diffusivities of the cations normalized to those of Si. The $D_{\mathrm{Zr}}/D_{\mathrm{Si}}$ and $D_{\mathrm{Hf}}/D_{\mathrm{Si}}$ ratios in rhyolite melts most relevant to zircon crystallization are close to ~1 (Zhang et al., 2010). Using the relationship established by Watkins et al. (2017), we calculate $\beta \simeq 0.054 \pm 0.059$ for both Zr and Hf (**Fig. 3.21**). Using Eq. 3.23, we therefore have,

$$\frac{D_{^{94}\mathrm{Zr}}}{D_{^{90}\mathrm{Zr}}} = \left(\frac{89.905}{93.906}\right)^{0.054\pm0.059} = 0.9977 \pm 0.0026 \quad , \tag{3.24}$$

$$\frac{D_{^{179}\mathrm{Hf}}}{D_{^{177}\mathrm{Hf}}} = \left(\frac{176.943}{178.946}\right)^{0.054\pm0.059} = 0.9994 \pm 0.0007 \quad , \tag{3.25}$$

The differences in diffusivities $D_{^{94}\mathrm{Zr}}/D_{^{90}\mathrm{Zr}}$ and $D_{^{179}\mathrm{Hf}}/D_{^{177}\mathrm{Hf}}$ are thus –2.3±2.6 and –0.6±0.7 ‰ (Δ_D, see Eq. A10), respectively.

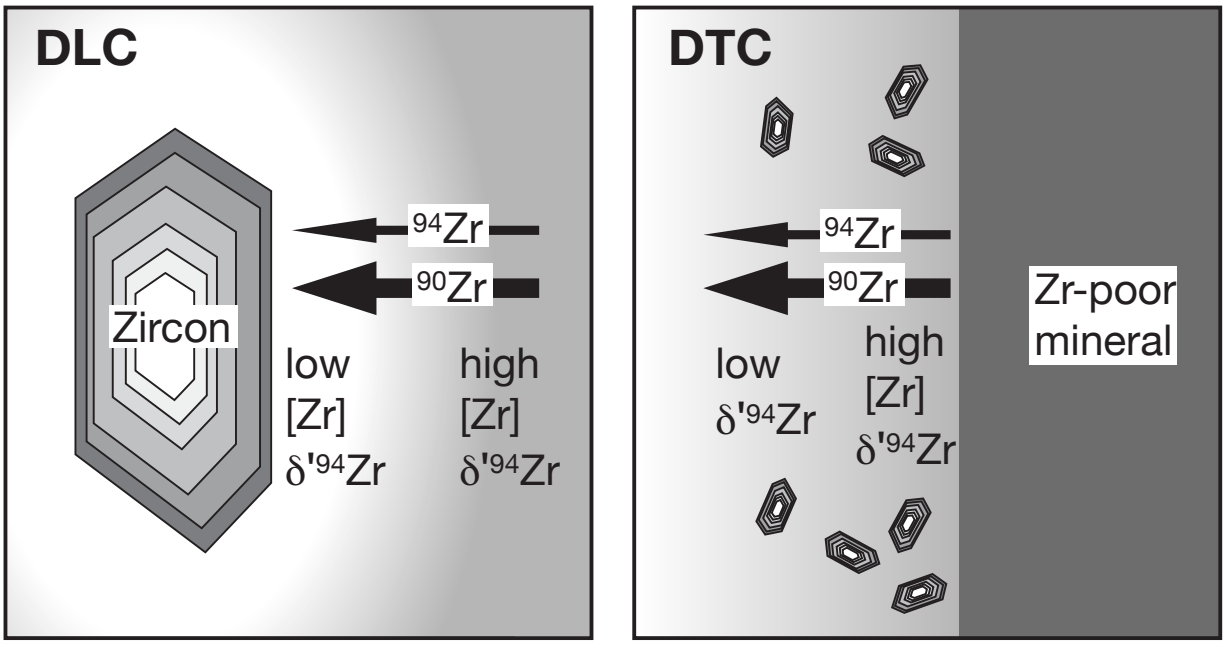

Figure 3.20 Schematic models of diffusive Zr isotopic fractionation during crystallization. **Left panel:** In the diffusion-limited crystallization model (DLC), the growth of zircon is limited by the diffusive supply of Zr to the surface from a far-field medium that is supersaturated. Because the light isotopes diffuse faster than the heavier ones, the liquid at the interface with the zircon will have low δ'^{94}Zr, while further away from the interface the liquid will have high δ'^{94}Zr. This model would predict zircons to have low δ'^{94}Zr but reservoir effects in the liquid would also lead to the crystallization of zircons with high δ'^{94}Zr. **Right panel:** In the diffusion-triggered crystallization model (DTC), the growth of a Zr-poor mineral would push Zr away from the interface and lead to high δ'^{94}Zr at the interface in the liquid and low δ'^{94}Zr further away. The whole diffusive boundary layer would have elevated Zr concentration. This could trigger the saturation and crystallization of zircon, which would inherit some of the fractionated Zr isotopic composition from the diffusive boundary from which they grew.

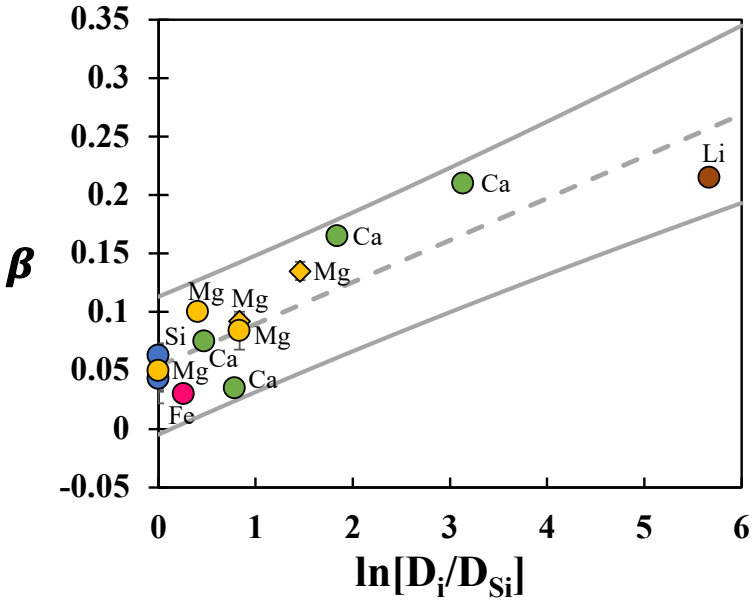

Figure 3.21 β exponents as a function of the ratio of cation diffusivities normalized by those of Si in silicate melt (modified from Watkins et al. (2017)). The β exponents for Zr and Hf isotopes were estimated by linearly regressing this trend to $\ln[D_{Zr}/D_{Si}]$ and $\ln[D_{Hf}/D_{Si}]$ ~0 because the diffusivities of both Zr and Hf are close to Si (Zhang et al., 2010). The two grey lines are the 95% prediction intervals. This empirical correlation correlates the degree of diffusion-driven isotopic fractionation (β) with a measure of solute-solvent interaction $\ln[D_i/D_{Si}]$ (Watkins et al., 2017). In aluminosilicate melt, the solvent molecule is SiO_4^{4-}, which is the reason why the quantity $\ln[D_i/D_{Si}]$ is used to describe solute-solvent interaction.

3.4.3.1 Diffusion-limited crystallization (DLC) of zircon

The first setting where Zr isotopes could have been fractionated is during diffusion-limited growth of zircon from a supersaturated medium. The growth of zircon will deplete the surrounding medium in Zr, which has to be supplied by diffusion from the far-field medium (Bindeman and Melnik, 2016; Zhang and Xu, 2016). Because light isotopes diffuse faster than heavy ones, Zr delivered to the growing crystal will be enriched in the light isotopes of Zr, while the medium

further away will be enriched in the heavy isotopes of Zr (Richter et al., 2009). The formalism developed by Dauphas and Rouxel (2006) can be applied here to model isotopic fractionation during diffusion-limited growth of zircon from an infinite medium. The growth rate cannot be arbitrarily set to a constant value, as it depends on the supply of Zr to the growing crystal through diffusion. This has important consequences for isotopic fractionation. Most importantly, during diffusion-limited growth, the δ'^{94}Zr value of the growing crystal will be offset from that of the surrounding medium even when the system has reached a pseudo steady-state. The reason is that the diffusive boundary layer keeps growing as the square-root of time, so from a mass-balance point of view, the light isotopic enrichment of the growing crystal can be offset by the heavy isotopic enrichment of the diffusive boundary layer.

We used the equations provided by Dauphas and Rouxel (2006) to calculate the Zr concentration and isotopic composition profiles in the liquid away from the interface of a spherical zircon growing in a diffusion-limited regime and these are plotted in **Fig. 3.22** (we also provide movies as **Supplementary Materials** showing the evolutions of these two variables as a function of time, **Mov. 1 and 2**, movie titles and captions are in **Supplementary Materials** as well). Very rapidly, the system reaches a pseudo steady-state whereby the concentration and isotopic profiles follow a self-similar solution that stretches as the square-root of time. Dauphas and Rouxel (2006) derived an approximate solution for the isotopic composition of the crystal (assuming spherical geometry) that is valid up to a supersaturation of $S \simeq 5$ to 10,

$$\delta'^{94}\mathrm{Zr}_{\mathrm{zircon}} \simeq \left[\frac{\Delta'^{94}\mathrm{Zr}_{\mathrm{eq,\ zircon\text{-}melt}}}{S} + \left(1-\frac{1}{S}\right)\left(\frac{D_{^{94}\mathrm{Zr}}}{D_{^{90}\mathrm{Zr}}}-1\right)10^3\right], \tag{3.26}$$

where $S = C_\infty / C_{sat}$ is the degree of supersaturation (C_∞ and C_{sat} are the far-field and saturation concentrations, respectively) and $\Delta'^{94}\mathrm{Zr}_{\mathrm{eq,\ zircon\text{-}melt}}$ is the equilibrium isotopic

fractionation between zircon and silicate melt. Note that diffusive fractionation associated with growth of a planar crystal is a factor of ~2 lower than that predicted for a sphere (Eq. 54 of Dauphas and Rouxel (2006)).

In **Fig. 3.23**, we plot the expected isotopic fractionation as a function of the degree of supersaturation. The $\delta'^{94}\mathrm{Zr}_{\mathrm{zircon}}$ here is the isotopic composition in the crystal relative to that in the far-field growth medium. With $\beta_{\mathrm{Zr}} = 0.113$ in Eq. 3.24, we can reach a $\delta'^{94}\mathrm{Zr}$ value for zircon of -4.4 ‰. This is similar to the lowest $\delta'^{94}\mathrm{Zr}$ values of -4.278 ‰ measured by Ibanez-Meija and Tissot (2019). Ibanez-Meija and Tissot (2019) found a range of $\delta'^{94}\mathrm{Zr}$ values extending to +0.905 ‰. The formula of Dauphas and Rouxel (2006) assumes growth from an infinite medium. In practice, in a finite system (Bindeman and Melnik, 2016), the diffusive enrichment in the light isotopes of the growing crystal will leave behind a residual melt that will become enriched in the heavy isotopes of Zr, so we do expect the production of zircon with positive $\delta'^{94}\mathrm{Zr}$ values. As indicated by Eq. 3.26, the parameter that determines whether equilibrium or diffusive kinetic isotopic composition is expressed in a crystal is the degree of supersaturation of the medium, which also influences the growth rate. Therefore, $\delta'^{94}\mathrm{Zr}$ measurements of zircons could provide direct clues on the cooling and crystallization history of the host magma body. For purely diffusion-limited growth, the degree of supersaturation S influences the crystal growth rate through (derived from Eq. 56 of Dauphas and Rouxel (2006); C_{zircon} is the Zr concentration in zircon),

$$R = \sqrt{\frac{2C_{sat}(S-1)Dt}{C_{zircon}}} \quad , \tag{3.27}$$

$$\frac{dR}{dt} = \frac{1}{2}\sqrt{\frac{2C_{sat}(S-1)D}{C_{zircon}}}\frac{1}{\sqrt{t}} = \frac{C_{sat}(S-1)D}{RC_{zircon}} \quad , \tag{3.28}$$

$$S = 1 + \frac{dR}{dt} \times \frac{RC_{zircon}}{DC_{sat}} \quad , \tag{3.29}$$

Neglecting equilibrium isotopic fractionation in Eq. 3.26 and injecting Eq. 3.29 in Eq. 3.26, we thus have,

$$\delta'^{94}\mathrm{Zr}_{\mathrm{zircon}} \simeq \left[1 - \frac{1}{1+\frac{dR}{dt}\times\frac{RC_{zircon}}{DC_{sat}}}\right]\left(\frac{D_{94\mathrm{Zr}}}{D_{90\mathrm{Zr}}} - 1\right)10^3\,, \tag{3.30}$$

In **Fig. 3.24**, we use this equation to plot the expected Zr isotopic fractionation in zircon $\delta'^{94}\mathrm{Zr}_{\mathrm{zircon}}$ as a function of growth rate dR/dt at different temperatures (different D and C_{sat} values) and different supersaturations. In Eq. 3.30, we consider crystals of 10, 100 μm in radius (R). As discussed by Zhang and Xu (2016), zircons larger than ~10 μm in an open magma are expected to partially grow through advection of Zr to a diffusive boundary layer. Watson and Müller (2009) investigated numerically the isotopic consequences of such a model. The zircons measured by Ibanez-Meija and Tissot (2019) are less than 10 μm in size and grew in inter-cumulus liquid pockets, where advection is most likely limited. In such settings (late crystallization of residual liquid pockets), it is conceivable that diffusive growth could play a role even for zircons larger than 10 μm. The Zr diffusivities at different temperatures are calculated using the experimental results from Zhang and Xu (2016). Zirconium saturation concentrations (C_{sat}) at different temperatures are calculated using the model presented in Boehnke et al. (2013). The Zr concentration in zircon is ~500,000 ppm. The result of our calculation (**Fig. 3.24**) shows that the extremely light δ'^{94}Zr values (-4.278 ‰) reported by Ibanez-Meija and Tissot (2019) in ~10 μm zircons crystallized at ~850 °C can be explained if they grew in a diffusion-limited regime at a supersaturation of ~7.8, corresponding to a growth rate of ~0.4 μm/yr. We are not aware of any independent constraint on the zircon growth rate in the specific anorthositic gabbro studied by Ibanez-Meija and Tissot (2019), but our inferred growth rate is in line with the results of Zhang

and Xu (2016) who gave values in the range 0.01-1.0 μm/yr for variably hydrated rhyolitic melts. We conclude that diffusion-limited crystallization of zircon is a possible mechanism to explain the variable Zr isotopic compositions measured in zircon grains (Ibañez-Mejia and Tissot, 2019).

Inglis et al. (2019) argued that the heavy Zr isotopic compositions of differentiated rocks from Hekla could be explained by fractional crystallization of zircon with δ'^{94}Zr values shifted by -0.5 ‰ relative to the melt. As shown in **Fig. 3.23**, such low δ'^{94}Zr values in zircon can be produced in the DLC model by growth from a melt characterized by Zr supersaturations of ~1.1 to 2.2, depending on the value of β_{Zr}. Zircons from the Hekla volcano are typically 40×160 μm in size and were formed at temperatures of ~750-850 °C (Carley et al., 2011). Assuming a characteristic size of 36 μm (a sphere of 36 μm radius has the same volume as a cylinder of 20 μm radius and 160 μm length) and a temperature of 800 °C, the supersaturations of 1.1 to 2.2 correspond to growth rates of 0.0004 to 0.0044 μm/yr, which is slightly smaller than the range given by Zhang and Xu (2016). A caveat to this calculation is that it assumes that Zr transport is entirely diffusive. Zircons would grow faster if advective transport took place, which would also dampen kinetic isotopic fractionation. The zircon-melt isotopic fractionation calculated by Inglis et al. (2019) is uncertain as it relies solely on bulk rock measurements. Without further isotopic characterizations of the mineral carriers of Zr in Hekla, it is difficult to robustly interpret bulk rock Zr isotopic analyses. To summarize, the removal of isotopically light zircon formed by the DLC process could possibly drive residual magmas to evolve towards heavy Zr isotopic compositions, as is observed (Inglis et al., 2019; Feng et al., 2020; Tian et al., 2020).

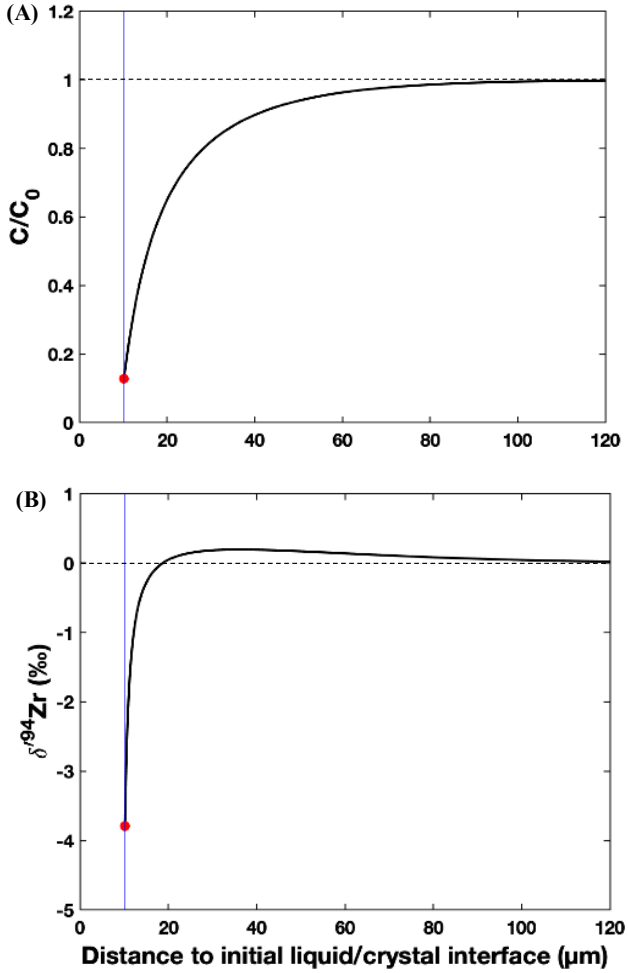

Figure 3.22 Zr concentration (A) and isotopic composition (B) profiles in the liquid away from the interface of a growing zircon in a diffusion-limited regime (DLC model) at the time when the zircon has reached 10 μm in size (the blue line is the liquid-solid interface). The red dot is the liquid concentration and isotopic composition at the interface. Both concentration and isotopic composition are relative to the liquid at infinity. As zircon grows from a supersaturated medium, the liquid and crystal near the liquid-crystal interface get enriched in the light isotopes of Zr due to their faster diffusion, while the liquid further away in the diffusive boundary layer gets enriched in the heavy isotopes due to their slower diffusion. The calculations were done using Eqs. 55, 49, 50 for diffusion-limited growth in a spherical geometry (Dauphas and Rouxel, 2006) with a Zr diffusivity of $D = 10^{-4}$ μm^2/s (Zhang and Xu, 2016), Zr saturation concentrations $C_{sat} = 1806$ ppm (Boehnke et al., 2013), Zr concentration in zircon of 500,000 ppm, and a supersaturation $S = C_\infty/C_{sat} = 7.8$, a diffusive Zr isotopic fractionation factor $\Delta_D = -4.9$ ‰ ($\beta_{Zr} = 0.113$ in Eq. 3.24). (A and B correspond to **Movie 1 and 2**).

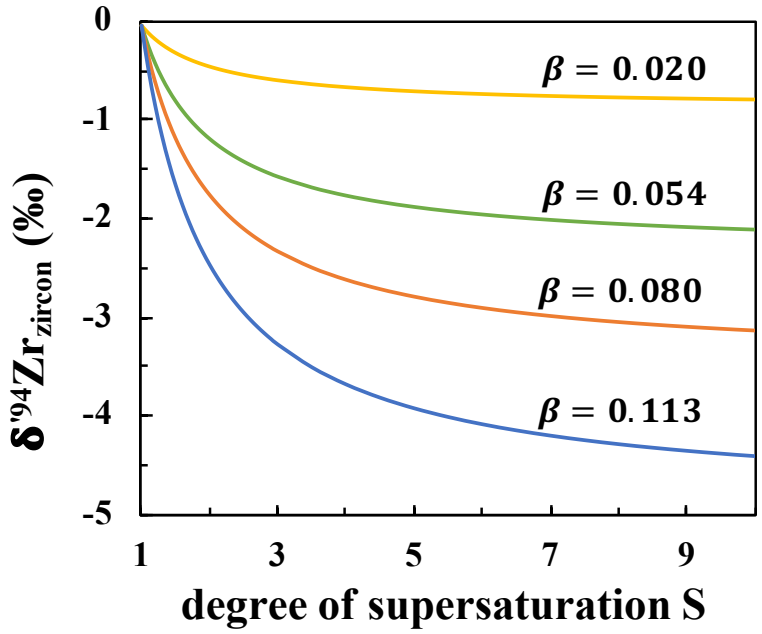

Figure 3.23 Expected δ'^{94}Zr variations in zircon as a function of the degree of supersaturation during diffusion-limited zircon growth from silicate melt with different diffusive β exponents for Zr isotopes (Eq. 3.26). $\delta'^{94}Zr_{zircon}$ is the isotopic composition in the crystal relative to that in the far-field growth medium.

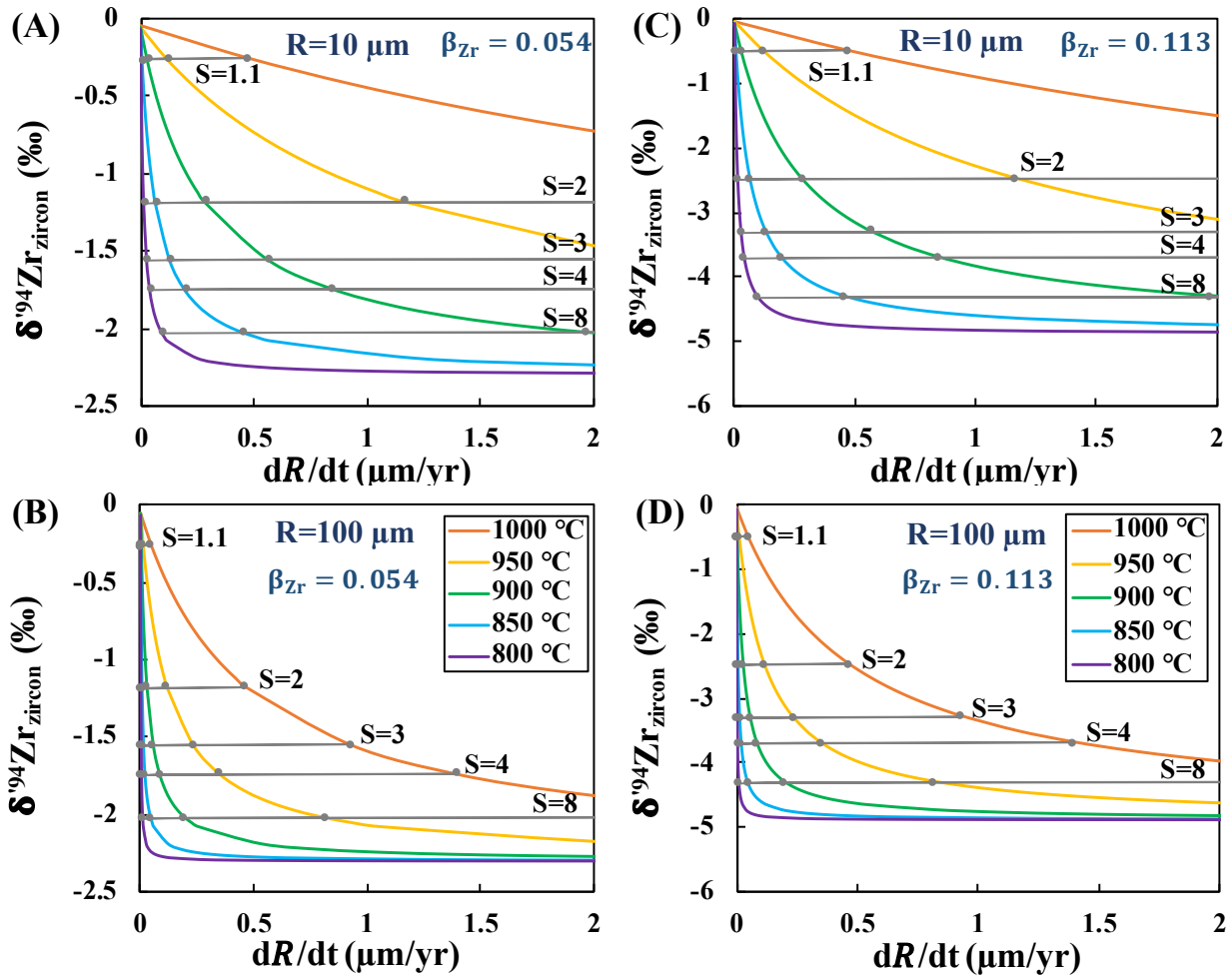

Figure 3.24 Expected $\delta'^{94}Zr$ fractionations in zircon as a function of growth rate at different temperatures and different supersaturations (Eqs. 3.26 and 3.30). (A)-(B) use a diffusive Zr isotopic fractionation factor $\Delta_D = -2.3$ ‰ ($\beta_{Zr} = 0.054$ in Eq. 3.24); (C)-(D) use a diffusive Zr isotopic fractionation factor $\Delta_D = -4.9$ ‰ ($\beta_{Zr} = 0.113$ in Eq. 3.24). $\delta'^{94}Zr_{zircon}$ is the isotopic composition in the crystal relative to that in the far-field growth medium. This figure shows that measuring $\delta'^{94}Zr_{zircon}$ can help estimate the degree of supersaturation and zircon growth rate if the temperature can be independently constrained.

3.4.3.2 Diffusion-triggered crystallization (DTC) of zircon during the growth of Zr-poor minerals

The highly fractionated zircons measured by Ibanez-Meija and Tissot (2019) are closely associated with plagioclase, clinopyroxene and ilmenite, and are interpreted to have crystallized from inter-cumulus liquid pockets. The second setting where diffusive isotopic fractionation could have taken place is therefore in the diffusive boundary layers formed around Zr-poor minerals, as was first described for apatite by Harrison and Watson (1984). When Zr-poor minerals grow, Zr excluded from their crystal lattice accumulates in the liquid at the interface with the solid (Smith et al., 1955), and the concentration gradient thus formed relaxes by Zr diffusion from the solid-liquid interface to the far field. Because light isotopes diffuse faster than heavy ones (Richter et al., 2009), Zr at the interface get enriched in the heavy isotopes while the liquid further away gets enriched in the light isotopes. Zircon crystallized from liquid in this boundary layer could inherit the isotopic fractionation imparted by diffusion. Given the great incompatibility of Zr in most minerals, the concentration in the liquid at the interface of those growing crystals could be much higher than the far-field. In steady-state and planar geometry, the constant growth rate model of Smith et al. (1955) predicts that the liquid at the interface can be enriched relative to the far-field by a factor of $1/K$, where K is the mineral/liquid partition coefficient (Smith et al., 1955). Based on partitioning data for olivine, pyroxene, and feldspar (GERM database, https://earthref.org/KDD/e:40/), we calculate that the Zr enrichments at the liquid/solid interface could reach factors of ~7-100, ~1-70, and ~2-1100, respectively. These dramatic enrichments could have led Zr concentration to exceed zircon saturation and trigger their crystallization. The zircon thus formed would inherit Zr from the diffusion boundary layer, which would have been

fractionated isotopically by diffusive transport. We call this second model diffusion-triggered crystallization (DTC) (**Fig. 3.20**). Note that DTC and DLC could have occurred concurrently if the diffusive layer around Zr-poor minerals was highly supersaturated and the growth of zircon itself was diffusion-limited.

The models of Smith et al. (1955), Jambon (1980) and Watson and Müller (2009) are well suited to explore diffusive isotopic fractionation created by the exclusion of Zr from growing Zr-poor crystals. Using the framework of Smith et al. (1955) for diffusive transport away from a planar crystal growing at constant speed, we derive the analytical equations of the isotopic composition in the liquid and solid in transient and at steady-state (see **Appendix** for details). For the concentration, Smith et al. (1955) give the transient liquid concentration C_l relative to the initial (and far-field) concentration C_0 as a function of (1) the distance x_l from the original interface expressed with the dimensionless variable $u = \dot{R}x_l/D$, where $\dot{R} = dR/dt$ is the growth rate and D is the diffusivity in the melt, and (2) the time t elapsed since the start of crystal growth expressed with the dimensionless variable $w = \dot{R}^2 t/D$,

$$\frac{C_l(u,w)}{C_0} = 1 + \frac{1-K}{2K}\mathrm{e}^{-u}\mathrm{erfc}\left(\frac{u-w}{2\sqrt{w}}\right) - \frac{1}{2}\mathrm{erfc}\left(\frac{u+w}{2\sqrt{w}}\right) + \left(1 - \frac{1}{2K}\right)e^{-(1-\mathrm{K})(u+Kw)}\mathrm{erfc}\left[\frac{u+(2K-1)w}{2\sqrt{w}}\right], \quad (3.31)$$

In **Appendix**, we show that the isotopic composition in the melt can be written as,

$$\delta_{l,2/1} \simeq A\Delta_D + B\Delta_K\,, \quad (3.32)$$

with $\Delta_D = (D_2/D_1 - 1)1000$ the term describing isotopic fractionation imparted by differences in the diffusivities of the isotopes involved, and $\Delta_K = (K_2/K_1 - 1)1000 = (\alpha_{2/1} -$

1)1000 the equilibrium isotopic fractionation between mineral and melt. A and B are given by the following formulas,

$$A = \frac{e^{-Kw-\frac{(u+w)^2}{4w}}(-1+K)\left\{2e^{u+Kw}K\sqrt{w}+e^{\frac{(u+w)^2}{4w}}\sqrt{\pi}\left[-e^{Kw}u\times\mathrm{erfc}\left(\frac{u-w}{2\sqrt{w}}\right)-e^{K(u+Kw)}(-1+2K)(u+Kw)\mathrm{erfc}\left(\frac{u+(2K-1)w}{2\sqrt{w}}\right)\right]\right\}}{\left\{\sqrt{\pi}\left[e^{u}K+e^{u}K\times\mathrm{erfc}\left(\frac{u+w}{2\sqrt{w}}\right)-(-1+K)\mathrm{erfc}\left(\frac{u-w}{2\sqrt{w}}\right)+e^{K(u+(-1+K)w)}(-1+2K)\mathrm{erfc}\left(\frac{u+(2K-1)w}{2\sqrt{w}}\right)\right]\right\}},$$

(3.33)

$$B = \frac{e^{-\frac{(u+w)^2}{4w}}\left\{2e^{u}K(-1+2K)w+\sqrt{\pi}\sqrt{w}\left[e^{\frac{(u+w)^2}{4w}}\mathrm{erfc}\left(\frac{u-w}{2\sqrt{w}}\right)-e^{\frac{1}{4}\left((2+4K)u+\frac{u^2}{w}+(1-2K)^2w\right)}\left(1+K(-1+2K)(u+(-1+2K)w)\right)\mathrm{erfc}\left(\frac{u+(2K-1)w}{2\sqrt{w}}\right)\right]\right\}}{\left\{\sqrt{\pi}\sqrt{w}\left[(-1+K)\mathrm{erfc}\left(\frac{u-w}{2\sqrt{w}}\right)+e^{u}K\left(-2+\mathrm{erfc}\left(\frac{u+w}{2\sqrt{w}}\right)\right)-e^{K(u+(-1+K)w)}(-1+2K)\mathrm{erfc}\left(\frac{u+(2K-1)w}{2\sqrt{w}}\right)\right]\right\}},$$

(3.34)

In **Fig. 3.25**, we plot the Zr concentration and isotopic composition in the growing Zr-poor crystal and melt growth medium at three times until the crystal grows to 1 cm in size (we also provide movies as **Supplementary Materials**, **Mov. 3, 4 and 5**). The concentrations and isotopic compositions in **Fig. 3.25** are normalized to those in the far-field growth medium composition. In the liquid, incompatible Zr accumulates. The concentration in the solid is always in equilibrium with the liquid at the interface where the two concentrations relate with each other by the partition coefficient $C_{s,\mathrm{interface}} = KC_{l,\mathrm{interface}}$. The concentration in the growing crystal $C_{s,\mathrm{interface}}$ therefore increases as the concentration in the liquid at the interface $C_{l,\mathrm{interface}}$ builds up until the concentration in the crystal is equal to that in the far-field and the liquid interface concentration is enriched by a factor of $1/K$ (**Figs. 3.25A, 3.26A**). The Zr that accumulates in the liquid at the interface diffuses away from that interface into the far field. Since light Zr isotopes can diffuse faster than heavy ones (Richter et al., 2009), the solid-liquid interface has high δ'^{94}Zr, which is transferred into the Zr-poor crystal as it grows. The liquid further away in the diffusive boundary

layer has low δ'^{94}Zr (**Fig. 3.25B, C**). As the system evolves towards steady-state (**Fig. 3.26**; movies are provided as **Supplementary Materials**, **Mov. 6, 7 and 8**), the isotopic composition of the crystal and the liquid interface approach that of the far field medium but the liquid in the diffusive boundary layer keeps a low δ'^{94}Zr value. From a mass-balance point of view, this low δ'^{94}Zr value is balanced by the high δ'^{94}Zr value of the early crystal grown during the transient period.

As discussed above and by Harrison and Watson (1984) for apatite, the elevated Zr concentration in the diffusive boundary layer could trigger the saturation and crystallization of zircon (DTC model). These newly-crystallized zircons would inherit some of the fractionated Zr isotopic composition of the diffusive boundary layer from which they grew, which span slightly positive and highly negative δ'^{94}Zr values (**Fig. 3.26B, C**). The most negative δ'^{94}Zr value achieved at steady state is (see derivations in **Appendix**),

$$\delta_l = 1000\left(\frac{D_{^{94}\mathrm{Zr}}}{D_{^{90}\mathrm{Zr}}} - 1\right) \times ProductLog[\tfrac{1-K}{eK}], \tag{3.35}$$

For clinopyroxene or plagioclase, the values of K are 0.08 and 0.004 (geometric mean values for equilibrium with basaltic melt, GERM database), and we would predict isotopic fractionations that could reach -2.8 and -7.6 ‰, respectively for $\beta_{Zr} = 0.054$ (Eq. 3.24; **Fig. 3.26B** and **Fig. 3.28B**), and -6.0 and -16.2 ‰, respectively for $\beta_{Zr} = 0.113$ (Eq. 3.24; **Fig. 3.26C** and **Fig. 3.28C**). From Eq. 3.35, we find that different Zr partition coefficients between minerals and melt K, different diffusive Zr isotopic fractionation factor Δ_D (or the β_{Zr} exponent in Eq. 3.24), and different growth timescales of the Zr-poor minerals result in a range of δ'^{94}Zr values of the liquid in the diffusive boundary layer (see **Figs. 3.25, 3.26, 3.27, 3.28**) that can readily explain the values measured by Ibanez-Meija and Tissot (2019). In **Fig. 3.29**, we plot the expected probability

density function (PDF) of the Zr isotopic composition of Zr atoms in the diffusive boundary layer (*i.e.*, at any given time, the fraction of Zr atoms in the diffusive boundary layer with an enrichment higher than 3 that have a certain isotopic composition) (movies **Mov. 9 and 10** are provided as **Supplementary Materials**). We find more or less uniform distributions, while Ibanez-Meija and Tissot (2019) found many zircons with δ'^{94}Zr values around 0-1 ‰ and a long tail of δ'^{94}Zr values extending to -4 ‰. Comparing these PDFs is, however, fraught with difficulties as there is no compelling reason to think that Zr atoms in zircons reflect a snapshot of the diffusive boundary layer. If DTC is the correct model, the distribution of δ'^{94}Zr values could help pinpoint when and where in the development of diffusive boundary layers zircons can form.

While both positive and negative δ'^{94}Zr values are encountered in the diffusion boundary layer considered in the DTC model (**Figs. 3.25, 3.26**, **3.27, 3.28**), the distribution is skewed towards low δ'^{94}Zr. This is also shown in **Fig. 3.29**, where we plot the average δ'^{94}Zr value of the boundary layer where the melt is Zr-supersaturated by at least of factor of 3. The shift towards low δ'^{94}Zr values in the boundary layer is due to the removal of isotopically heavy Zr in the growing Zr-poor mineral (*e.g.*, clinopyroxene or plagioclase). At first sight, the development of low δ'^{94}Zr values in zircons formed by DTC is consistent with the -0.5 ‰ δ'^{94}Zr fractionation calculated by Inglis et al. (2019) for zircon in Hekla. However, for these zircons to drive Zr isotopic fractionation in the magma, they would have to be separated from the Zr-poor minerals whose crystallization drove zircon saturation, which may be difficult to achieve. Future studies investigating Zr-poor minerals will help test if zircons formed around them were formed by diffusion-triggered crystallization.

To summarize, isotopic fractionation induced by diffusion in boundary layers around growing Zr-poor crystals (DTC model) can readily explain the range of $\delta'^{94}Zr$ values measured in zircons. An appealing aspect of this scenario is that the formation of a such a Zr-rich boundary layer could also be the trigger for zircon saturation and crystallization. As with the DLC model outlined in Sect. 2.4.3.1, the DTC model provides the framework to tie $\delta'^{94}Zr$ values measured in zircons to the cooling history of the host magma.

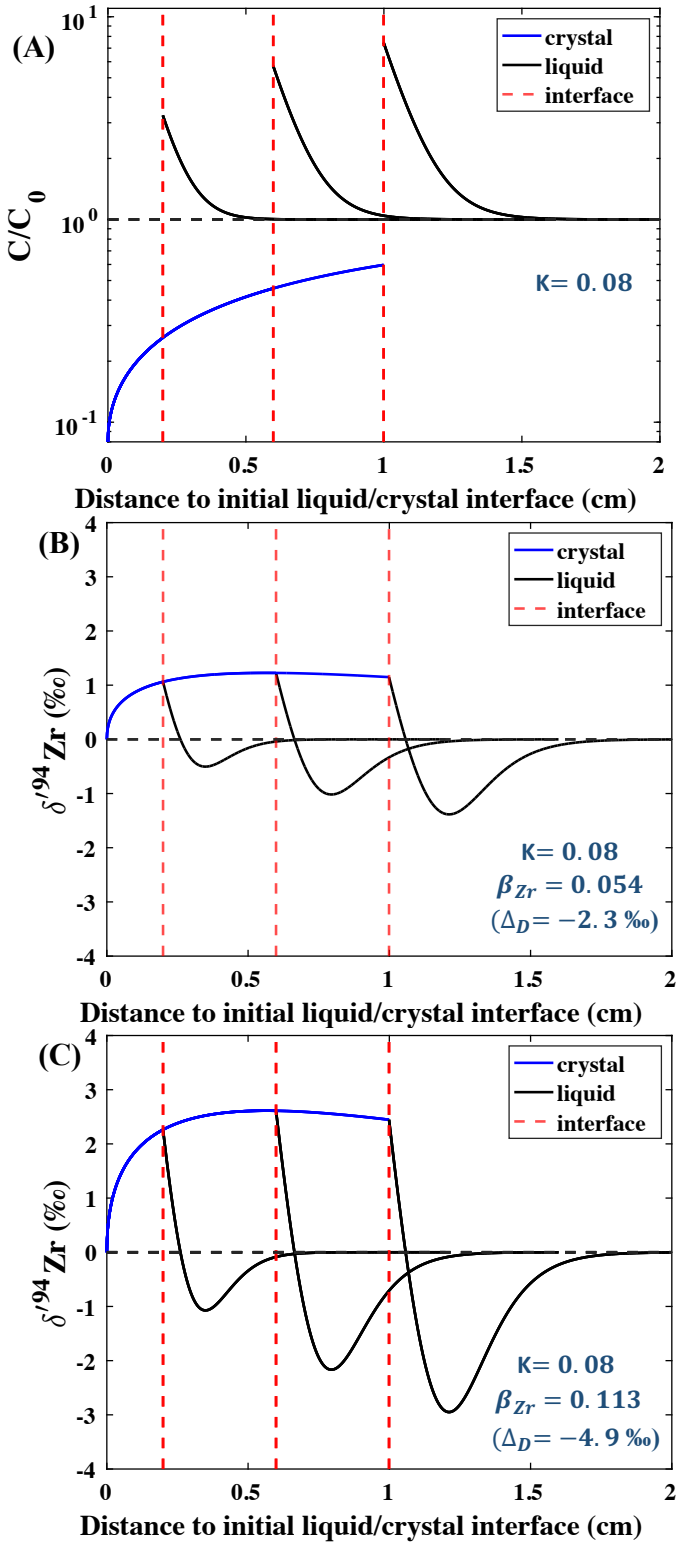

Figure 3.25 Evolution of the Zr concentration (A) and isotopic composition (B, C) in a growing Zr-poor crystal (blue line) and in the surrounding melt growth medium (black line) in three

Figure 3.25 *continued*

snapshots taken at 0.6, 1.9, and 3.2 kyr (DTC model; see Sect. 2.4.3.2. for details). The concentration and isotopic composition are normalized to the far-field growth medium. The diffusive boundary layer has elevated Zr concentration, which could trigger zircon saturation and crystallization, thus inheriting the isotopic composition in the diffusive boundary layer. The curves were calculated using Eqs. 3.31-34, and A21, A23. We used the partition coefficient of clinopyroxene $K = 0.08$ (the geometric mean of the values compiled in GERM database), diffusivity for Zr in melt $D = 10^{-4}$ $\mu m^2/s$ at 950 ℃ (Zhang and Xu, 2016), a growth rate of $\dot{R} = 10^{-7} \mu m/s$ (so that $\dot{R}/D = 10$ cm^{-1} which is in the realm of possibilities (Watkins et al. 2017)), and a diffusive isotopic fractionation factor $\Delta_D = -2.3$ and -4.9 ‰ ($\beta_{Zr} = 0.054$ and 0.113 in Eq. 3.24, respectively). (A, B and C correspond to **Movie 3, 4 and 5**).

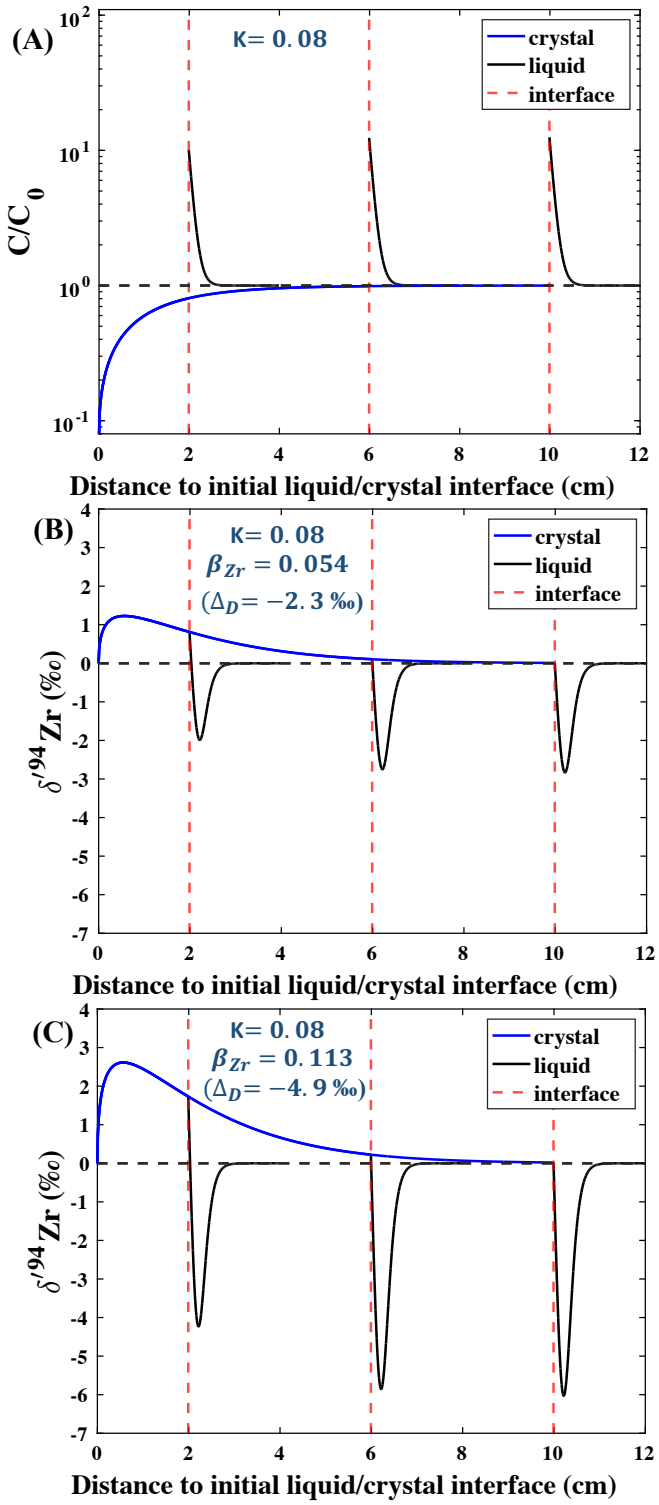

Figure 3.26 Same as **Fig. 3.25** but for a longer duration allowing the system to achieve steady-state (note that this calculation is not aimed at reproducing natural conditions as crystals would

Figure 3.26 *continued*
stop growing before reaching steady-state). Zr concentration (A) and isotopic composition (B, C) in the growing Zr-poor crystal (blue line) and in the melt growth medium (black line) in three snapshots taken at 6, 19, and 32 kyr. Note the difference in x-axis scale with **Fig. 3.25**. (A, B and C correspond to **Movie 6, 7 and 8**).

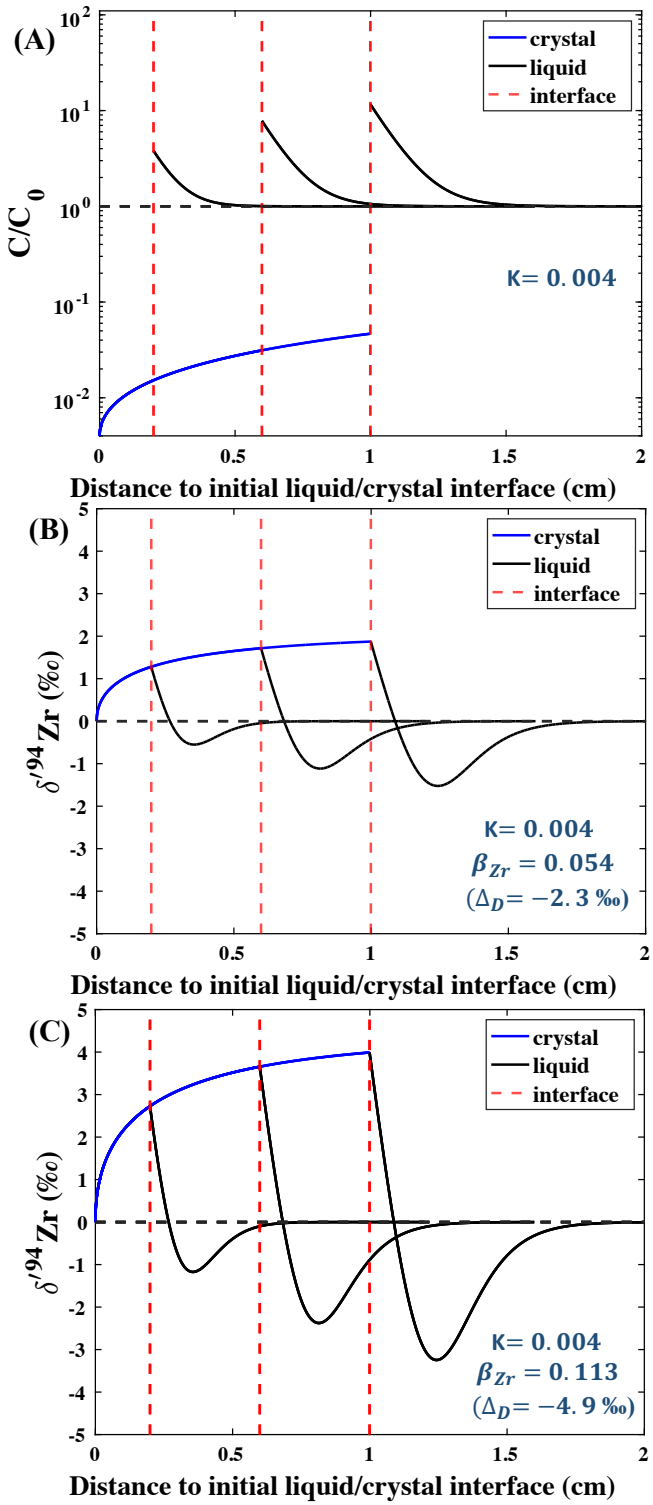

Figure 3.27 Same as **Fig. 3.25** except that we use the partition coefficient of plagioclase $K = 0.004$ (the geometric mean of the values compiled in GERM database).

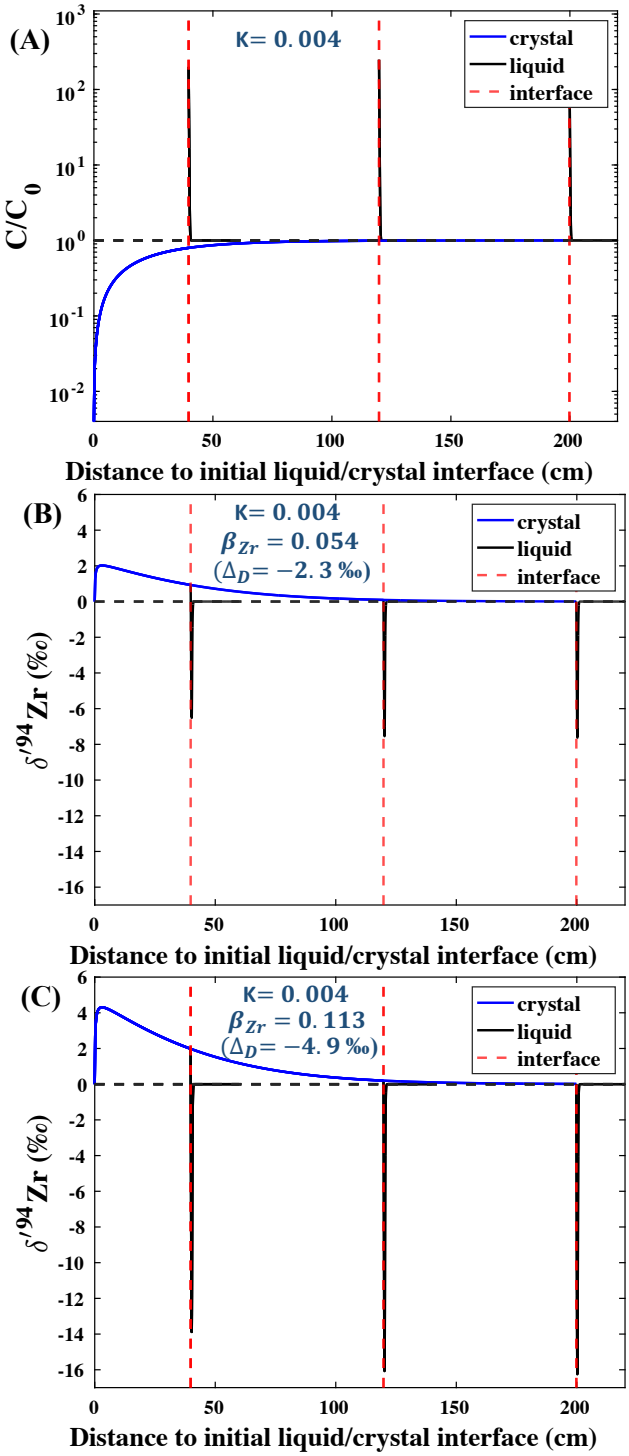

Figure 3.28 Same as **Fig. 3.26** except that we use the partition coefficient of plagioclase $K = 0.004$ (the geometric mean of the values compiled in GERM database), and the three snapshots are taken at 126, 380, and 634 kyr.

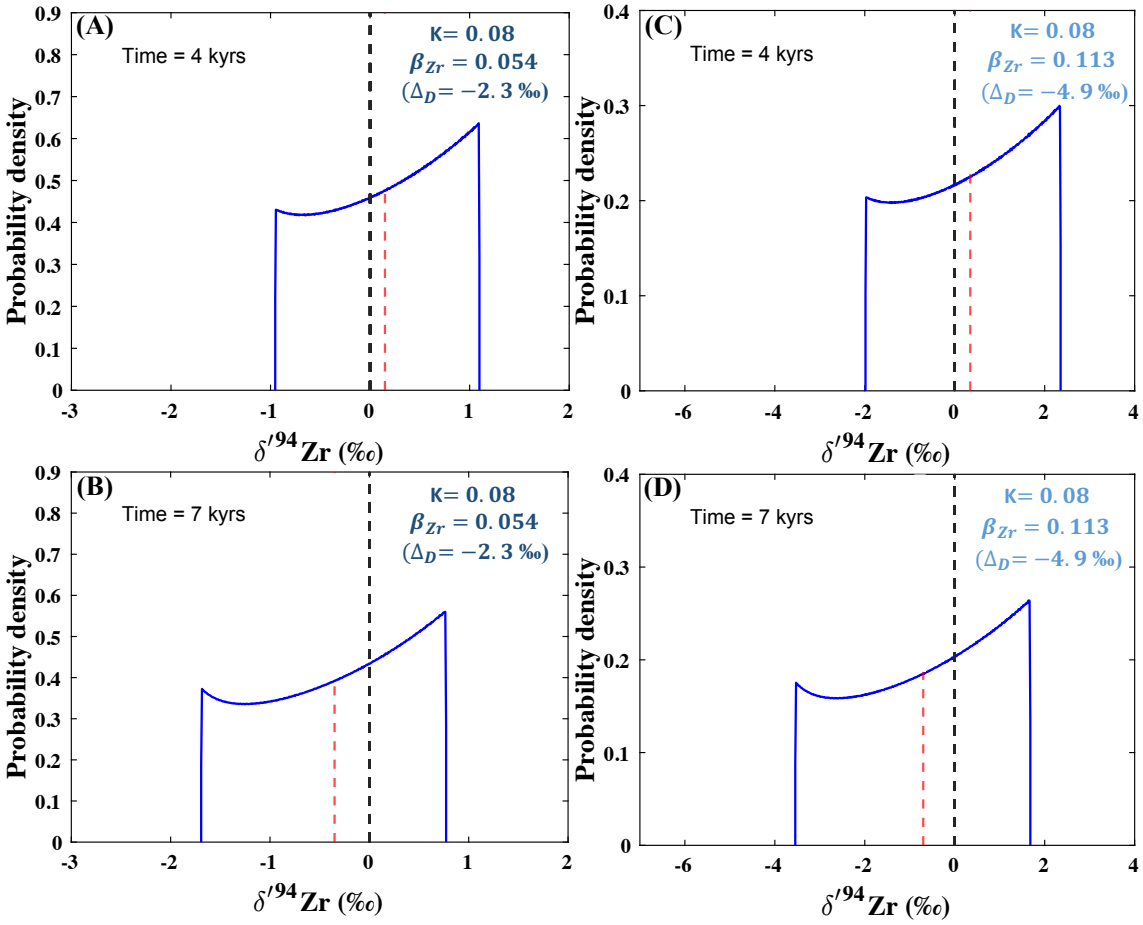

Figure 3.29 Expected probability density distribution functions (PDFs) of the Zr isotopic compositions of Zr atoms in the diffusive boundary layer around a low-Zr growing crystal at 4 and 7 kyr. The dashed red vertical line is the average isotopic composition of the boundary layer where the melt is Zr-supersaturated by at least of factor of 3. We only consider here locations where $C/C_0 > 3$ possibly conducive to zircon saturation. (A)-(B) use a diffusive Zr isotopic fractionation factor $\Delta_D = -2.3$ ‰ ($\beta_{Zr} = 0.054$ in Eq. 3.24); (C)-(D) use a diffusive Zr isotopic fractionation factor $\Delta_D = -4.9$ ‰ ($\beta_{Zr} = 0.113$ in Eq. 3.24). As the Zr-poor mineral grows (time increases from (A) to (B), or from (C) to (D)), the δ'^{94}Zr distributions of the diffusion-triggered crystallized (DTC) zircons shift to more negative δ'^{94}Zr values. (A, B and C, D correspond to **Movie 9 and 10**).

3.4.4 Combined Zr and Hf fractionations

One manner to distinguish between equilibrium and kinetic isotopic fractionation is, in theory, to compare δ'^{94}Zr and δ'^{179}Hf. We performed *ab initio* calculations of the equilibrium fractionation factor of Hf in a variety of minerals (**Fig. 3.7, Table 3.2**). Zirconium and hafnium form bonds of similar strengths and as discussed in the results section, at equilibrium we expect the isotopic fractionations of Zr and Hf between two phases A and B to scale as,

$$\frac{\Delta'^{94/90}Zr_{A-B}}{\Delta'^{179/177}Hf_{A-B}} \approx \frac{\left(\frac{1}{M^{90}}-\frac{1}{M^{94}}\right)}{\left(\frac{1}{M^{177}}-\frac{1}{M^{179}}\right)} = 7.5 \ , \tag{3.36}$$

Combining the diffusivity ratios of Zr and Hf isotopes (Eqs. 3.24 and 3.25), we expect to first-order that kinetic isotopic fractionation induced by diffusion will produce isotopic fractionations for Zr and Hf that scale as (see the formulas in Sio et al. 2013; Kin I Sio and Dauphas, 2017; Dauphas and Rouxel, 2006; Watson and Muller, 2009; for a variety of diffusion geometries),

$$\frac{\delta'^{94/90}\mathrm{Zr}}{\delta'^{179/177}\mathrm{Hf}} \approx \frac{1-\frac{D^{94}}{D^{90}}}{1-\frac{D^{179}}{D^{177}}} \approx 3.8 \ , \tag{3.37}$$

This shows that equilibrium and diffusion-driven kinetic isotopic fractionation are expected to produce very distinct $\frac{\delta'^{94}\mathrm{Zr}}{\delta'^{179}\mathrm{Hf}}$ values. No δ'^{179}Hf value has been reported but its combination with δ'^{94}Zr measurements should provide a diagnostic tool to tell when Zr isotopic fractionation in magmas reflects diffusive processes and use those effects to estimate the growth rate and cooling history of zircons.

3.4.5 Potential usage in metamorphic zircons

Zirconium stable isotopic variations can potentially help unravel the complex processes involved in metamorphic zircon formation. For example, our *ab initio* calculations show that under amphibolite conditions (500-700 °C), Zr in amphibole should be fractionated in δ'^{94}Zr by 0.22-0.35 ‰, or 0.55-0.86 ‰ relative to Zr in ilmenite (**Table 3.2**, we use tremolite to approximate the fractionation in amphibole, the two ranges correspond to two substitution mechanisms for the calculations of tremolite). It is thus conceivable that metamorphic zircon formed from the decomposition of amphibole (Fraser et al., 1997) would inherit the Zr isotopic composition of amphibole, which we expect to be distinct from the Zr isotopic composition of the zircon formed by the breakdown of ilmenite (Bingen et al., 2001). Inter-mineral fractionations between zircon and co-existing Zr-bearing metamorphic minerals may also help recognizing equilibrium parageneses and inferring equilibration temperatures.

3.5 Conclusion

This study presents first-principle calculations of equilibrium Zr and Hf isotopic fractionation factors in a variety of Zr-rich phases as well as a large number of minerals where Zr is present at trace level in substitution with other elements. The minerals studied include Ca-catapleiite, a mineral that previous EXAFS studies showed contains Zr in a coordination environment similar to that encountered in silicate melts. We find that in the temperature range relevant to magmatic zircon crystallization, there is negligible equilibrium Zr isotopic fractionation between zircon/baddeleyite and melt. In general, equilibrium Zr isotopic fractionation between silicate minerals and melt is not significant either. Iron-titanium oxides (ilmenite and magnetite)

have the potential to produce non-negligible mass-dependent fractionation of Zr isotopes. However, we show through modeling using Rhyolite-MELTS that the relatively low concentration of Zr in these Fe,Ti-oxide mineral offers limited leverage to greatly modify the melt composition during magmatic differentiation before zircon saturation.

Kinetic effects associated with diffusion-limited crystallization (DLC) of zircon can potentially produce significant light Zr isotope enrichments in zircon. Reservoir effects in the liquid would also lead to the crystallization of zircons with high $\delta'^{94}\mathrm{Zr}$. Diffusion-triggered crystallization (DTC) of zircon from the diffusive boundary layer developed during the growth of Zr-poor minerals can produce zircons with both positive and negative $\delta'^{94}\mathrm{Zr}$ values. If diffusion-driven kinetic effects are the main mechanism at play, Zr isotopic analyses of zircons would provide a means of constraining the cooling history of the host magma. We show that correlating Zr and Hf isotopic measurements can help identify kinetic effects in zircons, as equilibrium and diffusive kinetic effects are expected to impart different correlations between $\delta'^{94}\mathrm{Zr}$ and $\delta'^{179}\mathrm{Hf}$ values.

3.6 Appendix

3.6.1 Derivation of diffusion-driven kinetic isotopic effects produced by the accumulation of an incompatible element in a diffusive boundary layer

3.6.1.1 General equations for the liquid concentration during transient

Smith et al. (1955) provide analytical equations of concentration profiles for planar crystal growth at constant rate. The general equation for the concentration in the liquid at some distance

x_l from the advancing interface relative to the concentration in the far field (or the initial liquid concentration) is,

$$\frac{C_l(x_l)}{C_0} = 1 + \frac{1-K}{2K}\exp\left(-\frac{\dot{R}}{D}x_l\right)\mathrm{erfc}\left(\frac{x_l-\dot{R}t}{2\sqrt{Dt}}\right) - \frac{1}{2}\mathrm{erfc}\left(\frac{x_l+\dot{R}t}{2\sqrt{Dt}}\right) + \left(1-\frac{1}{2K}\right)\exp\left[-(1-\mathrm{K})\frac{\dot{R}}{D}\left(x_l + K\dot{R}t\right)\right]\mathrm{erfc}\left[\frac{x_l+(2K-1)\dot{R}t}{2\sqrt{Dt}}\right], \quad \text{(A1)}$$

where x_l is the distance measured from the interface, C_0 is the concentration in the liquid at infinity, K is the solid/liquid partition coefficient, $\dot{R}$ is the growth rate (constant), and D is the diffusivity of the trace element in the liquid. If we express the concentration in terms of dimensionless distance u,

$$u = \frac{\dot{R}}{D}x_l, \quad \text{(A2)}$$

and dimensionless time w,

$$w = \frac{\dot{R}^2 t}{D}, \quad \text{(A3)}$$

then the concentration in the liquid can be rewritten as,

$$\frac{C_l(x_l)}{C_0} = 1 + \frac{1-K}{2K}\exp(-u)\,\mathrm{erfc}\left(\frac{u-w}{2\sqrt{w}}\right) - \frac{1}{2}\mathrm{erfc}\left(\frac{u+w}{2\sqrt{w}}\right) + \left(1-\frac{1}{2K}\right)\exp[-(1-\mathrm{K})(u+Kw)]\,\mathrm{erfc}\left[\frac{u+(2K-1)w}{2\sqrt{w}}\right], \quad \text{(A4)}$$

3.6.1.2 General equations for the liquid isotopic composition during transient

Following Sio et al. (2018), we can use the expressions for the concentration profile to calculate the isotopic composition profile. We write the concentration as a function of diffusivity D and partition coefficient K as,

$$C_l = f(D,K) \times C_0, \quad \text{(A5)}$$

If we consider two isotopes 2 and 1, we can write,

$$\frac{C_{l,1}}{C_{0,1}} = f(D_1, K_1)\ , \tag{A6}$$

$$\frac{C_{l,2}}{C_{0,2}} \simeq f(D_1, K_1) + \frac{\partial f}{\partial D} \times (D_2 - D_1) + \frac{\partial f}{\partial K} \times (K_2 - K_1)\ , \tag{A7}$$

The isotopic ratio is therefore,

$$\frac{C_{l,2}/C_{l,1}}{C_{0,2}/C_{0,1}} \simeq 1 + \frac{D}{f}\frac{\partial f}{\partial D} \times \left(\frac{D_2}{D_1} - 1\right) + \frac{K}{f}\frac{\partial f}{\partial K} \times \left(\frac{K_2}{K_1} - 1\right), \tag{A8}$$

In δ notation, this can take the form,

$$\delta_l \simeq D\,\frac{\partial lnf}{\partial D} \times \left(\frac{D_2}{D_1} - 1\right) \times 1000 + K\,\frac{\partial lnf}{\partial K} \times \left(\frac{K_2}{K_1} - 1\right) \times 1000\ , \tag{A9}$$

We introduce the following notations,

$$\Delta_D \simeq \left(\frac{D_2}{D_1} - 1\right) \times 1000\ , \tag{A10}$$

$$\Delta_K \simeq \left(\frac{K_2}{K_1} - 1\right) \times 1000\ , \tag{A11}$$

where Δ_K is the equilibrium isotopic fractionation between solid and liquid. The isotopic composition in the liquid then takes the form,

$$\delta_l \simeq D\,\frac{\partial lnf}{\partial D} \times \Delta_D + K\,\frac{\partial lnf}{\partial K} \times \Delta_K\ , \tag{A12}$$

From the concentration profile (eq. A4),

$$D\,\frac{\partial lnf}{\partial D} =$$

$$\frac{e^{-Kw-\frac{(u+w)^2}{4w}}(-1+K)\left\{2e^{u+Kw}K\sqrt{w}+e^{\frac{(u+w)^2}{4w}}\sqrt{\pi}\left[-e^{Kw}u\times\mathrm{erfc}\left(\frac{u-w}{2\sqrt{w}}\right)-e^{K(u+Kw)}(-1+2K)(u+Kw)\mathrm{erfc}\left(\frac{u+(2K-1)w}{2\sqrt{w}}\right)\right]\right\}}{\left\{\sqrt{\pi}\left[e^{u}K+e^{u}K\times\mathrm{erfc}\left(\frac{u+w}{2\sqrt{w}}\right)-(-1+K)\mathrm{erfc}\left(\frac{u-w}{2\sqrt{w}}\right)+e^{K(u+(-1+K)w)}(-1+2K)\mathrm{erfc}\left(\frac{u+(2K-1)w}{2\sqrt{w}}\right)\right]\right\}}\ , \tag{A13}$$

$$K\frac{\partial lnf}{\partial K} =$$

$$\frac{e^{-\frac{(u+w)^2}{4w}}\left\{2e^{u}K(-1+2K)w+\sqrt{\pi}\sqrt{w}\left[e^{\frac{(u+w)^2}{4w}}\mathrm{erfc}\left(\frac{u-w}{2\sqrt{w}}\right)-e^{\frac{1}{4}\left((2+4K)u+\frac{u^2}{w}+(1-2K)^2w\right)}\left(1+K(-1+2K)(u+(-1+2K)w)\right)\mathrm{erfc}\left(\frac{u+(2K-1)w}{2\sqrt{w}}\right)\right]\right\}}{\left\{\sqrt{\pi}\sqrt{w}\left[(-1+K)\mathrm{erfc}\left(\frac{u-w}{2\sqrt{w}}\right)+e^{u}K\left(-2+\mathrm{erfc}\left(\frac{u+w}{2\sqrt{w}}\right)\right)-e^{K(u+(-1+K)w)}(-1+2K)\mathrm{erfc}\left(\frac{u+(2K-1)w}{2\sqrt{w}}\right)\right]\right\}} \quad .$$

(A14)

Combining equations (A12- A14) gives the isotopic composition in the liquid as a function of time and distance from the interface.

3.6.1.3 Liquid concentration and isotopic composition at steady-state

Smith et al. (1955) also provide the analytical equation of the concentration profile in the liquid at steady-state,

$$\frac{C_l(x_l)}{C_0} = 1 + \frac{1-K}{K}\exp\left(-\frac{\dot{R}}{D}x_l\right) = 1 + \frac{1-K}{K}\exp(-u)\ , \tag{A15}$$

In the same manner as outlined above, we calculate that the isotopic composition at steady-state in δ notation is,

$$\delta_l \simeq \frac{(1-K)u}{1+K(e^u-1)}\Delta_D + \frac{1}{K-1-Ke^u}\Delta_K\ , \tag{A16}$$

3.6.1.4 Maximum isotopic fractionation in the liquid at steady-state

At steady-state, we can also calculate the maximum isotopic fractionation in the liquid in the diffusive boundary layer. In equation (A16), we set $\Delta_K = 0$, so we have,

$$\delta_l \simeq \frac{(1-K)u}{1+K(e^u-1)}\Delta_D\ , \tag{A17}$$

The location of the maximum isotopic composition is calculated by solving for u in the following equation,

$$\frac{\partial \delta_l}{\partial u} = \frac{\Delta_D (K-1)(K-1+e^u K(u-1)}{(1+(e^u-1)K)^2} = 0 \,, \tag{A18}$$

and then injecting it in eq. A17, which yields,

$$\delta_l = \Delta_D \times ProductLog[\tfrac{1-K}{eK}] \,, \tag{A19}$$

where $ProductLog[z]$ is the principal solution for the transcendental equation $z = we^w$.

3.6.1.5 Concentration and isotopic composition in the solid

For the growing solid, the distance between the solid-liquid interface and the origin of the solid (position of the interface at time zero) is

$$x_s = \dot{R}t \,, \tag{A20}$$

The concentration in the solid is equal to K times the liquid concentration at $x_l = 0$ or $u = 0$, thus in the transient, the concentration in the growing solid is,

$$C_s(x_s) = C_{l(x_l=0)} \times K \;\; , \tag{A21}$$

From equation (A4), we have,

$$\frac{C_s(x_s)}{C_0} = K - \frac{1}{2}\mathrm{erfc}\left(\frac{\sqrt{w}}{2}\right) + \left(\mathrm{K} - \frac{1}{2}\right)\exp[-\mathrm{K}(1-\mathrm{K})w]\,\mathrm{erfc}\left[\frac{(2K-1)\sqrt{w}}{2}\right], \tag{A22}$$

and the isotopic composition in the growing solid is,

$$\delta_s = \delta_{l(u=0)} + \Delta_K \,, \tag{A23}$$

$$\delta_s = D\frac{\partial lnf}{\partial D}(u=0) \times \Delta_D + [1 + K\frac{\partial lnf}{\partial K}(u=0)] \times \Delta_K \;\; , \tag{A24}$$

From equations (A13) and (A14), we have,

$$D\frac{\partial lnf}{\partial D}(u=0) = \frac{e^{-\frac{1}{4}(1+4K)w}(-1+K)[2e^{Kw}K\sqrt{w} - e^{\left(\frac{1}{4}+K^2\right)w}K(-1+2K)\sqrt{\pi}w \times \mathrm{erfc}\left(\frac{(2K-1)\sqrt{w}}{2}\right)]}{\sqrt{\pi}\left[K + K\times\mathrm{erfc}\left(\frac{\sqrt{w}}{2}\right) - (-1+K)\mathrm{erfc}\left(-\frac{\sqrt{w}}{2}\right) + e^{(-1+K)Kw}(-1+2K)\mathrm{erfc}\left(\frac{(2K-1)\sqrt{w}}{2}\right)\right]}, \tag{A25}$$

$$1 + K\frac{\partial lnf}{\partial K}(u = 0) =$$

$$\frac{1+2e^{-\frac{w}{4}}K(-1+2K)w+\sqrt{\pi}\sqrt{w}\left[1+\mathrm{erfc}\left(\frac{\sqrt{w}}{2}\right)-e^{(-1+K)Kw}\left(1+(1-2K)^2Kw\right)\mathrm{erfc}\left(\frac{(2K-1)\sqrt{w}}{2}\right)\right]}{\sqrt{\pi}\sqrt{w}\left[(-1+K)\mathrm{erfc}\left(-\frac{\sqrt{w}}{2}\right)+K\left(-2+\mathrm{erfc}\left(\frac{\sqrt{w}}{2}\right)\right)-e^{(-1+K)Kw}(-1+2K)\mathrm{erfc}\left(\frac{(2K-1)\sqrt{w}}{2}\right)\right]}\ , \tag{A26}$$

and at steady-state for the solid, $C_s(x_s) = C_0$, $\delta_s = 0$.

3.7 References

Akram W., Schönbächler M., Bisterzo S. and Gallino R. (2015) Zirconium isotope evidence for the heterogeneous distribution of s-process materials in the solar system. *Geochimica et Cosmochimica Acta* **165**, 484–500.

Akram W., Schönbächler M., Sprung P. and Vogel N. (2013) Zirconium—Hafnium isotope evidence from meteorites for the decoupled synthesis of light and heavy neutron-rich nuclei. *The Astrophysical Journal* **777**, 169.

Alfe D., Price G. D. and Gillan M. J. (1999) Oxygen in the Earth's core: a first-principles study. *Physics of the Earth and Planetary Interiors* **110**, 191–210.

Amelin Y., Lee D.-C., Halliday A. N. and Pidgeon R. T. (1999) Nature of the Earth's earliest crust from hafnium isotopes in single detrital zircons. *Nature* **399**, 252–255.

Aranovich L. Y. and Bortnikov N. (2018) New Zr–Hf geothermometer for magmatic zircons. *Petrology* **26**, 115–120.

Bigeleisen J. and Mayer M. G. (1947a) Calculation of Equilibrium Constants for Isotopic Exchange Reactions. *The Journal of Chemical Physics* **15**, 261.

Bigeleisen J. and Mayer M. G. (1947b) Calculation of equilibrium constants for isotopic exchange reactions. *The Journal of Chemical Physics* **15**, 261–267.

Bindeman I. N. and Melnik O. E. (2016) Zircon survival, rebirth and recycling during crustal melting, magma crystallization, and mixing based on numerical modelling. *Journal of Petrology* **57**, 437–460.

Bingen B., Austrheim H. and Whitehouse M. (2001) Ilmenite as a source for zirconium during high-grade metamorphism? Textural evidence from the Caledonides of western Norway and implications for zircon geochronology. *Journal of Petrology* **42**, 355–375.

Blanchard M., Dauphas N., Hu M., Roskosz M., Alp E., Golden D., Sio C., Tissot F., Zhao J. and Gao L. (2015) Reduced partition function ratios of iron and oxygen in goethite. *Geochimica et Cosmochimica Acta* **151**, 19–33.

Blichert-Toft J. and Albarède F. (1997) The Lu-Hf isotope geochemistry of chondrites and the evolution of the mantle-crust system. *Earth and Planetary Science Letters* **148**, 243–258.

Blöchl P. E. (1994) Projector augmented-wave method. *Physical Review B* **50**, 17953–17979.

Boehnke P., Watson E. B., Trail D., Harrison T. M. and Schmitt A. K. (2013) Zircon saturation re-revisited. *Chemical Geology* **351**, 324–334.

Bowring S. A., Erwin D., Jin Y., Martin M., Davidek K. and Wang W. (1998) U/Pb zircon geochronology and tempo of the end-Permian mass extinction. *Science* **280**, 1039–1045.

Brimhall G. H. and Dietrich W. E. (1987) Constitutive mass balance relations between chemical composition, volume, density, porosity, and strain in metasomatic hydrochemical systems: results on weathering and pedogenesis. *Geochimica et Cosmochimica Acta* **51**, 567–587.

Carley T. L., Miller C. F., Wooden J. L., Bindeman I. N. and Barth A. P. (2011) Zircon from historic eruptions in Iceland: reconstructing storage and evolution of silicic magmas. *Mineralogy and Petrology* **102**, 135.

Chopra R., Richter F. M., Watson E. B. and Scullard C. R. (2012) Magnesium isotope fractionation by chemical diffusion in natural settings and in laboratory analogues. *Geochimica et Cosmochimica Acta* **88**, 1–18.

Claiborne L. L., Miller C. F. and Wooden J. L. (2010) Trace element composition of igneous zircon: a thermal and compositional record of the accumulation and evolution of a large silicic batholith, Spirit Mountain, Nevada. *Contributions to Mineralogy and Petrology* **160**, 511–531.

Claiborne L. L., Miller C., Walker B., Wooden J., Mazdab F. and Bea F. (2006) Tracking magmatic processes through Zr/Hf ratios in rocks and Hf and Ti zoning in zircons: an example from the Spirit Mountain batholith, Nevada. *Mineralogical Magazine* **70**, 517–543.

Dauphas N., Hu M. Y., Baker E. M., Hu J., Tissot F. L., Alp E. E., Roskosz M., Zhao J., Bi W. and Liu J. (2018) SciPhon: a data analysis software for nuclear resonant inelastic X-ray scattering with applications to Fe, Kr, Sn, Eu and Dy. *Journal of synchrotron radiation* **25**, 1581–1599.

Dauphas N., John S. G. and Rouxel O. (2017) Iron isotope systematics. *Reviews in Mineralogy and Geochemistry* **82**, 415–510.

Dauphas N., Roskosz M., Alp E., Golden D., Sio C., Tissot F., Hu M., Zhao J., Gao L. and Morris R. (2012) A general moment NRIXS approach to the determination of equilibrium Fe isotopic fractionation factors: application to goethite and jarosite. *Geochimica et Cosmochimica Acta* **94**, 254–275.

Dauphas N. and Rouxel O. (2006) Mass spectrometry and natural variations of iron isotopes. *Mass Spectrometry Reviews* **25**, 515–550.

Dauphas N. and Schauble E. A. (2016) Mass fractionation laws, mass-independent effects, and isotopic anomalies. *Annual Review of Earth and Planetary Sciences* **44**, 709–783.

Dauphas N., Teng F.-Z. and Arndt N. T. (2010) Magnesium and iron isotopes in 2.7 Ga Alexo komatiites: mantle signatures, no evidence for Soret diffusion, and identification of diffusive transport in zoned olivine. *Geochimica et Cosmochimica Acta* **74**, 3274–3291.

Davis A. M., Zhang J., Greber N. D., Hu J., Tissot F. L. and Dauphas N. (2018) Titanium isotopes and rare earth patterns in CAIs: evidence for thermal processing and gas-dust decoupling in the protoplanetary disk. *Geochimica et cosmochimica acta* **221**, 275–295.

Deng Z., Chaussidon M., Savage P., Robert F., Pik R. and Moynier F. (2019) Titanium isotopes as a tracer for the plume or island arc affinity of felsic rocks. *Proceedings of the National Academy of Sciences* **116**, 1132–1135.

Deng Z., Moynier F., Sossi P. and Chaussidon M. (2018) Bridging the depleted MORB mantle and the continental crust using titanium isotopes.

DePaolo D. J. (2011) Surface kinetic model for isotopic and trace element fractionation during precipitation of calcite from aqueous solutions. *Geochimica et cosmochimica acta* **75**, 1039–1056.

Eggins S., Rudnick R. and McDonough W. (1998) The composition of peridotites and their minerals: a laser-ablation ICP–MS study. *Earth and planetary science letters* **154**, 53–71.

El Goresy A., Zinner E., Matsunami S., Palme H., Spettel B., Lin Y. and Nazarov M. (2002) Efremovka 101.1: A CAI with ultrarefractory REE patterns and enormous enrichments of Sc, Zr, and Y in fassaite and perovskite. *Geochimica et Cosmochimica Acta* **66**, 1459–1491.

Elfers B.-M., Sprung P., Messling N. and Münker C. (2020) The combined Zr and Hf isotope inventory of bulk rock and sequentially leached chondrite samples. *Geochimica et Cosmochimica Acta* **270**, 475–491.

Elfers B.-M., Sprung P., Pfeifer M., Wombacher F., Peters S. T. and Münker C. (2018) Variable distribution of s-process Hf and W isotope carriers in chondritic meteorites–Evidence from 174Hf and 180W. *Geochimica et Cosmochimica Acta* **239**, 346–362.

Fahey A., Goswami J., McKeegan K. and Zinner E. (1987) 26Al, 244Pu, 50Ti, REE, and trace element abundances in hibonite grains from CM and CV meteorites. *Geochimica et Cosmochimica Acta* **51**, 329–350.

Farges F., Brown G. E. and Velde D. (1994) Structural environment of Zr in two inosilicates from Cameroon: mineralogical and geochemical implications. *American Mineralogist* **79**, 838–847.

Farges F., Ponader C. W. and Brown Jr G. E. (1991) Structural environments of incompatible elements in silicate glass/melt systems: I. Zirconium at trace levels. *Geochimica et Cosmochimica Acta* **55**, 1563–1574.

Feng L., Hu W., Jiao Y., Zhou L., Zhang W., Hu Z. and Liu Y. (2020) High-precision stable zirconium isotope ratio measurements by double spike thermal ionization mass spectrometry. *Journal of Analytical Atomic Spectrometry* **35**, 736–745.

Finch R. J., Hanchar J. M., Hoskin P. W. and Burns P. C. (2001) Rare-earth elements in synthetic zircon: Part 2. A single-crystal X-ray study of xenotime substitution. *American Mineralogist* **86**, 681–689.

Fraser G., Ellis D. and Eggins S. (1997) Zirconium abundance in granulite-facies minerals, with implications for zircon geochronology in high-grade rocks. *Geology* **25**, 607–610.

Greber N. D. and Dauphas N. (2019) The chemistry of fine-grained terrigenous sediments reveals a chemically evolved Paleoarchean emerged crust. *Geochimica et cosmochimica acta* **255**, 247–264.

Greber N. D., Dauphas N., Bekker A., Ptáček M. P., Bindeman I. N. and Hofmann A. (2017a) Titanium isotopic evidence for felsic crust and plate tectonics 3.5 billion years ago. *Science* **357**, 1271–1274.

Greber N. D., Dauphas N., Puchtel I. S., Hofmann B. A. and Arndt N. T. (2017b) Titanium stable isotopic variations in chondrites, achondrites and lunar rocks. *Geochimica et cosmochimica acta* **213**, 534–552.

Grossman L. and Ganapathy R. (1976a) Trace elements in the Allende meteorite—I. Coarse-grained, Ca-rich inclusions. *Geochimica et Cosmochimica Acta* **40**, 331–344.

Grossman L. and Ganapathy R. (1976b) Trace elements in the Allende meteorite—II. Fine-grained. Ca-rich inclusions. *Geochimica et Cosmochimica Acta* **40**, 967–977.

Grove T. L. and Baker M. B. (1984) Phase equilibrium controls on the tholeiitic versus calc-alkaline differentiation trends. *Journal of Geophysical Research: Solid Earth* **89**, 3253–3274.

Grove T. L., Elkins-Tanton L. T., Parman S. W., Chatterjee N., Müntener O. and Gaetani G. A. (2003) Fractional crystallization and mantle-melting controls on calc-alkaline differentiation trends. *Contributions to Mineralogy and Petrology* **145**, 515–533.

Gualda G. A., Ghiorso M. S., Lemons R. V. and Carley T. L. (2012) Rhyolite-MELTS: a modified calibration of MELTS optimized for silica-rich, fluid-bearing magmatic systems. *Journal of Petrology* **53**, 875–890.

Gucsik A., Zhang M., Koeberl C., Salje E. K. H., Redfern S. A. T. and Pruneda J. M. (2004) Infrared and Raman spectra of ZrSiO 4 experimentally shocked at high pressures. *Mineralogical Magazine* **68**, 801–811.

Guo J.-L., Wang Z., Zhang W., Moynier F., Cui D., Hu Z. and Ducea M. N. (2020) Significant Zr isotope variations in single zircon grains recording magma evolution history. *Proceedings of the National Academy of Sciences* **117**, 21125–21131.

Harper Jr C. L. (1996) Evidence for 92gNb in the early solar system and evaluation of a new p-process cosmochronometer from 92gNb/92Mo. *The Astrophysical Journal* **466**, 437.

Harrison T., Blichert-Toft J., Müller W., Albarede F., Holden P. and Mojzsis S. J. (2005) Heterogeneous Hadean hafnium: evidence of continental crust at 4.4 to 4.5 Ga. *Science* **310**, 1947–1950.

Harrison T. M. and Watson E. B. (1984) The behavior of apatite during crustal anatexis: equilibrium and kinetic considerations. *Geochimica et Cosmochimica Acta* **48**, 1467–1477.

Hawkesworth C. J., Dhuime B., Pietranik A., Cawood P., Kemp A. I. and Storey C. (2010) The generation and evolution of the continental crust. *Journal of the Geological Society* **167**, 229–248.

Helz R. T., Kirschenbaum H., Marinenko J. and Qian R. (1994) *Whole-rock analyses of core samples from the 1967, 1975, 1979 and 1981 drillings of Kilauea Iki lava lake, Hawaii*., US Geological Survey,.

Herzfeld K. F. and Teller E. (1938) The vapor pressure of isotopes. *Physical Review* **54**, 912.

Hopkins M., Harrison T. M. and Manning C. E. (2008) Low heat flow inferred from> 4 Gyr zircons suggests Hadean plate boundary interactions. *Nature* **456**, 493–496.

Howard C., Hill R. and Reichert B. (1988) Structures of ZrO2 polymorphs at room temperature by high-resolution neutron powder diffraction. *Acta Crystallographica Section B: Structural Science* **44**, 116–120.

Huang D., Badro J., Brodholt J. and Li Y. (2019) Ab Initio Molecular Dynamics Investigation of Molten Fe–Si–O in Earth's Core. *Geophysical Research Letters* **46**, 6397–6405.

Huang F., Chen L., Wu Z. and Wang W. (2013) First-principles calculations of equilibrium Mg isotope fractionations between garnet, clinopyroxene, orthopyroxene, and olivine: Implications for Mg isotope thermometry. *Earth and Planetary Science Letters* **367**, 61–70.

Ibañez-Mejia M. and Tissot F. L. (2019) Extreme Zr stable isotope fractionation during magmatic fractional crystallization. *Science Advances* **5**, eaax8648.

Iizuka T., Lai Y.-J., Akram W., Amelin Y. and Schönbächler M. (2016) The initial abundance and distribution of 92Nb in the Solar System. *Earth and Planetary Science Letters* **439**, 172–181.

Inglis E. C., Creech J. B., Deng Z. and Moynier F. (2018) High-precision zirconium stable isotope measurements of geological reference materials as measured by double-spike MC-ICPMS. *Chemical Geology* **493**, 544–552.

Inglis E. C., Moynier F., Creech J., Deng Z., Day J. M., Teng F.-Z., Bizzarro M., Jackson M. and Savage P. (2019) Isotopic fractionation of zirconium during magmatic differentiation and the stable isotope composition of the silicate Earth. *Geochimica et Cosmochimica Acta* **250**, 311–323.

Ionov D. (2004) Chemical variations in peridotite xenoliths from Vitim, Siberia: inferences for REE and Hf behaviour in the garnet-facies upper mantle. *Journal of Petrology* **45**, 343–367.

Ireland T., Compston W. and Heydegger H. (1985) Titanium isotopic anomalies in hibonites from the Murchison carbonaceous chondrite. *Geochimica et Cosmochimica Acta* **49**, 1989–1993.

Jackson M. G., Hart S. R., Saal A. E., Shimizu N., Kurz M. D., Blusztajn J. S. and Skovgaard A. C. (2008) Globally elevated titanium, tantalum, and niobium (TITAN) in ocean island basalts with high 3He/4He. *Geochemistry, Geophysics, Geosystems* **9**.

Jambon A. (1980) Isotopic fractionation: A kinetic model for crystals growing from magmatic melts. *Geochimica et Cosmochimica Acta* **44**, 1373–1380.

Johnson A. C., Aarons S. M., Dauphas N., Nie N. X., Zeng H., Helz R. T., Romaniello S. J. and Anbar A. D. (2019) Titanium isotopic fractionation in Kilauea Iki lava lake driven by oxide crystallization. *Geochimica et Cosmochimica Acta* **264**, 180–190.

Juster T. C., Grove T. L. and Perfit M. R. (1989) Experimental constraints on the generation of FeTi basalts, andesites, and rhyodacites at the Galapagos Spreading Center, 85 W and 95 W. *Journal of Geophysical Research: Solid Earth* **94**, 9251–9274.

Keyser D. J. and Guillem A. F. (2014) Microporous zirconium silicate for the treatment of hyperkalemia.

Kin I Sio C. and Dauphas N. (2017) Thermal and crystallization histories of magmatic bodies by Monte Carlo inversion of Mg-Fe isotopic profiles in olivine. *Geology* **45**, 67–70.

Leya I., Schönbächler M., Wiechert U., Krähenbühl U. and Halliday A. N. (2008) Titanium isotopes and the radial heterogeneity of the solar system. *Earth and Planetary Science Letters* **266**, 233–244.

Lodders K. (2003) Solar system abundances and condensation temperatures of the elements. *The Astrophysical Journal* **591**, 1220.

MacPherson G. J. (1994) Refractory inclusions in the prototypical CM chondrite, Mighei. *Geochimica et Cosmochimica Acta* **58**, 5599–5625.

Martin P. M. and Mason B. (1974) Major and trace elements in the Allende meteorite. *Nature* **249**, 333–334.

McDonough W. F. and Sun S.-S. (1995) The composition of the Earth. *Chemical geology* **120**, 223–253.

Méheut M., Lazzeri M., Balan E. and Mauri F. (2009) Structural control over equilibrium silicon and oxygen isotopic fractionation: A first-principles density-functional theory study. *Chemical Geology* **258**, 28–37.

Merlino S., Pasero M., Bellezza M., Pushcharovsky D. Y., Gobetchia E. R., Zubkova N. V. and Pekov I. V. (2004) The crystal structure of calcium catapleiite. *Canadian Mineralogist* **42**, 1037–1045.

Millet M.-A., Dauphas N., Greber N. D., Burton K. W., Dale C. W., Debret B., Macpherson C. G., Nowell G. M. and Williams H. M. (2016) Titanium stable isotope investigation of magmatic processes on the Earth and Moon. *Earth and planetary science letters* **449**, 197–205.

Miyashiro A. and Shido F. (1975) Tholeiitic and calc-alkalic series in relation to the behaviors of titanium, vanadium, chromium, and nickel. *American Journal of Science* **275**, 265–277.

Mojzsis S. J., Harrison T. M. and Pidgeon R. T. (2001) Oxygen-isotope evidence from ancient zircons for liquid water at the Earth's surface 4,300 Myr ago. *Nature* **409**, 178–181.

Münker C., Pfänder J. A., Weyer S., Büchl A., Kleine T. and Mezger K. (2003) Evolution of planetary cores and the Earth-Moon system from Nb/Ta systematics. *Science* **301**, 84–87.

Nebel O., van Westrenen W., Vroon P. Z., Wille M. and Raith M. M. (2010) Deep mantle storage of the Earth's missing niobium in late-stage residual melts from a magma ocean. *Geochimica et Cosmochimica Acta* **74**, 4392–4404.

Niederer F., Papanastassiou D. and Wasserburg G. (1981) The isotopic composition of titanium in the Allende and Leoville meteorites. *Geochimica et Cosmochimica Acta* **45**, 1017–1031.

Niemeyer S. and Lugmair G. (1981) Ubiquitous isotopic anomalies in Ti from normal Allende inclusions. *Earth and Planetary Science Letters* **53**, 211–225.

Oeser M., Dohmen R., Horn I., Schuth S. and Weyer S. (2015) Processes and time scales of magmatic evolution as revealed by Fe–Mg chemical and isotopic zoning in natural olivines. *Geochimica et Cosmochimica Acta* **154**, 130–150.

O'Neill H. S. C. and Palme H. (2008) Collisional erosion and the non-chondritic composition of the terrestrial planets. *Philosophical Transactions of the Royal Society A: Mathematical, Physical and Engineering Sciences* **366**, 4205–4238.

Orians K. J., Boyle E. A. and Bruland K. W. (1990) Dissolved titanium in the open ocean. *Nature* **348**, 322–325.

Padilla A., Miller C., Carley T., Economos R., Schmitt A., Coble M., Wooden J., Fisher C., Vervoort J. and Hanchar J. (2016) Elucidating the magmatic history of the Austurhorn silicic intrusive complex (southeast Iceland) using zircon elemental and isotopic geochemistry and geochronology. *Contributions to Mineralogy and Petrology* **171**, 69.

Patchett P. J., Kouvo O., Hedge C. E. and Tatsumoto M. (1982) Evolution of continental crust and mantle heterogeneity: evidence from Hf isotopes. *Contributions to Mineralogy and Petrology* **78**, 279–297.

Patchett P. and Tatsumoto M. (1980) Hafnium isotope variations in oceanic basalts. *Geophysical Research Letters* **7**, 1077–1080.

Perdew J. P., Burke K. and Ernzerhof M. (1996) Generalized Gradient Approximation Made Simple. *Physical Review Letters* **77**, 3865–3868.

Peters S. T., Münker C., Pfeifer M., Elfers B.-M. and Sprung P. (2017) Distribution of p-process 174Hf in early solar system materials and the origin of nucleosynthetic Hf and W isotope anomalies in Ca–Al rich inclusions. *Earth and Planetary Science Letters* **459**, 70–79.

Pfänder J. A., Jung S., Münker C., Stracke A. and Mezger K. (2012) A possible high Nb/Ta reservoir in the continental lithospheric mantle and consequences on the global Nb budget–Evidence from continental basalts from Central Germany. *Geochimica et Cosmochimica Acta* **77**, 232–251.

Pfänder J. A., Münker C., Stracke A. and Mezger K. (2007) Nb/Ta and Zr/Hf in ocean island basalts—implications for crust–mantle differentiation and the fate of Niobium. *Earth and Planetary Science Letters* **254**, 158–172.

Polyakov V., Mineev S., Clayton R., Hu G., Gurevich V., Khramov D., Gavrichev K., Gorbunov V. and Golushina L. (2005) Oxygen isotope fractionation factors involving cassiterite (SnO2): I. Calculation of reduced partition function ratios from heat capacity and X-ray resonant studies. *Geochimica et cosmochimica acta* **69**, 1287–1300.

Ptáček M. P., Dauphas N. and Greber N. D. (2020) Chemical evolution of the continental crust from a data-driven inversion of terrigenous sediment compositions. *Earth and planetary science letters* **539**, 116090.

Quintard P. E., Barbéris P., Mirgorodsky A. P. and Merle-Méjean T. (2004) Comparative Lattice-Dynamical Study of the Raman Spectra of Monoclinic and Tetragonal Phases of Zirconia and Hafnia. *Journal of the American Ceramic Society* **85**, 1745–1749.

Richter F. M., Davis A. M., DePaolo D. J. and Watson E. B. (2003) Isotope fractionation by chemical diffusion between molten basalt and rhyolite. *Geochimica et Cosmochimica Acta* **67**, 3905–3923.

Richter F. M., Watson E. B., Mendybaev R. A., Teng F.-Z. and Janney P. E. (2008) Magnesium isotope fractionation in silicate melts by chemical and thermal diffusion. *Geochimica et Cosmochimica Acta* **72**, 206–220.

Richter F. M., Watson E. B., Mendybaev R., Dauphas N., Georg B., Watkins J. and Valley J. (2009) Isotopic fractionation of the major elements of molten basalt by chemical and thermal diffusion. *Geochimica et Cosmochimica Acta* **73**, 4250–4263.

Roskosz M., Amet Q., Fitoussi C., Dauphas N., Bourdon B., Tissandier L., Hu M., Said A., Alatas A. and Alp E. (2020) Redox and structural controls on tin isotopic fractionations among magmas. *Geochimica et Cosmochimica Acta* **268**, 42–55.

Ross P.-S. and Bédard J. H. (2009) Magmatic affinity of modern and ancient subalkaline volcanic rocks determined from trace-element discriminant diagrams. *Canadian Journal of Earth Sciences* **46**, 823–839.

Rudnick R. and Gao S. (2003) Composition of the continental crust. *The crust* **3**, 1–64.

Rudnick R. L., Barth M., Horn I. and McDonough W. F. (2000) Rutile-bearing refractory eclogites: missing link between continents and depleted mantle. *Science* **287**, 278–281.

Schauble E. A. (2004) Applying stable isotope fractionation theory to new systems. *Reviews in Mineralogy and Geochemistry* **55**, 65–111.

Schauble E. A. (2011) First-principles estimates of equilibrium magnesium isotope fractionation in silicate, oxide, carbonate and hexaaquamagnesium(2+) crystals. *Geochimica et Cosmochimica Acta* **75**, 844–869.

Schoene B., Eddy M. P., Samperton K. M., Keller C. B., Keller G., Adatte T. and Khadri S. F. (2019) U-Pb constraints on pulsed eruption of the Deccan Traps across the end-Cretaceous mass extinction. *Science* **363**, 862–866.

Schönbächler M., Lee D.-C., Rehkämper M., Halliday A. N., Fehr M. A., Hattendorf B. and Günther D. (2003) Zirconium isotope evidence for incomplete admixing of r-process components in the solar nebula. *Earth and Planetary Science Letters* **216**, 467–481.

Schönbächler M., Rehkämper M., Halliday A. N., Lee D.-C., Bourot-Denise M., Zanda B., Hattendorf B. and Günther D. (2002) Niobium-zirconium chronometry and early solar system development. *Science* **295**, 1705–1708.

Sheldon N. D. and Tabor N. J. (2009) Quantitative paleoenvironmental and paleoclimatic reconstruction using paleosols. *Earth-Science Reviews* **95**, 1–52.

Simon J., Jordan M., Tappa M., Schauble E., Kohl I. and Young E. (2017) Calcium and titanium isotope fractionation in refractory inclusions: tracers of condensation and inheritance in the early solar protoplanetary disk. *Earth and Planetary Science Letters* **472**, 277–288.

Simon S. B., Davis A. M. and Grossman L. (1996) A unique ultrarefractory inclusion from the Murchison meteorite. *Meteoritics & Planetary Science* **31**, 106–115.

Sio C. K., Roskosz M., Dauphas N., Bennett N. R., Mock T. and Shahar A. (2018) The isotope effect for Mg-Fe interdiffusion in olivine and its dependence on crystal orientation, composition and temperature. *Geochimica et Cosmochimica Acta* **239**, 463–480.

Sio C. K. I., Dauphas N., Teng F.-Z., Chaussidon M., Helz R. T. and Roskosz M. (2013) Discerning crystal growth from diffusion profiles in zoned olivine by in situ Mg–Fe isotopic analyses. *Geochimica et Cosmochimica Acta* **123**, 302–321.

Sisson T. and Grove T. (1993) Experimental investigations of the role of H 2 O in calc-alkaline differentiation and subduction zone magmatism. *Contributions to mineralogy and petrology* **113**, 143–166.

Smirnov V., Antonova O., Smirnov S., Goldberg M., Komlev V. and Barinov S. (2017) Effect of titanium and zirconium substitutions for calcium on the formation and structure of tricalcium phosphate and hydroxyapatite. *Inorganic Materials* **53**, 1254–1260.

Smith V. G., Tiller W. A. and Rutter J. (1955) A mathematical analysis of solute redistribution during solidification. *Canadian Journal of Physics* **33**, 723–745.

Sohrin Y., Fujishima Y., Ueda K., Akiyama S., Mori K., Hasegawa H. and Matsui M. (1998) Dissolved niobium and tantalum in the North Pacific. *Geophysical research letters* **25**, 999–1002.

Solomatova N. and Caracas R. (2019) Pressure-induced coordination changes in a pyrolitic silicate melt from ab initio molecular dynamics simulations. *Journal of Geophysical Research: Solid Earth* **124**, 11232–11250.

Sprung P., Kleine T. and Scherer E. E. (2013) Isotopic evidence for chondritic Lu/Hf and Sm/Nd of the Moon. *Earth and Planetary Science Letters* **380**, 77–87.

Sprung P., Scherer E. E., Upadhyay D., Leya I. and Mezger K. (2010) Non-nucleosynthetic heterogeneity in non-radiogenic stable Hf isotopes: Implications for early solar system chronology. *Earth and Planetary Science Letters* **295**, 1–11.

Stavros F., Yang A., Leon A., Nuttall M. and Rasmussen H. S. (2014) Characterization of structure and function of ZS-9, a K+ selective ion trap. *PLoS One* **9**, e114686.

Stixrude L. and Karki B. (2005) Structure and freezing of MgSiO3 liquid in Earth's lower mantle. *Science* **310**, 297–299.

Syme R. W. G., Lockwood D. J. and Kerr H. J. (1977) Raman spectrum of synthetic zircon (ZrSiO 4) and thorite (ThSiO 4). *Journal of Physics C: Solid State Physics* **10**, 1335–1348.

Taylor S. R. and McLennan S. M. (1985) The continental crust: its composition and evolution.

Teng F.-Z., Dauphas N., Helz R. T., Gao S. and Huang S. (2011) Diffusion-driven magnesium and iron isotope fractionation in Hawaiian olivine. *Earth and Planetary Science Letters* **308**, 317–324.

Tian S., Inglis E., Creech J., Zhang W., Wang Z., Hu Z., Liu Y. and Moynier F. (2020) The zirconium stable isotope compositions of 22 geological reference materials, 4 zircons and 3 standard solutions. *Chemical Geology*, 119791.

Togo A. and Tanaka I. (2015) First principles phonon calculations in materials science. *Scripta Materialia* **108**, 1–5.

Tompkins H. G., Zieman L. J., Ibañez-Mejia M. and Tissot F. L. (2020) Zirconium stable isotope analysis of zircon by MC-ICP-MS: Methods and application to evaluating intra-crystalline zonation in a zircon megacryst. *Journal of Analytical Atomic Spectrometry*.

Trinquier A., Elliott T., Ulfbeck D., Coath C., Krot A. N. and Bizzarro M. (2009) Origin of nucleosynthetic isotope heterogeneity in the solar protoplanetary disk. *Science* **324**, 374–376.

Urey H. C. (1947) The thermodynamic properties of isotopic substances ed. S.-I. Karato. *Journal of the Chemical Society (Resumed)*, 562.

Valley J., Lackey J., Cavosie A., Clechenko C., Spicuzza M., Basei M., Bindeman I., Ferreira V., Sial A. and King E. (2005) 4.4 billion years of crustal maturation: oxygen isotope ratios of magmatic zircon. *Contributions to Mineralogy and Petrology* **150**, 561–580.

Vervoort J. D. and Blichert-Toft J. (1999) Evolution of the depleted mantle: Hf isotope evidence from juvenile rocks through time. *Geochimica et cosmochimica acta* **63**, 533–556.

Vervoort J., Patchett P., Gehrels G. E. and Nutman A. (1996) Constraints on early Earth differentiation from hafnium and neodymium isotopes. *Nature* **379**, 624–627.

Wade J. and Wood B. (2001) The Earth's 'missing'niobium may be in the core. *Nature* **409**, 75–78.

Wang W., Huang S., Huang F., Zhao X. and Wu Z. (2020) Equilibrium inter-mineral titanium isotope fractionation: Implication for high-temperature titanium isotope geochemistry. *Geochimica et Cosmochimica Acta* **269**, 540–553.

Wang W., Qin T., Zhou C., Huang S., Wu Z. and Huang F. (2017) Concentration effect on equilibrium fractionation of Mg-Ca isotopes in carbonate minerals: Insights from first-principles calculations. *Geochimica et Cosmochimica Acta* **208**, 185–197.

Wang W., Zhou C., Liu Y., Wu Z. and Huang F. (2019) Equilibrium Mg isotope fractionation among aqueous Mg2+, carbonates, brucite and lizardite: Insights from first-principles molecular dynamics simulations. *Geochimica et Cosmochimica Acta* **250**, 117–129.

Watkins J. M., DePaolo D. J., Huber C. and Ryerson F. J. (2009) Liquid composition-dependence of calcium isotope fractionation during diffusion in molten silicates. *Geochimica et Cosmochimica Acta* **73**, 7341–7359.

Watkins J. M., DePaolo D. J., Ryerson F. J. and Peterson B. T. (2011) Influence of liquid structure on diffusive isotope separation in molten silicates and aqueous solutions. *Geochimica et Cosmochimica Acta* **75**, 3103–3118.

Watkins J. M., DePaolo D. J. and Watson E. B. (2017) Kinetic fractionation of non-traditional stable isotopes by diffusion and crystal growth reactions. *Reviews in Mineralogy and Geochemistry* **82**, 85–125.

Watkins J. M., Liang Y., Richter F., Ryerson F. J. and DePaolo D. J. (2014) Diffusion of multi-isotopic chemical species in molten silicates. *Geochimica et Cosmochimica Acta* **139**, 313–326.

Watson E. B. and Harrison T. (2005) Zircon thermometer reveals minimum melting conditions on earliest Earth. *Science* **308**, 841–844.

Watson E. B. and Harrison T. M. (1983) Zircon saturation revisited: temperature and composition effects in a variety of crustal magma types. *Earth and Planetary Science Letters* **64**, 295–304.

Watson E. B. and Müller T. (2009) Non-equilibrium isotopic and elemental fractionation during diffusion-controlled crystal growth under static and dynamic conditions. *Chemical Geology* **267**, 111–124.

Wilde S. A., Valley J. W., Peck W. H. and Graham C. M. (2001) Evidence from detrital zircons for the existence of continental crust and oceans on the Earth 4.4 Gyr ago. *Nature* **409**, 175–178.

Wood B. J., Smythe D. J. and Harrison T. (2019) The condensation temperatures of the elements: A reappraisal. *American Mineralogist: Journal of Earth and Planetary Materials* **104**, 844–856.

Yang H., Lin J.-F., Hu M. Y., Roskosz M., Bi W., Zhao J., Alp E. E., Liu Jin, Liu Jiachao and Wentzcovitch R. M. (2019) Iron isotopic fractionation in mineral phases from Earth's lower mantle: Did terrestrial magma ocean crystallization fractionate iron isotopes? *Earth and Planetary Science Letters* **506**, 113–122.

Zeng H., Rozsa V. F., Nie N. X., Zhang Z., Pham T. A., Galli G. and Dauphas N. (2019) Ab Initio Calculation of Equilibrium Isotopic Fractionations of Potassium and Rubidium in Minerals and Water. *ACS Earth and Space Chemistry* **3**, 2601–2612.

Zhang J., Dauphas N., Davis A. M., Leya I. and Fedkin A. (2012) The proto-Earth as a significant source of lunar material. *Nature Geoscience* **5**, 251–255.

Zhang J., Dauphas N., Davis A. M. and Pourmand A. (2011) A new method for MC-ICPMS measurement of titanium isotopic composition: Identification of correlated isotope anomalies in meteorites. *Journal of Analytical Atomic Spectrometry* **26**, 2197–2205.

Zhang W., Wang Z., Moynier F., Inglis E., Tian S., Li M., Liu Y. and Hu Z. (2019) Determination of Zr isotopic ratios in zircons using laser-ablation multiple-collector inductively coupled-plasma mass-spectrometry. *Journal of Analytical Atomic Spectrometry* **34**, 1800–1809.

Zhang Y., Ni H. and Chen Y. (2010) Diffusion data in silicate melts. *Reviews in Mineralogy and Geochemistry* **72**, 311–408.

Zhang Y. and Xu Z. (2016) Zircon saturation and Zr diffusion in rhyolitic melts, and zircon growth geospeedometer. *American Mineralogist* **101**, 1252–1267.

Zinner E. K., Fahey A. J., Goswami J. N., Ireland T. R. and McKeegan K. D. (1986) Large Ca-48 anomalies are associated with Ti-50 anomalies in Murchison and Murray hibonites. *The Astrophysical Journal* **311**, L103–L107.

4 LU-HF MEASUREMENTS OF SINGLE ZIRCON GRAINS

This chapter is based on: Chen, X., Dauphas, N., McKeegan K.D., Schoene B., Barboni M. (2022). Lu-Hf measurements of single zircon grains. *J. Anal. At. Spectrom.*, *(in prep)*.

4.1 Introduction

Several previous studies addressing the magmatic and impact histories of the moon used the robust chronometers recorded in zircons by coupling U-Pb and Lu-Hf isotopic analyses of single lunar zircon grains (Taylor et al., 2009; Barboni et al., 2017). The results of those analyses on detrital zircons were used to derive a minimum age for the isolation of the KREEP reservoir, which is the very last residual melt produced by crystallization of the Lunar Magma Ocean and the combined datasets in these two studies gave an early model age of ~4.51 Ga (Taylor et al., 2009; Barboni et al., 2017). However, the age of the moon remains to be a debated issue as the derived age of KREEP from zircon analyses is ~120 to 150 Myr older than estimates based on Sm-Nd and Pb-Pb isochrons in ferroan anorthosites (Borg et al., 2011), dating of Mg suite lunar crustal rocks (Carlson et al., 2014) and the source formation age of mare basalts (Borg et al., 2019). Moreover, this minimum age for the differentiation of the lunar crust is mostly based on four zircons with the least radiogenic Hf isotopic compositions.

In addition, there are several potential difficulties associated with the zircon approach. One is that most lunar zircons are small so that the amount of Hf available for isotopic analysis is small, and the previous analyses were done without matrix purification, which limits the precision attainable. Another is that it relies on extreme unradiogenic isotopic analyses of zircons so measurement accuracy of every single data point is critical. Previous lunar zircon εHf results were reported at 1 to 4 epsilon uncertainties (2σ). Higher precision and high-accuracy measurements are needed to provide more robust constraints on the minimum age of formation of the Moon and crystallization of the LMO.

As a part of the collaborative efforts to establish a more precise and accurate age of final solidification of the lunar magma ocean, we have developed a new analytical method on the Lu-Hf isotope systematics of single zircon grains. We use an ion exchange procedure to purify Zr and Hf from the interfering Yb and Lu elements (*e.g.* (Blichert-Toft and Albarède, 1997b; Münker et al., 2001; Iizuka et al., 2015; Vervoort and Kemp, 2016) in the digestion solutions of individual lunar zircons retrieved after U-Pb chemistry. Compared to previous procedures, this new procedure can tackle small zircons with limited amount of Hf, and the high-precision Hf isotopic analysis results in much smaller errors than applying a peak-stripping method (Barboni et al., 2017). It also has an additional advantage to allow us to recover the purified Zr for future isotopic studies.

4.2 Methods

4.2.1 Zirconium and Hafnium separation

A two-stage procedure (following the modified procedure of (Iizuka et al., 2015) and (Zhang, 2012) was developed for separating Zr and Hf. In the first step, TODGA resin is used to collect a zirconium-hafnium cut following the titanium separation methods (Zhang et al., 2011b). In the second step, Ln-Spec resin is used to further separate heavy REE, Zr and Hf (**Table 4.1**). To optimize the chemical separation procedures in the second step, calibration of elution curves were done using 1) a multi-element standard solution containing Zr, Hf and 24 other elements (including all the HFSEs and REEs). Single element ICP-MS standard solutions (Spex CertiPrep) at concentrations of 1000 µg/mL were used for preparing the standard mixture (**Fig. 4.1**). 2) Similar calibration of elution curves were also performed on the solutions retrieved after U-Pb chemistry of some terrestrial zircon standards (AS3, 91500) and synthetic zircon doped with REE (MUNZirc

32a) (**Fig 4.2**). Zirconium and Hafnium purifications of the standard mixture as well as the reference zircon solutions were conducted on a 0.35 mL Teflon column (length = 20 cm, diameter = 1.5 mm) loaded with Ln-Spec resin (100 – 150 μm). The columns were set up in a vacuum box with flow rate kept at ~1-2 mL per hour. The resin was cleaned with 18 mL of 6 N HCL + 0.06 N HF and then with 14 mL of 6 N HCL + 0.2 N HF to ensure the removal of any possible Zr and Hf in the resin before loading the sample solutions and the resin was preconditioned with 6 mL of 2.5 N HCL. The sample solutions were loaded onto the column in ~ 0.5 mL of 2.5 N HCL and matrix elements were removed with 12 mL of 6 N HCL + 1 % H_2O_2. Zirconium was first eluted in 18 mL of 6 N HCL + 0.06 N HF. Hafnium was finally eluted in 14 mL of 6 N HCL + 0.2 N HF (**Table 4.1**). Following chemical separations, the Zr cuts and Hf cuts were dried down respectively, taken back in ~1 mL of Aqua Regia (3:1 mixture of HCL:HNO_3) and dried again before being re-dissolved in concentrated HNO_3. The re-dissolved solutions were dried again to near dryness (right before complete evaporation) and taken back in 0.3 N HNO_3 + 0.07 N HF for isotopic analysis.

Table 4.1 Chromatographic extraction protocol of Zr and Hf

Step	**Volume (mL)**	**Acid**	**Step**	**Volume (mL)**	**Acid**
column 1 (2 mL TODGA; 0.8 cm diameter × 4 cm length)			**column 2** (0.35 mL Ln-Spec; 1.5 mm diameter × 20 cm length)		
Clean	10	3 M HNO3	Clean	18	6 M HCL-0.06 M HF
	10	3 M HNO3-1 wt% H2O2		14	6 M HCL-0.2 M HF
	4	H2O	Precondition	6	2.5 M HCL
Precondition	15	12 M HNO3	Load	0.5	2.5 M HCL
Load	10	12 M HNO3	Rinse matrix	12	6 M HCL-1 wt% H2O2
Rinse matrix	10	12 M HNO3	Elute Zr	18	6 M HCL-0.06 M HF
Elute Ti	10	12 M HNO3-1 wt% H2O2	Hf	14	6 M HCL-0.2 M HF
Fe	10	3 M HNO3			
Zr and Hf	20	3 M HNO3-0.3M HF			

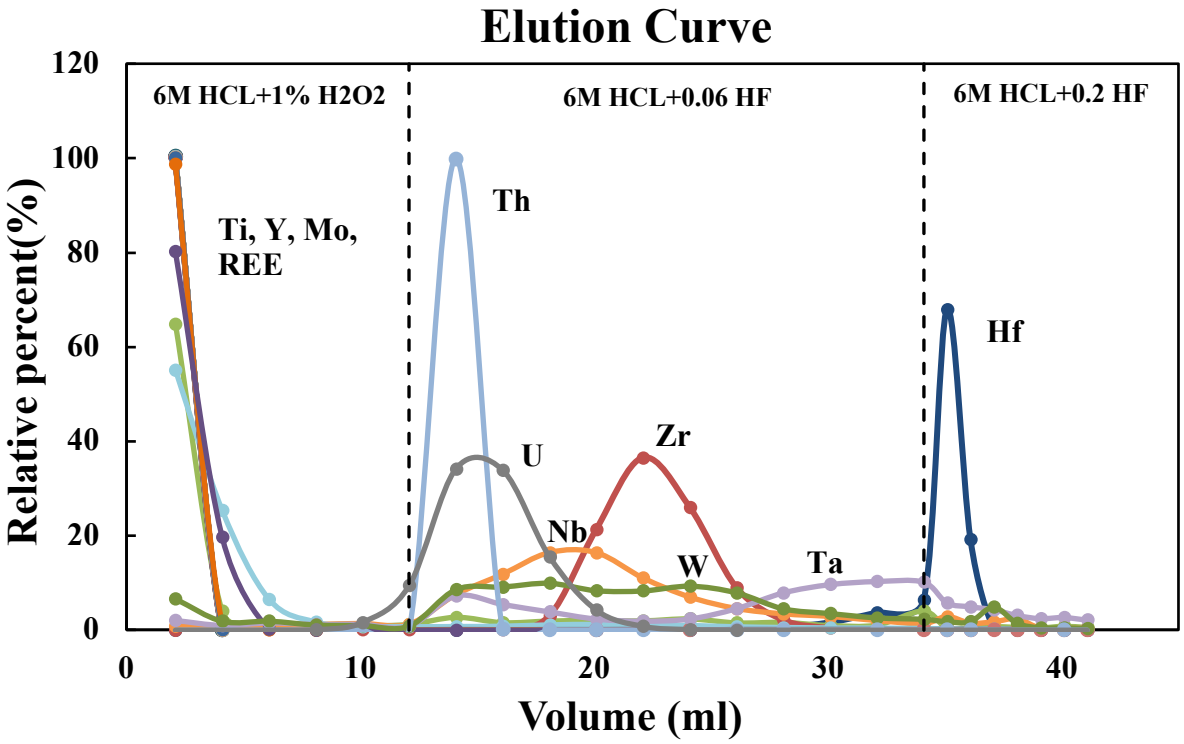

Figure 4.1 The elution curve of a multi-element standard solution on a 0.35 mL Teflon column loaded with Ln-Spec resin. Matrix elements were removed with 12 mL of 6 N HCL + 1 % H_2O_2. Zirconium was first eluted in 22 mL of 6 N HCL + 0.06N HF. Hafnium was finally eluted in 7 mL of 6 N HCL + 0.2 N HF.

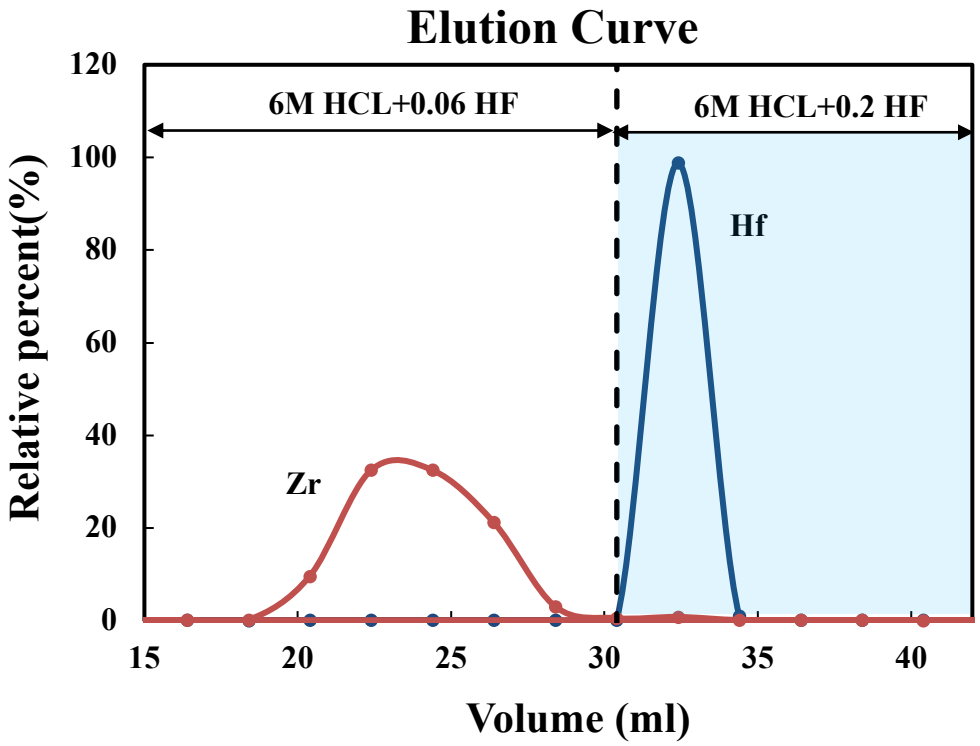

Figure 4.2 The elution curve of terrestrial zircon standard AS3 retrieved after U-Pb chemistry on a 0.35 mL Teflon column loaded with Ln-Spec resin. Matrix elements were removed with 12 mL of 6 N HCL + 1 % H_2O_2. Zirconium was first eluted in 18 mL of 6 N HCL + 0.06N HF. Hafnium was finally eluted in 7 mL of 6 N HCL + 0.2 N HF.

4.2.2 Mass spectrometry for Hf isotopic analyses

The Hf isotope analyses were performed on a Neptune Plus multi-collector inductively coupled plasma mass spectrometer (ThermoFinnigan) connected to an Aridus II desolvating nebulizer. Matrix purification drastically decreases interferences and permits the use of high-transmission Jet sample and X-skimmer cones, which enhances the sensitivity of the instrument. The purified Hf fractions were dissolved in 0.3 N HNO_3 + 0.07 N HF. The achieved sensitivity was ~2 V/10 ppb for ^{177}Hf (18.60%) at a sample uptake rate of ~100 µL/min. For isotope ratio

measurements of purified Hf fractions, the isotopes ^{174}Hf, ^{176}Hf, ^{177}Hf, ^{178}Hf, ^{179}Hf, and ^{180}Hf as well as ^{172}Yb, ^{175}Lu, and ^{184}W were monitored with static mode on nine Faraday cups. ^{172}Yb was measured to monitor the interferences from ^{174}Yb and ^{176}Yb, ^{175}Lu was measured to monitor the interferences from ^{176}Lu, and ^{184}W was measured to monitor the interferences from ^{180}W. We found that the interferences of Yb, Lu, and W on Hf isotopes are negligible due to efficient separation of Hf in the ion exchange chemistry. We ran ~1-10 ppb solutions and each measurement was done in low resolution and took 30 cycles with each cycle taking 8.389 seconds integration time. The 0.3 N HNO_3 + 0.07 N HF acid medium was measured at the beginning and end of each sequence and the average value was subtracted from subsequent sample and standard measurements. Individual sample measurements were bracketed by the analysis of JMC-Hf 475 standard solutions whose concentrations were adjusted to match those of the samples that they bracket. The Hf procedural blank was below detection limit (~5pg).

4.3 Results and Discussions

4.3.1 Correction of interferences and internal normalization for Hf isotopes

The mass bias factor (β) was calculated by normalizing the measured ^{179}Hf/^{177}Hf ratios in the samples and bracketing standards to a fixed value of 0.7325 (Patchett et al., 1982b) with an exponential mass fractionation law,

$$\left(\frac{^{179}Hf}{^{177}Hf}\right)_{measure} = \left(\frac{^{179}Hf}{^{177}Hf}\right)_{normalized\ ratio} \times \left(\frac{m_{179}}{m_{177}}\right)^{\beta}, \quad (4.1)$$

where m_{179} and m_{177} are the masses of the corresponding isotopes, and β represents the instrumental mass bias and is internally calculated cycle by cycle. The interference atoms'

contributions were calculated assuming the same mass fractionation law with Hf with $\beta_{Yb} = \beta_{Lu} = \beta_W = \beta_{Hf}$ and using the natural variations of Yb, Lu and W isotopes,

$$^{176}Yb = (^{172}Yb)_{measure} \times (\frac{^{176}Yb}{^{172}Yb})_{natural\ variation} \times (\frac{m_{176}}{m_{172}})^{\beta}\ , \quad (4.2)$$

$$^{176}Lu = (^{175}Lu)_{measure} \times (\frac{^{176}Lu}{^{175}Lu})_{natural\ variation} \times (\frac{m_{176}}{m_{175}})^{\beta}\ , \quad (4.3)$$

$$^{180}W = (^{184}W)_{measure} \times (\frac{^{180}W}{^{184}W})_{natural\ variation} \times (\frac{m_{180}}{m_{184}})^{\beta}\ , \quad (4.4)$$

Because of the efficient purification of Hf during column chemistry, the measured Yb, Lu and W in our samples were all below detection limits. The Hf isotopic ratios of all samples corrected for mass bias and interference atoms were further determined relative to the bracketing standard runs and are expressed as $\varepsilon^{174,176,178,180}$Hf, which are the deviations of the ^{174,176,178,180}Hf/^{177}Hf ratios from the standard solution (JMC-Hf 475) in parts per ten thousand,

$$\varepsilon^{i}Hf = [\frac{(^{i}Hf/^{177}Hf)_{sample}}{(^{i}Hf/^{177}Hf)_{JMC-Hf475}} - 1] \times 10^{4}\ , \quad (4.5)$$

These εHf ratios were further normalized to reference values of ^{180}Hf/^{177}Hf = 1.886666, ^{178}Hf/^{177}Hf = 1.467168, and ^{176}Hf/^{177}Hf = 0.282160 for Johnson Matthey Company (JMC)-Hf 475 (Blichert-Toft et al., 1997) to allow comparison with literature values. The external reproducibility was evaluated by daily repeated analyses of the standard bracketing by itself and all errors (2σ) are reported as 95% confidence interval (95% CI).

4.3.2 Achievable precision tests

The measurement errors directly depend on the signal intensities and it is the actual Hf concentration in the solution that affects the signal intensities. The currently achieved sensitivity was around 0.22V for ^{177}Hf (18.60%) at 1ng/g (ppb) for Hf with a sample uptake rate of ~100

μL/min. In **Fig. 4.3**, we show the theoretically achievable precision curve (solid blue line) on Hf isotopes when measuring Hf isotopic composition bracketing with JMC-475 Hf standard solution at given concentrations on a Neptune MC-ICP-MS. This is done by calculating the isotope ratio uncertainties resulting from counting statistics and Johnson noise (Dauphas et al., 2014). This theoretical limit is the minimum error when measuring Hf isotopes at certain setup of the MC-ICP-MS, corresponding to the currently achieved sensitivity. The calculated curve shows that when the signal on ^{177}Hf is less than ~0.7 V, the measurement errors on ε^{176}Hf increase drastically as the signal decreases, while when the signal on ^{177}Hf is larger than ~0.7 V, the measurement errors on ε^{176}Hf decrease steadily as the signal increases (see **Fig. 4.3A**).

We also plot the actual measurement uncertainties (2σ) of ε^{176}Hf as a function of the Hf concentration in solutions on top of the theoretical curve (see **Fig. 4.3**). The internal errors are the 2σ of JMC-475 Hf standard bracketing by itself within 30 cycles in each measurement and further taking the average of around 20-30 measurements in one sequence run. The external reproducibilities are the 2SD of JMC-475 Hf standard bracketing by itself in each sequence. There are several sequences run at different signal intensities (different Hf concentrations correspondingly), aiming at pushing the limit to measurements at very low Hf concentrations. The internal and external errors from actual measurements agree well with the theoretically achievable precisions, which demonstrates that the current instrumental setup is already at the best conditions for Hf isotopes measurements using MC-ICP-MS. This curve is also a very helpful tool to check the actual measurements in a timely manner especially when measuring precious samples.

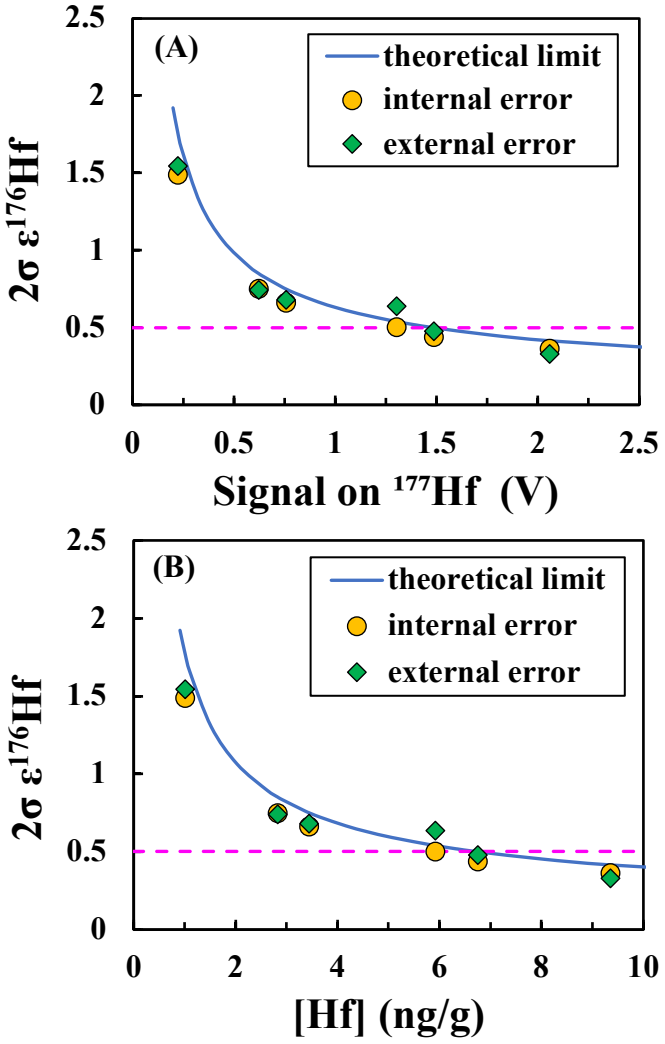

Figure 4.3 The measurement uncertainties (2σ) of ε^{176}Hf as a function of (A) ^{177}Hf signal intensity; (B) corresponding Hf concentration in the measured solutions (at the sensitivity of 0.22V for ^{177}Hf (18.60%) at 1ng/g (ppb) for Hf with a sample uptake rate of ~100 μL/min). The solid blue line is the theoretically achievable precision on ε^{176}Hf by calculating the isotope ratio uncertainties resulting from counting statistics and Johnson noise (Dauphas et al., 2014). The pink dashed line is where the 2σ equals 0.5ε. The internal and external errors from actual measurements agree well with the theoretically achievable precisions, which demonstrates that the current instrumental setup is already at the best conditions for Hf isotopes measurements using MC-ICP-MS.

4.3.3 Terrestrial zircon standards

To ensure the accuracy of our whole analytical procedure, we performed multiple analyses of three dissolved natural zircon standards (AS3, 91500 and MUD TANK) and one dissolved synthetic zircon doped with REE (MUNZirc 32a). **Fig. 4.4** shows the relative difference to the literature values (expressed in $\varepsilon^{176}Hf$) of these four zircon references (AS3, 91500, MUD TANK and MUNZirc 32a). Different data points shown for these zircon standards AS3, 91500, MUD TANK and MUNZirc 32a are their replicates processed separately through Zr-Hf column chemistry at different time. As the signal (correspondingly Hf concentration) of the measured solutions increases, the differences between measurements of zircon standards and literature reported values (Woodhead and Hergt, 2005) become smaller along with smaller uncertainties. Overall, all data points of 91500, MUD TANK and MUNZirc 32a fall within the error of their expected values from literature. Notice that **Fig. 4.4** only shows the low Hf concentration range ([Hf] up to 10 ng/g), with larger amounts of Hf available for multiple analyses, the accuracy and precision will be better than the figure shows.

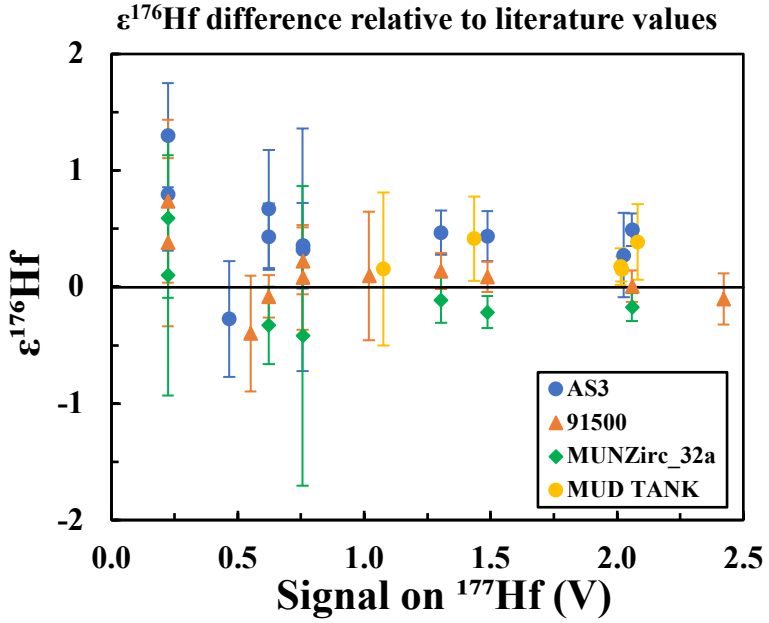

Figure 4.4 The relative difference to the literature values (expressed in ε^{176}Hf, Woodhead and Hergt 2005) of the four zircon references (AS3, 91500, MUD TANK and MUNZirc 32a) as a function of ^{177}Hf signal intensity. As the signal (correspondly Hf concentration) of the measured solutions increases, the differences between measurements of zircon standards and literature reported values (Woodhead and Hergt, 2005) become smaller along with smaller uncertainties.

4.3.4 Lunar zircons

4.3.4.1 Correction for radiogenic ingrowth and neutron capture effects for single zircon

All the precision tests and the terrestrial zircon results shown in previous sections gave us confidence of the accuracy of our measurements on Hf isotopic systematics in lunar zircons within the stated precisions.

For lunar zircons, the measured present-day ^{176}Hf/^{177}Hf values are further corrected for radiogenic ^{176}Hf ingrowth since zircon crystallization by combining TIMS high-precision U-Pb crystallization ages and Lu/Hf ratios in those samples. The Lu/Hf of each zircon was measured

using sample-standard bracketing by ICP-MS. Hf isotopic composition in single zircon is reported as $\varepsilon^{176}Hf_{CHUR}$ value, which is the deviation of the $^{176}Hf/^{177}Hf$ ratios from the chondritic uniform reservoir (CHUR) in parts per ten thousand at the identical time when zircon crystallized,

$$\varepsilon^{176}Hf_{CHUR} = [\frac{(^{176}Hf/^{177}Hf)_{zircon}}{(^{176}Hf/^{177}Hf)_{CHUR}} - 1] \times 10^4 , \quad (4.6)$$

Each $\varepsilon^{176}Hf_{CHUR}$ in zircon data is finally corrected for neutron capture (NC) effects (Sprung et al., 2010b, 2013b; Barboni et al., 2017) which mainly change the isotope ratio used for mass bias corrections (in this case $^{179}Hf/^{177}Hf$). This can cause the $\varepsilon^{176}Hf_{CHUR}$ values shift by several ε units. (i) We first followed the similar procedure done in (Barboni et al., 2017), which fitted the neutron capture induced shift in $\varepsilon^{176}Hf$ (expressed in $\Delta\varepsilon^{176}Hf$) versus the $^{178}Hf/^{177}Hf$ offset from terrestrial values (expressed in $\varepsilon^{178}Hf$) reported by (Sprung et al., 2013b) with a linear regression. And then applied this correlation to the lunar zircon $\varepsilon^{178}Hf$ data to calculate the shift in $\varepsilon^{176}Hf$ values induced by neutron capture effect. The lunar zircons analyzed in this study have offsets from 0 to 1.6 $\varepsilon^{178}Hf$ relative to the terrestrial value, resulting in $\varepsilon^{176}Hf$ values shifting from 0 to 4.2 epsilon. (ii) We also used this same rationale to fit the $\Delta\varepsilon^{176}Hf$ versus $\varepsilon^{180}Hf$ data reported by (Sprung et al., 2013b) with another linear regression. And then applied this second correlation to the lunar zircon $\varepsilon^{180}Hf$ data to calculate the shift in $\varepsilon^{176}Hf$ values induced by neutron capture effect. The lunar zircons analyzed in this study have offsets from 0 to 2 $\varepsilon^{180}Hf$ relative to the terrestrial value, resulting in $\varepsilon^{176}Hf$ values shifting from 0 to 3.1 epsilon. (iii) Since the NC-induced shifts $\Delta\varepsilon^{176}Hf$ have linear correlations with both $\varepsilon^{178}Hf$ and $\varepsilon^{180}Hf$ values, we further fitted the $\Delta\varepsilon^{176}Hf$ versus $\varepsilon^{178}Hf$ and $\varepsilon^{180}Hf$ data reported by (Sprung et al., 2013b) with a linear combination as $\Delta\varepsilon^{176}Hf = m_1 \times \varepsilon^{178}Hf + m_2 \times \varepsilon^{180}Hf$. Then once again applied this correlation to the lunar zircon $\varepsilon^{178}Hf$ and $\varepsilon^{180}Hf$ data to calculate the shift $\Delta\varepsilon^{176}Hf$ induced by neutron capture effect,

resulting in 0 to 3.2 epsilon shift. The calculated NC-induced shifts $\Delta\varepsilon^{176}Hf$ using $\varepsilon^{178}Hf$ data, $\varepsilon^{180}Hf$ data, and combing $\varepsilon^{178}Hf$ and $\varepsilon^{180}Hf$ data were all in good agreement and showed the reliability of these correction procedures (see **Fig. 4.5**).

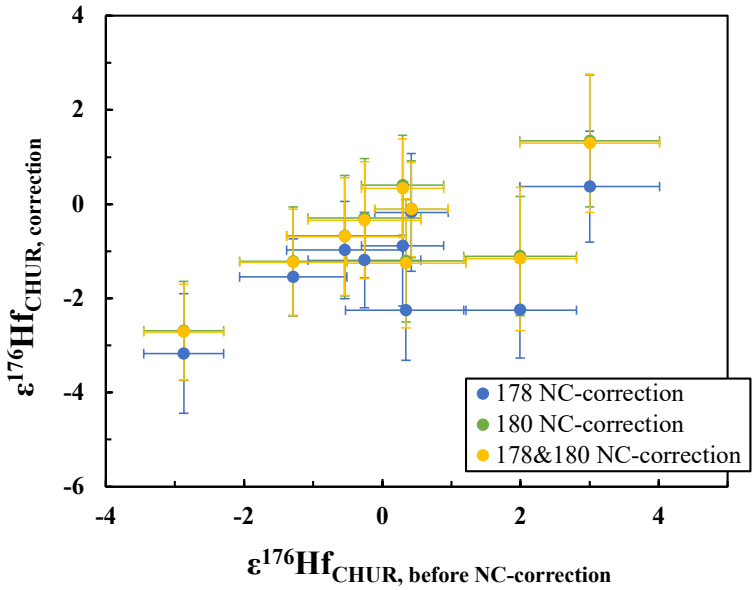

Figure 4.5 The single zircon corrected $\varepsilon^{176}Hf_{CHUR}$ values as a function of the $\varepsilon^{176}Hf_{CHUR}$ values before neutron capture corrections. Each zircon $\varepsilon^{176}Hf_{CHUR}$ value in this study was corrected for neutron capture effects using the lunar zircon $\varepsilon^{178}Hf$, $\varepsilon^{180}Hf$ and combing $\varepsilon^{178}Hf$ and $\varepsilon^{180}Hf$ values with the correlations derived from data reported by Sprung et al. (2013). The results show that the corrected $\varepsilon^{176}Hf_{CHUR}$ values using different NC-correction methods agree well with each other.

4.3.4.2 Final error propagations and improvements

Fig. 4.6 show the results of 9 lunar zircons measured in this study so far (see also **Table 4.2**). The final error of each $\varepsilon^{176}Hf(t)_{CHUR}$ value is calculated by propagating errors resulting from measurements of $^{176}Hf/^{177}Hf$, $^{178}Hf/^{177}Hf$ or $^{180}Hf/^{177}Hf$, $^{176}Lu/^{177}Hf$, crystallization age t. Besides, the uncertainties from the solar system initial $^{176}Hf/^{177}Hf$ and chondritic $^{176}Lu/^{177}Hf$ values (Iizuka

et al., 2015) are propagated through Monte Carlo Simulations and displayed as error envelopes around the CHUR evolution line. The derivations of the error propagation of each individual data point are shown below,

Hf isotopic composition in single zircon relative to the chondritic uniform reservoir (CHUR) at the time when zircon crystallized is expressed as,

$$\varepsilon^{176}Hf(t)_{CHUR} = (\left(\frac{^{176}Hf}{^{177}Hf}\right)_{zircon,t} \Big/ \left(\frac{^{176}Hf}{^{177}Hf}\right)_{CHUR,t} - 1) \times 10^4, \quad (4.7)$$

Expand the expressions of the $^{176}Hf/^{177}Hf$ ratios of zircon and CHUR at time t respectively, we have,

$$\varepsilon^{176}Hf(t)_{CHUR} = \left\{\left[\left(\frac{^{176}Hf}{^{177}Hf}\right)_{zircon,present} - \left(\frac{^{176}Lu}{^{177}Hf}\right)_{zircon} \times (e^{\lambda t} - 1)\right] / [\left(\frac{^{176}Hf}{^{177}Hf}\right)_{SS,0} + \left(\frac{^{176}Lu}{^{177}Hf}\right)_{CHUR} \times (e^{\lambda(4567.3-t)} - 1)] - 1\right\} \times 10^4, \quad (4.8)$$

where $\left(\frac{^{176}Hf}{^{177}Hf}\right)_{SS,0}$ is the solar system initial $^{176}Hf/^{177}Hf$ ratio.

Change equation (8) to logarithmic expression for error propagations,

$$\frac{\varepsilon^{176}Hf(t)_{CHUR}}{10^4} = \ln\left\{\left[\left(\frac{^{176}Hf}{^{177}Hf}\right)_{zircon,present} - \left(\frac{^{176}Lu}{^{177}Hf}\right)_{zircon} \times (e^{\lambda t} - 1)\right] / [\left(\frac{^{176}Hf}{^{177}Hf}\right)_{SS,0} + \left(\frac{^{176}Lu}{^{177}Hf}\right)_{CHUR} \times (e^{\lambda(4567.3-t)} - 1)]\right\}, \quad (4.9)$$

Then equation (9) is further simplified as,

$$\frac{\varepsilon^{176}Hf(t)_{CHUR}}{10^4} = \ln[\left(\frac{^{176}Hf}{^{177}Hf}\right)_{zircon,present} - \left(\frac{^{176}Lu}{^{177}Hf}\right)_{zircon} \times (e^{\lambda t} - 1)] - \ln[\left(\frac{^{176}Hf}{^{177}Hf}\right)_{SS,0} + \left(\frac{^{176}Lu}{^{177}Hf}\right)_{CHUR} \times (e^{\lambda(4567.3-t)} - 1)], \quad (4.10)$$

For equation (10) we denote:

$f1 = \varepsilon^{176}Hf(t)_{CHUR}$, $\mathrm{A} = \left(\frac{^{176}Hf}{^{177}Hf}\right)_{zircon,present}$, $B = \left(\frac{^{176}Lu}{^{177}Hf}\right)_{zircon}$, $C = t$ (zircon crystallization age), $D = \left(\frac{^{176}Hf}{^{177}Hf}\right)_{SS,0}$, $\mathrm{E} = \left(\frac{^{176}Lu}{^{177}Hf}\right)_{CHUR}$

Thus equation (10) becomes,

$$\frac{f1}{10^4} = \ln[\mathrm{A} - B \times (e^{\lambda C} - 1)] - \ln[D + \mathrm{E} \times (e^{\lambda(4567-C)} - 1)]\,, \tag{4.11}$$

Take the derivatives,

$$\frac{df1}{10^4} = \mathrm{d}\{\ln[\mathrm{A} - B \times (e^{\lambda C} - 1)]\} - \mathrm{d}\{\ln[D + \mathrm{E} \times (e^{\lambda(4567-C)} - 1)]\}\,, \tag{4.12}$$

$$\frac{df1}{10^4} = \frac{1}{\mathrm{A} - B\times(e^{\lambda C}-1)}\,dA + \frac{-(e^{\lambda C}-1)}{\mathrm{A} - B\times(e^{\lambda C}-1)}\,d\mathrm{B} + \left[\frac{-\lambda B e^{\lambda C}}{\mathrm{A} - B\times(e^{\lambda C}-1)} + \frac{\lambda \mathrm{E}\times e^{\lambda(4567-C)}}{D + \mathrm{E}\times(e^{\lambda(4567-C)}-1)}\right]\mathrm{dC} +$$

$$\frac{-1}{D + \mathrm{E}\times(e^{\lambda(4567-C)}-1)}\,\mathrm{dD} + \frac{-(e^{\lambda(4567-C)}-1)}{D + \mathrm{E}\times(e^{\lambda(4567-C)}-1)}\,\mathrm{dE}\,, \tag{4.13}$$

Except for the systematic errors from the CHUR parameters, the propagated error for single data point is,

$$\sigma_{f1}^2 = 10^8 \times \left[\left(\frac{\partial f1}{\partial A}\right)^2 \sigma_A^2 + \left(\frac{\partial f1}{\partial B}\right)^2 \sigma_B^2 + \left(\frac{\partial f1}{\partial C}\right)^2 \sigma_C^2\right], \tag{4.14}$$

In the last step, each $\varepsilon^{176}\mathrm{Hf}_{\mathrm{CHUR}}$ in zircon data is further corrected for neutron capture (NC) effects,

$$\varepsilon^{176}Hf(t)_{NC\ correction} = \varepsilon^{176}Hf(t)_{CHUR} + \Delta\varepsilon^{176}Hf(t)\,, \tag{4.15}$$

The neutron capture induced shift in $\varepsilon^{176}\mathrm{Hf}$ (expressed in $\Delta\varepsilon^{176}\mathrm{Hf}$) is calculated by applying the fitted correlations to the lunar zircon $\varepsilon^{178}\mathrm{Hf}$ or $\varepsilon^{180}\mathrm{Hf}$ or combing $\varepsilon^{178}\mathrm{Hf}$ and $\varepsilon^{180}\mathrm{Hf}$ data,

$$\Delta\varepsilon^{176}Hf(t) = \mathrm{slope178} \times \varepsilon^{178}Hf\,, \tag{4.16}$$

$$\Delta\varepsilon^{176}Hf(t) = \mathrm{slope180} \times \varepsilon^{180}Hf\,, \tag{4.17}$$

$$\Delta\varepsilon^{176}Hf(t) = m_1 \times \varepsilon^{178}Hf + m_2 \times \varepsilon^{180}Hf\,, \tag{4.18}$$

In equation (16) or (17) we denote:

$f2 = \Delta\varepsilon^{176}Hf(t)$, A = slope178 or A = slope180 , $B = \varepsilon^{178}Hf$ or $B = \varepsilon^{180}Hf$

Thus the propagated error resulting from neutron capture correction using equation (16) or (17) is,

$$\sigma_{f2}^2 = B^2\sigma_A^2 + A^2\sigma_B^2 , \quad (4.19)$$

Similarly in equation (18) we denote:

$f2 = \Delta\varepsilon^{176}Hf(t)$, A = m_1 , $B = \varepsilon^{178}Hf$, $C = m_2$, $D = \varepsilon^{180}Hf$

Thus the propagated error resulting from neutron capture correction using equation (18) is,

$$\sigma_{f2}^2 = B^2\sigma_A^2 + A^2\sigma_B^2 + D^2\sigma_C^2 + C^2\sigma_D^2 , \quad (4.20)$$

The final error is,

$$\sigma_f^2 = \sigma_{f1}^2 + \sigma_{f2}^2 , \quad (4.21)$$

The calculations of the contributions of each term to the final error (**Table 4.3**) show that the final error of $\varepsilon^{176}Hf(t)_{CHUR}$ is mainly determined by two error sources: $^{176}Hf/^{177}Hf$, $^{178}Hf/^{177}Hf$ or $^{180}Hf/^{177}Hf$. Besides, the value and uncertainty of the solar system initial $^{176}Hf/^{177}Hf$ are taken from literature and it is a systematic uncertainty that affect all data. As the signal on ^{177}Hf (or Hf concentration in equivalent) increases, the uncertainties of $^{176}Hf/^{177}Hf$ and $^{178}Hf/^{177}Hf$ or $^{180}Hf/^{177}Hf$ decrease, and their contributions (%) to the final error also decrease (see also **Fig. 4.3**). With higher amount of Hf available in the samples for measurements, we could thus significantly decrease the final propagated errors of each single data point.

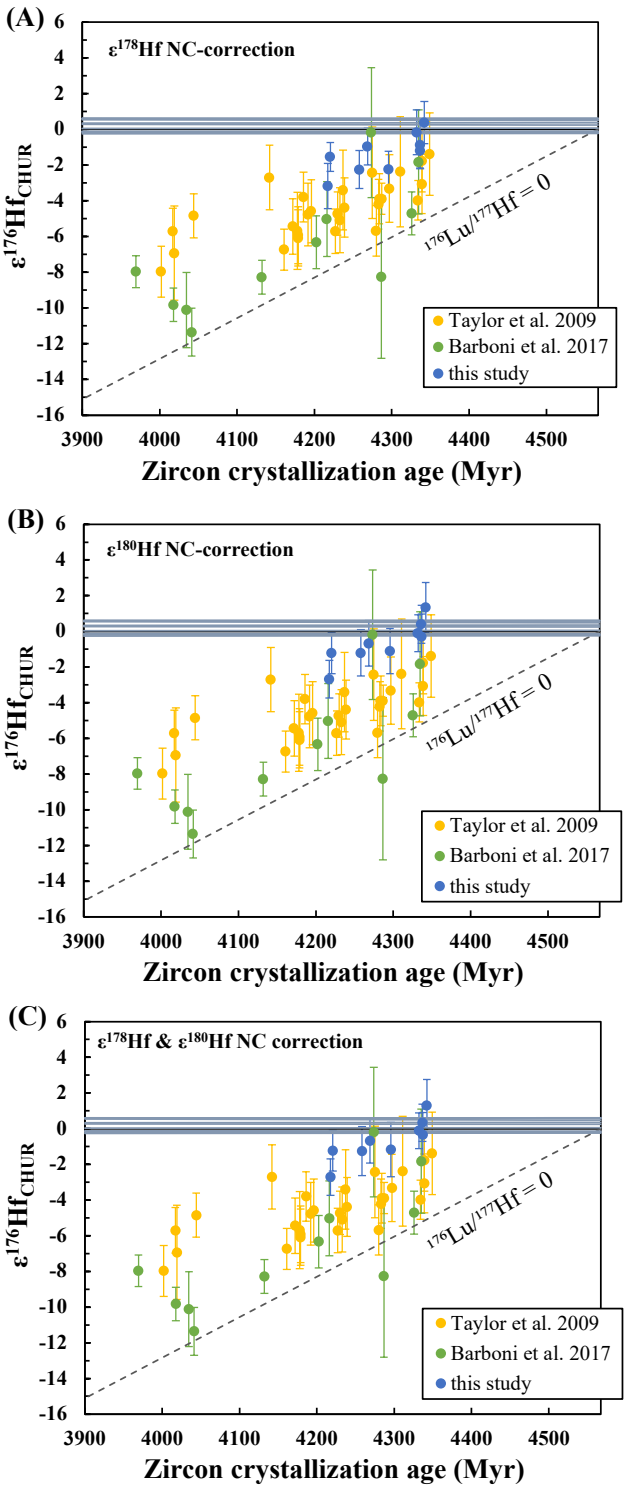

Figure 4.6 The single zircon $\varepsilon^{176}Hf_{CHUR}$ value as a function of $^{207}Pb/^{206}Pb$ zircon crystallization age (A) each zircon $\varepsilon^{176}Hf_{CHUR}$ value in this study was corrected for neutron capture effects using

Figure 4.6 *continued*
the lunar zircon $\varepsilon^{178}Hf$ value with the correlation derived from data reported by Sprung et al. (2013); (B) similar as (A) except for using lunar zircon $\varepsilon^{180}Hf$ value; (C) similar as (A,B) except for combing lunar zircon $\varepsilon^{178}Hf$ and $\varepsilon^{180}Hf$ values for the correction of neutron capture effects. All the errors are 2σ.

Table 4.2 Hf isotopic compositions of 9 lunar zircons

samples	$^{176}Hf/^{177}Hf$	2σ*	$^{178}Hf/^{177}Hf$	2σ*	$^{180}Hf/^{177}Hf$	2σ*	$^{176}Lu/^{177}Hf$	2σ
14163 Z26_L1	0.280062	0.000023	1.467316	0.000034	1.886476	0.000110	0.000648	0.000022
72275 Z1	0.280004	0.000023	1.467220	0.000034	1.886661	0.000110	0.001000	0.000026
14163 Z89	0.280077	0.000023	1.467406	0.000034	1.886312	0.000110	0.000822	0.000028
14163 Z9_L1	0.280117	0.000023	1.467192	0.000034	1.886651	0.000110	0.001958	0.000071
14163 Z26_L2	0.280037	0.000023	1.467314	0.000034	1.886489	0.000110	0.000619	0.000012
72275 Z1_L2	0.280008	0.000014	1.467234	0.000063	1.886678	0.000101	0.000868	0.000097
72275 Z1_L1	0.280017	0.000014	1.467201	0.000063	1.886606	0.000101	0.000902	0.000041
14321 Z3_L2	0.280092	0.000014	1.467185	0.000063	1.886687	0.000101	0.002074	0.000091
14321 Z3_L1	0.280087	0.000009	1.467183	0.000014	1.886674	0.000098	0.001496	0.000240

*errors reported here are the external reproducibilities of JMC-475 Hf standard

Table 4.3 Error contributions (%) of each term to the final error of ε176HfCHUR in zircon data

samples	176Hf/177Hf pre	176Lu/177Hf	age t	slope	ε178Hf
14163 Z26_L1	47.59%	0.32%	25.76%	0.360%	25.97%
72275 Z1	64.27%	0.61%	0.01%	0.061%	35.05%
14163 Z89	63.43%	0.67%	0.03%	1.250%	34.61%
14163 Z9_L1	61.90%	4.12%	0.20%	0.012%	33.77%
14163 Z26_L2	58.64%	0.12%	8.82%	0.432%	31.99%
72275 Z1_L2	16.18%	5.24%	0.11%	0.061%	78.41%
72275 Z1_L1	16.89%	0.97%	0.27%	0.016%	81.85%
14321 Z3_L2	16.35%	4.43%	0.01%	0.004%	79.21%
14321 Z3_L1	16.37%	74.60%	0.02%	0.007%	9.00%

	176Hf/177Hf pre	176Lu/177Hf	age t	slope	ε180Hf
14163 Z26_L1	33.71%	0.23%	18.25%	0.013%	47.79%
72275 Z1	41.21%	0.39%	0.01%	0.000%	58.39%

Table 4.3 *continued*

14163 Z89	41.15%	0.44%	0.02%	0.056%	58.34%
14163 Z9_L1	40.21%	2.68%	0.13%	0.000%	56.98%
14163 Z26_L2	38.91%	0.08%	5.85%	0.013%	55.15%
72275 Z1_L2	23.43%	7.59%	0.16%	0.000%	68.82%
72275 Z1_L1	24.93%	1.43%	0.40%	0.002%	73.23%
14321 Z3_L2	23.77%	6.44%	0.01%	0.000%	69.79%
14321 Z3_L1	8.07%	36.79%	0.01%	0.000%	55.13%

	176Hf/177Hf pre	**176Lu/177Hf**	**age t**	**slope m1**	**ε178Hf**	**slope m2**	**ε180Hf**
14163 Z26_L1	30.68%	0.21%	16.609%	9.40%	0.04%	3.74%	39.33%
72275 Z1	42.90%	0.41%	0.008%	1.66%	0.06%	0.00%	54.97%
14163 Z89	28.44%	0.30%	0.015%	22.68%	0.04%	12.06%	36.46%
14163 Z9_L1	42.35%	2.82%	0.136%	0.35%	0.06%	0.03%	54.27%
14163 Z26_L2	35.22%	0.07%	5.295%	10.50%	0.05%	3.72%	45.15%
72275 Z1_L2	24.08%	7.80%	0.162%	3.70%	0.28%	0.03%	63.95%
72275 Z1_L1	26.24%	1.51%	0.423%	1.02%	0.31%	0.80%	69.70%
14321 Z3_L2	25.30%	6.85%	0.012%	0.25%	0.30%	0.09%	67.19%
14321 Z3_L1	8.51%	38.77%	0.012%	0.15%	0.01%	0.01%	52.54%

4.4 Conclusions

A new procedure is developed for high-precision and high-accuracy Hf (and Zr in future) isotopic analysis in single zircon grains. Both Hf and Zr are effectively separated from heavy REE elements in the individual zircon solutions retrieved after U-Pb chemistry. The instrumental setup for MC-ICP-MS ensures the achievable precisions to reach the lowest theoretical limits and provides the ability to measure small zircons with low amount of Hf. For lunar zircon samples, the final propagated errors (2σ) of the single zircon Hf isotopic composition significantly improve to around 1 to 1.5 epsilon uncertainties. Based on the current results, we estimated that single zircon

$\varepsilon^{176}Hf_{CHUR}$ value can reach precisions within $\pm 0.7\varepsilon$ (2σ) provided that enough amount of Hf is available for measurements (~20 ng Hf in one zircon).

4.5 References

Barboni M., Boehnke P., Keller B., Kohl I. E., Schoene B., Young E. D. and McKeegan K. D. (2017) Early formation of the Moon 4.51 billion years ago. *Science advances* **3**, e1602365.

Blichert-Toft J. and Albarède F. (1997) The Lu-Hf isotope geochemistry of chondrites and the evolution of the mantle-crust system. *Earth and Planetary Science Letters* **148**, 243–258.

Blichert-Toft J., Chauvel C. and Albarède F. (1997) Separation of Hf and Lu for high-precision isotope analysis of rock samples by magnetic sector-multiple collector ICP-MS. *Contributions to Mineralogy and Petrology* **127**, 248–260.

Borg L. E., Connelly J. N., Boyet M. and Carlson R. W. (2011) Chronological evidence that the Moon is either young or did not have a global magma ocean. *Nature* **477**, 70–72.

Borg L. E., Gaffney A. M., Kruijer T. S., Marks N. A., Sio C. K. and Wimpenny J. (2019) Isotopic evidence for a young lunar magma ocean. *Earth and Planetary Science Letters* **523**, 115706.

Carlson R. W., Borg L. E., Gaffney A. M. and Boyet M. (2014) Rb-Sr, Sm-Nd and Lu-Hf isotope systematics of the lunar Mg-suite: the age of the lunar crust and its relation to the time of Moon formation. *Philosophical Transactions of the Royal Society A: Mathematical, Physical and Engineering Sciences* **372**, 20130246.

Dauphas N., Chen J. H., Zhang J., Papanastassiou D. A., Davis A. M. and Travaglio C. (2014) Calcium-48 isotopic anomalies in bulk chondrites and achondrites: Evidence for a uniform isotopic reservoir in the inner protoplanetary disk. *Earth and Planetary Science Letters* **407**, 96–108.

Iizuka T., Yamaguchi T., Hibiya Y. and Amelin Y. (2015) Meteorite zircon constraints on the bulk Lu− Hf isotope composition and early differentiation of the Earth. *Proceedings of the National Academy of Sciences* **112**, 5331–5336.

Münker C., Weyer S., Scherer E. and Mezger K. (2001) Separation of high field strength elements (Nb, Ta, Zr, Hf) and Lu from rock samples for MC-ICPMS measurements. *Geochemistry, Geophysics, Geosystems* **2**.

Patchett P. J., Kouvo O., Hedge C. E. and Tatsumoto M. (1982) Evolution of continental crust and mantle heterogeneity: evidence from Hf isotopes. *Contributions to Mineralogy and Petrology* **78**, 279–297.

Sio C., Borg L. and Cassata W. (2020) The timing of lunar solidification and mantle overturn recorded in ferroan anorthosite 62237. *Earth and Planetary Science Letters* **538**, 116219.

Sprung P., Kleine T. and Scherer E. E. (2013) Isotopic evidence for chondritic Lu/Hf and Sm/Nd of the Moon. *Earth and Planetary Science Letters* **380**, 77–87.

Sprung P., Scherer E. E., Upadhyay D., Leya I. and Mezger K. (2010) Non-nucleosynthetic heterogeneity in non-radiogenic stable Hf isotopes: Implications for early solar system chronology. *Earth and Planetary Science Letters* **295**, 1–11.

Taylor D. J., McKeegan K. D. and Harrison T. M. (2009) Lu–Hf zircon evidence for rapid lunar differentiation. *Earth and Planetary Science Letters* **279**, 157–164.

Vervoort J. D. and Kemp A. I. S. (2016) Clarifying the zircon Hf isotope record of crust–mantle evolution. *Chemical Geology* **425**, 65–75.

Woodhead J. D. and Hergt J. M. (2005) A preliminary appraisal of seven natural zircon reference materials for in situ Hf isotope determination. *Geostandards and Geoanalytical Research* **29**, 183–195.

Zhang J. (2012) *Titanium isotope cosmochemistry*., The University of Chicago.

Zhang J., Dauphas N., Davis A. M. and Pourmand A. (2011) A new method for MC-ICPMS measurement of titanium isotopic composition: Identification of correlated isotope anomalies in meteorites. *Journal of Analytical Atomic Spectrometry* **26**, 2197–2205.

5 CONCLUSIONS

Isotopic variations of various elements especially those non-traditional elements prove to be very effective in tracing geochemical processes, with generally small variations at per mil level, they are however powerful tools to address big scale questions spanning from the beginning of galaxy formation until present day, which depend upon the specific samples those variations are detected and verified. The analytical capabilities provided by the continuous improvements in instrumentations allow the geoscientists to explore more and more interesting isotopic systems with great potentials to provide new insights into our understanding of important geologic questions/problems. In this dissertation, I applied the uranium stable isotopic variations in sedimentary rocks to trace the oceanic anoxia in the past, and I explored the potential usage of zirconium and hafnium stable isotopes to trace the planetary differentiation processes from a theoretical point of view.

In the first project regarding U isotopes, it has been well understood that in the modern ocean, U reduction and incorporation into anoxic sediments causes a large isotopic fractionation which shifts the seawater $\delta^{238}U$ value relative to the riverine input of approximately +0.6 ‰. Plus the long residence time of U in the modern oceans (~400 kyr), the U isotopic composition of marine sediments reflects the global uranium balance between anoxic and other non-anoxic sinks. Thus the U isotopic compositions of open-marine carbonates, shales and Fe-Mn oxides have emerged as paleo-redox proxies to reconstruct the past changes in the redox state of the global ocean. I have measured the U concentrations and isotopic compositions of 95 carbonates spanning

ages from 3250 Ma to present, along with compilations of a large datasets of uranium in carbonates, shales and Fe-Mn oxides from literatures. With the understanding of modern uranium oceanic cycle, we expected that for the Archean and possibly Proterozoic, near-quantitative U removal to extensive anoxic sediments should have shifted uranium isotopic composition of seawater and carbonates towards lower values. Instead, our measurements reveal that many Archean and Proterozoic carbonates have unfractionated $\delta^{238}U$ values similar to those of continents and riverine runoff, and the $\delta^{238}U$ values between coeval carbonates and shales appear to be not consistent either. These results are inconsistent with the view that the U isotopic composition of seawater simply reflects the areal extent of anoxic sediments in the past.

With the first attempts in modeling U residence time and ocean mixing time in the past, we consider a plausible explanation for our measurement results, the residence time of U could have been much shorter in the Precambrian oceans when anoxic settings were much more extensive, thus the common assumptions used to reconstruct ocean paleo-redox conditions at a global scale may be invalid. And alternatively the process of incorporation of U into anoxic sediments in the Precambrian might cause a smaller U isotopic fractionation than in the modern because of differences in the efficiency or mechanism of uranium removal. Our study highlights the challenges inherent to applying knowledge of the modern marine U isotopic cycle to periods of Earth's history when ocean-floor anoxia was much more extended, anoxic basins were ferruginous, and atmospheric oxygen content was significantly lower than present.

In the second project regarding Zr and Hf stable isotopes, we use density functional theory (DFT) to calculate the equilibrium isotopic fractionation factors of zirconium (Zr) in a variety of minerals including zircon, baddeleyite, Ca-catapleiite, ilmenite, geikielite, magnetite, apatite, K-

feldspar, quartz, olivine, clinopyroxene, orthopyroxene, amphibole, and garnet. We also report equilibrium isotopic fractionation factors for Hf in zircons, Ca-catapleiite, and ilmenite. These calculations show that coordination environment is an important control on Zr and Hf isotopic fractionation, with minerals with Zr and Hf in low coordinations predicted to be enriched in the heavy isotopes of Zr and Hf, relative to those with Zr and Hf in high coordinations. At equilibrium, zircon, which hosts Zr and Hf in 8-fold coordination, is predicted to have low $^{94}Zr/^{90}Zr$ and $^{179}Hf/^{177}Hf$ ratios compared to silicate melt, which hosts Zr and Hf in 6-fold coordination. We further explore several models with these calculation results and our modeling results indicate that little equilibrium isotopic fractionation for Zr is expected during magmatic differentiation and zircon crystallization.

We show through isotopic transport modeling that the Zr isotopic variations that were documented in igneous rocks are likely due to diffusion-driven kinetic isotopic fractionation. The two settings where this could take place are (*i*) diffusion-limited crystallization of zircon (DLC model) and (ii) diffusion-triggered crystallization of zircon (DTC model) in the boundary layer created by the growth of Zr-poor minerals. Fractional crystallization of zircons enriched in light Zr isotopes by diffusion can drive residual magmas towards heavy Zr isotopic compositions. Our diffusive transport model gives the framework to interpret Zr isotope data and gain new insights into the cooling history of igneous rocks and the setting of zircon crystallization.

In the third project aiming to establish a more precise and accurate age of final solidification of the lunar magma ocean, I have developed a new analytical method using the Lu-Hf isotopic system to get the ages of single zircon grains. An ongoing effort is devoted to applying

this method on ~50 lunar zircon samples, the preliminary results indicated that the previously published old Hf model ages may suffer inaccuracies due to lack of matrix purifications.

SUPPLEMENTARY MATERIALS

These materials are available online.

Supplementary Table 1 (Chapter 2)

--Compilation of uranium concentrations and uranium isotopic compositions in carbonates, shales and iron-rich rocks.

Supplementary Movies (Chapter 3)

--Movies of the Zr concentration and Zr isotopic profiles in DLC and DTC models.